AERODYNAMIC INTERACTION EFFECTS OF A HELICOPTER ROTOR AND FUSELAGE

Grant Number: NCC-1245

Final Report
November 1999

David D. Boyd, Jr.
Senior Research Associate

Richard W. Barnwell
Professor
Virginia Polytechnic Institute and State University

Abstract

A three year Cooperative Research Agreement between the Subsonic Aerodynamics Branch of the NASA Langley Research Center and the Virginia Polytechnic Institute and State University (Va. Tech) has been completed. This document presents results from this three year endeavour.

Introduction

The development of computational methods for predicting flight performance characteristics of vehicles has been the subject of intense research for many years. During this time, computational fluid dynamics methods for realistic aircraft configurations have been developed. However, these methods typically have focused on fixed wing aircraft operating in steady state flight conditions. Prediction methods for rotorcraft have lagged far behind fixed wing methods due to the inherent unsteadiness and general complexity of rotorcraft flowfields. For example, in level, "steady" forward flight, rotor blades encounter unsteady flow due to the rotation of the blades. Even in hover, the flowfield is unsteady due to the asymmetry of the fuselage about the axis of rotation of the rotor blades.

Many methods have been developed in the past for predicting aerodynamic interactions between a rotor and a fuselage with varying degrees of success. These methods are outlined and referenced in the three Appendices to this document. In addition, the Appendices describe in detail the method developed here.

The present computational technique, which is described in the Appendices, was developed over a three year period. The following sections outline the research effort and the accomplishments made in each of the three years.

Year 1

The first year of the effort covers the period from November 1996 to November 1997. There were three primary goals set for this first period. These goals were geared toward feasibility studies, review of appropriate literature, and review of computer codes to determine the most promising path to take in the development of an efficient unsteady model. These goals were as follows:

1. Review previous work leading to the pressure disk model used in the INS3D-UP incompressible Navier-Stokes code.

2. Review the Generalized Dynamic Wake Theory (GDWT) to determine suitability for use as an unsteady pressure disk model coupled to a Navier-Stokes code.

3. Examine possible candidate Navier-Stokes codes to determine suitability for time-averaged as well as time-accurate computations using a pressure disk model.

All of these goals were accomplished in the first year. From the first item above, an understanding of the current pressure disk model was obtained. For the second item above, a new computer code was written. This code, described in detail in the Appendices, was a developed specifically to compute the unsteady inflow and unsteady pressure jump to be used in conjunction with a Navier-Stokes

computer code. Work on the third item consisted of examination of three Navier-Stokes codes. The first was INS3D, an incompressible code. While this is a versatile code, the convergence characteristics and CPU times of the code run in unsteady mode, while coupled to the GDWT, appeared to be unacceptable for the cases examined. The second code examined was CFL3D. Again, this is a versatile code and is widely used and well supported. Though the GDWT was never coupled to this code, discussions with the authors of CFL3D led to the conclusions that the current overset grid capabilities and the time-accurate convergence characteristics of the code would deem it unacceptable for the purposes of this research. The third code examined was OVERFLOW. This code is well supported and has advanced overset grid capabilities, excellent time-accurate characteristics, and a low Mach number steady state capability which are appropriate for this research. Based on these rationales, OVERFLOW was chosen as the Navier-Stokes code for this research.

Year 2

The second year of the effort covers the period from November 1997 to November 1998. Again, there were three primary goals set for this second year period. While the first year goals were geared toward feasibility studies and literature review, the second year goals focused on implementation of items from the first year. These goals were as follows:

1. Begin coupling the GDWT to the OVER-FLOW code as a time-averaged pressure disk model.

2. Implement the GDWT in the OVER-FLOW code as a time-accurate model.

3. Investigate possible extensions to the GDWT/OVERFLOW model.

All of the second year goals were completed in this year. Both the first and second items were completed and are detailed in the Appendices. A number of extensions were explored in this year as well. The paper in Appendix I was written during this second year period. It describes the time-averaged and time-accurate model used for an isolated rotor. Time-averaged and time-accurate induced inflow predictions are shown to compare well with experimental data. Results from this paper were presented at the 54th Annual Forum of the American Helicopter Society in Washington, D.C. in May 1998.

Year 3

The primary focus of the third year of the effort was refining the model and making comparisons between experimental data and predictions. Appendix II is a Ph.D. dissertation that was written in this third year. This dissertation outlines in detail the method that was developed in the first two years. Predictions of time-averaged induced inflow, time-accurate induced inflow, steady surface pressures, time-accurate surface pressures for various configurations (an isolated fuselage, an isolated rotor, and a rotor/fuselage combination) are shown to compare well with experimental data.

Summary

In conclusion, a three year Cooperative Research Agreement has been completed. The

goal of creating an efficient method to compute unsteady interactional effects between a helicopter rotor and fuselage has been accomplished. The method is capable of predicting steady and unsteady induced inflow and steady and unsteady surface pressures on rotor and fuselage configurations. Currently, due to limitations that are introduced by almost all computational Navier-Stokes models, the predictive capability of the method is limited to moderate flight speeds. Note that this limitation is placed on the method by a particular component of the model and not by the overall method itself. Very low speed flight, including hover, will require further research into reducing or eliminating computational restrictions imposed by current Navier-Stokes codes.

APPENDIX I

Rotor-Fuselage Interactional Aerodynamics: An Unsteady Rotor Model

D. Douglas Boyd, Jr.
Senior Research Associate

Richard W. Barnwell
Professor

Virginia Polytechnic Institute and State University
Hampton, VA 23681-2199

Abstract

An unsteady helicopter rotor model suitable for the study of rotor-fuselage interactional aerodynamics has been developed. The model couples a Generalized Dynamic Wake Theory (GDWT) code with a thin-layer Navier-Stokes code through an unsteady pressure jump boundary condition. The unsteady boundary condition models each rotor blade as a radially varying, time dependent pressure jump between adjacent grid planes. A non-rotating cylindrical grid is used for the isolated rotor case, and the unsteady boundary condition models the blades as a pressure jump traveling around the rotor disk. To demonstrate the coupling of the two codes, calculations are compared to experimental unsteady and time-averaged inflow data.

Notation

A_{fact}	ratio of blade area in GDWT to area used in OVERFLOW, dimensionless
c	local blade chord, dimensionless on R
e_0	total energy per unit mass per unit volume
E_{add}	additional energy per unit mass per unit volume due to P_g, dimensionless
m, r	harmonic number
$[M]$	apparent mass matrix
M	Mach number
$[L^c], [L^s]$	cosine and sine components of L-matrix
L	local load per unit span, dimensionless on $\rho\Omega^2 R^3$
n, j	polynomial number
P_g	local pressure, dimensionless on P_∞
$\bar{P}, \bar{Q}$	normalized Legendre functions
$\bar{r}$	radial location, dimensionless on R
R	rotor radius, *meters*
q_i	i-th component of perturbation velocity, dimensionless on ΩR
i	dimensionless time, dimensionless on Ω^{-1}
V_∞	freestream speed, dimensionless on ΩR
w	normal component of induced velocity, positive downward, dimensionless on ΩR
w_l	local mean normal component of induced velocity, positive downward, dimensionless on ΩR
z	coordinate normal to rotor disk plane, dimensionless on R
α, β	coefficients of the normal downwash series expansion
α_{eff}	effective angle of attack, *rad*
β_0	mean coning angle, *rad*
γ	ratio of specific heats
θ	local blade pitch, *rad*
$\theta_0, \theta_c, \theta_s$	mean and first harmonic components of local blade pitch, *rad*
λ	component of freestream normal to rotor disk, dimensionless on ΩR, positive down

---

μ	advance ratio (component of freestream velocity parallel to rotor disk), dimensionless on ΩR
$\nu, \eta, \bar{\psi}$	ellipsoidal coordinates, dimensionless
ξ	dimensionless coordinate along freestream line, positive pointing upstream from rotor
ρ	density, kg/m^3
Φ	pressure function, dimensionless on $\rho\Omega^2 R^2$
Φ^A, Φ^V	acceleration and momentum components of pressure function, dimensionless on $\rho\Omega^2 R^2$
ψ	azimuth angle, rad/sec
Ω	rotor rotational speed, rad/sec
$(\ )^*$	derivative with respect to i

Introduction

Unsteady interactional aerodynamics between a helicopter fuselage and rotor are not well understood. There exist a number of computational methodologies available to study these interactional effects. These range from superimposing isolated rotor and isolated fuselage effects to Navier-Stokes simulation of the entire problem [1-5]. Each of these methods have their respective advantages. For example, linearly superimposing the effects of an isolated rotor and isolated fuselage has the advantage of being a quick, simple method and works well when the nonlinear effects, such as flow separation, are negligible. On the other hand, Navier-Stokes simulations have the advantage of including all aspects of the flow field in a single calculation. Each of these methods also have disadvantages. For example, the superposition technique does not work well when the interactional effects are not truly linear, (e.g. with flow separation), while full simulations may take many hours or even days of CPU time to execute. The hybrid method that is presented here draws from advantages of methods on either end of the spectrum.

For typical shapes currently used for helicopter fuselages, flow separation is a common occurrence. This is typically the case even if one were to examine the isolated fuselage independent of the rotor system [6]. For isolated fuselage computations, a steady state solution is typically sought. Therefore, many of the solution acceleration techniques such as multigrid, grid sequencing, and preconditioning may be employed to obtain an economical solution to the isolated fuselage

case. However, the inclusion of the rotor system to the computation adds even another level of complexity. If only the approximation to time-averaged rotor inflow effects are desired, several methods have been developed [3, 7, 8]. If, however, viscous effects on a fuselage under the influence of unsteady rotor inflow effects are needed when separation is expected, only Navier-Stokes simulations of the entire problem including time-accurate representation of the moving blade geometry are presently available. For example, Meakin [5] used the unsteady, thin-layer Navier-Stokes equations to compute the flow field around a complete tiltrotor aircraft, including three-bladed rotors and moving overset grid systems for a hypothetical flight condition. Ahmad, et al., [9] also used the thin-layer Navier-Stokes equations to compute the unsteady blade pressures and flowfield on an isolated two-bladed rotor using moving overset embedded grids. In [6, 9] a first order time accurate scheme was used which necessitated the use of very small time steps. Even though solutions in [9] show a converged (periodic) solution in three to five rotor revolutions, 1152 time steps were required per revolution at a cost of 45 Cray C-90 hours.

The current work is designed to examine techniques to reduce the computational times required to provide unsteady calculations that include a rotor model while maintaining the capability to calculate viscous flows on a fuselage. It is not to replace the full simulations or the simpler analyses, but rather to provided an additional tool to the researcher or designer.

Method

The current method employs a hybrid approach which allows a quick assessment of the time-averaged and time-accurate rotor-fuselage interactional aerodynamics. A simple, fast-running Generalized Dynamic Wake Theory [10, 11] method is used to trim an isolated rotor and generate a time dependent pressure distribution to represent the rotor blades in the plane of the rotor disk. This set of unsteady, periodic pressures is used in a version of the thin-layer Navier-Stokes code, OVERFLOW [12], which was modified under the current effort to include an unsteady pressure jump boundary condition between adjacent planes in a non-rotating cylindrical grid for the isolated rotor.

GDWT

Details of the GDWT can be found in [10, 11]; however, for completeness, an outline of the theory is given here. In addition, the current method of time integration of the GDWT equations is presented as is the current method of trimming the rotor to specified thrust, roll, and pitch moments.

The GDWT [10, 11] begins with the mass conservation equation and the incompressible, linearized Euler equations:

$$q_{i,i} = 0 \qquad (1)$$

$$\overset{*}{q}_i - V_\infty q_{i,\xi} = -\Phi_{,i} \qquad (2)$$

where repeated subscripts imply that the summation convention is being used and commas imply that derivatives are being taken. The pressure function, Φ, can be split into two components, Φ^A and Φ^V corresponding respectively to the two terms on the left hand side of equation (2), each of which satisfies Laplace's equation. The boundary conditions are that the pressure function matches the known blade loading at the rotor and that it equals zero at infinity.

When written in ellipsoidal coordinates, the solution to Laplace's equation for the pressure potential on a circular planform, along with the conditions that the pressure perturbation equals zero at infinity and that the pressure potential is zero at the edge of the planform, can be written in closed form as follows:

$$\Phi = -\frac{1}{2} \sum_{m=0}^{\infty} \sum_{n=m+1, m+3, \ldots}^{\infty} \bar{P}_n^m(\nu) \bar{Q}_n^m(i\eta)$$

$$[\tau_n^{mc} \cos(m\bar{\psi}) + \tau_n^{ms} \sin(m\bar{\psi})] \qquad (3)$$

where ν, η, and $\bar{\psi}$ are dimensionless ellipsoidal coordinates, $\bar{P}$ and $\bar{Q}$ are normalized Legendre functions, τ_n^{mc} and τ_n^{ms} are the unknown coefficients of the cosine and sine functions and are themselves functions of the dimensionless time variable, i. Since Φ^A and Φ^V each satisfy Laplace's equation, equation (3) can be applied to Φ^A and Φ^V separately. Examining only the normal component of the perturbation velocity and integrating along a streamline from a point on the rotor disk back to infinity, leads to the following equations for the normal component of perturbation velocity:

$$w = -\frac{1}{V_\infty} \int_0^\infty \frac{\partial \Phi^V}{\partial z} d\xi \qquad (4)$$

$$\overset{*}{w} = -\frac{\partial \Phi^A}{\partial z}\bigg|_{\eta=0} \qquad (5)$$

where $(\ )^*$ denotes a derivative with respect to dimensionless time and z is the direction normal to the rotor disk. Expanding the w component of velocity in an expansion similar to that used for Φ and superimposing the Φ^A and Φ^V components results in the following set of first order differential equations for the unknown, time-dependent coefficients ("states" of

the model), α and β, of the w velocity component expansion:

$$[M]\{\overset{*}{\alpha}_j^r\} + [L^c]^{-1}\{\alpha_j^r\} = \{\tau_n^{mc}\} \qquad (6)$$

$$[M]\{\overset{*}{\beta}_j^r\} + [L^s]^{-1}\{\beta_j^r\} = \{\tau_n^{ms}\} . \qquad (7)$$

Closed form expressions for $[M]$, $[L^c]^{-1}$, $[L^s]^{-1}$, τ_n^{mc}, and τ_n^{ms} are given in [10, 11]. As described in references 10 and 11, the τ functions depend on the loading model chosen by the user. The following loading model is used:

$$\alpha_{eff} = \theta - \frac{\left(w_I - \lambda + \beta_0 \mu \cos\psi - \frac{c\theta}{2}\right)}{\bar{r} + \mu \sin\psi} \qquad (8)$$

$$\theta = \theta_0 + \theta_c \cos\psi + \theta_s \sin\psi \qquad (9)$$

$$L = \frac{\pi c (\bar{r} + \mu \sin\psi)^2}{\sqrt{1 - M^2}} \alpha_{eff} \qquad (10)$$

This loading model includes angle of attack effects due to (1) the freestream component of inflow normal to the disk, (2) the induced inflow feedback from the GDWT, (3) the mean coning angle of the blades, (4) the pitch rate, (5) the tangential velocity variations due rotor rotation, and (6) the increase in lift with Mach number. In equation (10), a lift curve slope of 2π has been assumed. A very simple stall model is also included in the method whereby the effective angle of attack is not allowed to increase above 10 degrees. However, it has been found that, for the cases presented here, the results from this model are not sensitive to the 10 degree maximum angle of attack.

Also described in these references is a technique to generalize equations (6) and (7) to include effects of the mean induced inflow on the wake skew angle. It is this non-linear version of the GDWT that is used in the results presented in this paper.

Equations (6) and (7) form a set of first order ordinary differential equations that can be solved by various techniques. Here, a Jameson-style Runge-Kutta integration [13] is used to solve for α and β, and thus for w, at each successive time step. Time integration is carried out over a specified number of rotor revolutions. That leads to the complete loading and downwash solution on the rotor disk. This loading information is in turn used in an outer trim loop for the isolated rotor.

The rotor trim condition is determined using a modified Newton-Raphson technique [14]. In this technique, the rotor state is first determined based on a specified collective, lateral, and longitudinal pitch setting. These controls are then each perturbed

independently to form a "derivative matrix" which is used to determine the successive collective, lateral, and longitudinal pitch settings for the rotor based on the changes noted in the rotor thrust, roll, and pitch moments due to the control perturbations. These successive determinations of the pitch settings are continued until the rotor is trimmed to within a specified root-mean-square change in the thrust, roll, and pitch moments. This trim technique is classified as a *modified* Newton-Raphson technique since the derivative matrix is held fixed throughout the trim procedure rather than being recalculated at each step of the iteration as it would be done in a classic Newton-Raphson method.

Once the rotor has been trimmed, the unsteady loading and unsteady downwash are known for the entire rotor disk. The unsteady downwash has a frequency content consistent with the specified number of harmonics and shape functions chosen by the user in the GDWT method. Four harmonics provide good correlation between predicted and measured downwash when using a loading model that assumes the blades are modeled as a "pressure delta function" or pressure spike traveling around the rotor azimuth. This is the method used in this paper. In addition, since the non-linear version of the GDWT is used, the calculated loading is coupled to the calculated downwash. Thus, the loading, which initially was two-dimensional, has now been corrected to account for effects up to a frequency of four per revolution. It is this discrete, unsteady rotor disk pressure distribution which is to be used as a boundary condition in the thin-layer Navier-Stokes code.

OVERFLOW

In this section, the thin-layer Navier Stokes code, OVERFLOW, and the method used to couple OVERFLOW to the GDWT code is discussed.

For purposes of this study, the thin-layer Navier-Stokes code, OVERFLOW (version 1.7v), was chosen as a baseline code based on its robustness, its convergence times for unsteady cases, and its low Mach number capabilities. For this study, this version of OVERFLOW was modified to include an unsteady pressure jump boundary condition. This boundary condition is applied between two user specified planes which are separated by a user specified "iblanked" plane. (As is common practice, an "iblanked" region is one which is assumed to be outside the computational domain and in which no computations are performed.) The new boundary condition is implemented as an . additional energy term which is added to the quantity ρe_0 in the following form:

$$E_{add} = \frac{P_g A_{fact}}{\gamma - 1} \qquad (11)$$

where P_g is the dimensionless pressure determined by the local load per unit span (from the GDWT code) divided by the local blade segment chord at the current grid point, γ is the ratio of specific heats, and A_{fact} is the ratio of the total blade area in the GDWT to the total area on which the pressure is applied in OVERFLOW in order to maintain the same overall thrust between the two methods. For the two specified planes where the boundary condition is applied, one half of the additional energy term is placed on each plane. The code is then executed in the time-accurate mode until a periodic inflow solution is obtained.

Code Coupling

In the current effort, the GDWT code and OVERFLOW are used together in a "loose" coupling. That is, the GDWT code and OVERFLOW are both stand-alone codes that are executed sequentially. Since the GDWT code calculates the isolated rotor trim loading, a trim calculation is not needed in OVERFLOW. Thus, OVERFLOW is required only to execute enough time steps to obtain a periodic solution.

The common link between the two codes is that the same rotor system pressure distribution is used in each; the GDWT calculates a pressure distribution that is subsequently used in OVERFLOW. However, there is a difference in how the pressure distributions are used in each code. The GDWT, as applied here, assumes a that the loading is a delta function at the mid-chord of the blade, whereas OVERFLOW assumes that the loading is applied on grid line which has associated with it an area "wedge" in the cylindrical grid used for the rotor. In addition, the GDWT uses the linearized Euler equations and OVERFLOW uses the Navier-Stokes equations. Therefore, the common pressure distribution when used in each code will produce slightly different inflow characteristics due to the slightly different physical assumptions. Since the GDWT does not include a fuselage model, it will be necessary to iterate between the two codes when a fuselage is introduced into the OVERFLOW solution. An iterative capability has been implemented in the codes, but is not necessary in the present work since only the isolated rotor case is shown.

In order to include fuselage effects in the GDWT, an iterative technique has been developed in which the inflow from the GDWT and OVERFLOW are compared on a similar frequency basis. Since the GDWT provides inflow information only up to user specified frequency, the inflow calculated by OVERFLOW is filtered to match the GDWT frequency for purposes of the comparison. A difference is taken between the GDWT inflow and the filtered OVERFLOW inflow. This difference is then used in the GDWT code as an "inflow

correction" to account for differences in the two codes and assumptions made therein. The GDWT code is re-executed, and the entire procedure may be repeated as needed.

Experimental Data

All of the experimental data used in this paper are from laser velocimeter inflow measurements obtained at the NASA Langley 14- by 22-Foot Tunnel [15]. Two different blade planforms were used in the test, one tapered and one rectangular. Only the data for a rotor with a 4-bladed, tapered planform is presented in this paper. This rotor has constant chord (3.15 inches) over the inboard 75 percent of the span and an approximately 3-to-1 taper ratio over the outer 25 percent of the span such that the tip chord is approximately one inch. The blades have a linear twist of -13 degrees, a root cutout at 25 percent span, a solidity of 0.0977 and radius of 32.5 inches. The thrust coefficient was 0.0065. Inflow data used here were taken in a plane approximately 2.6 inches above the tip path plane of the rotor for all azimuth stations 30 degrees apart and at a number of radial stations. The flight condition chosen for this comparison has a 3 degree nose down shaft tilt and an advance ratio of 0.23. Data samples were processed at a resolution of 128 samples per revolution or about every 2.8 degrees of blade travel.

Results

GDWT Time-Averaged Results

In this section, results will be presented from the GDWT code before the coupling with OVERFLOW.

Figure 1 shows a contour plot comparison between the time-averaged, measured inflow ratio and the GDWT code prediction for the baseline case. For the GDWT calculations, 4 harmonics and 15 states were used. It can be seen that many of the major time-averaged flow features are captured, as discussed in [16]. An upwash region can be see along the front of the disk in both the measurement and in the prediction. The prediction matches the location of the zero induced inflow ratio line well, but the predicted gradients of the inflow, especially on the advancing and retreating sides, are higher than the gradients of the inflow in the measured data. Other features such as the strong downwash region in the first quadrant are predicted well. Some of the discrepancies in the inflow distribution can be attributed to the fact that there was a fuselage body and hub present when the experiment was conducted [16], but the GDWT in this case includes no fuselage or hub effects.

GDWT Time-Accurate Results

Figure 2 shows a comparison of the measured and predicted unsteady inflow ratio with mean inflow ratios removed for nine experimental measurement locations. The measurements are located above the rotor plane along 3 radial lines at azimuth angles of 30, 180, and 300 degrees and at 3 spanwise locations of r/R=0.60, 0.78, 0.90. These measurement locations are marked with the letters A-J (excluding the letter I) on figure 1. In all of the plots in figure 2, the measured and predicted data show a general four per revolution oscillation in the inflow as is expected for a four bladed rotor. The locations D-F (r/R=0.78) in this figure show that predictions of unsteady inflow peak-to-peak magnitudes and phases are predicted well. For all of the plots in this figure, good phase predictions are displayed, but peak-to-peak predictions are not as good. The measured data generally show sharp blade passage pulses at the beginning of each oscillation cycle. The predictions using the GDWT in this manner are not expected to predict these sharp blade passage pulses, since only the first four harmonics of inflow are being computed (i.e., only 15 states in the GDWT model are used). However, the discrete loading distribution used in the GDWT to calculate the inflow is not as strongly affected by the number of harmonics used. It is these loading values that are to be used in OVERFLOW. It has been shown that using many more states can improve the correlations of the time-accurate inflow [17]; but the corresponding improvement in the loading distribution is much smaller and hence much less necessary. The results presented in figures 1-2 give a general confidence that the GDWT code is working correctly.

OVERFLOW Time-Averaged Results

With the loading predictions from the GDWT code, OVERFLOW is executed in two stages. First, to minimize the number of time steps required to converge to a periodic solution, a mean flow is established by using a steady-state computation with a constant pressure jump equivalent to an equal distribution of thrust on the rotor. Then, the case is restarted in time-accurate mode using the GDWT determined unsteady pressure jump boundary condition. For the cases presented here, the grid topology consists of a single stretched cylindrical grid which extends 1.5 rotor radii above and below, 2.5 rotor radii ahead and to either side of, and 4.5 rotor radii behind the rotor (see figure 3). A grid size of 115x129x56 was used in the vertical, azimuthal, and radial directions, respectively. The rotor portion of the grid is in the vertical center of the grid and occupies a grid of 129x30 (minus the inner 6 radial stations, to account for the blade root cutout). A

freestream/characteristic (Reimann invariant) boundary condition was used at the outer boundaries; a periodic boundary condition was used at the $\psi=0$ degrees location; an axis boundary condition was used along the rotor axis; the new unsteady boundary condition was used along two planes in the vertical center of the grid (separated by a single, iblanked plane of the same size as the rotor planes) and extends from the root cutout location to the rotor edge. For all of the cases examined here, 1408 time steps (a multiple of the number of time steps per revolution) were sufficient to obtain a converged steady state solution. Here, convergence was determined by a two order of magnitude drop in the L2-norm of the residual. Though typically a larger residual drop considered crucial to a converged solution, a two orders of magnitude drop in residual is sufficient here due to the small values of the initial residual. This steady state calculation was then followed by two revolutions of unsteady calculations, which was sufficient to obtain periodicity in the solution.

The computations presented use the following methods in OVERFLOW: (1) central difference calculations of the right-hand side of the equations, (2) 3-factor diagonal left-hand side inversion, (3) a matrix dissipation scheme, and (4) Newton sub-iterations.

Figure 4 shows a contour plot comparison between the time-averaged, measured inflow ratio and the OVERFLOW prediction which has been filtered to contain the same frequency content as the GDWT prediction presented in figure 1. For purposes of comparisons later in the paper, this case is referred to as the "baseline case". Since the highest frequency available in the measured time-averaged contour plot is six per revolution (due to Nyquist cut-off considerations), this filtering also places the OVERFLOW prediction on a frequency basis similar to those measured data. Generally, the major time-averaged features seen in figure 1 are also seen in the figure 4. It can be seen in figure 4 that the location of the zero induced inflow line is not as well predicted, but the overall levels are well predicted. Also, in contrast to the results presented in figure 1, the gradients of inflow (spacings between the contour lines) are predicted well. As with the GDWT time-averaged results presented earlier, some of the discrepancies in the flow field can be attributed to the fact that the experimental data includes the effects of a fuselage and hub. An example of these discrepancies can be seen on the retreating side of the rotor disk near the center of the contour plot. At that location in the predicted results, a region of near zero inflow can be seen which is not present in the measured data. Since the predictions do not use a hub or hub wake model, there are no hub blockage effects in the flowfield and the flow is free to travel through the center of the

rotor disk where there is no blade loading. Since it is the rotor loading and hub/fuselage blockage effects that actually cause the induced inflow flowfield, it can be deduced that the near zero inflow region near the center of the rotor disk is at least partially caused by the low loading and lack of hub model in the hub region.

OVERFLOW Time-Accurate Results

Figure 5 shows a comparison of the measured unsteady inflow and the predicted unsteady inflow. In these plots, the sharp blade-passage pulses are seen at the beginning of each oscillation cycle, and the magnitudes and phases of these pulses are predicted well.

Sensitivities

To show the sensitivity of the above results to particular parameters related to the solution procedure, several of the relevant parameters pertaining to the solution procedure are explored. They include the number of Newton sub-iterations, the use of viscous terms, the time step (azimuthal resolution) used, and the outer boundary condition used. In addition, the amount of CPU time required for each case is presented.

Newton Sub-iterations

In the case presented above, six Newton sub-iterations were used at each time step in the unsteady portion of the calculations. To demonstrate that six sub-iterations is sufficient, the baseline case was re-executed with ten sub-iterations (instead of six) starting from the same steady state conditions. Figure 6 shows the normalized L2-norm of the conservative variables *versus* Newton sub-iteration number for the last time step in the case. It can be seen that there is little advantage to using more than six Newton sub-iterations. This is further demonstrated by figures 7 and 8, which show that there is virtually no difference in the time-averaged or time-accurate inflows. Thus, the use of six Newton sub-iterations is adequate for the current case.

Viscous Terms

Since the case presented here is an isolated rotor with no surface in the flowfield, viscous terms in the flow solver were not used. To show that these terms are not dominant in this particular case, the above baseline case was re-executed with all of the thin-layer viscous terms activated in the flow solver. Figures 9-10 demonstrate that these terms are not a dominant influence in the isolated rotor case. However, these viscous terms will be required when a fuselage or other solid surface is introduced into the solution.

Time Step

All of the above cases used 128 time steps per revolution. To test the adequacy of this time step (and azimuthal resolution), the entire case were re-executed with a doubled time step, *i.e.*, with 64 azimuth steps per revolution. The resulting time averaged and time accurate calculations are shown in figures 11-12. Both of these figures show that 64 time steps per revolution is adequate to capture the gross features of the time averaged and time accurate inflow. Due to the similarities between the 64 time step per revolution case and the original 128 time step per revolution case, it appears that the 128 time step per revolution case is quite adequate for these predictions.

Outer Boundary

In all of the above cases, the outer boundary is relatively close in proximity to the rotor disk. This raises a question as to the effect of the outer boundary on the solution. To demonstrate the effect of the outer boundary on the solution, the boundary condition there was changed from a Reimann invariant (freestream/characteristic) condition to simply a freestream condition and the baseline case was re-executed. Figures 13-14 show the results of the computations with the freestream outer boundary condition. Figure 13 shows a good match with the baseline time averaged plot. In figure 14, it can be seen that there is a slight blade-to-blade difference at the beginning of the revolution which disappears by the end of the revolution. This is evidence that, formally, one more revolution should be calculated, however, for the remaining blade passages, it can be seen that the gross effects of the outer boundary condition on the unsteady inflow are small. This implies that the solution is relatively insensitive to what is happening at the outer boundary.

CPU times

All of the steady and unsteady calculations using OVERFLOW were run on a Cray C-90. Table 1 shows a comparison of the CPU times for each of the cases presented above. As can be seen in the table, the CPU time required is relatively inexpensive.

Table 1:

Case	CPU (hr:min)
Baseline	4:16
Newton Sub-iteration	5:39
Viscous Terms	5:01

Table 1:

Case	CPU (hr:min)
Time Step	1:38
Outer Boundary	4:06

Concluding Remarks

(1) An unsteady helicopter rotor model using an unsteady pressure jump boundary condition has been developed and included in the thin-layer Navier-Stokes, overset grid code, OVERFLOW.

(2) Even though isolated rotor calculations are presented here for the purposes of demonstrating the model, excellent agreement is shown between time averaged and unsteady measured and predicted inflow ratios at a plane above the rotor disk, and CPU requirements for the isolated rotor method are found to be reasonable.

(3) It has been demonstrated that suitable parameters were chosen with regard to the number of Newton sub-iterations used, the viscous terms used, the time step used, and the outer boundary conditions used.

Acknowledgments

References

[1] Berry, J.D., "A Method of Computing the Aerodynamic Interactions of a Rotor-Fuselage Configuration in Forward Flight," Doctor of Philosophy Thesis, Georgia Institute of Technology, Atlanta, GA, May 1990.

[2] Berry, J.D., Letnikov, V.B., Bavykina, I., Chaffin, M.S., "A Comparison of Interactional Aerodynamics Methods for a Helicopter in Low Speed Forward Flight," Proceedings of the 23rd European Rotorcraft Forum, Volume 1, pp. 33.1-33.9, September 16-18, 1997, Dresden, Germany.

[3] Chaffin, M.S., Berry, J.D., "Navier-Stokes Simulation of a Rotor Using a Distributed Pressure Disk Method," 51st Annual Forum Proceedings, Volume 1, American Helicopter Society, pp 112-136, May 1995.

[4] Boyd, Jr., D.D., Brooks, T.F., Burley, C.L., Jolly, Jr., J.R., "Aeroacoustic Codes for Rotor Harmonic and BVI Noise - Camrad.Mod1/HIRES: Methodology and Users' Manual," NASA TM 110297.

[5] Meakin, R., "Moving Body Overset Grid Methods for Complete Aircraft Tiltrotor Simulations," Paper AIAA-93-3350, Presented at the 11th AIAA Computational Fluid Dynamics Conference, June 6-9, 1993, Orlando, FL.

[6] Chaffin, M.S., Berry, J.D., "Navier-Stokes and Potential Theory Solutions for a Helicopter Fuselage and Comparison With Experiment," NASA TM 4566, June 1994.

[7] Rajagopalan, R.G., Mathur, S.J., "Three Dimensional Analysis of a Rotor in Forward Flight," Journal of the American Helicopter Society, July 1993.

[8] Zori, L.A.J., Rajagopalan, R.G., "Navier-Stokes Calculations of Rotor-Airframe Interaction in Forward Flight," Presented at the 48th Annual Forum of the American Helicopter Society, Washington, D.C., June 1992.

[9] Ahmad, J., Duque, Earl, P.N., "Helicopter Rotor Blade Computation in Unsteady Flows Using Moving Embedded Grids," AIAA Paper 94-1922, Presented at the 12th AIAA Applied Aerodynamics Conference, Colorado Springs, CO, June 20-22, 1994.

[10] Peters, D.A., Cheng, J.H., "Finite State Induced Inflow Models Part II: Three Dimensional Rotor Disk," Journal of Aircraft, Volume 32, Number 2, March-April 1995.

[11] Peters, D.A., Boyd, Jr., D.D., Cheng, J.H., "Finite State Induced Inflow Model for Rotors in Hover and Forward Flight," Presented at the 43rd Annual Forum of the American Helicopter Society, St. Louis, MO, May 18-20, 1987.

[12] Buning, P.G., Jespersen, D.C., Pullium, T.H., Chan, W.M., Slotnick, J.P., Krist, S.E., Renze, K.J., "OVERFLOW User's Manual: Version 1.7v," June 11, 1997.

[13] Walters, R.W., "Class Notes for AOE 6145 - Computational Fluid Dynamics I," Department of Aerospace and Ocean Engineering, Virginia Polytechnic and State University, Fall 1994.

[14] Johnson, W., "A Comprehensive Analytical Model of Rotorcraft Aerodynamics and Dynamics Part I: Analytical Development," NASA TM 81182, June 1980.

[15] Althoff, S.L., Elliott, J.W., Sailey, R.H., "Inflow Measurement Made with a Laser Velocimeter on a Helicopter in Forward Flight," Volumes V, NASA TM 100545, April 1988.

[16] Peters, D.A., He, C.J., "Correlation of Measured Induced Velocities with a Finite-State Wake Model," Presented at the 45th Annual National Forum of the American Helicopter Society, Boston, MA., May 1989.

[17] He, C.J., "Development and Application of a Generalized Dynamic Wake Theory For Lifting Rotors," Ph.D. Thesis, Aerospace Engineering Department, Georgia Institute of Technology, Atlanta, GA, July 1989.

Measured　　　　　　　　　**Predicted**
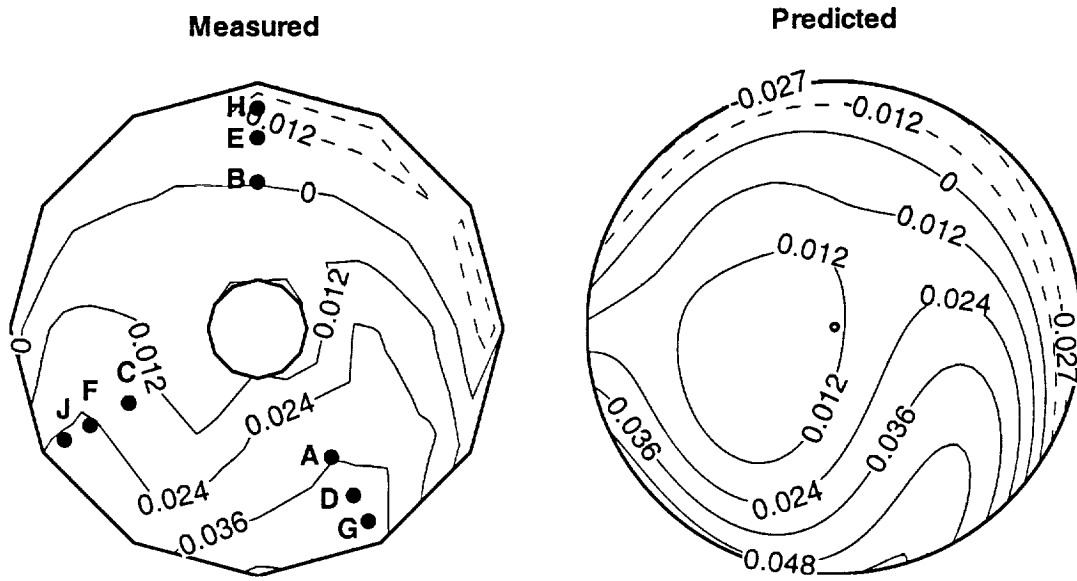
Figure 1: Measured and GDWT Predicted Time Averaged Inflow Ratio

r/R = 0.60

.... Measured
————— Predicted

Location A Location B Location C

r/R = 0.78

Location D Location E Location F

r/R = 0.90

Location G Location H Location J

Ref. Blade Location Ref. Blade Location Ref. Blade Location
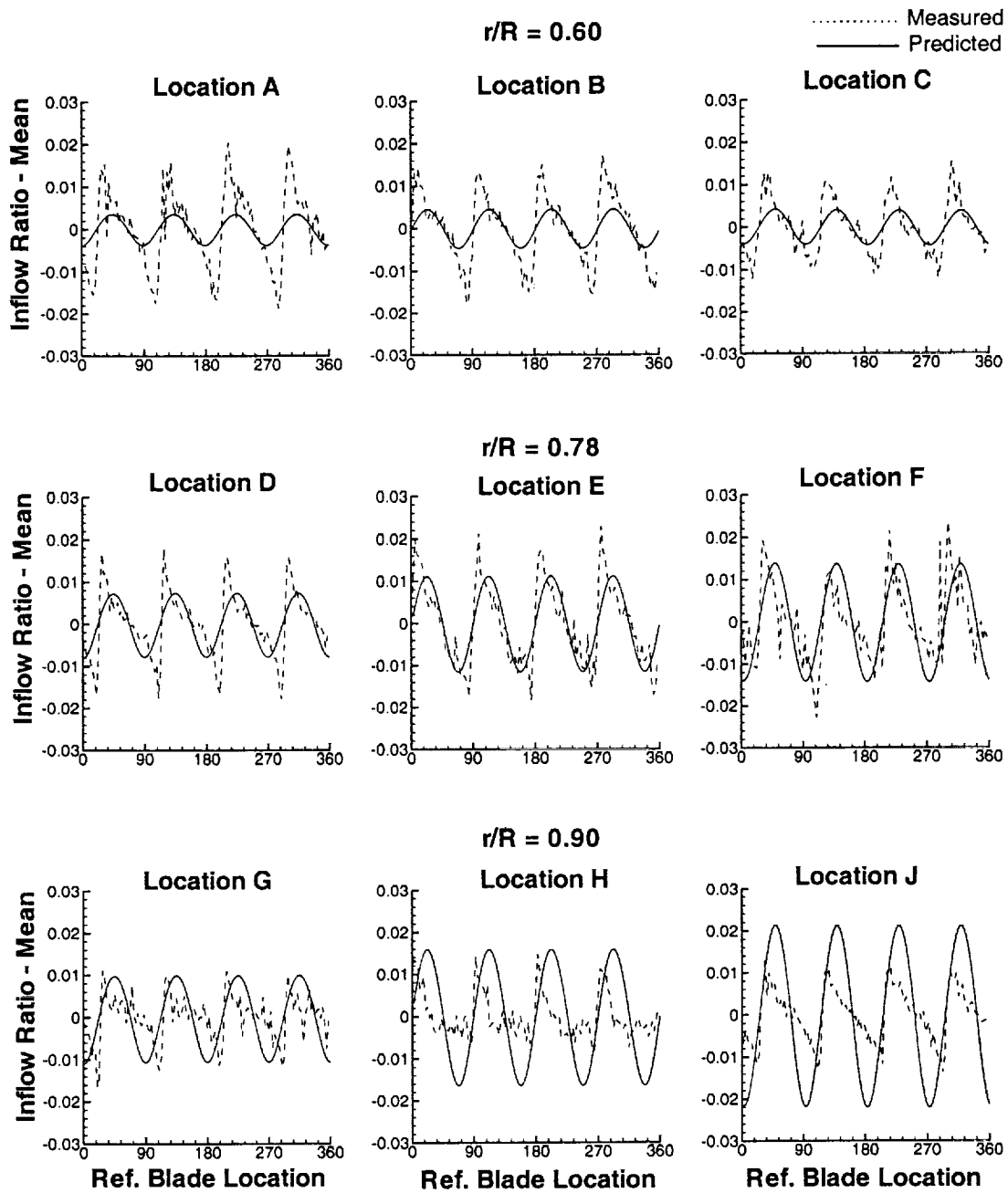
Figure 2: Measured and GDWT Predicted Time Histories of Induced Inflow for Azimuth Angles of 30, 180, and 300 degrees at Three Radial Stations of r/R = 0.60, 0.78, 0.90
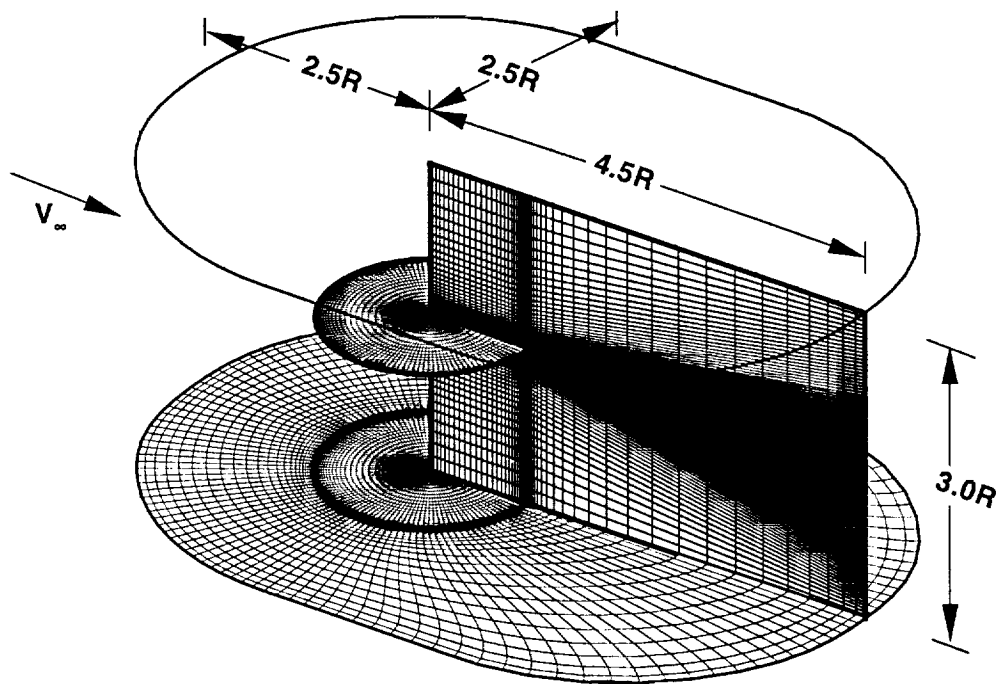
Figure 3: Schematic of Isolated Rotor Grid Topology as Viewed from Behind and Above Rotor on the Retreating Side

Measured

**Predicted
(Baseline)**
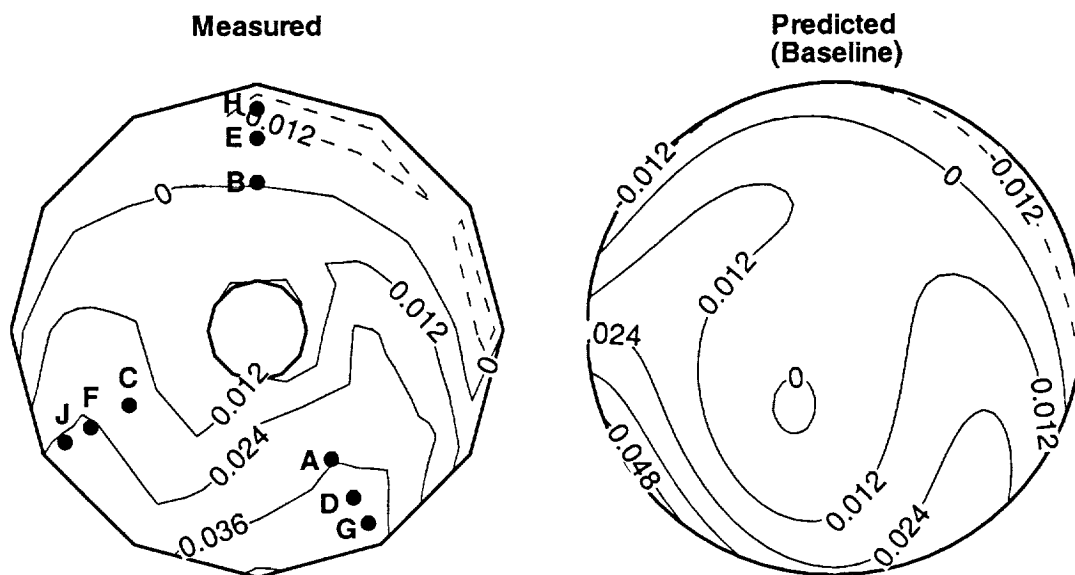
Figure 4: Measured and OVERFLOW-GDWT Predicted (Baseline) Time Averaged Inflow Ratio
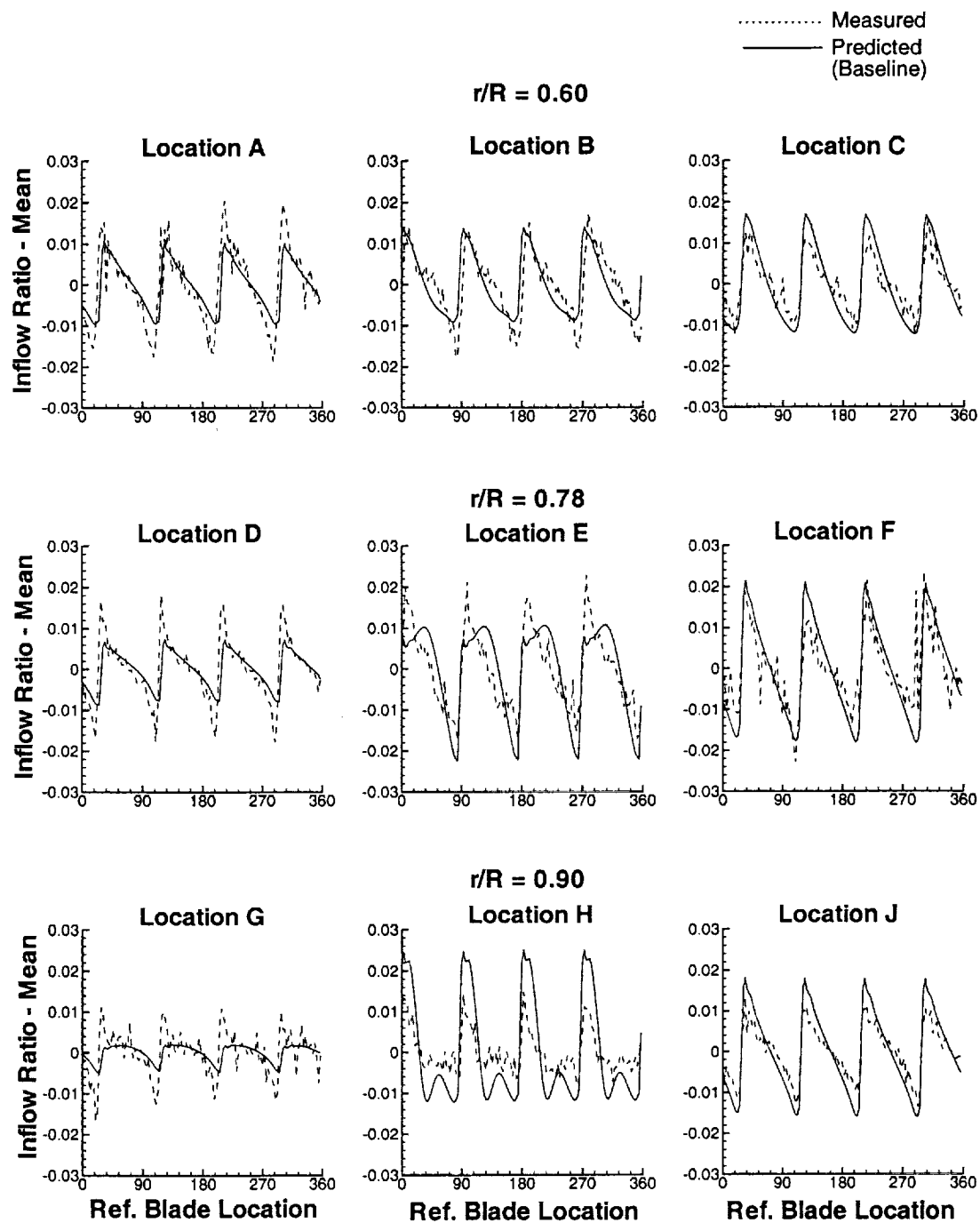
Figure 5: Measured and OVERFLOW-GDWT Predicted (Baseline) Time Histories of Induced Inflow for Azimuth Angles of 30, 180, and 300 degrees at Three Radial Stations of r/R = 0.60, 0.78, 0.90
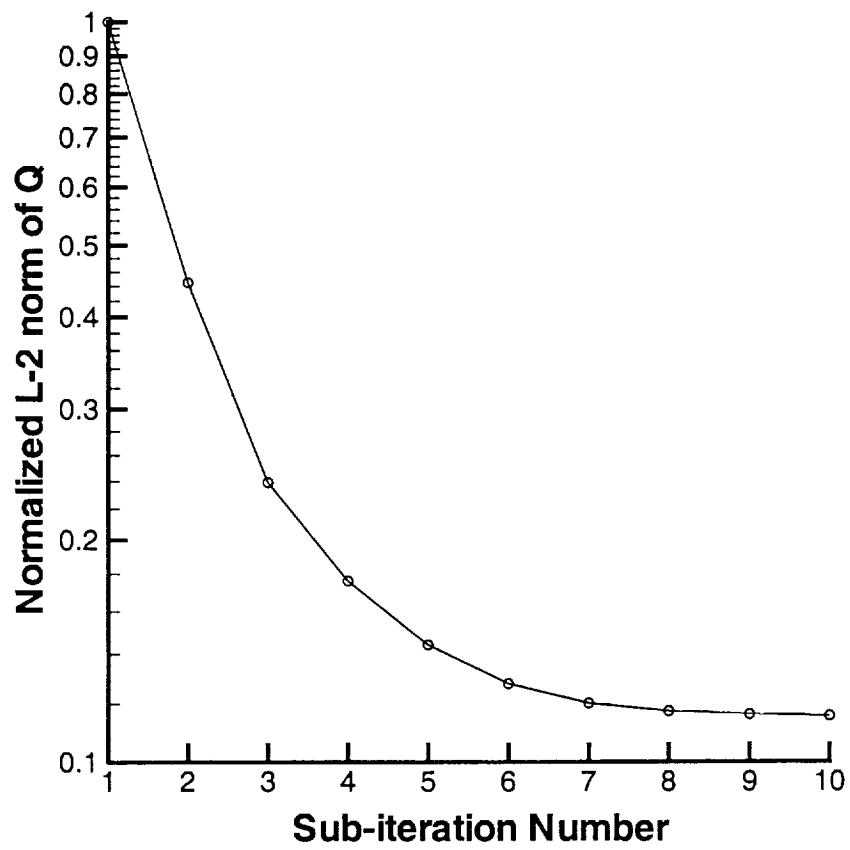
Figure 6: Normalized L-2 norm of Conservative Variables *vs.* Newton Sub-iteration Number

Baseline

**Baseline with 10
Newton Sub-iterations**
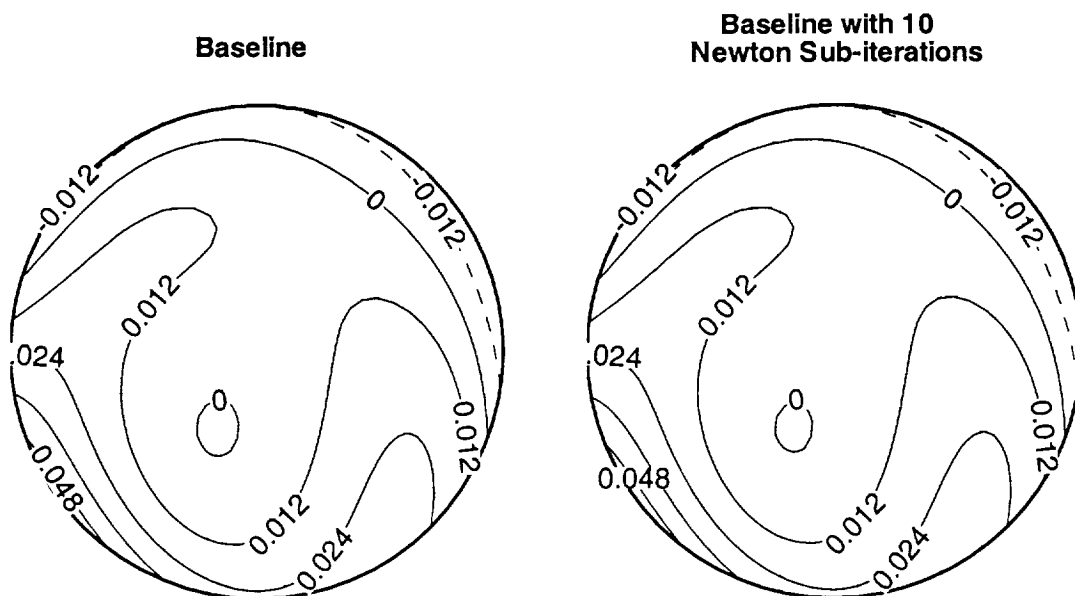
Figure 7: Time Averaged Inflow Ratio for Baseline *vs.* Baseline with 10 Newton
Sub-iterations
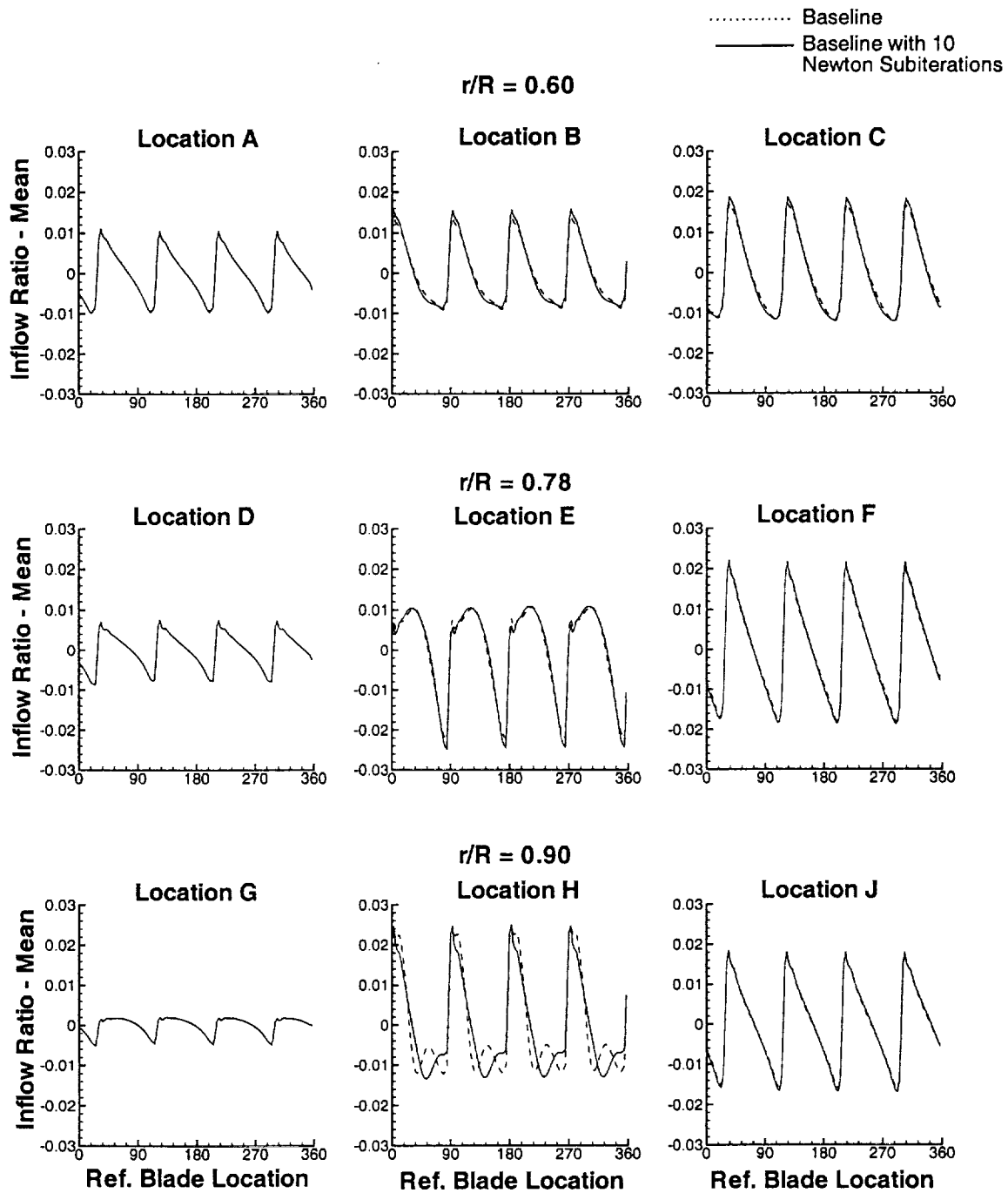
Figure 8: Time Histories of Induced Inflow for Baseline *vs.* Baseline with 10 Newton Sub-iteration for Azimuth Angles of 30, 180, and 300 degrees at Three Radial Stations of r/R = 0.60, 0.78, 0.90

Baseline

Baseline with Viscous Terms Included
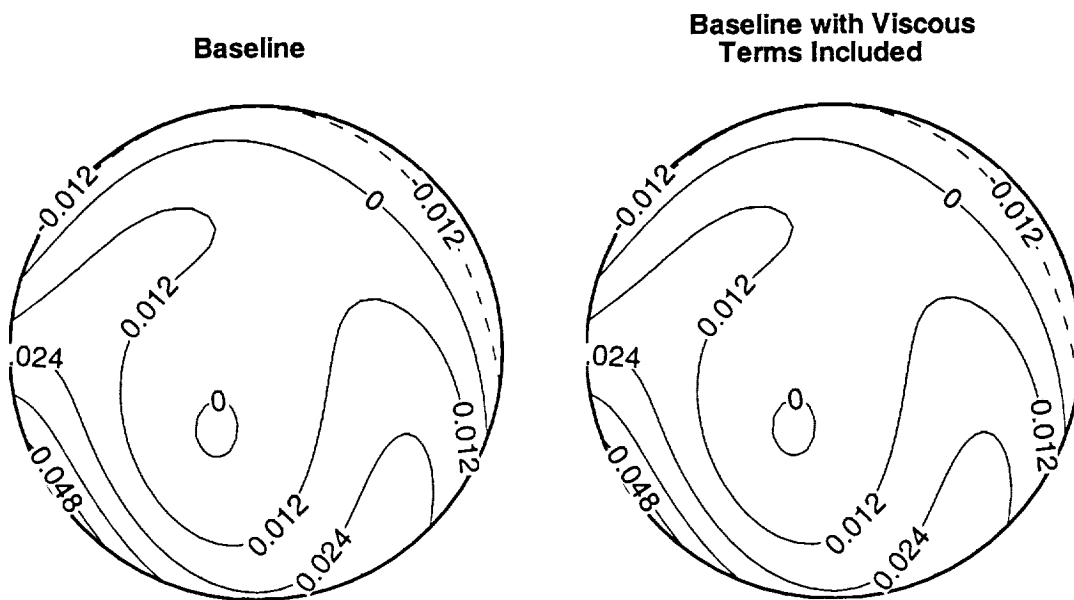
Figure 9: Time Averaged Inflow Ratio for Baseline *vs*. Baseline with Viscous Terms Included
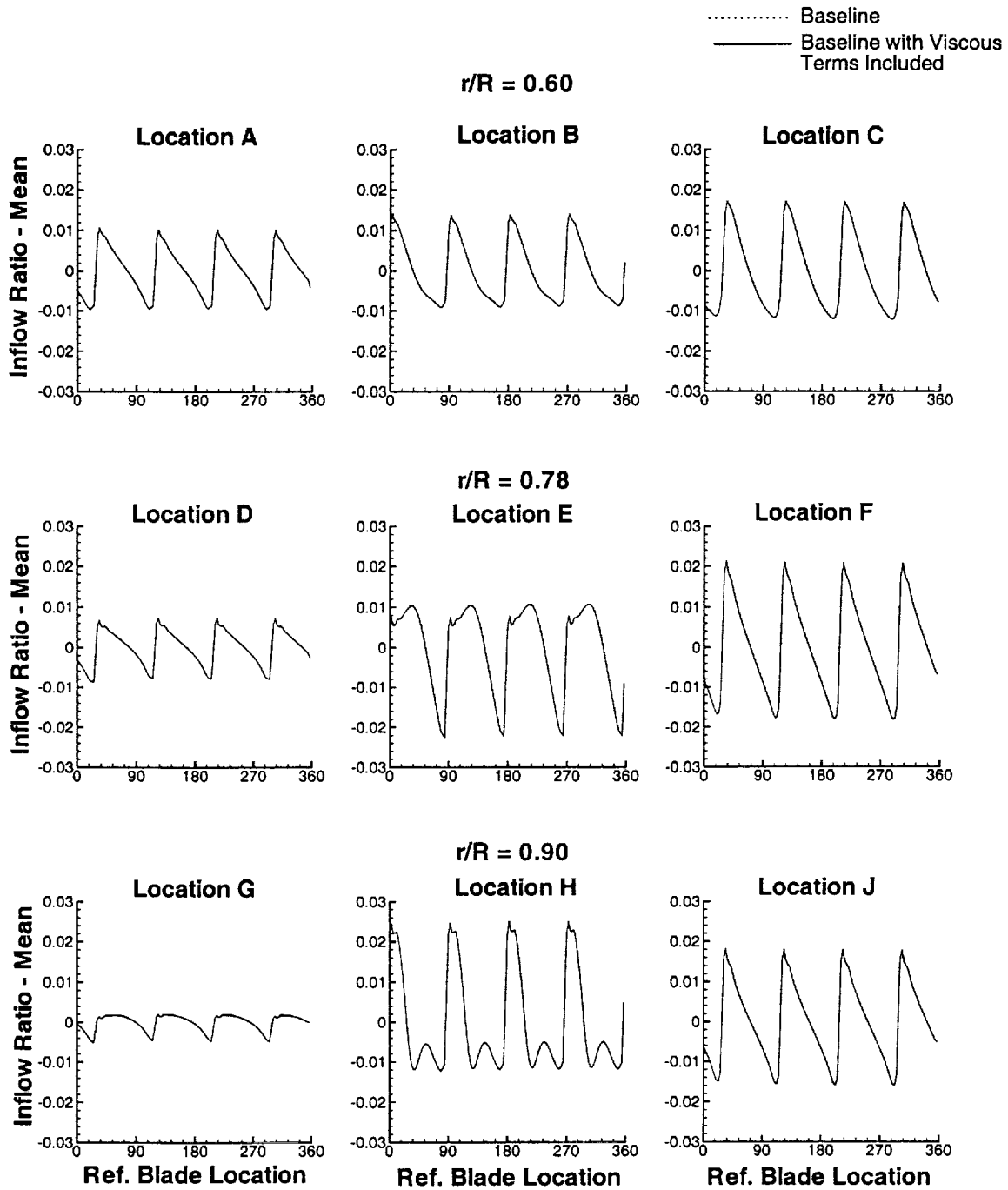
Figure 10: Time Histories of Induced Inflow for Baseline *vs.* Baseline with Viscous Terms Included for Azimuth Angles of 30, 180, and 300 degrees at Three Radial Stations of r/R = 0.60, 0.78, 0.90

Baseline **Baseline with Doubled Time Step**
(Halved Azimuth Resolution)
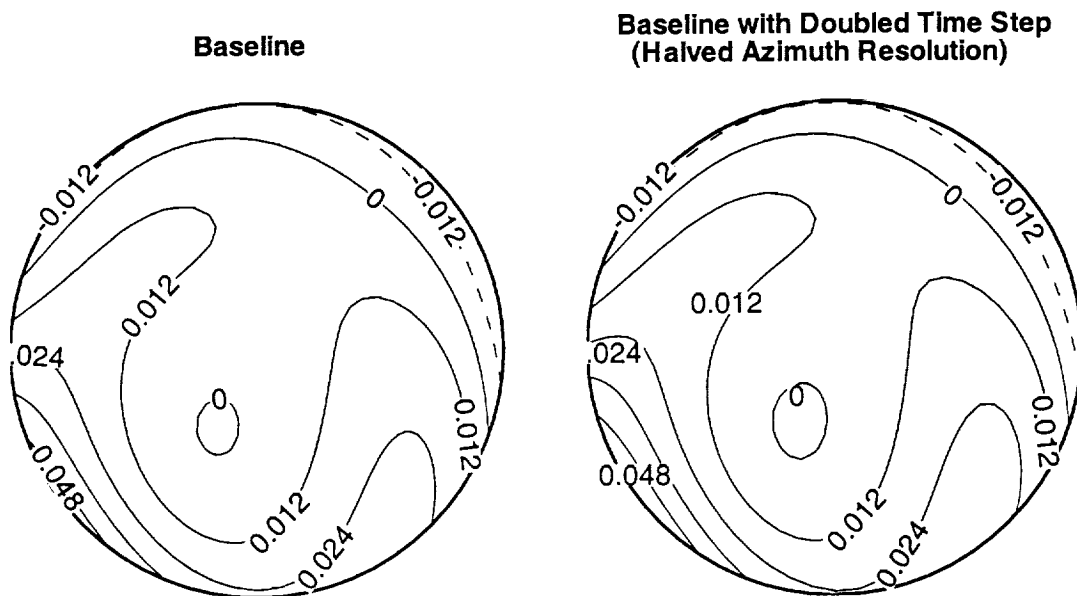
Figure 11: Time Averaged Inflow Ratio for Baseline *vs.* Baseline with Doubled
Time Step (Halved Azimuth Resolution)
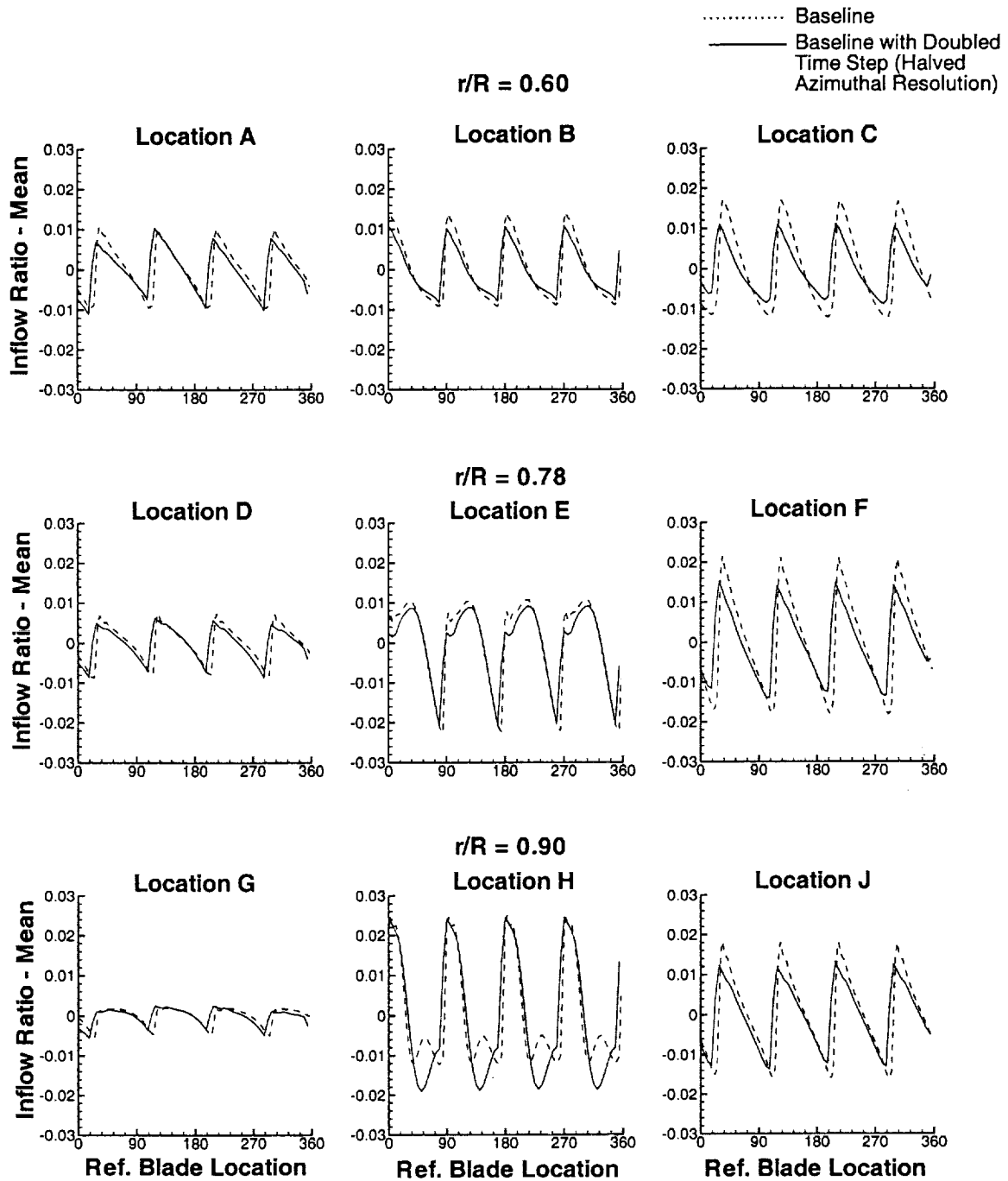
Figure 12: Time Histories of Induced Inflow for Baseline *vs.* Baseline with Doubled Time Step (Halved Azimuthal Resolution) for Azimuth Angles of 30, 180, and 300 degrees at Three Radial Stations of r/R = 0.60, 0.78, 0.90

Baseline

**Baseline with Freestream
Outer Boundary Condition**
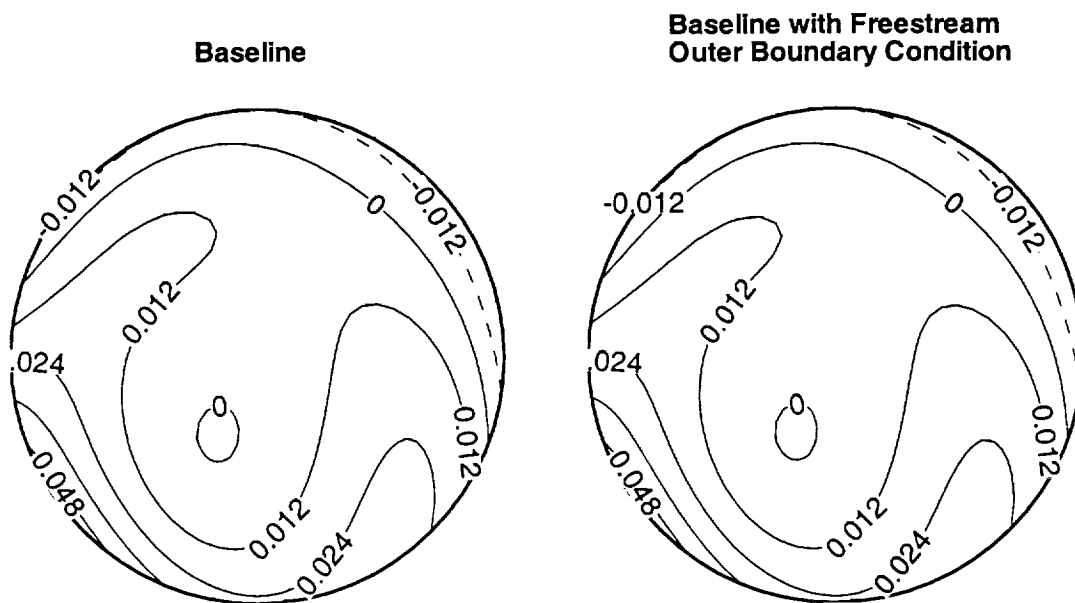
Figure 13: Time Averaged Inflow Ratio for Baseline *vs.* Baseline with Freestream
Outer Boundary Condition
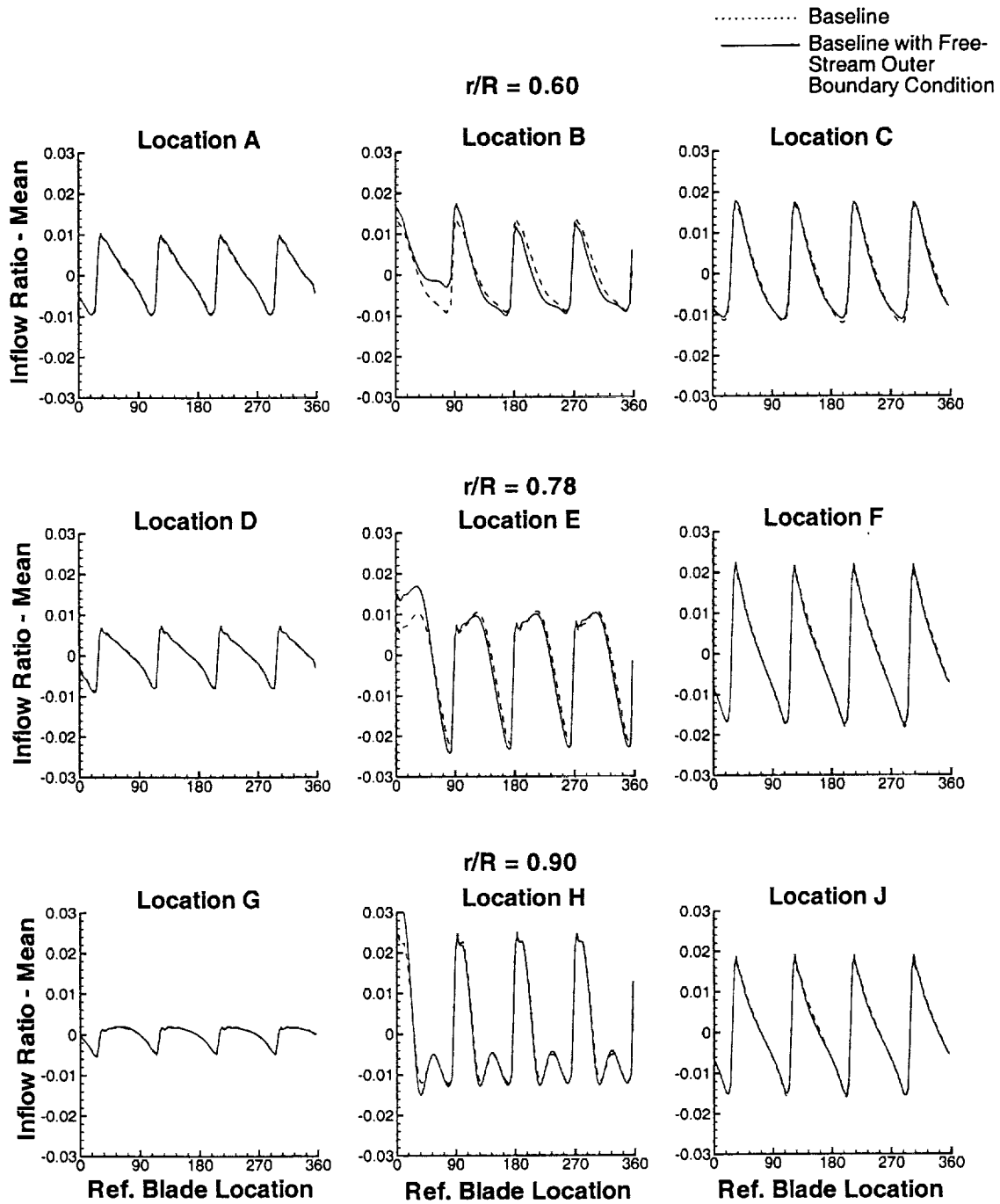
Figure 14: Time Histories of Induced Inflow for Baseline *vs.* Baseline with Freestream Outer Boundary Condition for Azimuth Angles of 30, 180, and 300 degrees at Three Radial Stations of r/R = 0.60, 0.78, 0.90

APPENDIX II

ROTOR/FUSELAGE UNSTEADY INTERACTIONAL AERODYNAMICS: A NEW COMPUTATIONAL MODEL

By

David Douglas Boyd, Jr.

DISSERTATION SUBMITTED TO THE FACULTY OF THE
VIRGINIA POLYTECHNIC INSTITUTE AND STATE UNIVERSITY
IN PARTIAL FULFILLMENT OF THE REQUIREMENTS FOR THE DEGREE OF
DOCTOR OF PHILOSOPHY
IN
AEROSPACE ENGINEERING

COMMITTEE:
Richard W. Barnwell, Chair
Henry E. Jones
William Devenport
Russell H. Thomas
William H. Mason

July 27, 1999
Blacksburg, Virginia

ROTOR/FUSELAGE UNSTEADY INTERACTIONAL AERODYNAMICS: A NEW COMPUTATIONAL MODEL

David Douglas Boyd, Jr.

ABSTRACT

A new unsteady rotor/fuselage interactional aerodynamics model has been developed. This model loosely couples a Generalized Dynamic Wake Theory (GDWT) to a Navier-Stokes solution procedure. This coupling is achieved using a newly developed unsteady pressure jump boundary condition in the Navier-Stokes model. The new unsteady pressure jump boundary condition models each rotor blade as a moving pressure jump which travels around the rotor azimuth and is applied between two adjacent planes in a cylindrical, non-rotating grid. Comparisons are made between predictions using this new model and experiments for an isolated rotor and for a coupled rotor/fuselage configuration.

Acknowledgments

Nomenclature

a_∞	freestream speed of sound [m/sec]
a_n^m, b_n^m	series expansion coefficients [see Appendix A]
$A(\vec{r})$	local area ratio between blade and computational cell
i	the imaginary number, $\sqrt{-1}$
c	local blade chord normalized by R
$\bar{c}$	coefficient function [see Appendix A]
C_f, C_m	force and moment coefficients
C_p	pressure coefficient
C_p'	modified pressure coefficient
$C_p'^u$	unsteady component of modified pressure coefficient
C_T	thrust coefficient
$\bar{C}_T$	mean thrust coefficient
C_L	roll moment coefficient
$\bar{C}_L$	mean roll moment coefficient
C_M	pitch moment coefficient
$\bar{C}_M$	mean pitch moment coefficient
e_0	stagnation energy per unit mass [m^2/sec^2]
$\vec{F}, \vec{G}, \vec{H}$	inviscid fluxes (see equations (4.3) to (4.5))
$\vec{F}_v, \vec{G}_v, \vec{H}_v$	viscous fluxes (see equations (4.3) to (4.5))
$\bar{h}$	hinge offset location normalized by R

H_n^m	coefficient function [see Appendix A]
$[\tilde{L}^c]$	quasi-steady inflow matrix, cosine component
$[\tilde{L}^s]$	quasi-steady inflow matrix, sine component
L	sectional blade lift [N/m]
M	local Mach number
M_∞	freestream Mach number
N_T	number of azimuthal time steps per rotor revolution
P, p	pressure [N/m^2]
P_∞	freestream pressure [N/m^2]
$\bar{P}_n^m$	normalized, associated Legendre functions of the 1st kind
$\bar{Q}_n^m$	normalized, associated Legendre functions of the 2nd kind
q_i	i^{th} component of perturbation velocity [m/sec]
q_x, q_y, q_z	cartesian components of heat flux [J/(m^2 sec)]
$\vec{Q}$	vector of conservative variables $= [\rho, \rho u, \rho v, \rho w, \rho e_0]^T$
Q_i	i^{th} conservative variable
$\bar{r}$	radial location on disk, normalized by R
r	radial location on disk [m]
R	rotor radius [m]
$\mathcal{R}$	gas constant [J/(kg K)]
t	time [sec]
T	temperature [K]
$\bar{t}$	nondimensional time, normalized by Ω
V_∞	freestream velocity, normalized by ΩR
V_i	induced inflow velocity [m/sec]
V_n^m	elements of mass flow matrix
u, v, w	cartesian velocities [m/sec]
w	local normal component of velocity at rotor disk, normalized by ΩR
w_l	local normal component of w

Greek symbols

α_{eff}	effective angle of attack [rad]
α_s	rotor shaft tilt angle [rad]
β_0	blade mean coning angle [rad]
β_{1c}, β_{1s}	first harmonics of rotor flapping [rad]
β_0	blade mean coning angle [rad]
$\bar{\alpha}_j^r, \bar{\beta}_j^r$	induced inflow coefficients
γ	ratio of specific heats
δ_{ij}	Dirac delta function [see Appendix A]
ΔP	pressure jump [N/m^2]
ε	user specified tolerance
λ	freestream component normal to disk, normalized by ΩR, positive down
λ_i	induced inflow ratio $= V_i / (\Omega R)$
$\bar{\lambda}_i$	time averaged induced inflow ratio
$\lambda_{i,mean}$	mean component of λ_i
$\Lambda(\bar{r}, \psi)$	generic time averaged function [see Appendix A]
Φ	pressure function, normalized by $\rho \Omega^2 R^2$
$\bar{\phi}_n^m(\bar{r})$	radial expansion shape function
$\nu, \eta, \bar{\psi}$	dimensionless ellipsoidal coordinates
ψ	$\bar{\psi}$ on rotor disk
ψ_1	phase of first harmonic of blade pitch [rad]
ρ	local air density [kg/m^3]
ρ_∞	freestream air density [kg/m^3]
μ	rotor advance ratio $= V_\infty / \Omega R$
μ_i	induced inflow in μ direction, normalized by ΩR, positive downstream
$\mu_{i,mean}$	mean component of μ_i
θ	local blade pitch [rad]
$\theta_{tw}(\bar{r})$	built-in blade twist function [rad]
θ_0	blade collective pitch [rad]
θ_c, θ_s	cosine and sine components of blade pitch [rad]
θ_1	magnitude of first blade pitch harmonic [rad]

$\bar{\tau}_n^{mc}$	cosine part of pressure expansion of mth harmonic and n^{th} polynomial
$\bar{\tau}_n^{ms}$	sine part of pressure expansion of mth harmonic and n^{th} polynomial
τ_{ij}	stress tensor [m/sec]
ω_n	rigid flap natural frequency [cycles/revolution]
Ω	rotor rotational speed [rad/sec]

Subscripts

add	additional component
i	i^{th} component
$,i$	derivative with respect to i^{th} direction
n, j, q	polynomial number
ξ	coordinate along freestream line, positive pointing upstream
∞	freestream quantities

Superscripts

m, r, p	harmonic number
u	unsteady component

Operators & Acronyms

$\Delta(\cdot)$	operator used to denote an incremental value of $(\cdot)$
$\mathcal{F}(\cdot)$	filter operator
$(\cdot)!!$	double factorial [see Appendix A]
$\overset{*}{(\cdot)}$	derivative with respect to $\bar{t}$
$\hat{(\cdot)}$	reference quantities
$GDWT$	Generalized Dynamic Wake Theory
RLM	rotor loading model
$RFFM$	rotor/fuselage flowfield model

Contents

List of Figures

xiv

List of Tables

Chapter 1

Introduction

1.1 Motivation

It is well known that rotary wing aircraft aerodynamics are complicated. Unlike fixed wing aircraft, on which a steady-state flight condition typically implies steady-state aerodynamics, a rotary wing aircraft experiences a significant unsteady aerodynamic environment in all flight conditions, even in level, unaccelerated flight, due to the presence of the rotating wings (rotors). This aerodynamic environment includes the aerodynamic interactions, which are inherently unsteady and complex, between the rotor(s) and the fuselage. One example of the complexity associated with these interactions is the problem of flow separation phenomena. Whereas fixed wing aircraft typically have little significant flow separation in steady-state flight due to their streamlined fuselage shapes, rotary wing aircraft typically have blunt aft regions that are conducive to flow separation. Even in hover, the flow induced by the rotor(s) impinging on the fuselage tends to separate on the underside of the fuselage which is often a blunt surface. Sheridan and Smith [1] discuss many other examples and categories of rotorcraft interactional aerodynamics. They also state in their conclusions that:

> "... it will be necessary to develop tractable theories and analytical methods to account for all these phenomena. Interactional aerodynamics of the airframe is not as neatly packaged as rotor aerodynamics. Many of the interactions involve viscous processes, and in some aspect semi-empirical techniques may always be needed. But a start must be made in developing the required mathematical models so that we can cope with these problems adequately in the vehicle design phase."

1

In short, the above passage calls for the development of methods to address the coupled rotor/fuselage interactional aerodynamic effects, whereas previously, the rotor effects and fuselage effects were treated in isolation.

In the years since Sheridan and Smith's paper [1], many types of analyses have been developed and used in the prediction of the unsteady interactional aerodynamic characteristics of rotorcraft. Figure 1.1 is a graphic that depicts and categorizes several of the major methodologies.

In the area of relatively low computational expense and complexity (see figure 1.1), singularity methods have been used. These methods typically use singularities, such as a lifting line to represent the rotor blade, a system of vortices to represent the wake, and source, doublet, and/or vortex panels to model the fuselage. In a relatively inexpensive and computationally efficient manner, these methods are able to capture low order effects on each component due to the other component, such as the mean downwash on fuselage due to the rotor or the mean inflow at the rotor disk due to the fuselage. But, since the fuselage is typically modeled using a panel method, calculation of some interactional aerodynamic effects, such as flow separation due to rotor downwash, is difficult. In cases where viscous effects are predominant, the viscous flow effects must be either ignored, specified *a priori*, or determined by coupling the method to a boundary layer type model.

On the other end of the computational expense and complexity scale, at relatively high computational expense and complexity, are the methods involving computational fluid dynamics (CFD), in particular, Navier-Stokes methods. These types of methods have been used to calculate the entire flow field of the complete rotorcraft configuration, all in one computation. Even though these computational methods are theoretically able to capture all of the interactional aerodynamic couplings between the rotor(s) and fuselage, their computational expense is prohibitive for routine use.

There is a lack of methods available in the literature which fall between the singularity methods and the Navier-Stokes CFD methods for studying unsteady interactional aerodynamics of rotorcraft. The current research is motivated by the lack of available hybrid methods which are computationally efficient, yet are able to capture primary interactional aerodynamic effects between the rotor and fuselage. Figure 1.1 shows, with a dotted ellipse labeled "Hybrid Methods", where the current work falls on the computational expense and complexity scale.

1.2 Literature Review

As discussed previously, unsteady rotor/fuselage interactional aerodynamics generally fall into three categories: (1) singularity methods, (2) CFD methods, and (3) hybrid methods. In the following sections, a brief review of each is given.

1.2.1 Singularity Methods

Singularity methods are typically characterized by the use of a source, doublet, and/or vortex panel representation of the fuselage, a lifting line or lifting surface representation of the rotor, and a vortex lattice model representation of the rotor wake. For rotorcraft analyses, these methods are used to compute the flowfield of the complete vehicle. Johnson [2] provides an extensive discussion of singularity methods used for rotorcraft analyses up through the year 1986. Since that time, other singularity methods have been developed as well. Egolf and Lorber [3] used a source panel description of the fuselage, a lifting line blade model, and a prescribed vortex wake description of the rotor/fuselage system to model the unsteady rotor/fuselage flowfield. The prescribed vortex wake was prevented from cutting through the fuselage by displacing, in an *a priori* manner, the segments of the vortices that would otherwise have been inside the fuselage. No attempts were made to model the wake of the fuselage or the flow separation from the fuselage. Only limited comparisons were made to experimental data. Mavris, *et al.* [4] used a doublet representation of the fuselage, a lifting line blade model, and a free vortex wake description of the rotor/fuselage system. No modeling was used for the fuselage wake or fuselage flow separation. Also, vortex wake filaments that are inside the fuselage were excluded from the computations. Comparisons with experimental pressures show good agreement along the top of the fuselage, but agreement degrades on the sides of the fuselage. Mavris, *et al.* [4] attribute these discrepancies to flow separation on the fuselage and to inadequate vortex-surface interaction predictions. Berry [5] combined a fuselage source panel representation, a source-dipole representation for the rotor, and a distorting vortex-lattice representation of the rotor wake to model the rotor/fuselage system. Comparisons are made to measured time averaged and unsteady inflow velocities; no fuselage pressure comparisons are made which include the rotor influence. Quackenbush, *et al.* [6] used a source/doublet description of the fuselage, a vortex-lattice model for the rotor blades and a novel "Constant Vorticity Contour (CVC)" free wake model; fuselage flow separation was not modeled. Close surface/vortex interactions were modeled using selective remeshing of the curved vortex elements and using an

"Analytical/Numerical Matching (ANM)" scheme. Computational efficiency was improved by using "fast vortex methods" for wake-on-wake and wake-on-body computations. Generally good agreement with measured results are demonstrated for time averaged induced velocities above the rotor disk and for time averaged and unsteady pressures on the top centerline of the fuselage. Crouse [7] used a source panel description of the fuselage, a lifting line blade model, and a free tip vortex wake model without an inboard wake model to represent the rotor/fuselage system. Vortex wake elements that cross the fuselage surface are handled by splitting them into smaller segments, and shifting the collocation points of these smaller segments such that they are at a specified minimum distance from the fuselage surface. This method is similar in concept to that used by Egolf and Lorber [3] as discussed above. Good comparisons of unsteady pressures were shown on the top centerline of the tail boom of the fuselage. Boyd, *et al.* [8] included the open-loop effects of a fuselage, represented by a non-lifting fuselage source panel method, on the rotorcraft trim in a comprehensive rotorcraft analysis. This effect was implemented in the comprehensive analysis as an additional rotor inflow distribution plus an additional rotor wake distortion due to the presence of the fuselage. Effects of the rotor on the fuselage were not modeled. Though some computations have proved successful and can be computationally efficient, all of these singularity methods suffer from the inability to predict some of the rotor/fuselage interactional effects. For example, methods that use a source panel description of the fuselage do not have the capability to determine the lift or the lift change on a fuselage due to the rotor. Also, quantities such as flow separation and drag must either be ignored, must be specified *a priori*, or must be determined by coupling the method to a boundary layer model.

1.2.2 CFD Methods

In recent years, unsteady calculations on complete rotorcraft configurations using CFD methods have become possible. In addition, there are several degrees of complexity that can be modeled with CFD. For rotorcraft applications, methods have been developed to solve the full potential equation, the Euler equations, and the Navier-Stokes equations.

Chen and Bridgeman [9] coupled the three dimensional boundary layer equations to the full potential equations in a blade-fixed coordinate system for an isolated rotor. The three dimensional boundary layer equations assumed that the surface curvature effects were negligible and included additional terms in the x- and z-momentum equations to account for centrifugal and Coriolis forces in the boundary layer due to blade rotation. These equations were coupled by using a modified

tangency boundary condition. This modified boundary condition enforces a velocity component ("transpiration velocity") normal to the surface which "deflects the inviscid flow from the body surface thus simulating the displacement of the inviscid flow due to the momentum defect in the boundary-layer" [9]. Good comparisons were shown for integrated drag quantities (torque) on a non-lifting isolated rotor in hover for a range of hover tip Mach numbers. Also, good chordwise pressure coefficient comparisons were shown for two radial stations in a non-lifting, forward flight condition. Bridgeman, *et al.* [10] solved the unsteady, full potential equation coupled to a three dimensional boundary layer model for isolated rotors in hover and forward flight. This method is similar to that presented in [9], with a number modeling improvements. Though it is possible conceptually to include a fuselage in these full potential computations, this would be difficult in practice due to the blade-fixed coordinate systems typically used in such analyses. Thus, interactional aerodynamic computations would be difficult to compute using these existing tools.

Recent solutions to the Euler equations for isolated rotor applications have used unstructured grid techniques [11, 12, 13] to refine the grid system efficiently to better capture wake structures such as tip vortices. These techniques may be extended easily to include a fuselage body. However, since the Euler equations do not include viscous terms, computation of any viscous effects (*e.g.*, viscous drag on a fuselage) would, like the full potential equation examples above, still require coupling the method to a boundary layer analysis.

Navier-Stokes computations have also been developed for use in rotorcraft analysis. While time averaged Navier-Stokes methods have been developed and are quite practical to use [14, 15, 16, 17, 18], routine computations for unsteady flows on full configurations are not yet practical. Even so, several of these computations [19, 20] are found in the literature. Meakin [19] used a thin-layer Navier-Stokes method to calculate the flowfield around the Bell/Boeing V-22 Osprey tiltrotor aircraft, including the fuselage and the rotor, for a fictitious flight condition. Though this was a full aircraft simulation, the purpose of the computation was to demonstrate the feasibility of using a new domain connectivity algorithm for the moving, dynamic, overset grids for such a computation. Since the computations were performed to demonstrate a technology, no comparisons are made with experimental quantities. Srinivasan and Ahmad [20] used a Navier-Stokes scheme to calculate the quasi-steady flowfield for a hovering rotor mounted on a whirl tower. Due to the quasi-steady nature of the hovering condition, the equations were solved in the blade-fixed coordinate frame, using a momentum source term in the equations to account for the centrifugal force of the blade rotation. This simulation was also a feasibility study, so only a comparison of the predicted and measured mean thrust values were presented. For this simulation, which utilized

approximately 1.3 million grid points, a computational time of 14 Cray-YMP hours was quoted. Ahmad and Duque [21] used a thin-layer Navier-Stokes method with embedded, moving, overset grids to demonstrate the ability to calculate the unsteady flowfield of an isolated, two-bladed rotor in forward flight. Blade surface pressures at several radial and azimuthal and local normal load coefficients are compared to flight test data. These comparisons match reasonably well. Even though this computation did not include a fuselage body, the chimera grid scheme would render the task of including a body feasible, though at an additional computational cost. This isolated rotor computation required substantial computational resources; it required approximately 45 Cray C-90 hours and generated 40 Gigabytes of data.

Though most of these Navier-Stokes methods are suitable for computations over complete aircraft, including the helicopter rotor, all of the moving grid computations suffer from the requirement to re-compute the grid domain connectivity information at every time step; this technique is known as a "dynamic chimera scheme" and has two distinct disadvantages. First, regenerating the grid domain connectivity at every time step can be as computationally expensive as, or even more computationally expensive than, the actual flow solution. In addition, in some instances, the time step is restricted not by the flow or flow solver, but by the moving grid domain connectivity requirement that a "hole point" not become a "field point" at any time step [19]. This requirement can potentially limit the time step not to physical phenomena, but to grid cell size.

In addition to time step issues discussed above, other factors place limits on the current Navier-Stokes computations for rotorcraft. One issue is the numerical dissipation of concentrated vortices. It is well known that, in certain flight conditions, blade tip vortices can have a large effect on the rotor aerodynamics and that these vortices need to be computed in the flowfield over several rotor revolutions. Numerical studies discussed in the literature suggest that a 5th order scheme using 14 points across the vortex core produces satisfactory results for a vortex that is well-aligned with the grid [22]. However, in a typical rotorcraft simulation, the vortex location is not known *a priori* and thus the vortex in general will not be aligned well with the grid. Therefore a more strict resolution requirement is imposed on the numerical scheme [22]. For current methods either a prohibitively dense grid must be used to assure that the vortex is resolved well spatially, or grid adaption must be used to refine the grid in the regions that contain the vortices. Both methods are computationally expensive.

Another such issue is turbulence modeling. Many of the turbulence models in current use were developed for wall bounded flows. They are not well suited to the three dimensional, non-isotropic turbulence associated with rotor blade tip vortices.

1.2.3 Hybrid Methods

Considering the computational expense of current CFD methods, one possible approach to examining unsteady rotor/fuselage interactional aerodynamics is to use hybrid methods. For unsteady rotor/fuselage aerodynamics, several hybrid methods have been developed. One such hybrid method, developed by Steinhoff, *et al.* [23], modified the Navier-Stokes equations by adding a "vorticity confinement" term to the momentum equations. This new term is used to prevent, or counteract, numerical diffusion of concentrated vortical regions by "convecting" vorticity back toward the centroids of concentrated vorticity regions in the flowfield. This particular method is well suited for inclusion of a fuselage body. Boyd and Barnwell [24] first introduced a hybrid unsteady rotor model which weakly couples a Generalized Dynamic Wake Theory (GDWT) [25, 26, 27, 28] to a thin-layer Navier-Stokes model, OVERFLOW [29]. Extensive induced inflow comparisons were made between Laser Doppler Velocimeter (LDV) measurements and predictions. Even though the computations were for an isolated rotor, excellent agreement was found with measured quantities. Also presented was an outline of a method to couple a fuselage into the calculations using the overset grid capabilities in OVERFLOW. This new model uses the GDWT to obtain unsteady loading and unsteady induced inflow on the rotor, and then applies the unsteady loading inside OVERFLOW as a new unsteady pressure-jump, actuator disk-type, boundary condition. Another hybrid method, building on the previous literature [24], is developed in this research.

1.3   Present Approach

The objective of the current research is to develop an efficient, hybrid, unsteady computational model appropriate to the study of unsteady rotor/fuselage interactional aerodynamics.

In examining fully CFD, unsteady, moving grid methods for complete rotorcraft, it can be observed that small time steps are needed for method stability, for capturing aerodynamic effects that are on the order of the rotor blade chord size, and for proper usage of the dynamic chimera grid scheme. However, to capture the primary effects of rotor/fuselage interactional aerodynamics, chordwise aerodynamics on the rotor blade are of less importance than the gross loading on the rotor blade itself. This can be seen by the successes of some of the singularity methods which use lifting line rotor blade models (*i.e.*, no chordwise loading distribution on the rotor blade) discussed previously in the "Literature Review" section above. In addition, fully CFD methods compute the rotor loading internally and require a number of rotor revolutions to obtain a periodic solution. The

combined requirements of needing very small time steps and of needing several rotor revolutions to obtain a periodic solution are a large contributor to the computational expense of these methods.

A hybrid method is developed here which reduces the computational expense by separating the rotor loading calculation from the CFD component of the computation. This hybrid method is depicted schematically in figure 1.2. From the figure, it can be seen that there are three components to this hybrid method:

1. Rotor Loading Model,

2. Rotor/Fuselage Flowfield Model,

3. Coupling Model.

1.3.1   Rotor Loading Model

The present approach separates the rotor loading model from the rotor/fuselage flowfield model. Splitting the procedure into these two separate models allows an otherwise computationally expensive element, the rotor loading computation, to be accomplished using a efficient, simplified model apart from the CFD computation. To compute the rotor loading, the GDWT [25, 26, 27, 28], which will be discussed in detail in a subsequent chapter, is used here. Previous implementations of the GDWT have focused on calculation of the unsteady inflow for an isolated rotor. As a significant advance over previous models, the unsteady rotor portion of the model uses the GDWT to calculate unsteady inflow and unsteady loading. The unsteady loading on the rotor is determined in the form of a ΔP, or "pressure jump", across the rotor disk. This ΔP is then used as a boundary condition in the rotor/fuselage flowfield model.

1.3.2   Rotor/Fuselage Flowfield Model

The unsteady loading, as determined by the GDWT, is then used in conjunction with a Navier-Stokes model, in this case, OVERFLOW, to compute the time dependent flow over the fuselage including effects of a helicopter rotor. The loading is used in the Navier-Stokes method as an unsteady boundary condition in the flowfield. This boundary condition is effectively an unsteady actuator disk model. Though there will be concentrated regions of vorticity near the edges of an unsteady actuator disk model used as a boundary condition in this manner, these are not true

"tip vortices" and thus internal structure of these flow features is of secondary importance. This alleviates the need to develop prohibitively dense grids, use grid adaption, or use higher order schemes to resolve these concentrated vorticity regions. As such, turbulence modeling of the inside of these vortex structures becomes less important as well. So, by modeling the rotor as an unsteady actuator disk in OVERFLOW, several computationally expensive requirements typically needed for full CFD rotorcraft modeling are diminished. Using the above model, the Navier-Stokes method is then used to compute the periodic flowfield of the rotor/fuselage combination. Further details of this component will be discussed in a subsequent chapter.

1.3.3 Coupling Model

With the completion of the Navier-Stokes method, there are two solutions which were obtained with the same ΔP distribution: the GDWT solution, which is for an isolated rotor, and the OVER-FLOW solution, which contains both the rotor (as a boundary condition) and the fuselage body. The primary difference is that one solution contains a fuselage and the other does not. Since the loading in the GDWT depends on the rotor inflow, and since these inflow values are influenced by the presence of the fuselage, a method of coupling the two codes has been developed to account for the fuselage effects in the GDWT (and thus the rotor loading model). Since the fuselage effects on the rotor are assumed to consist of low frequency effects (as compared to the higher frequency blade-passage effects), the method employed here differences the time averaged inflow generated in the two successive solutions, and uses this difference as an "inflow correction" to the GDWT. This coupled process continues until only small differences are seen between successive iterations.
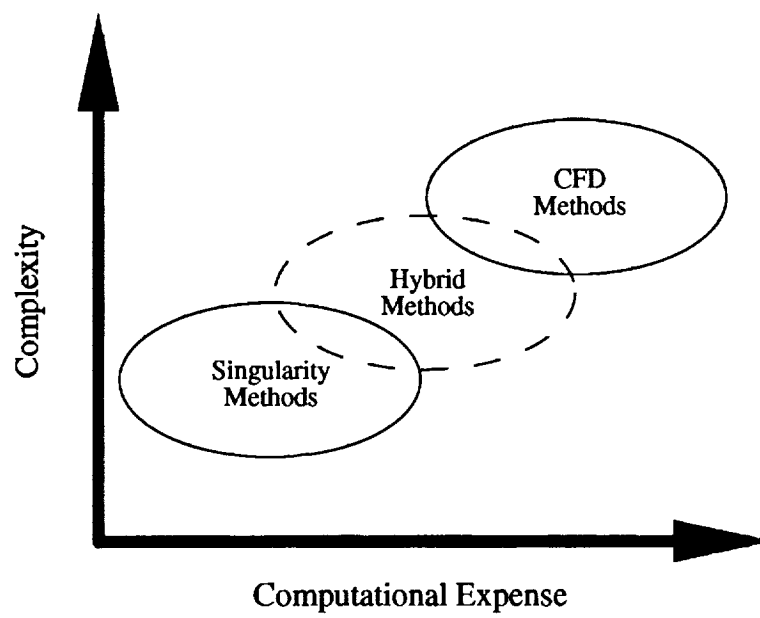
Figure 1.1: Analysis Types for Coupled Solutions.
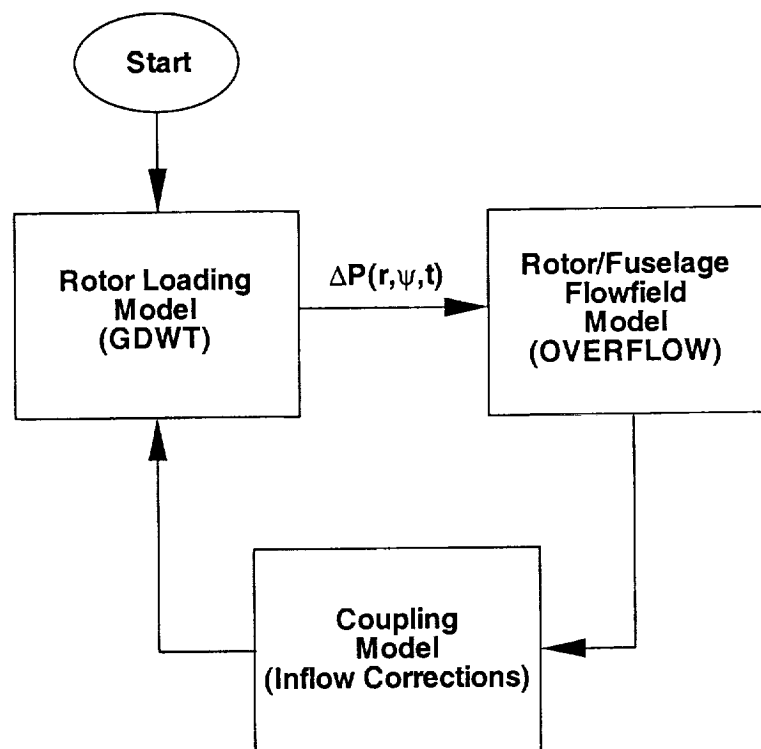
Figure 1.2: Current Hybrid Method.

Chapter 2

Rotor Loading Model: Generalized Dynamic Wake Theory

2.1 Introduction

The Generalized Dynamic Wake Theory (GDWT) of Peters, Boyd, and He [26], Peters and He [25], and He [27] is used in the present approach to obtain unsteady loading that is to be used in conjunction with OVERFLOW as discussed previously. In a later chapter, the OVERFLOW and the coupling technique between OVERFLOW and the GDWT will be discussed. Even though the GDWT is spelled out in detail in the literature, the present chapter will describe the GDWT for background purposes and describe the particular manner in which the theory is implemented for the current research.

2.2 General Description

The GDWT is a theory that was originally designed to pose the issue of unsteady aerodynamics of a helicopter rotor in a state-space form. This type of state-space form is desirable for inclusion in a rotor stability analysis since stability analyses for the rotor dynamics are usually presented in a state-space form as well. With the aerodynamics and dynamics of the rotor stated in similar forms, the solution of the system of equations is simplified.

2.3   GDWT Outline

There are several aerodynamic concepts which are combined in the development of the GDWT. First, the acceleration potential derived by Kinner [30] for circular wing planforms is used with slight modification. The original acceleration potential derived by Kinner is a general form for the solution to Laplace's equation (inviscid, linear, potential flow) in ellipsoidal coordinates. These modifications to Kinner's acceleration potential function (or pressure function), applied by Peters, Boyd, and He [26], Peters and He [25], and He [27], are made to eliminate terms in the potential that are not compatible with boundary conditions associated with a rotor. This modified acceleration potential, Φ, is then expressed using Legendre functions and transcendental functions in ellipsoidal coordinates as follows:

$$\Phi(v,\eta,\bar{\psi},\bar{t}) = -\frac{1}{2} \sum_{m=0}^{\infty} \sum_{n=m+1,m+3,...}^{\infty} \bar{P}_n^m(v)\bar{Q}_n^m(i\eta)\left[\tau_n^{mc}(\bar{t})\cos(m\bar{\psi}) + \tau_n^{ms}(\bar{t})\sin(m\bar{\psi})\right] \quad (2.1)$$

where the τ_n^{mc} and τ_n^{ms} terms are general coefficients of the pressure function and are, in general, functions of time and are determined from the loading on the rotor. The ellipsoidal coordinate system used here can be seen in figure 2.1. This figure shows a view of the xz plane with representative η and v values labeled. The $\bar{\phi}$ coordinate (not shown in figure 2.1) is an angular, azimuthal coordinate, measured around the z-axis. The "rotor disk" is defined by the following conditions:

$$\eta = 0 \quad (2.2)$$

$$v = \sqrt{1-\bar{r}^2} \quad (2.3)$$

$$\bar{\psi} = \psi \quad (2.4)$$

where $\bar{r}$ is the radial coordinate on the rotor disk, measured from the axis of rotation, and ψ is the angular, azimuthal coordinate measured about the axis of rotation. Equation (2.1) is effectively an expression for all admissible functions of loading on a rotor. To establish a link between loading on the rotor and induced inflow, the continuity equation and the linearized, incompressible Euler equations are used as follows:

$$q_{i,i} = 0 \quad (2.5)$$

$$\overset{*}{q_i} - V_\infty q_{i,\xi} = -\Phi_{,i} \tag{2.6}$$

$$q_1 = u \tag{2.7}$$

$$q_2 = v \tag{2.8}$$

$$q_3 = w \tag{2.9}$$

$$\tag{2.10}$$

where the summation convention is assumed over the index i, and ξ is the coordinate pointing upstream along a streamline. Using equations (2.5) and (2.6), it can be shown that the pressure function, Φ, satisfies Laplace's equation. Also, since these equations are linear, the pressure function can be split into a component associated with each of the two terms on the left hand side of equation (2.6). Each of these components, in turn, also satisfies Laplace's equation. As such, solutions can be derived for each component, then combined into a complete solution. The quantities used here are assumed to be total quantities, not perturbations. Also, it is assumed that only the velocity normal to the rotor disk is of interest and that it is of the following form:

$$w(\bar{r}, \psi, \bar{t}) = \sum_{r=0}^{\infty} \sum_{j=r+1, r+3, \dots}^{\infty} \bar{\phi}_j^r(\bar{r}) \left[\bar{\alpha}_j^r(\bar{t}) \cos(r\psi) + \bar{\beta}_j^r(\bar{t}) \sin(r\psi) \right] \tag{2.11}$$

With these assumptions, a closed form set of first order, non-linear differential equations, in state-space form, can be established for the induced inflow coefficients $\bar{\alpha}_j^r, \bar{\beta}_j^r$. These equations are as follows:

$$\left\{ \begin{array}{c} \vdots \\ \bar{\alpha}_n^m \\ \vdots \end{array} \right\}^* + [\tilde{L}^c]^{-1} \begin{bmatrix} \ddots & & \\ & V_n^m & \\ & & \ddots \end{bmatrix} \left\{ \begin{array}{c} \vdots \\ \bar{\alpha}_n^m \\ \vdots \end{array} \right\} = \left\{ \begin{array}{c} \vdots \\ \bar{\tau}_n^{mc} \\ \vdots \end{array} \right\} \tag{2.12}$$

$$\left\{ \begin{array}{c} \vdots \\ \bar{\beta}_n^m \\ \vdots \end{array} \right\}^* + [\tilde{L}^s]^{-1} \begin{bmatrix} \ddots & & \\ & V_n^m & \\ & & \ddots \end{bmatrix} \left\{ \begin{array}{c} \vdots \\ \bar{\beta}_n^m \\ \vdots \end{array} \right\} = \left\{ \begin{array}{c} \vdots \\ \bar{\tau}_n^{ms} \\ \vdots \end{array} \right\} \tag{2.13}$$

With these equations, the unsteady aerodynamics and induced inflow are cast in the time domain and in a state-space form. The problem has now been reduced to the computation of the states of the model, $\bar{\alpha}_n^m, \bar{\beta}_n^m$, given a loading on the rotor. This is a non-linear model since the loading and the inflow are coupled through mass flow parameter, V_n^m, in equations (2.12) and (2.13). As described

in reference [26], the mass flow parameter V_n^m, which accounts for the energy added to the flow by the rotor, takes the place of the V_∞ term that results from equation (2.6) in order to extent the theory and to cover the case of hover, where V_∞ approaches zero.

2.4 Solution Procedure

Though the details of the GDWT are discussed in the literature, few details are provided for the solution of this set of first order, non-linear differential equations. The procedure used in the current research is described here.

First, for a given set of rotor collective, lateral, and longitudinal pitch controls settings, the blade loading may be determined by any theory that can generate a loading given velocity (inflow) information. In the current research, as was done in previous literature [26, 25, 27], a two dimensional strip theory is employed. At first, this may seem to be an unnecessary restriction to a two dimensional theory. It has been shown [26, 25, 27] that this is not a restriction since the inflow and the loading are coupled. So, three dimensional effects, such as load reduction at the blade tip, are included in this theory. The equations of the strip theory used in this research are outlined below:

$$\theta(\bar{r},\psi) = \theta_{tw}(\bar{r}) + \theta_0 + \theta_c \cos\psi + \theta_s \sin\psi \tag{2.14}$$

$$\alpha_{eff} = \theta - \frac{(w + \mu\sin\alpha_s + \beta_0\mu\cos\psi - 0.5c\dot{\theta} + \Delta\bar{\lambda}_i)}{\bar{r} + \mu\sin\psi} \tag{2.15}$$

$$\frac{L}{\rho\Omega^2 R^3} = \frac{\pi c(\bar{r} + \mu\sin\psi)^2 \alpha_{eff}}{\sqrt{1 - M^2}} \tag{2.16}$$

Equation (2.16) gives the lift at a particular point on the rotor disk. Through the effective angle of attack, α_{eff}, this loading theory includes local effects of the blade pitch (θ), of the total induced inflow velocity (w), of the inflow due to the shaft tilt ($\mu\sin\alpha_s$), of the inflow due to the mean blade coning angle ($\beta_0\mu\cos\psi$), of the velocity at the 3/4 chord point due to blade pitch rate ($0.5c\dot{\theta}$), and of the inflow correction determined by the coupling scheme ($\Delta\bar{\lambda}_i$), described in a later chapter. In addition, the lift curve slope is assumed to be 2π per radian, the Prandtl-Glauert compressibility correction is applied to the lift, and a simple stall model is used which limits the maximum angle of attack to 10 degrees. Now, given the blade pitch settings of the rotor and the rotor operating conditions, the local sectional loading can be determined from equations (2.14), (2.15), and

(2.16). With the lift distribution determined, equations (2.12) and (2.13) are solved using a 4-stage Jameson-style Runge-Kutta technique [31] until periodic induced inflow is obtained; this usually occurs within two rotor revolutions. No blade dynamics model is used in this study and the blade hinge offset is assumed to be at the center of rotation (*i.e.*, the flap hinge is at the center of rotation).

With the above calculation complete, the mean thrust coefficient and mean hub moment coefficients can be determined from the following:

$$\bar{C}_T = \frac{4}{\sqrt{3\pi}} \int_0^{2\pi} \tau_1^{0c} d\psi \tag{2.17}$$

$$\bar{C}_M = \frac{4}{3\sqrt{5\pi}} \int_0^{2\pi} \tau_2^{1c} d\psi \tag{2.18}$$

$$\bar{C}_L = \frac{4}{3\sqrt{5\pi}} \int_0^{2\pi} \tau_2^{1s} d\psi \tag{2.19}$$

Since typically the initial pitch settings do not produce the desired thrust and moment coefficients on the rotor, they must be adjusted in subsequent iterations until the desired thrust and moment coefficients are obtained. This is known as "trimming" the isolated rotor; this accounts only for the desired loading on the isolated rotor and does not include any "feedback" forces from any other source (such as a fuselage). The trim procedure used in the current research for the isolated rotor is a modified Newton-Raphson technique adapted from the literature [32]. The following equation is used to determine the pitch setting "corrections" which are used to iteratively trim the isolated rotor:

$$\left\{ \begin{array}{c} \Delta\theta_0 \\ \Delta\theta_c \\ \Delta\theta_s \end{array} \right\} = \left[\begin{array}{ccc} \left(\dfrac{\partial C_T}{\partial \theta_0}\right) & \left(\dfrac{\partial C_T}{\partial \theta_c}\right) & \left(\dfrac{\partial C_T}{\partial \theta_s}\right) \\ \left(\dfrac{\partial C_M}{\partial \theta_0}\right) & \left(\dfrac{\partial C_M}{\partial \theta_c}\right) & \left(\dfrac{\partial C_M}{\partial \theta_s}\right) \\ \left(\dfrac{\partial C_L}{\partial \theta_0}\right) & \left(\dfrac{\partial C_L}{\partial \theta_c}\right) & \left(\dfrac{\partial C_L}{\partial \theta_s}\right) \end{array} \right]^{-1} \left\{ \begin{array}{c} \Delta C_T \\ \Delta C_M \\ \Delta C_L \end{array} \right\} \tag{2.20}$$

where the matrix of partial derivatives is called the "derivative matrix" and each partial derivative is determined by using a one-sided forward difference formula and by using an independent perturbation to each of the initial pitch settings. Each row in the derivative matrix is computed by an independent perturbation of each corresponding pitch setting and solving equations (2.12) and (2.13). Once computed, the derivative matrix is held unchanged throughout the subsequent rotor

trimming process. The $\Delta C_T, \Delta C_M$, and ΔC_L are the changes in the current thrust and moment coefficients required to match the desired values. The trimming process is considered complete when value of the following is true:

$$\sqrt{(\Delta C_T)^2 + (\Delta C_M)^2 + (\Delta C_L)^2} < \varepsilon \qquad (2.21)$$

where ε is a specified tolerance. Now, with the trim task complete, the unsteady loading and unsteady induced inflow are known.

At the end of the trim process, the unsteady loading is in the form of a sectional loading (*i.e.,* force per unit span). However, for use in OVERFLOW, the loading needs to be in the form of a pressure that will be applied to a grid point in the flowfield. The sectional loading is converted to a pressure (force per unit area) using the assumption that the force is evenly distributed over the chordwise and spanwise extent of the local blade section of interest. These pressures are now ready for use in OVERFLOW, which will be discussed in a later chapter.

Since the current research employs the GDWT in a manner in which it is not normally used, new computer coding has been developed here to compute required quantities from this theory, in combination with solution methods that have not previously been used with the GDWT. To validate that the new theory and models have been implemented correctly, a validation study is presented in the next chapter.
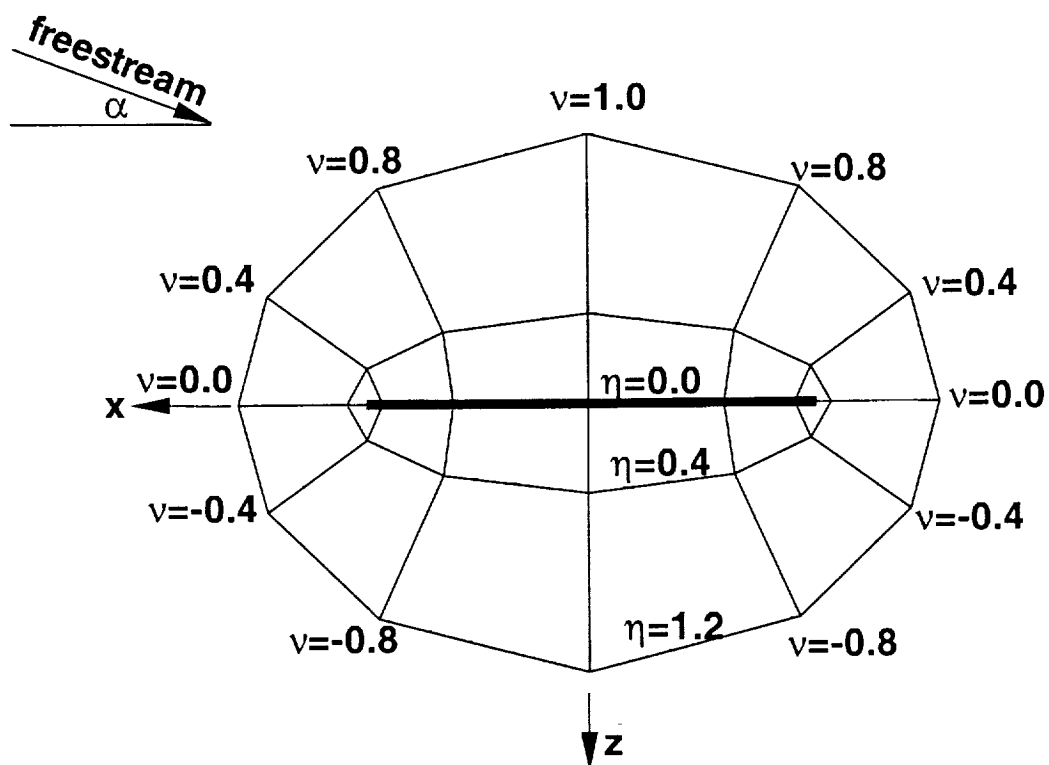
Figure 2.1: Ellipsoidal Coordinates.

Chapter 3

GDWT Validation

3.1 Introduction

Though there are numerous examples of the GDWT published in the literature, the present combination of the GDWT with the present solution procedures has not been explored in the past. Also, computer coding to do the actual computations with these combinations of theory and solution procedures was not available for the purposes of the current research. As such, validation is required to determine that the current model matches previously published literature on the subject. This validation effort is described in this chapter.

3.2 Experimental Setup

All of the experimental data used for the validation effort in this chapter was obtained from laser velocimeter inflow measurements made in the NASA Langley Research Center 14- by 22-Foot Subsonic Tunnel. The experimental setup and data used for this chapter is described in detail in references [33, 34, 35, 36]; for completeness, the experiments are described here in brief.

Two different planforms were used in this test, one rectangular and one tapered. A summary of the two geometries is given in table 3.1 and a picture of the configuration, installed in the tunnel, is shown in figure 3.1. In this figure, the rotor/fuselage configuration consists of a generic helicopter fuselage body, known as the ROtor Body INteraction (ROBIN) fuselage [37], and one of the two

rotor configurations, described above. Inflow data was taken on these two rotor configurations at several advance ratios (*i.e.,* forward speed divided by the rotor tip speed) for 12 azimuthal stations located 30 degrees apart (starting from an azimuth location of 0°, directly downstream of the rotor hub) and at a number of radial stations at each of these azimuth stations. Data samples were processed at a resolution of 128 samples per rotor revolution at each measurement location. For this chapter, the data is presented in two formats. The first format is the time averaged data, which is obtained by temporally averaging the unsteady data at each measurement location. The second format is time accurate data, which is the unsteady data before it is time averaged.

There are two advance ratios used in this chapter. The first, $\mu = 0.15$, can be though of as boundary between (1) very low speed flight, where the fuselage flowfield is completely dominated by the rotor wake, and (2) moderate forward flight, where the fuselage flowfield is no longer dominated by rotor wake interactions. The second, $\mu = 0.23$ can be thought of as a moderate forward flight case. At both speeds, pressure pulse effects on the fuselage from the passing rotor blades is felt.

The time averaged data will be presented in the form of contour plots of induced inflow ratio (*i.e.,* magnitude of induced inflow velocity divided by rotor tip speed) mapped over the entire rotor disk. The time accurate induced inflow ratio will be presented as time histories which depict the induced inflow ratio at a particular fixed point over the rotor disk. For the contour plots of the measured data, it is worth noting that, even though the temporal resolution in the time accurate measurements corresponds to approximately 2.8° of blade travel, the spatial resolution in the measured data is limited. This spatial resolution limit is imposed by the limited number of azimuthal locations at which measurements were taken over the rotor disk. For the contour plots, the implication is that, since there were only twelve azimuthal measurement locations, the spatial frequency content of the induced inflow data in the azimuthal direction is limited by the Nyquist criterion to six harmonics per rotor revolution. In addition, there are some measurement locations at which no data is available.

For the sole purpose of making consistent contour plots of measured data, which are presented subsequently, the time averaged data for induced inflow ratio over the rotor disk has been linearly interpolated onto a grid consisting of seventeen evenly spaced radial stations from the 20% radius location to the tip location and onto twelve evenly spaced azimuth locations around the rotor disk. Interpolation onto a regular grid in this manner serves to "full-in" measured data that is not available at particular locations over the rotor disk.

Table 3.2 lists the matrix of cases, measured and predicted, that a will be used for the validation effort in this chapter.

3.3 Time Averaged Induced Inflow

The following two sections present the time averaged, measured and predicted induced inflow ratio for several configurations. The quantities presented here are ones that have been derived from the measurements and predictions by time averaging the time accurate induced inflow ratio. Also, it should be noted here that the measured quantities include the effects of the ROBIN fuselage geometry and the predicted quantities do not include these effects (*i.e.*, the predictions are for an isolated rotor).

3.3.1 Rectangular Planform

Figure 3.2 shows a spatial contour plot comparison between the time averaged, measured and predicted induced inflow ratio for the rectangular planform at an advance ratio of 0.15, for a range of harmonics in the GDWT. Figure 3.2a is the measured data, including effects of the fuselage body. Figure 3.2b shows the GDWT predicted data using only two harmonics. Here, only the nominally linear streamwise gradient of induced inflow is predicted. Figure 3.2c shows the GDWT predicted data using four harmonics. In this figure, it can be seen that the major features of the measured data are predicted well. For example, the upwash on the forward section of the disk is predicted, though it does not cover as much of the forward region of the disk as in the measured data. The aft downwash regions, concentrated in the first and fourth rotor quadrants (see figure 3.18 for quadrant definitions), are also predicted. Figure 3.2d shows the GDWT predicted data using eight harmonics. In this figure, all of the same features are present as in figure 3.2c, but the details of the induced inflow are slightly different. Figure 3.3 shows the same data as in figure 3.2, but these are lateral and longitudinal subsets of the data and show the radial variation of measured and predicted induced inflow. Figure 3.3a shows measured and predicted lateral variation of the induced inflow ratio for 2, 4, and 8 harmonics; the advancing and retreating sides of the rotor disk are labeled. Figure 3.3b shows measured and predicted longitudinal variation of the inflow ratio for 2, 4, and 8 harmonics; the forward and aft portions of the rotor disk are labeled. Figures 3.4 and 3.5 show the same case as the previous two figures, except these predictions use 128 azimuth

steps per revolution instead of 64. No significant differences are apparent between the two different azimuthal resolutions; this shows that, for this particular case, 128 azimuth steps per revolution is a sufficient azimuthal resolution.

Figures 3.6 to 3.9 show the same contour plots and lateral/longitudinal plots as in figures 3.2 to 3.5, but for the higher advance ratio of 0.23. For this advance ratio, as with the lower advance ratio, little difference is seen between the use of 4 and 8 harmonics and little difference is seen between the use of 64 azimuthal steps and 128 azimuthal steps.

3.3.2   Tapered Planform

Figures 3.10 to 3.17 represent the same cases as in figures 3.2 to 3.9, but instead, using the tapered planform rotor. In comparison to the computations on the rectangular planform, the extent of the upwash region on the forward portion of the disk is better predicted based on the contour plots. Also, from the lateral and longitudinal plots, it can be seen that fewer harmonics are needed to predict the induced inflow behavior at the tip for the tapered planform. These findings for the contour plots and for the lateral and longitudinal plots are in agreement with findings in the published literature [25].

3.4   Time Accurate Induced Inflow

The previous sections presented the time averaged quantities derived from the experimental and predicted data. The following two sections present the unsteady induced inflow ratio components associated with the cases presented above except for the cases corresponding to two harmonics. These two harmonic cases are excluded at this point because using two harmonics does not adequately represent the time averaged induced inflow ratio distribution over the rotor disk. In order to show the time dependent quantities more clearly, the local time averaged quantities have been removed from each of the following plots. Figure 3.18 shows the measurement locations where the comparisons of the unsteady induced inflow will be made. The radial and azimuthal positions are shown for locations A through J. Locations A through I are used in this chapter. Location J will not be used in this chapter. It is, however, used in chapters 7 and 8 and is shown here for later reference.

3.4.1 Rectangular Planform

Figure 3.19 shows the unsteady component of induced inflow ratio at particular points on the rotor disk. The black dotted curves represent the measured data and the solid red lines represent the predicted data. In many of the measured data, a distinct set of four pulses per revolution can be seen. These pulses represent blade passages past the measurement location. The predictions at these measurement locations also show a periodic signature that generally matches the measurements in phase of the signals. Comparing figure 3.19 to figure 3.20 shows that for this configuration and this azimuthal resolution, the eight harmonic prediction matches the phase and amplitude better than the four harmonic prediction. Figures 3.21 and 3.22 show that the same holds for the 128 azimuth steps per revolution case. Figures 3.23 through 3.26 show that these results also hold for the higher advance ratio of 0.23. In these cases, it can be seen that, even using eight harmonics, the sharp, high frequency waveform of the measured inflow pulses is not matched well.

3.4.2 Tapered Planform

Figures 3.27 through 3.34 show the same features and results for the tapered blades as was presented for the rectangular blades above. As with the rectangular blade results, there is a typical, high frequency four per revolution pulse (waveform) indicative of blade passages seen at the measurement locations; the phase of these pulses generally matches the phase of the measured data. Also, as with the rectangular blade predictions, the eight harmonic results predict the amplitude better than the four per revolution results.

3.5 Observations

From the evidence presented in this chapter, the following observations can be made.

- Even though completely different methodology and computer coding from previous literature was used in the implementation and solution of the equations of the GDWT, the current results match well with the previously published literature [25, 27].

- The best overall choice for number of harmonics, considering both the advance ratio and configuration variations, is eight. This conclusion is influenced more by the time averaged

predictions than the time accurate predictions. This "weighting" toward the time averaged computations is influenced by the fact that the coupling model (discussed later in chapter 5) uses the time averaged quantities, not the time accurate quantities.

- Even with eight harmonics, it is not possible to simulate the sharpness of the blade passages.

- The induced inflow ratio predicted by the GDWT is relatively insensitive to the number of azimuthal steps used.

Based on the study presented in this chapter, and the observations presented in this section, it has been established that the new GDWT implementation is able to reproduce measured data in a manner comparable to previous literature. Thus, referring back to figure 1.2, the rotor loading model has been established. As such, the values of the ΔP pressure jump are now ready to be used in the rotor/fuselage model, which will be discussed in the next chapter.

Table 3.1: Rotor Geometries

Property	Rectangular	Tapered
radius	0.8606 meters	0.8255 meters
root chord	0.0660 meters	0.0800 meters
tip chord	0.0660 meters	0.0254 meters
taper ratio	(no taper)	3:1 past 0.75R
number of blades	4	4
root cutout location	0.24R	0.24R
flap/lag hinge location	0.06R	0.06R
sweep of quarter-chord	(none)	(none)
airfoil section	NACA 0012	NACA 0012
twist	-8°	-13°
precone	(none)	(none)
nominal thrust coefficient	0.0065	0.0065
solidity	0.0977	0.0977
nominal tip Mach number	0.55	0.55
approx. mean coning angle	1°	1°
shaft tilt	3° nose down	3° nose down

Table 3.2: Test and Prediction Matrix

Advance Ratio	No. Azimuths	No. Harmonics	Configuration
0.15	64	2,4,8	rectangular
0.15	128	2,4,8	rectangular
0.23	64	2,4,8	rectangular
0.23	128	2,4,8	rectangular
0.15	64	2,4,8	tapered
0.15	128	2,4,8	tapered
0.23	64	2,4,8	tapered
0.23	128	2,4,8	tapered
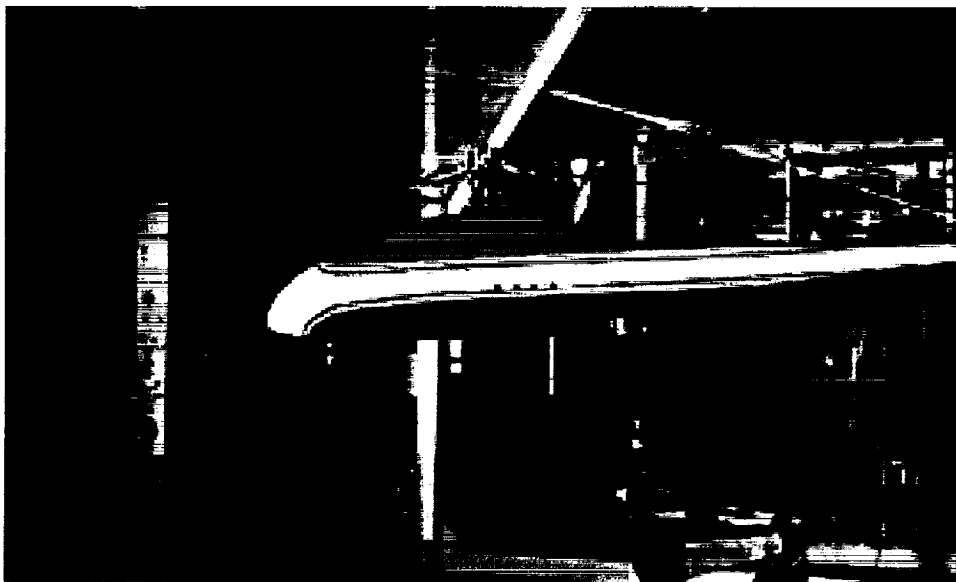
Figure 3.1: ROBIN Fuselage in the NASA Langley Research Center 14- by 22-Foot Subsonic Tunnel(1986).

Figure 3.2: Measured and GDWT Predicted Time Averaged Induced Inflow Ratio; Rectangular Planform, $\mu = 0.15$, 64 Azimuths.

Figure 3.3: Measured and GDWT Predicted Lateral and Longitudinal Time Averaged Induced Inflow Ratio; Rectangular Planform, $\mu = 0.15$, 64 Azimuths.

Figure 3.4: Measured and GDWT Predicted Time Averaged Induced Inflow Ratio; Rectangular Planform, $\mu = 0.15$, 128 Azimuths.

Figure 3.5: Measured and GDWT Predicted Lateral and Longitudinal Time Averaged Induced Inflow Ratio; Rectangular Planform, $\mu = 0.15$, 128 Azimuths.

Figure 3.6: Measured and GDWT Predicted Time Averaged Induced Inflow Ratio; Rectangular Planform, $\mu = 0.23$, 64 Azimuths.

Figure 3.7: Measured and GDWT Predicted Lateral and Longitudinal Time Averaged Induced Inflow Ratio; Rectangular Planform, $\mu = 0.23$, 64 Azimuths.
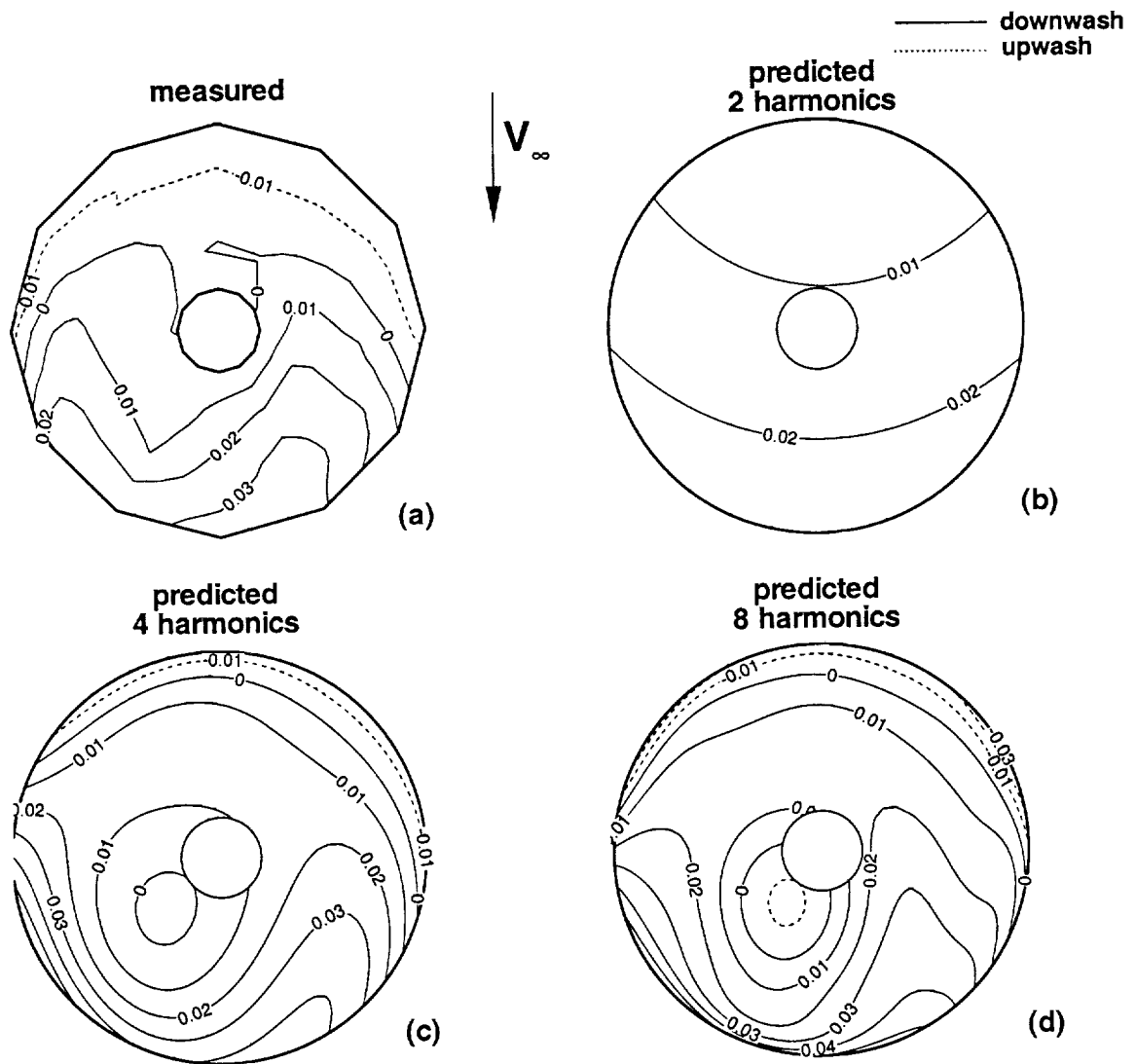
Figure 3.8: Measured and GDWT Predicted Time Averaged Induced Inflow Ratio; Rectangular Planform, $\mu = 0.23$, 128 Azimuths.
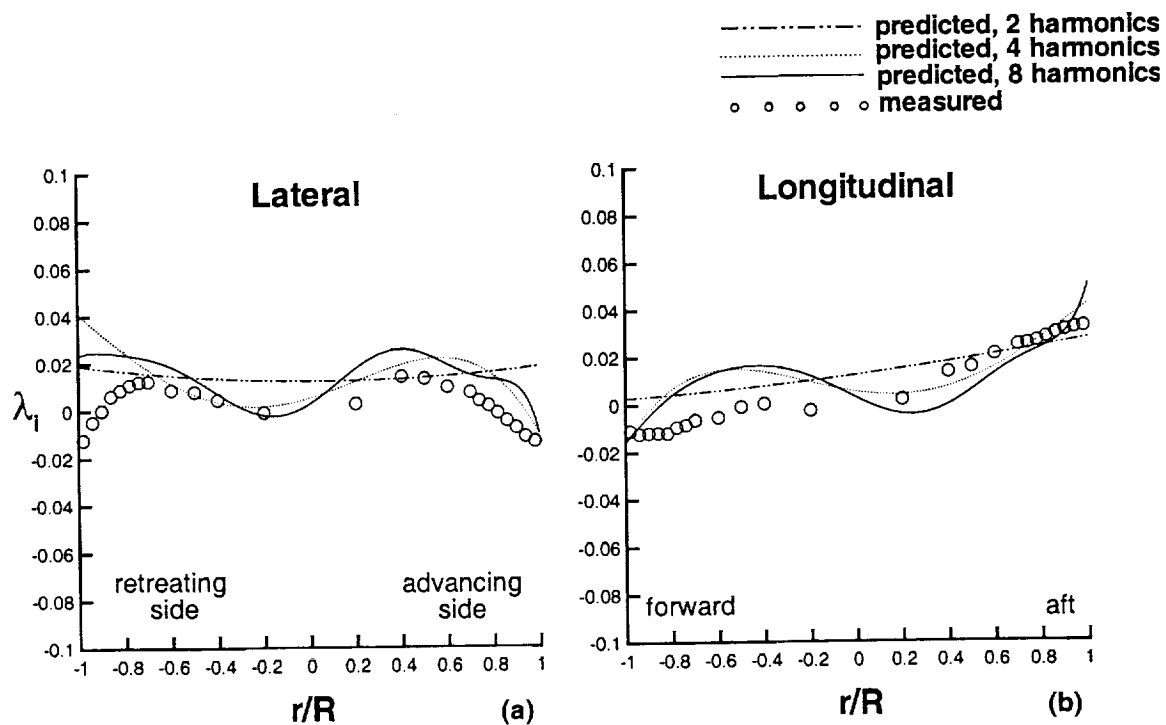
Figure 3.9: Measured and GDWT Predicted Lateral and Longitudinal Time Averaged Induced Inflow Ratio; Rectangular Planform, $\mu = 0.23$, 128 Azimuths.
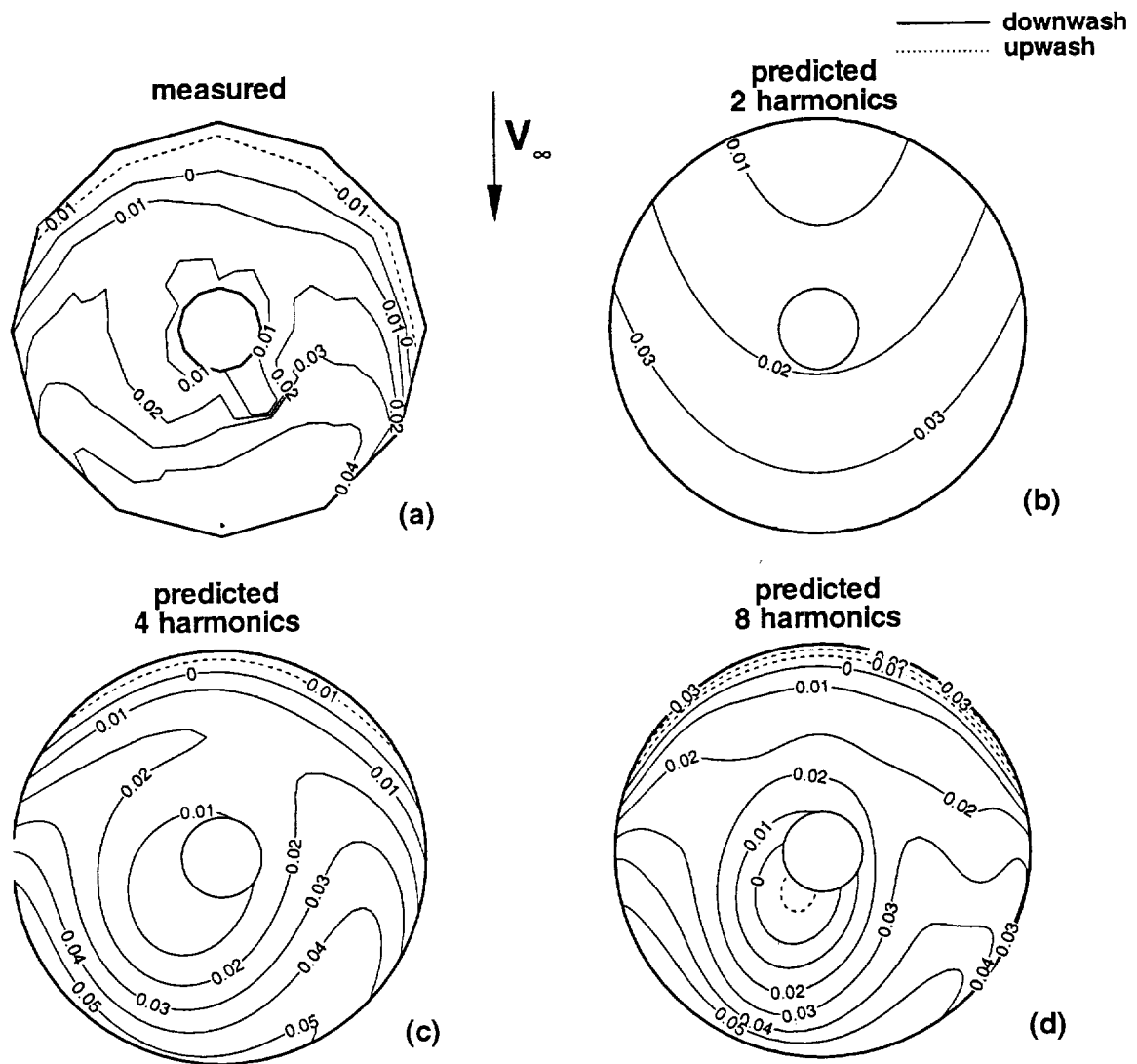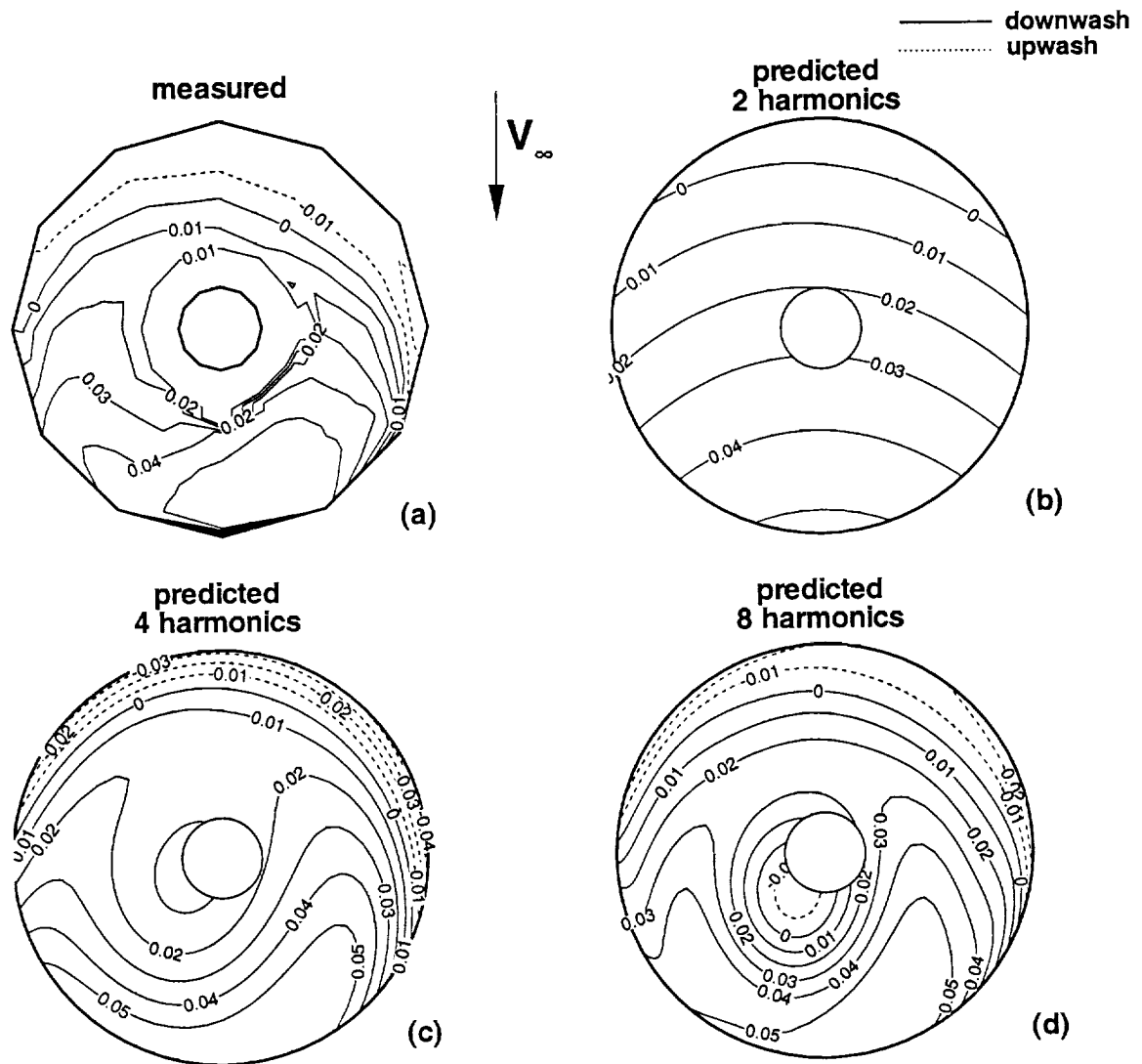
Figure 3.10: Measured and GDWT Predicted Time Averaged Induced Inflow Ratio; Tapered Planform, $\mu = 0.15$, 64 Azimuths.
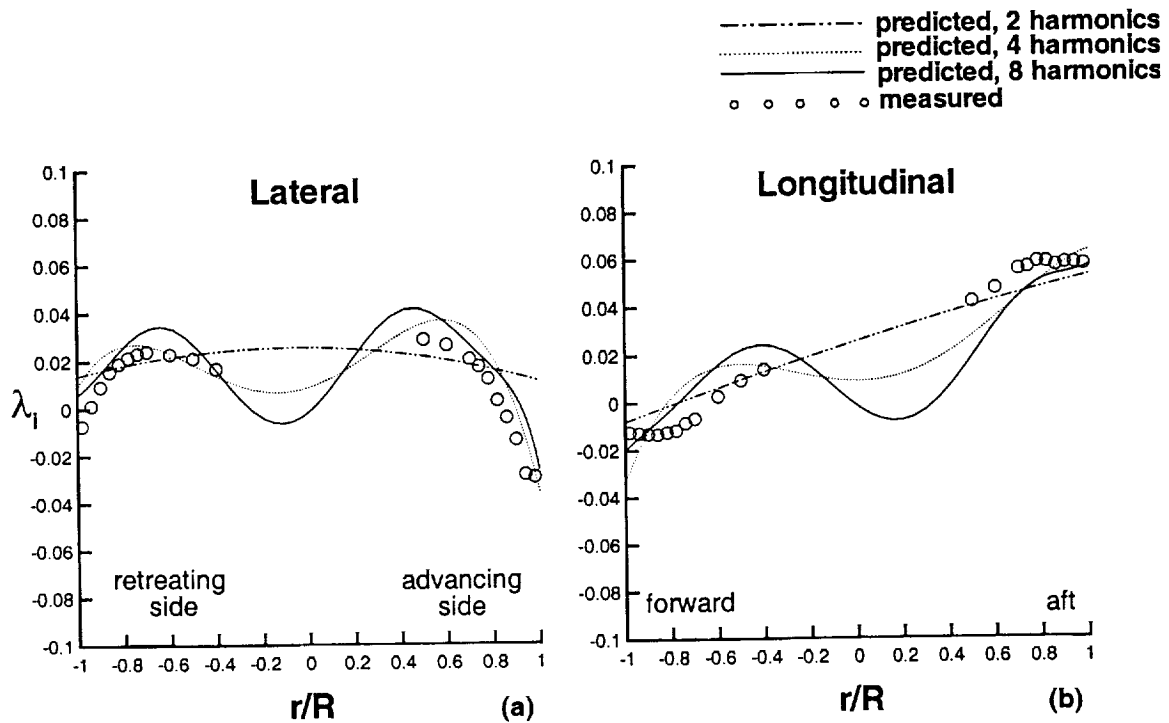
Figure 3.11: Measured and GDWT Predicted Lateral and Longitudinal Time Averaged Induced Inflow Ratio; Tapered Planform, $\mu = 0.15$, 64 Azimuths.
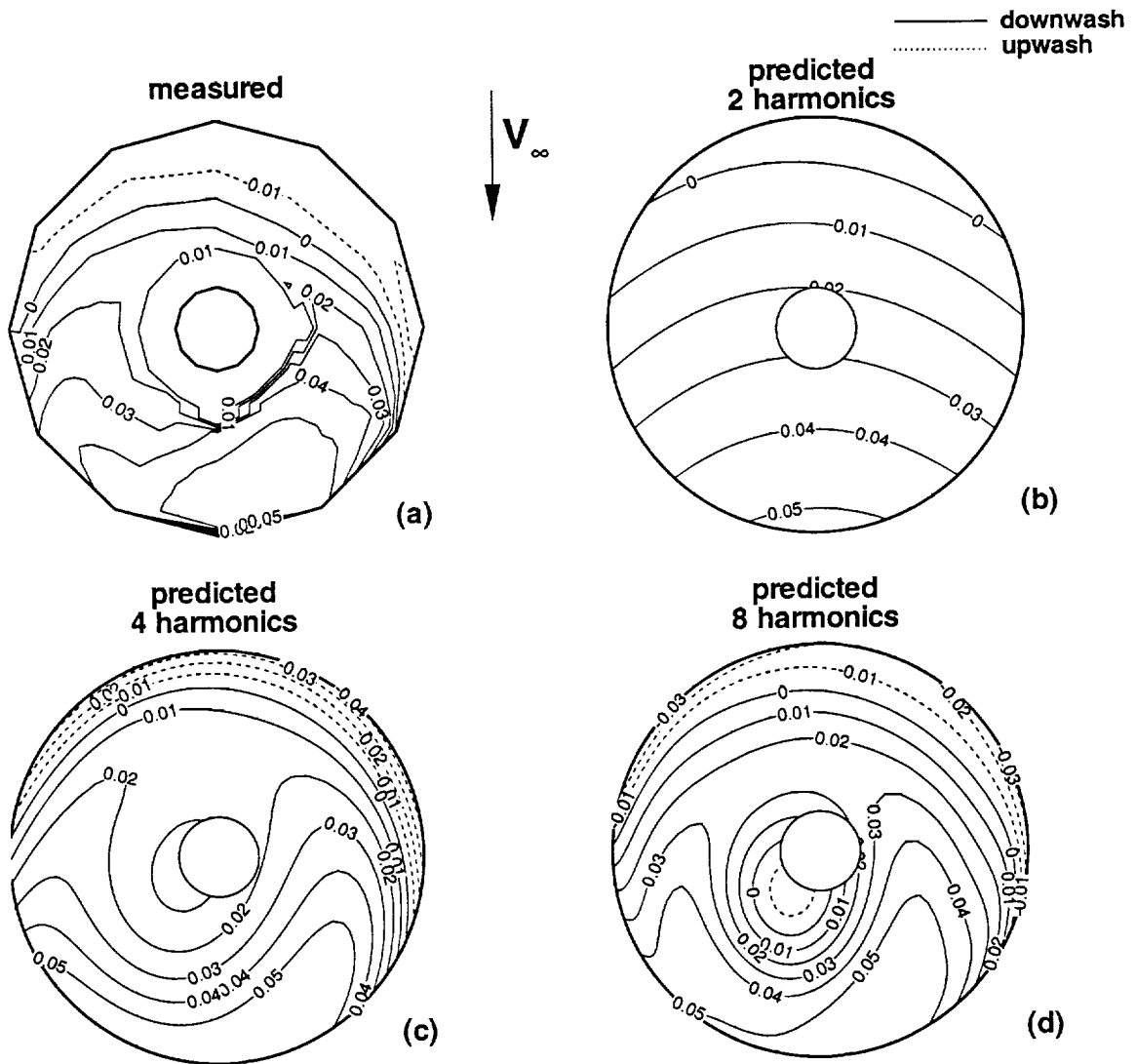
Figure 3.12: Measured and GDWT Predicted Time Averaged Induced Inflow Ratio; Tapered Planform, $\mu = 0.15$, 128 Azimuths.
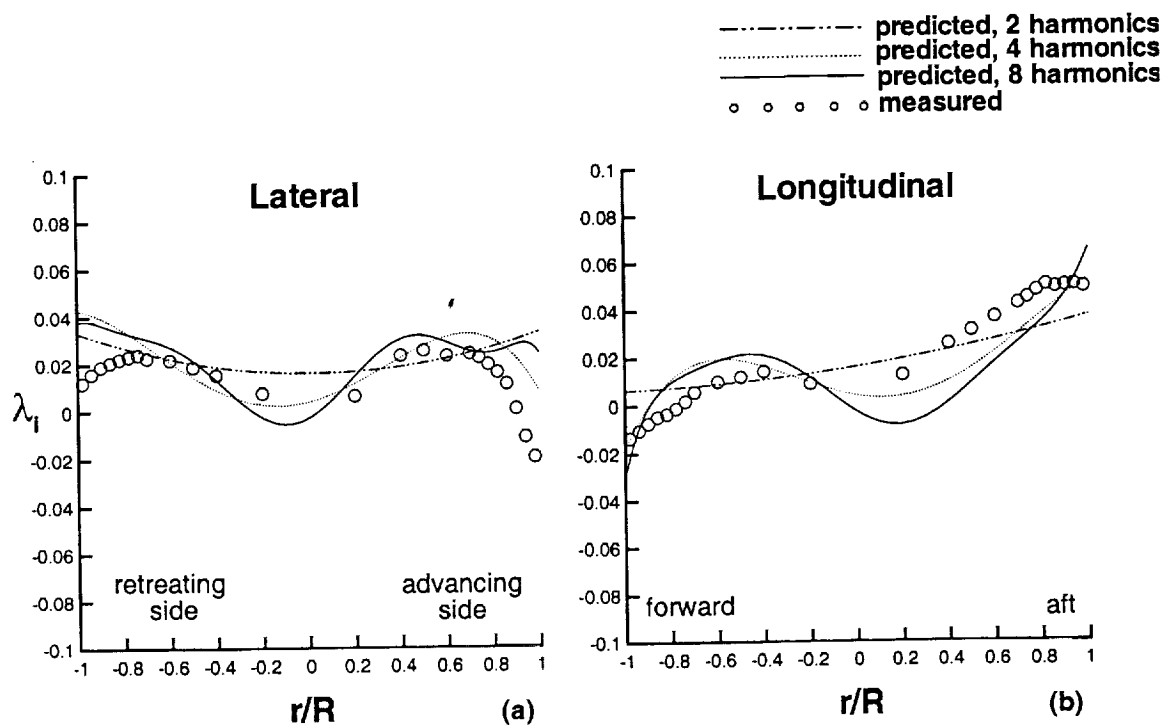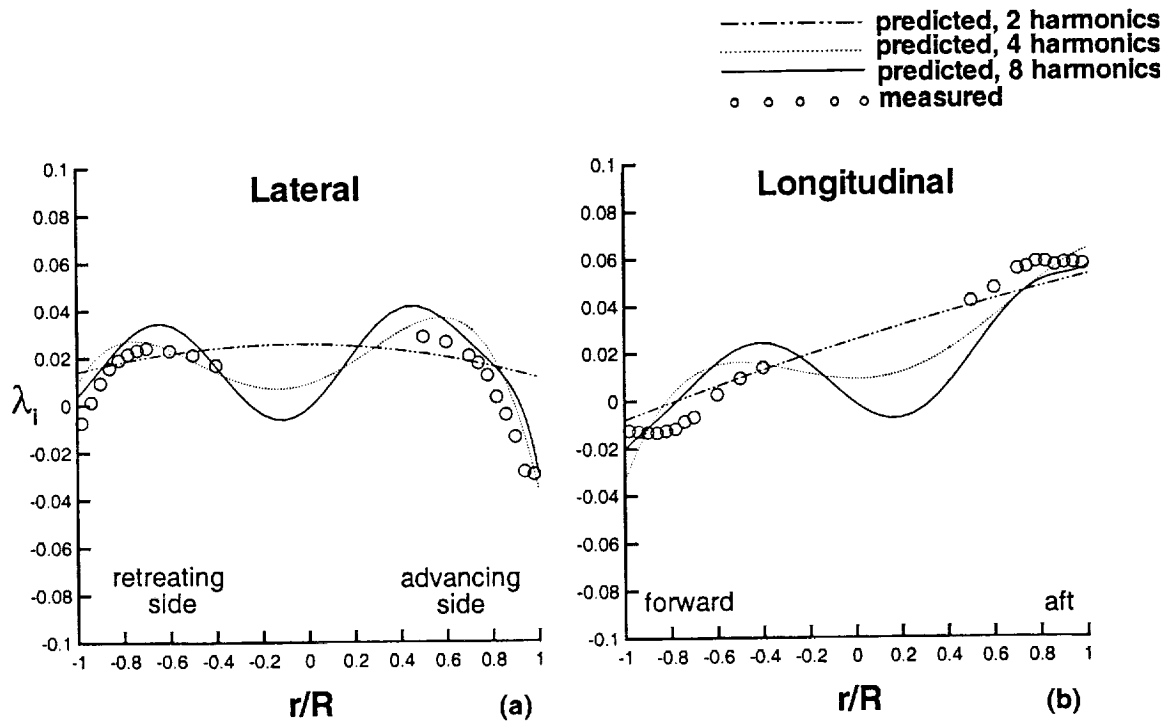
Figure 3.13: Measured and GDWT Predicted Lateral and Longitudinal Time Averaged Induced Inflow Ratio; Tapered Planform, $\mu = 0.15$, 128 Azimuths.
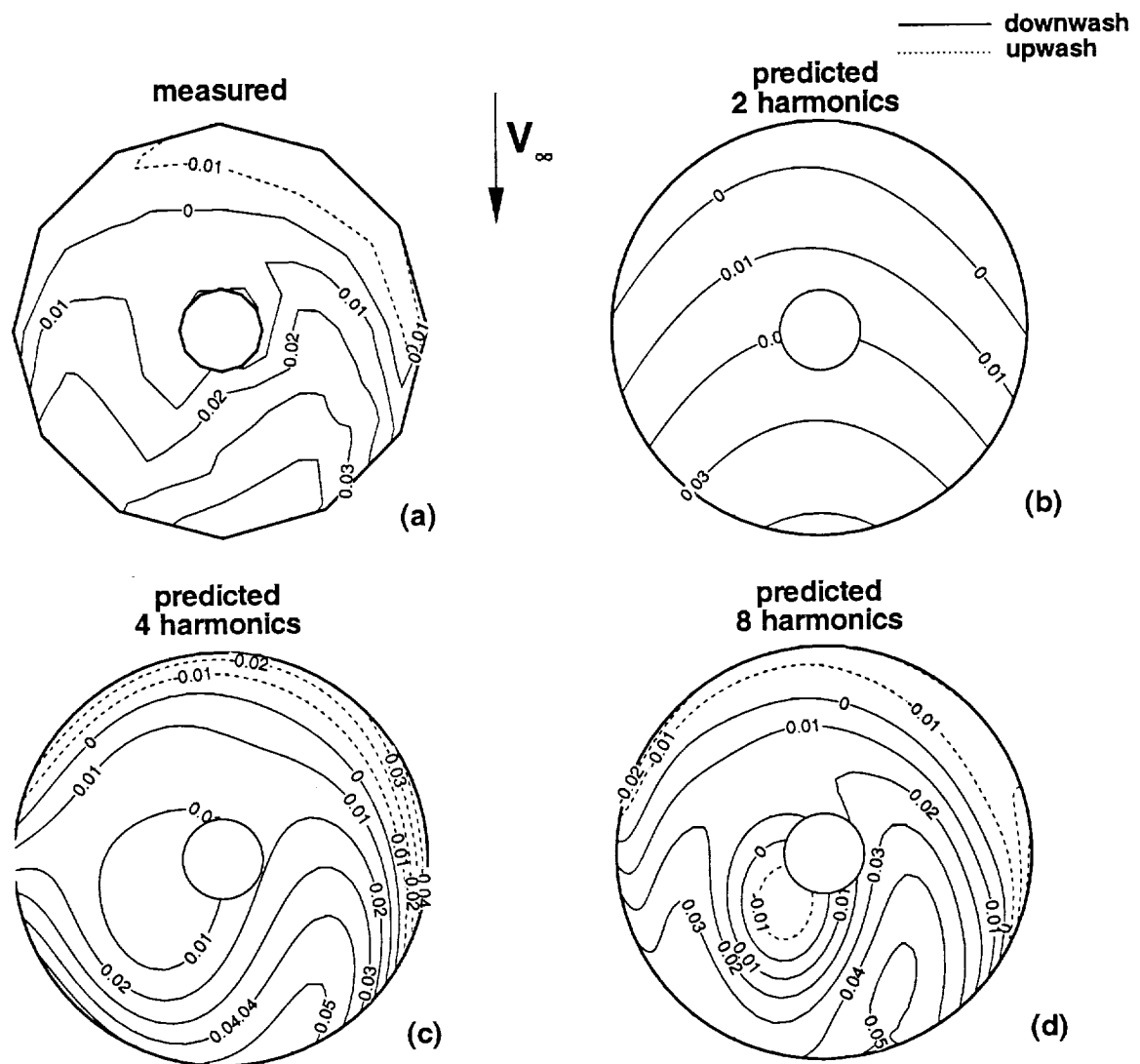
Figure 3.14: Measured and GDWT Predicted Time Averaged Induced Inflow Ratio; Tapered Planform, $\mu = 0.23$, 64 Azimuths.
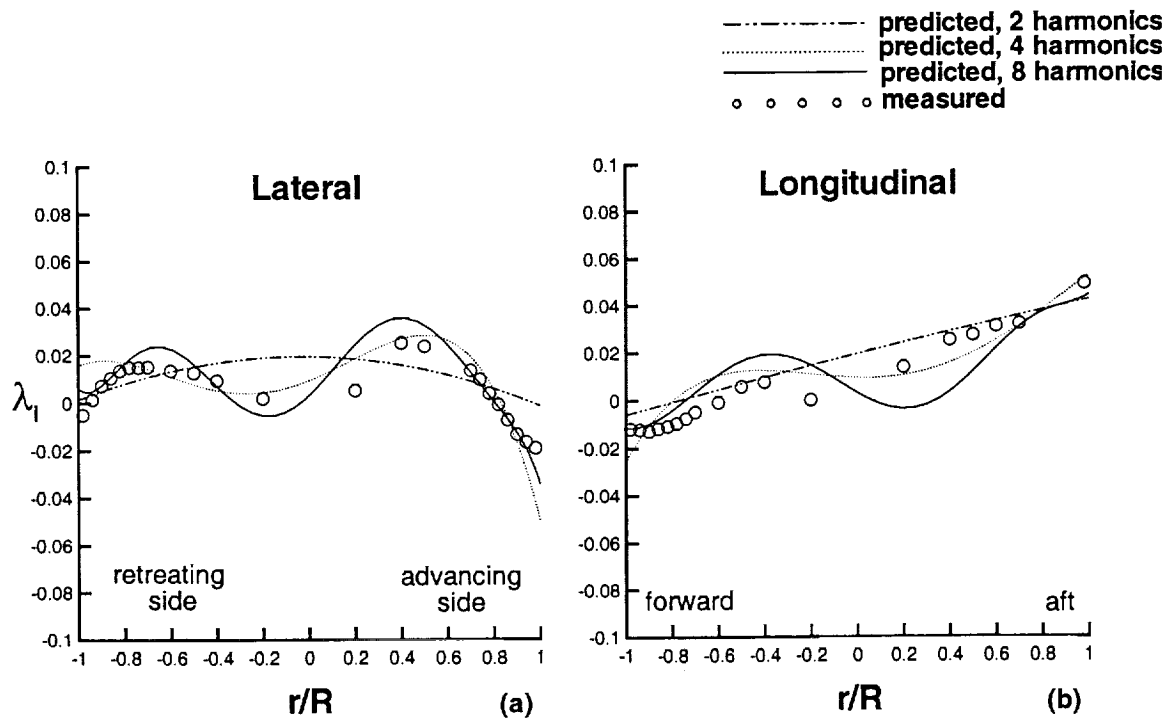
Figure 3.15: Measured and GDWT Predicted Lateral and Longitudinal Time Averaged Induced Inflow Ratio; Tapered Planform, $\mu = 0.23$, 64 Azimuths.
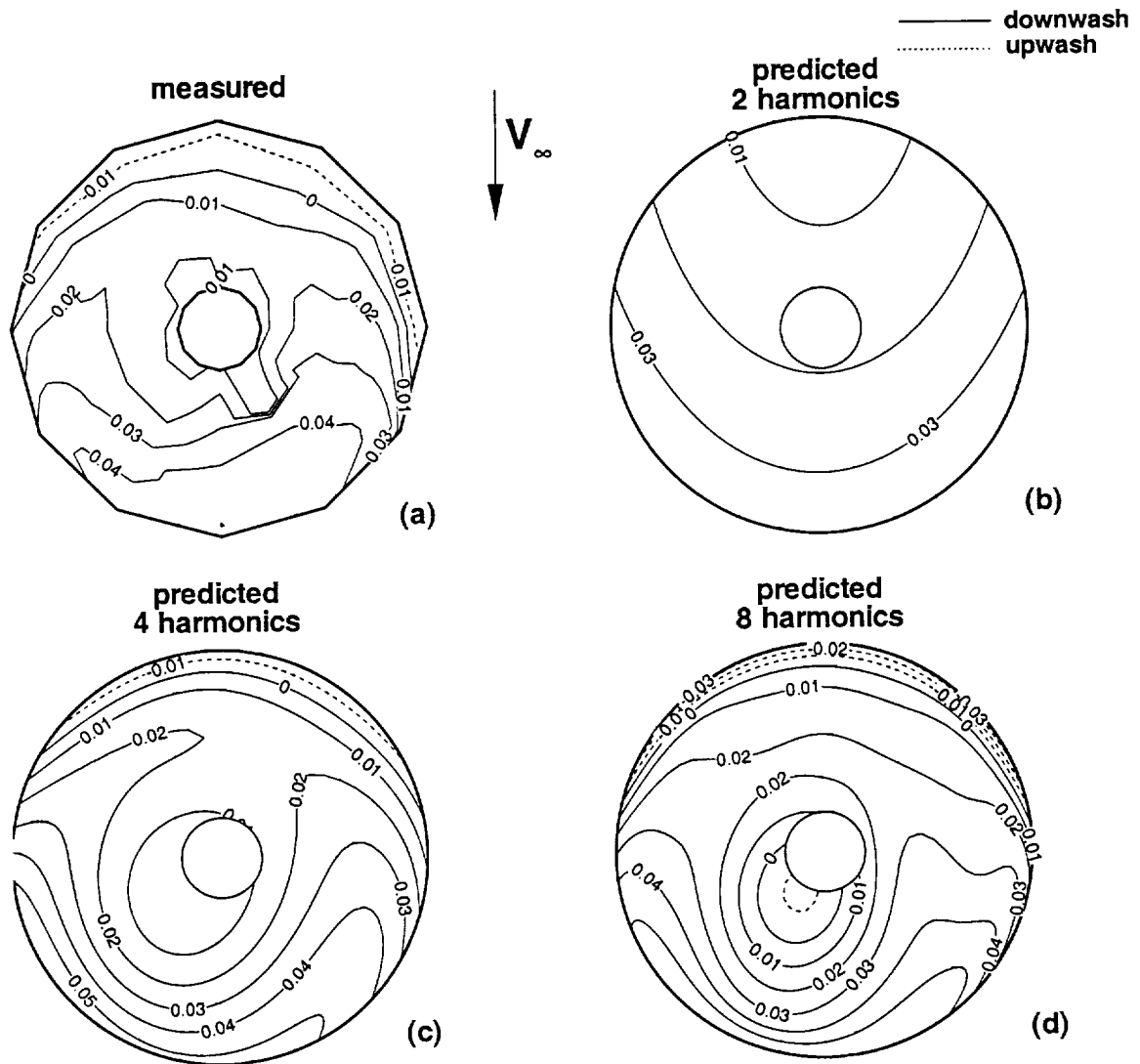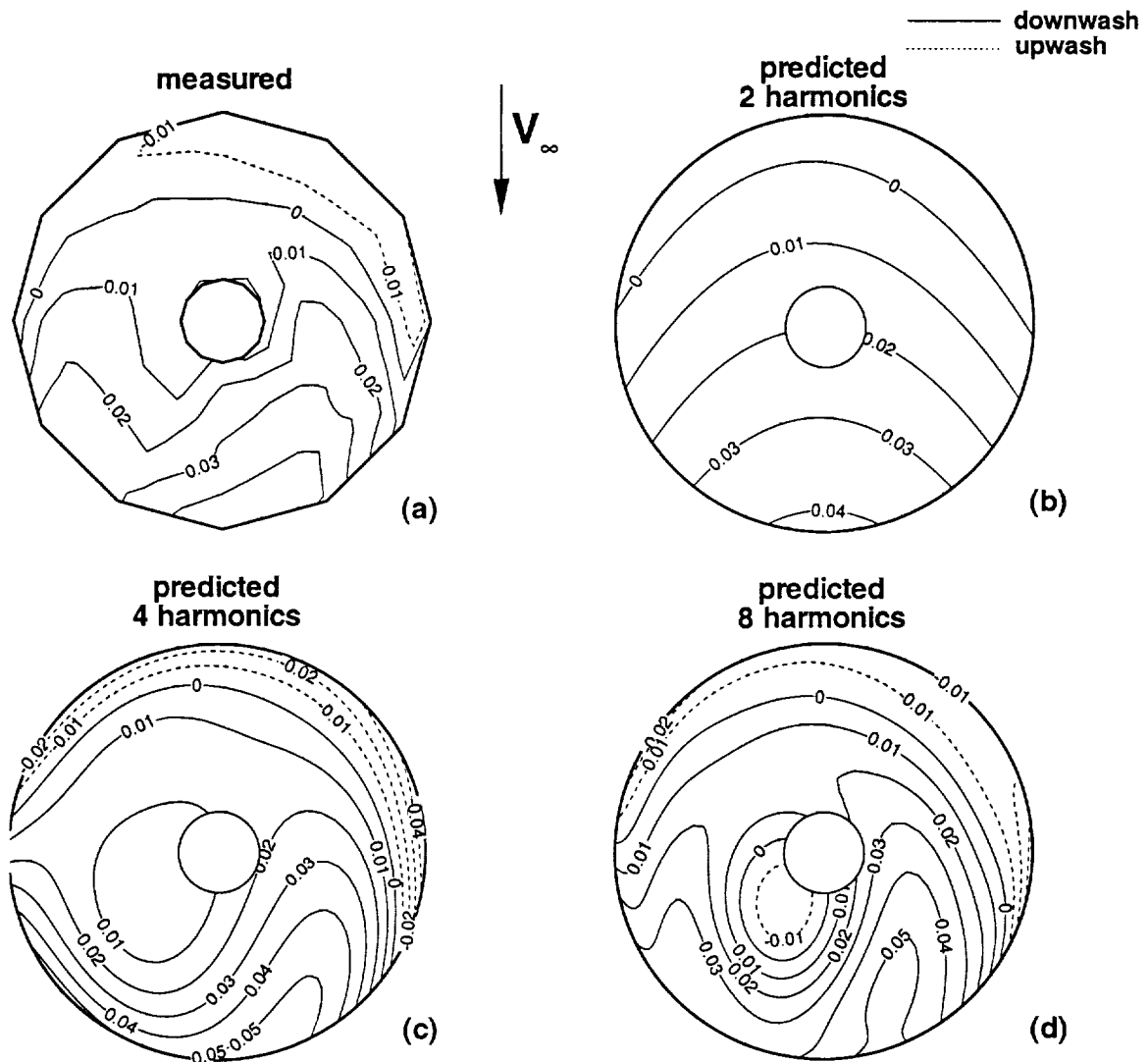
Figure 3.16: Measured and GDWT Predicted Time Averaged Induced Inflow Ratio; Tapered Planform, $\mu = 0.23$, 128 Azimuths.
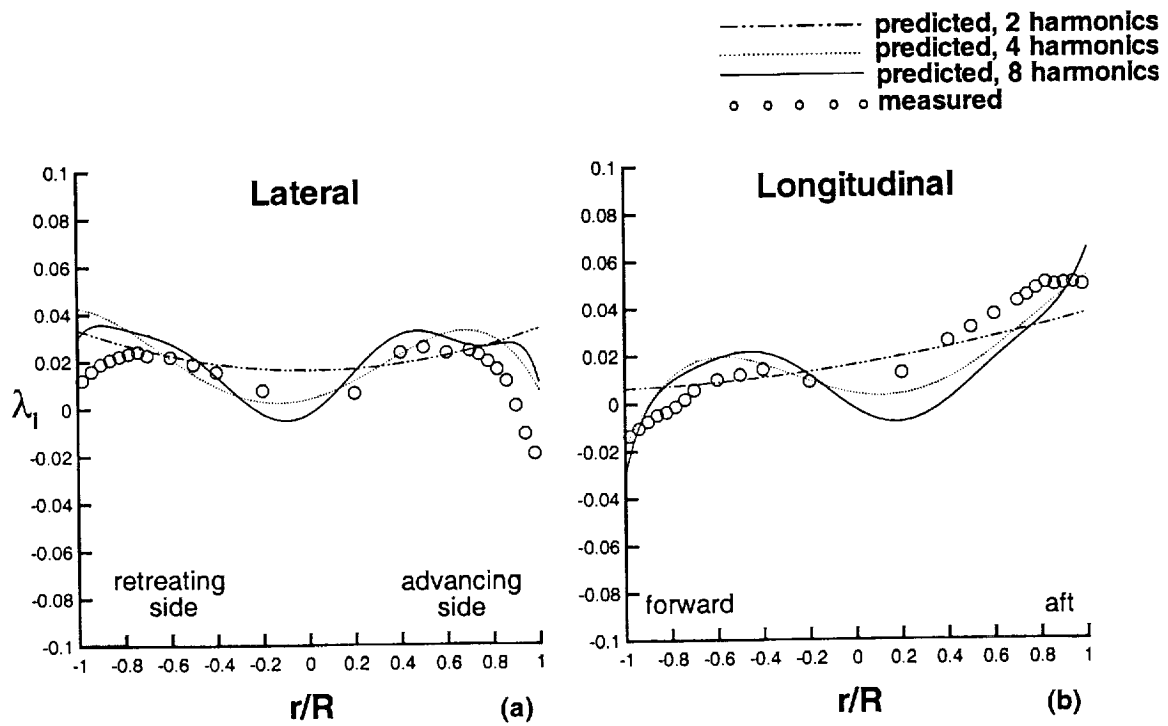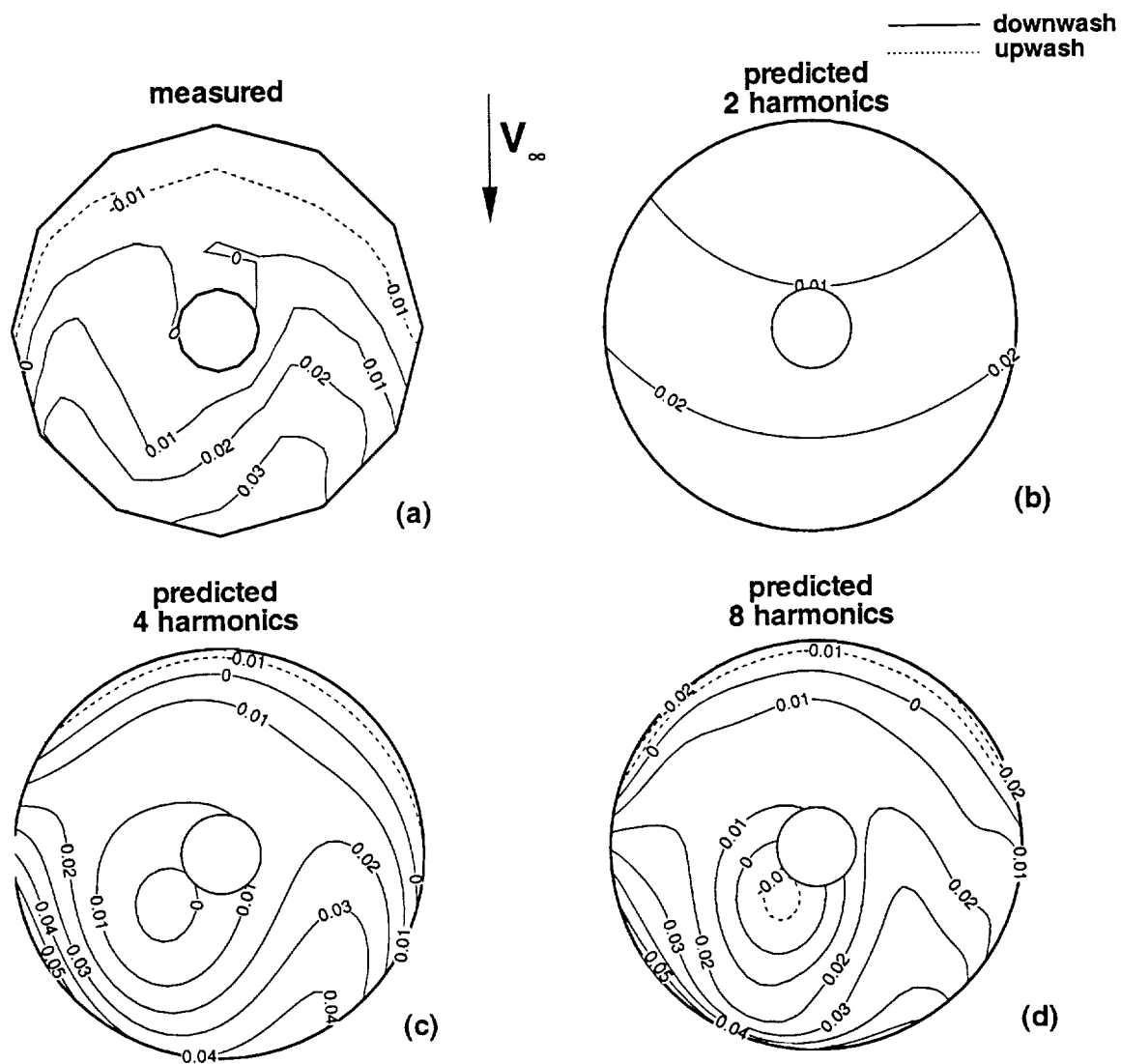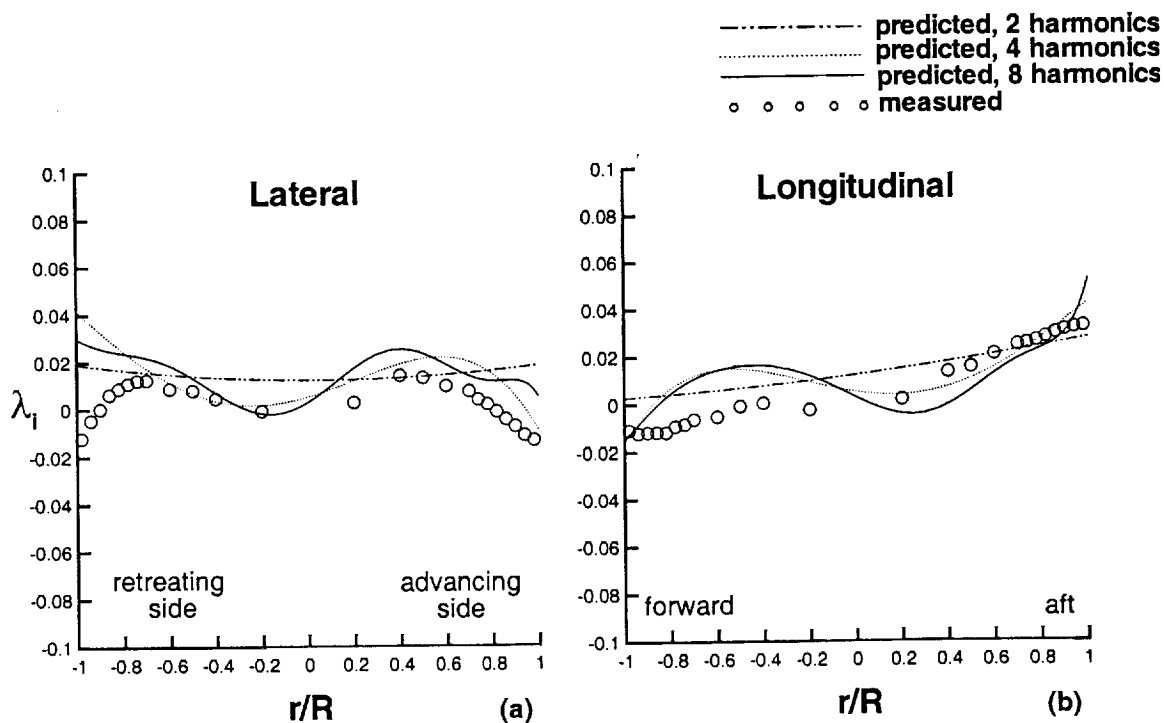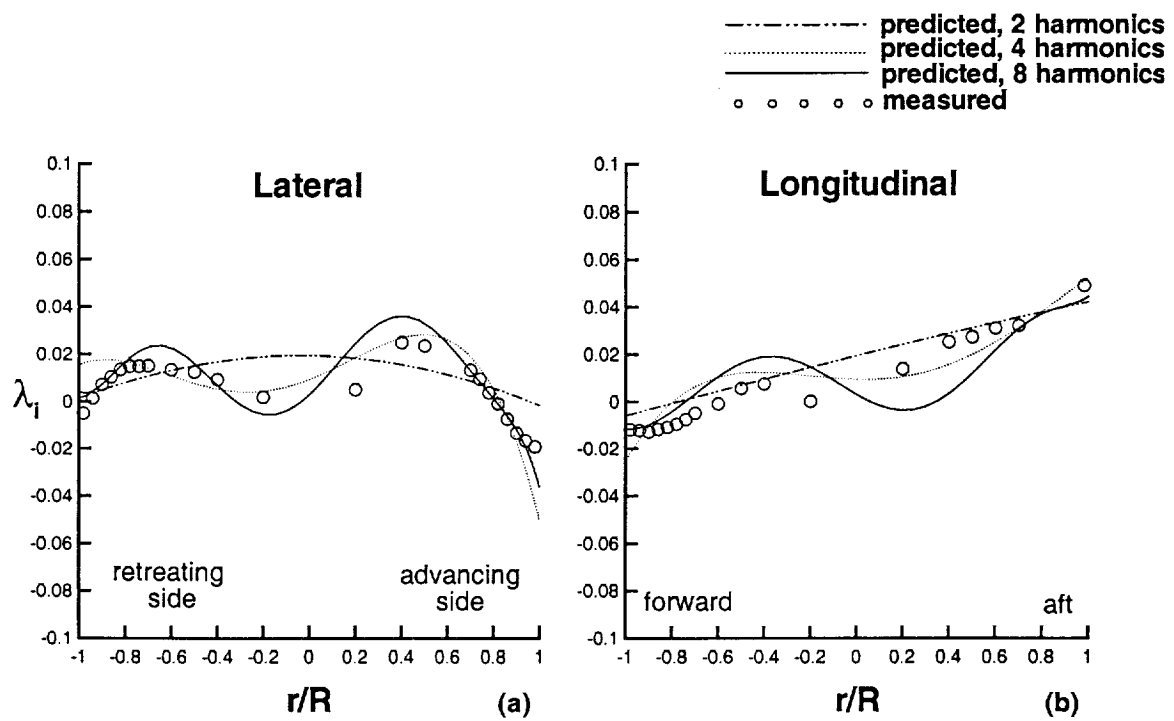
Figure 3.17: Measured and GDWT Predicted Lateral and Longitudinal Time Averaged Induced Inflow Ratio; Tapered Planform, $\mu = 0.23$, 128 Azimuths.
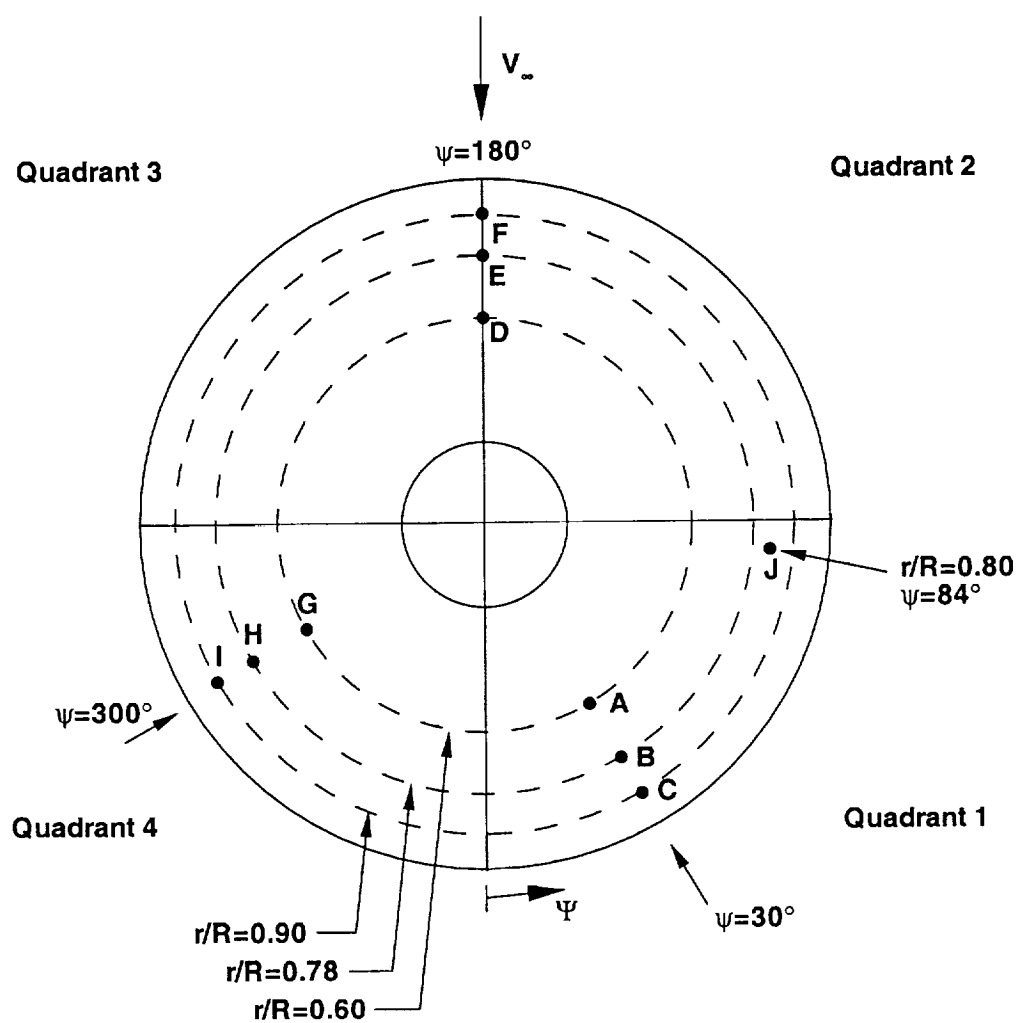
Figure 3.18: Locations Used in Comparisons.
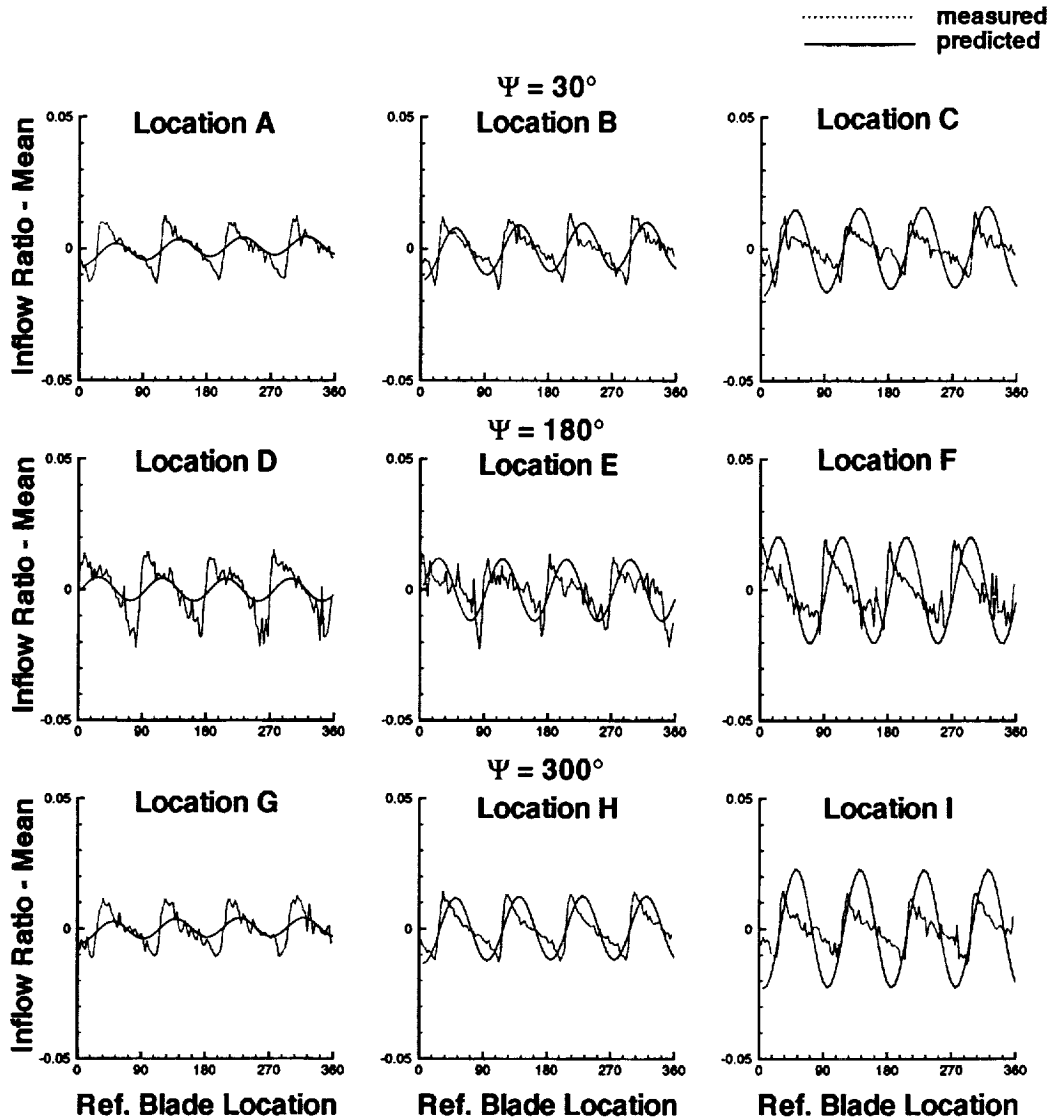
Figure 3.19: Measured and GDWT Predicted Unsteady Induced Inflow Ratio With Mean Values Removed; Rectangular Planform, $\mu = 0.15$, 64 Azimuths, 4 Harmonics.
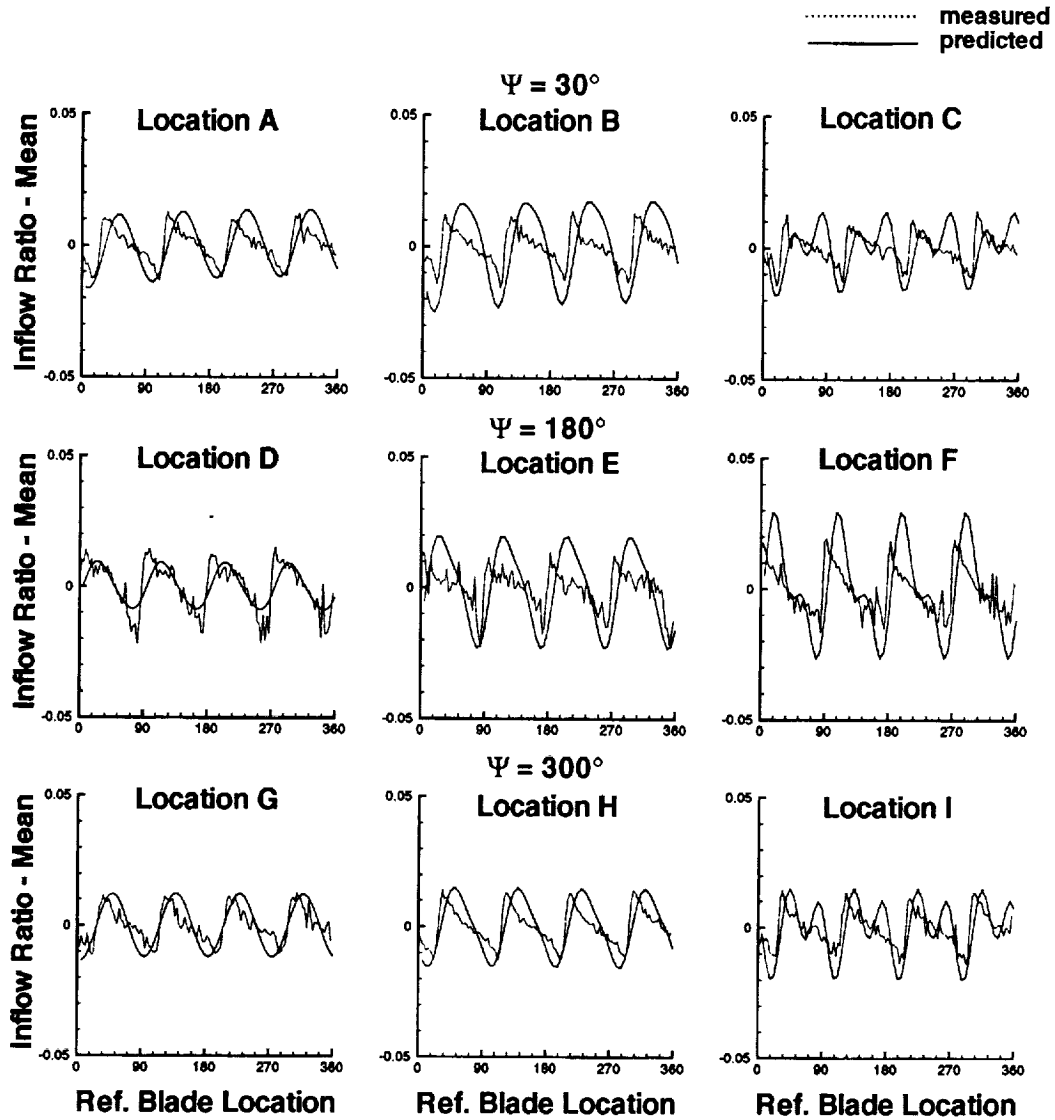
Figure 3.20: Measured and GDWT Predicted Unsteady Induced Inflow Ratio With Mean Values Removed; Rectangular Planform, $\mu = 0.15$, 64 Azimuths, 8 Harmonics.
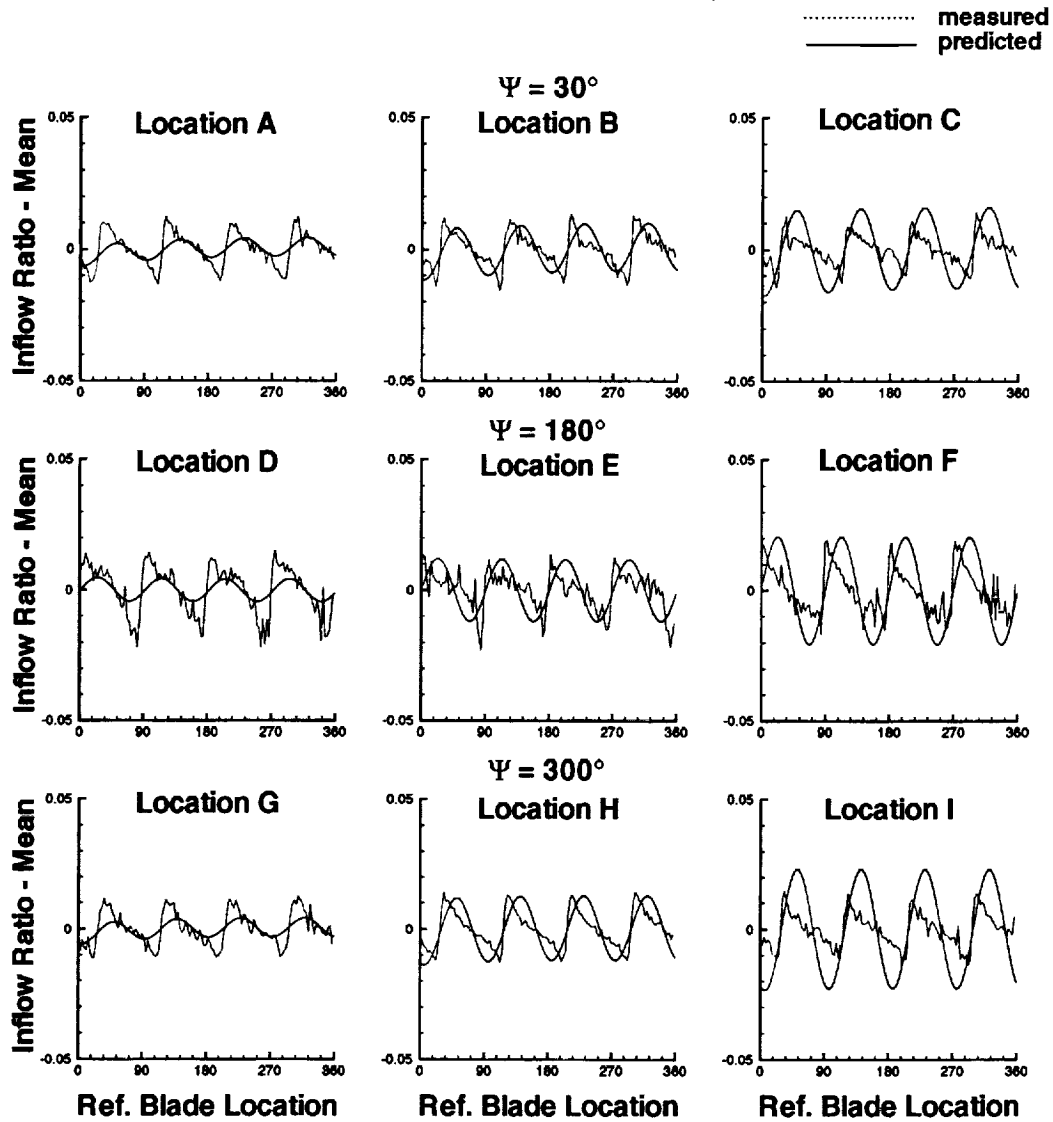
Figure 3.21: Measured and GDWT Predicted Unsteady Induced Inflow Ratio With Mean Values Removed; Rectangular Planform, $\mu = 0.15$, 128 Azimuths, 4 Harmonics.
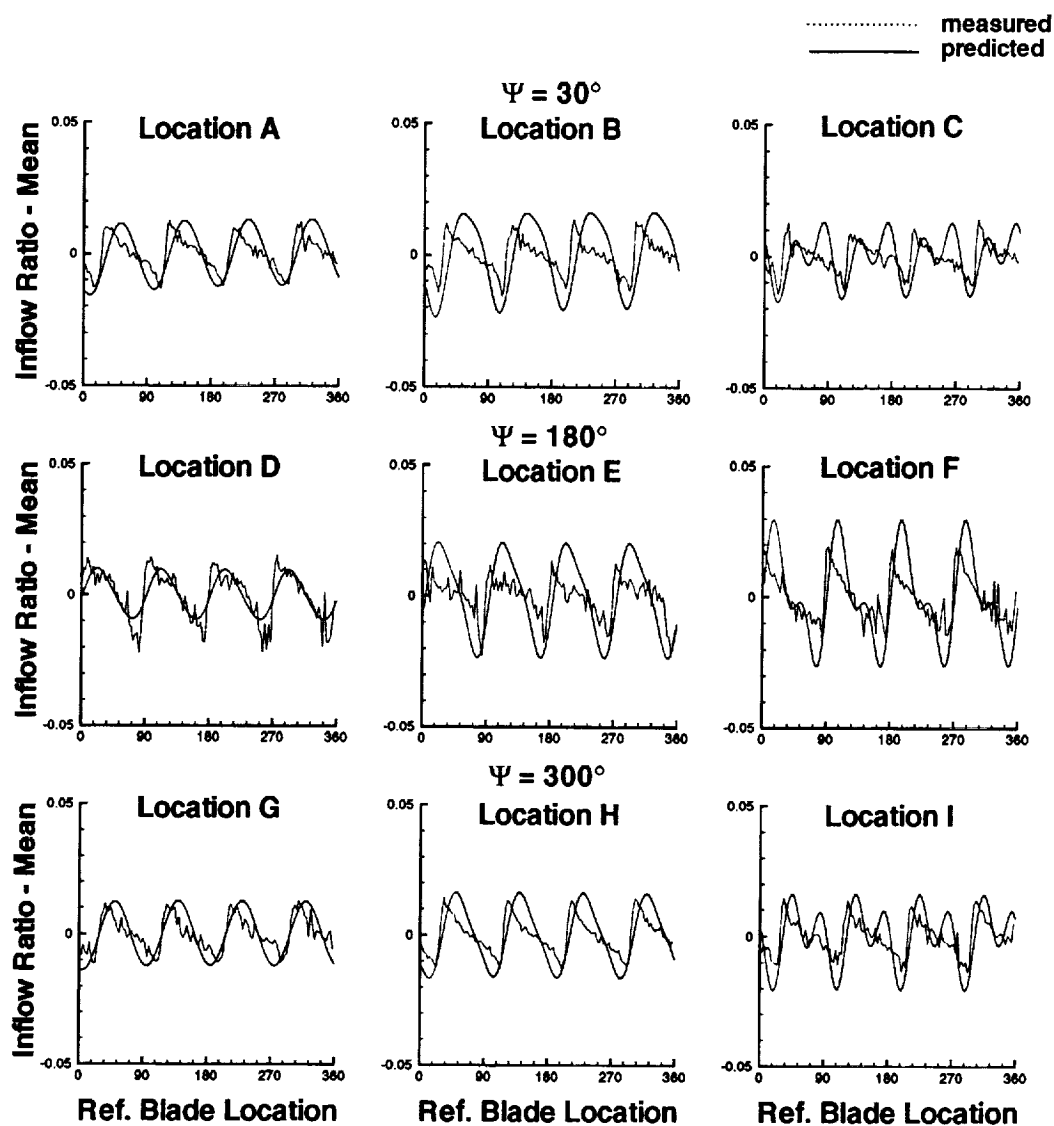
Figure 3.22: Measured and GDWT Predicted Unsteady Induced Inflow Ratio With Mean Values Removed; Rectangular Planform, $\mu = 0.15$, 128 Azimuths, 8 Harmonics.
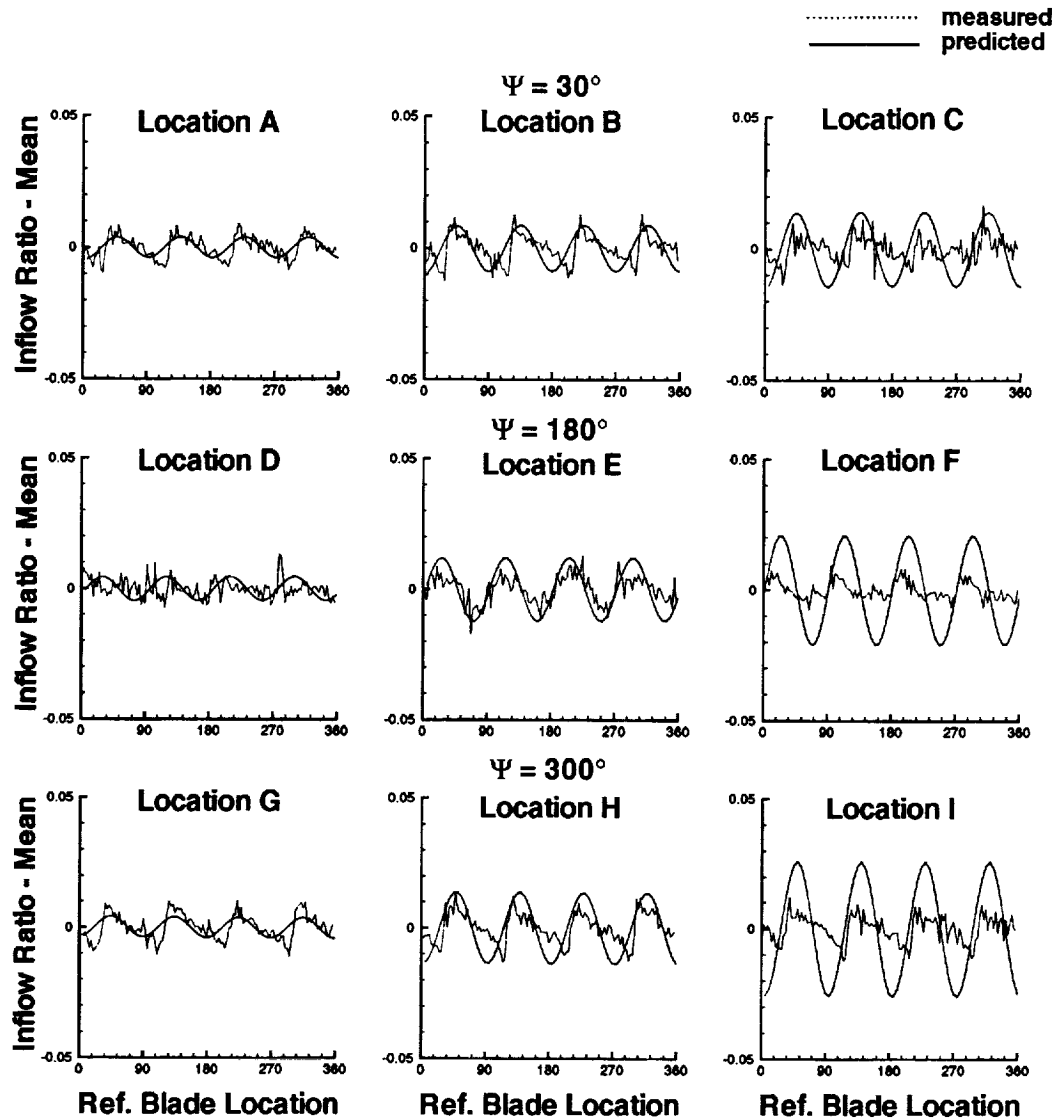
Figure 3.23: Measured and GDWT Predicted Unsteady Induced Inflow Ratio With Mean Values Removed; Rectangular Planform, $\mu = 0.23$, 64 Azimuths, 4 Harmonics.
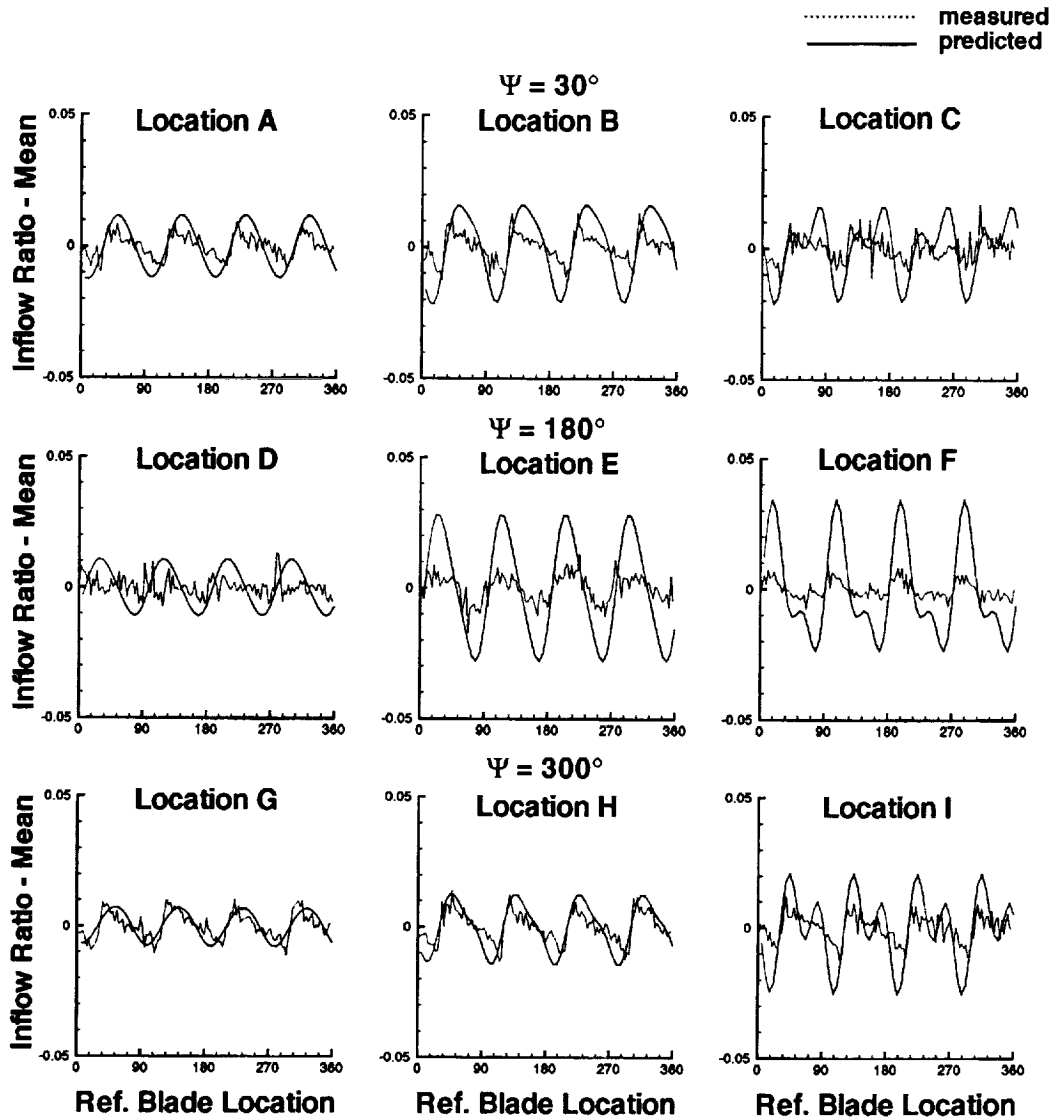
Figure 3.24: Measured and GDWT Predicted Unsteady Induced Inflow Ratio With Mean Values Removed; Rectangular Planform, $\mu = 0.23$, 64 Azimuths, 8 Harmonics.
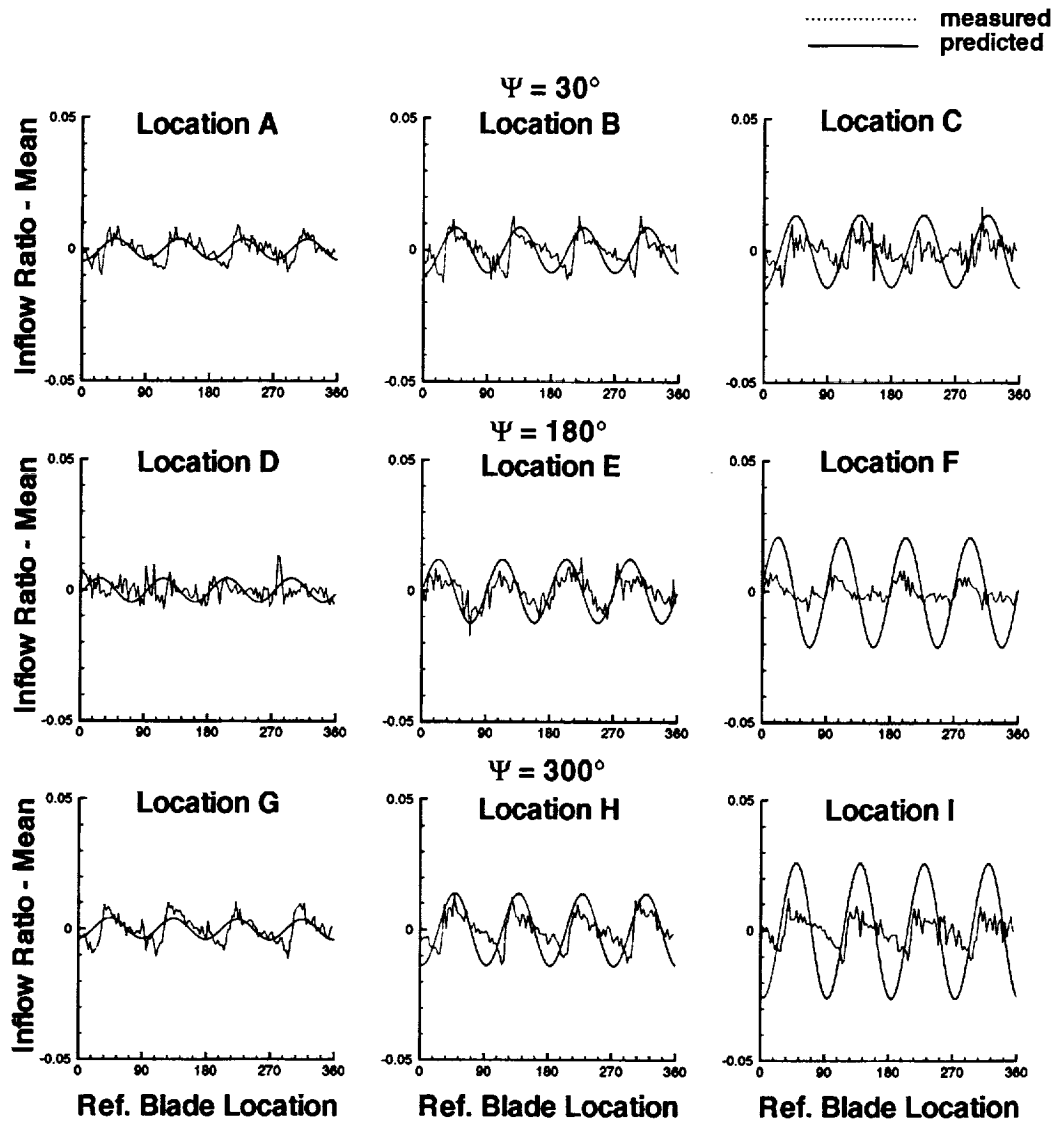
Figure 3.25: Measured and GDWT Predicted Unsteady Induced Inflow Ratio With Mean Values Removed; Rectangular Planform, $\mu = 0.23$, 128 Azimuths, 4 Harmonics.
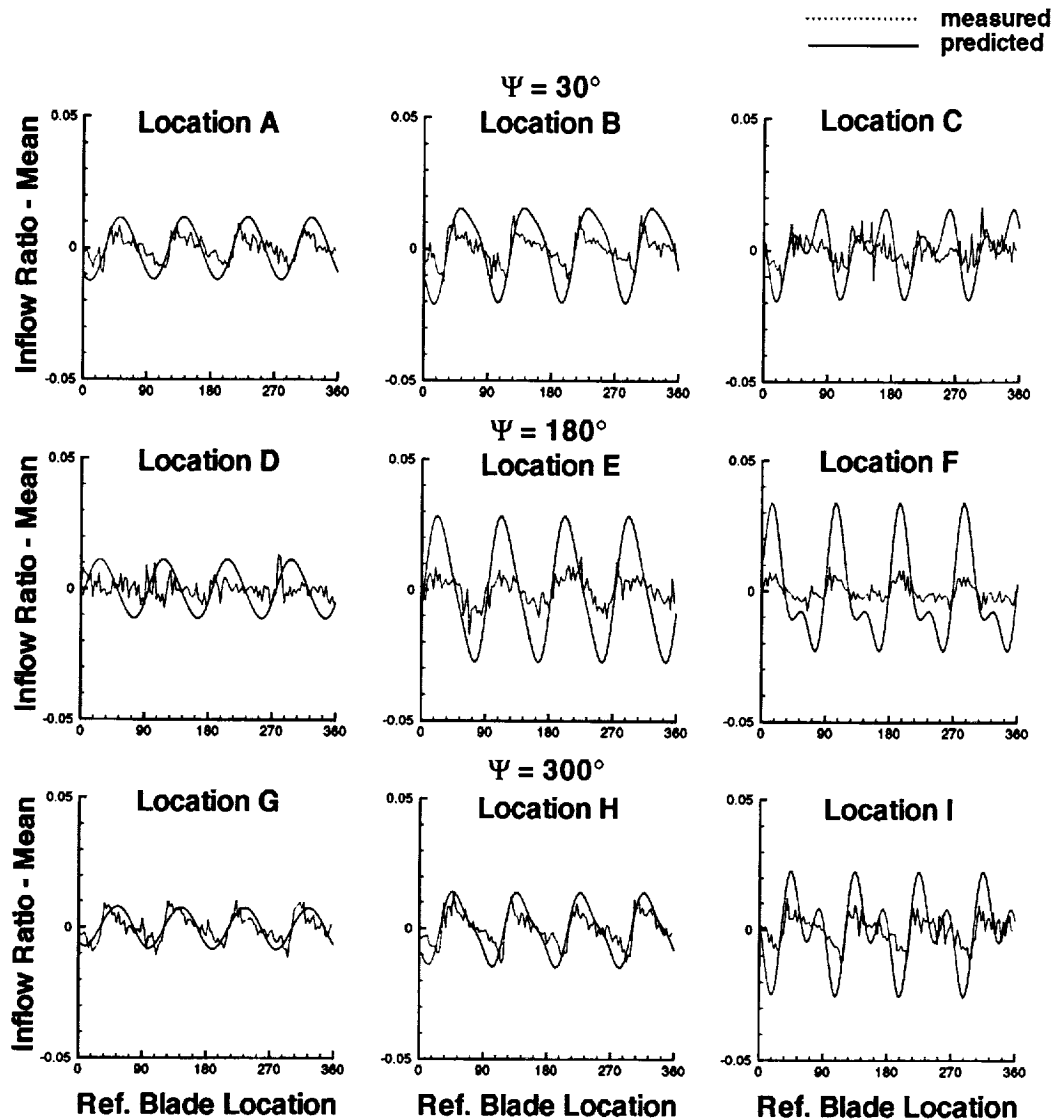
Figure 3.26: Measured and GDWT Predicted Unsteady Induced Inflow Ratio With Mean Values Removed; Rectangular Planform, $\mu = 0.23$, 128 Azimuths, 8 Harmonics.
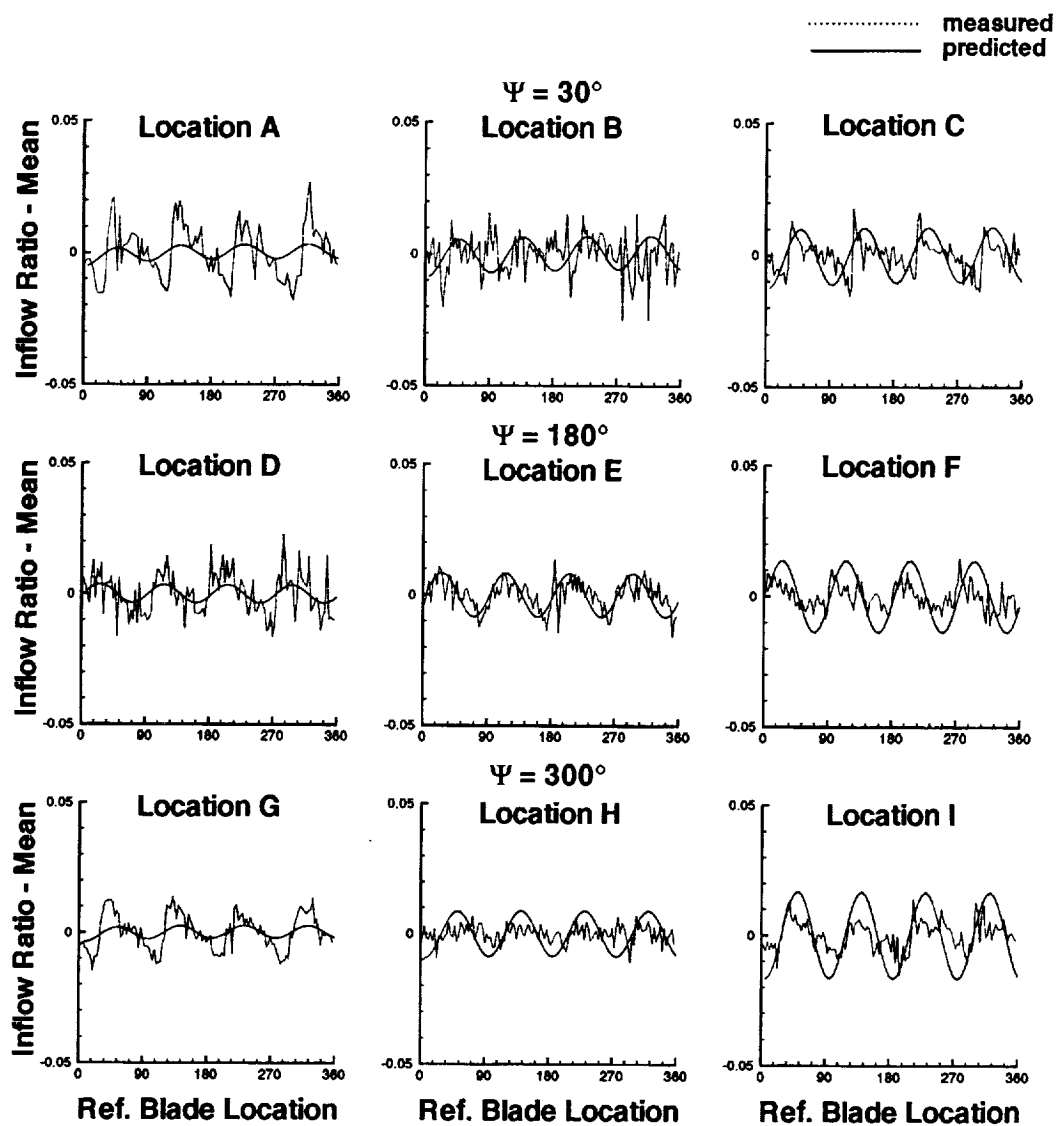
Figure 3.27: Measured and GDWT Predicted Unsteady Induced Inflow Ratio With Mean Values Removed; Tapered Planform, $\mu = 0.15$, 64 Azimuths, 4 Harmonics.
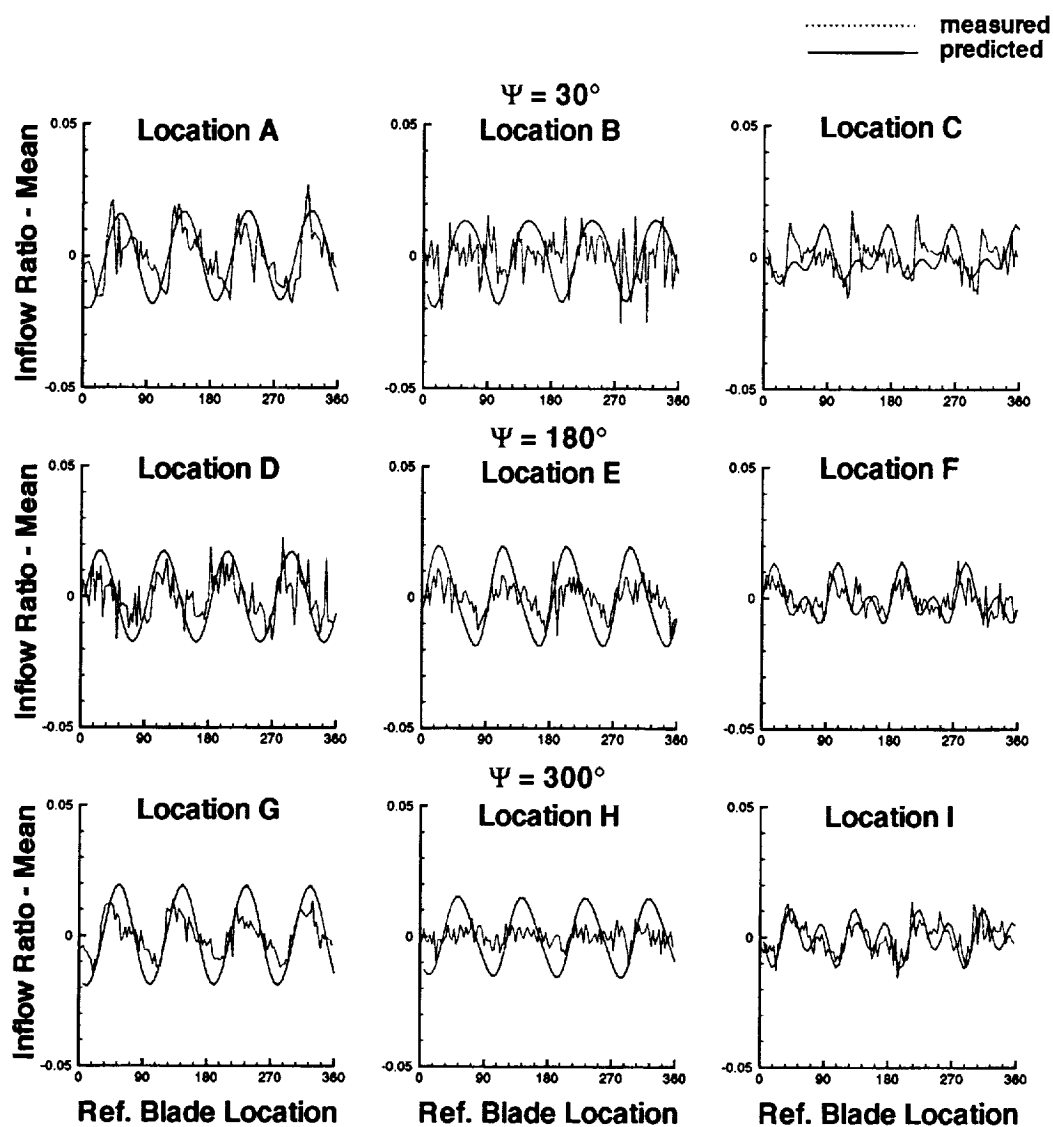
Figure 3.28: Measured and GDWT Predicted Unsteady Induced Inflow Ratio With Mean Values Removed; Tapered Planform, $\mu = 0.15$, 64 Azimuths, 8 Harmonics.
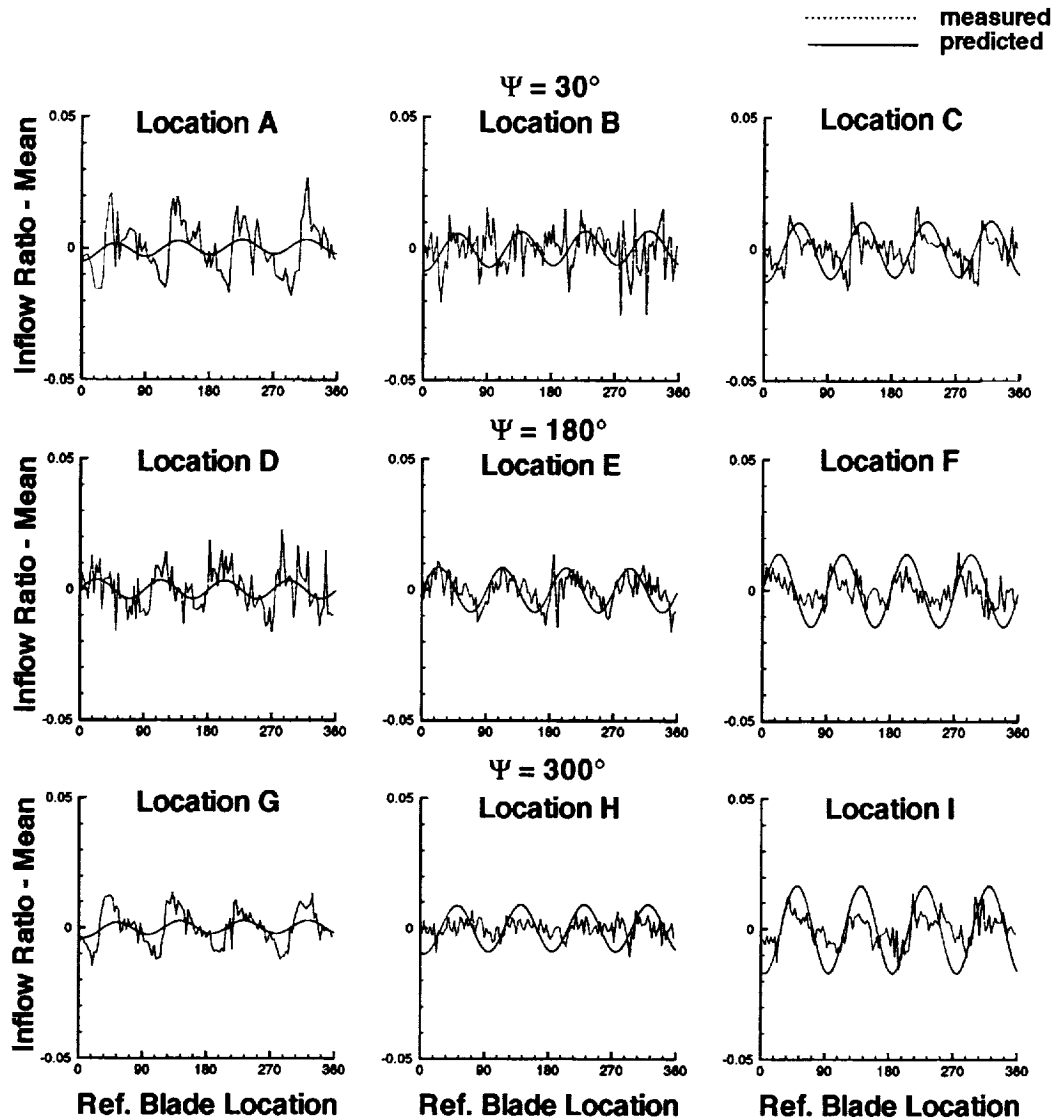
Figure 3.29: Measured and GDWT Predicted Unsteady Induced Inflow Ratio With Mean Values Removed; Tapered Planform, $\mu = 0.15$, 128 Azimuths, 4 Harmonics.
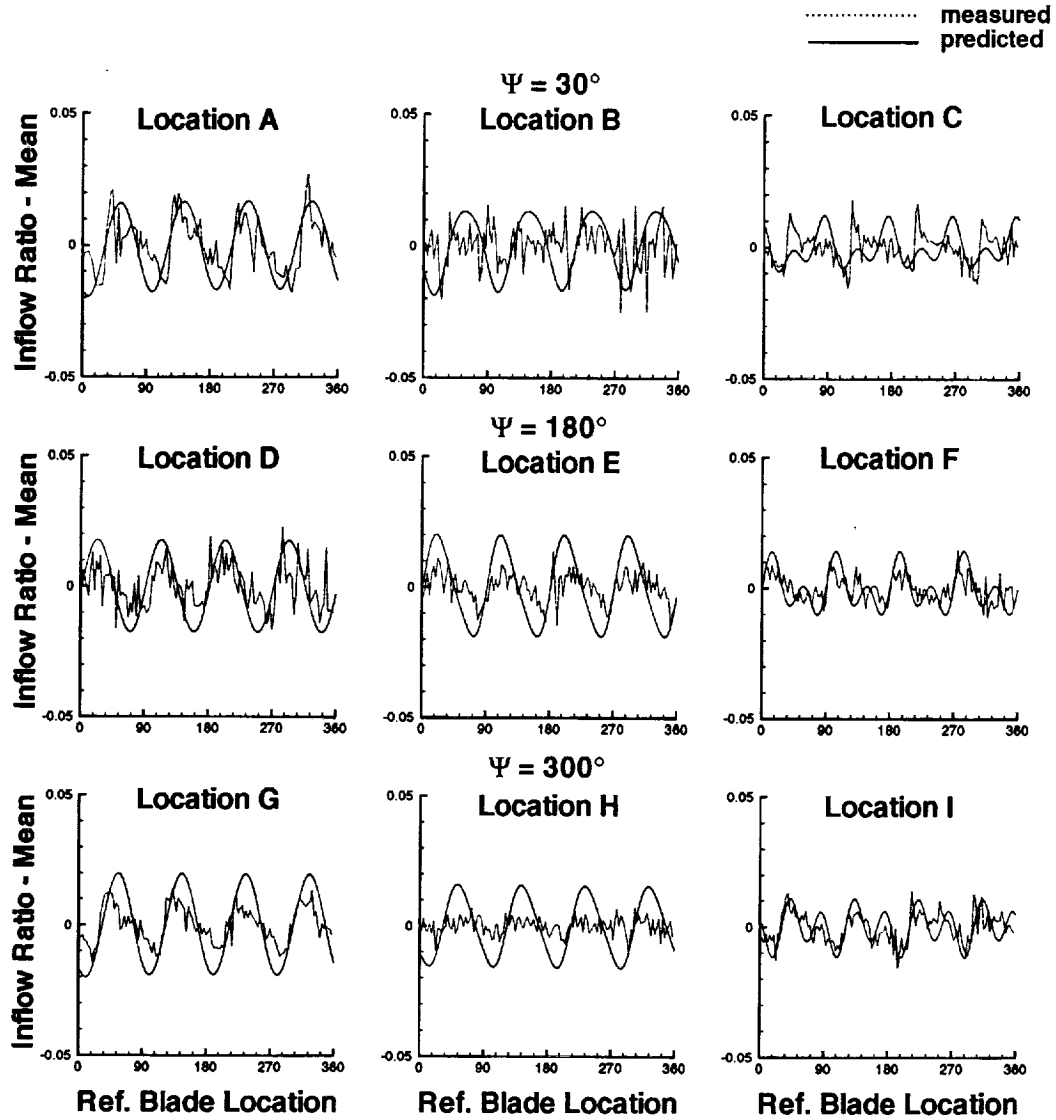
Figure 3.30: Measured and GDWT Predicted Unsteady Induced Inflow Ratio With Mean Values Removed; Tapered Planform, $\mu = 0.15$, 128 Azimuths, 8 Harmonics.
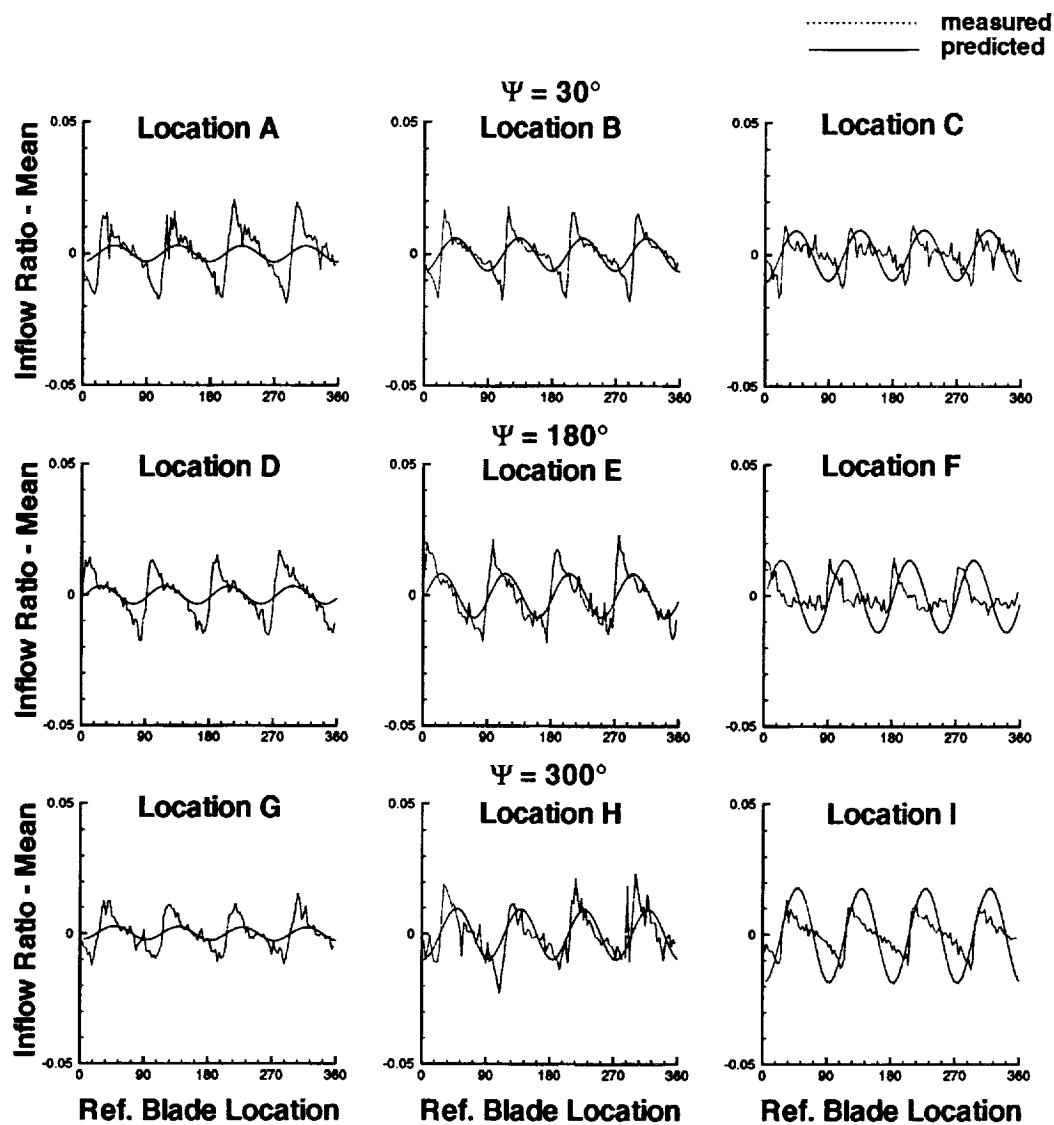
Figure 3.31: Measured and GDWT Predicted Unsteady Induced Inflow Ratio With Mean Values Removed; Tapered Planform, $\mu = 0.23$, 64 Azimuths, 4 Harmonics.
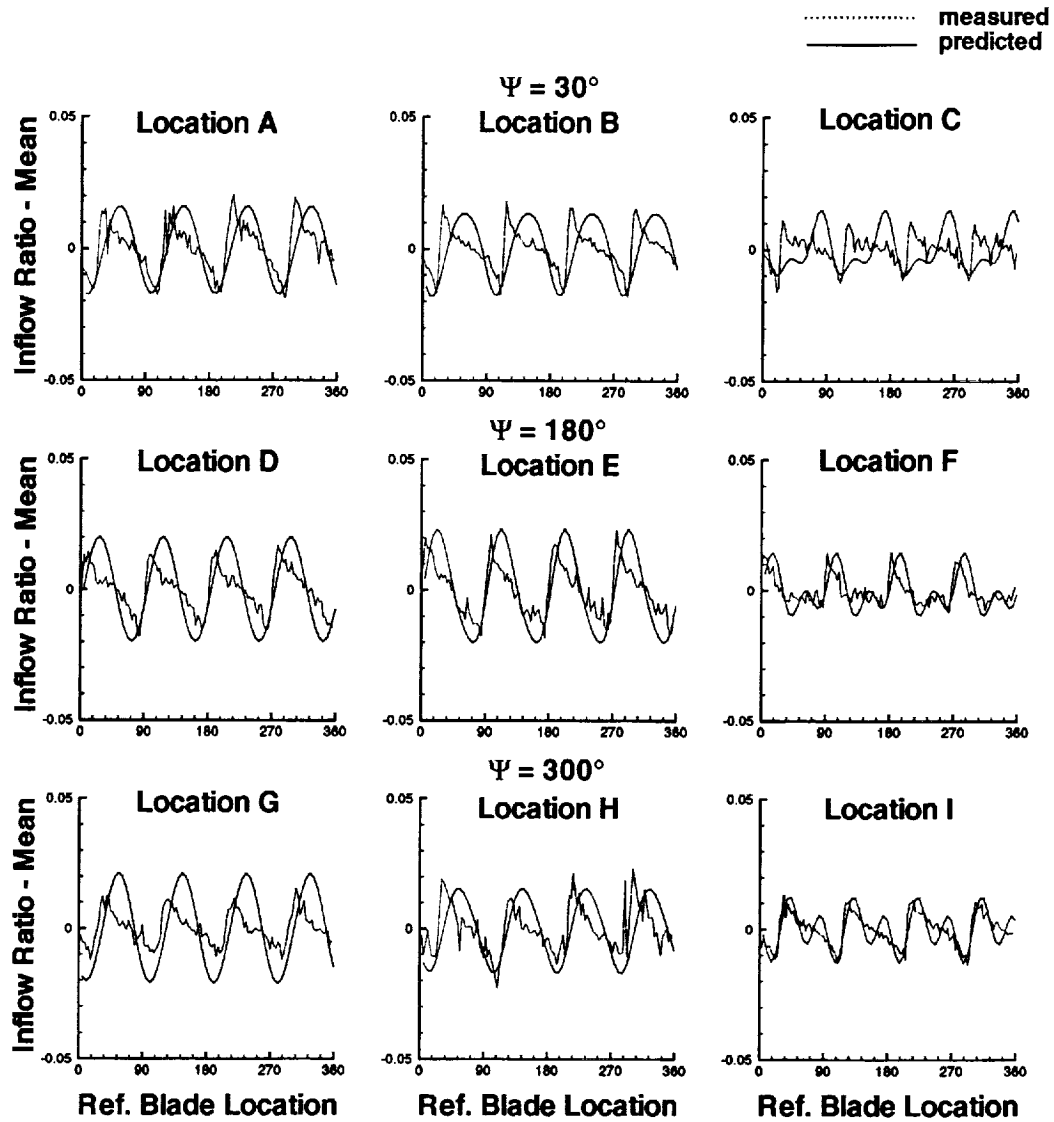
Figure 3.32: Measured and GDWT Predicted Unsteady Induced Inflow Ratio With Mean Values Removed; Tapered Planform, $\mu = 0.23$, 64 Azimuths, 8 Harmonics.
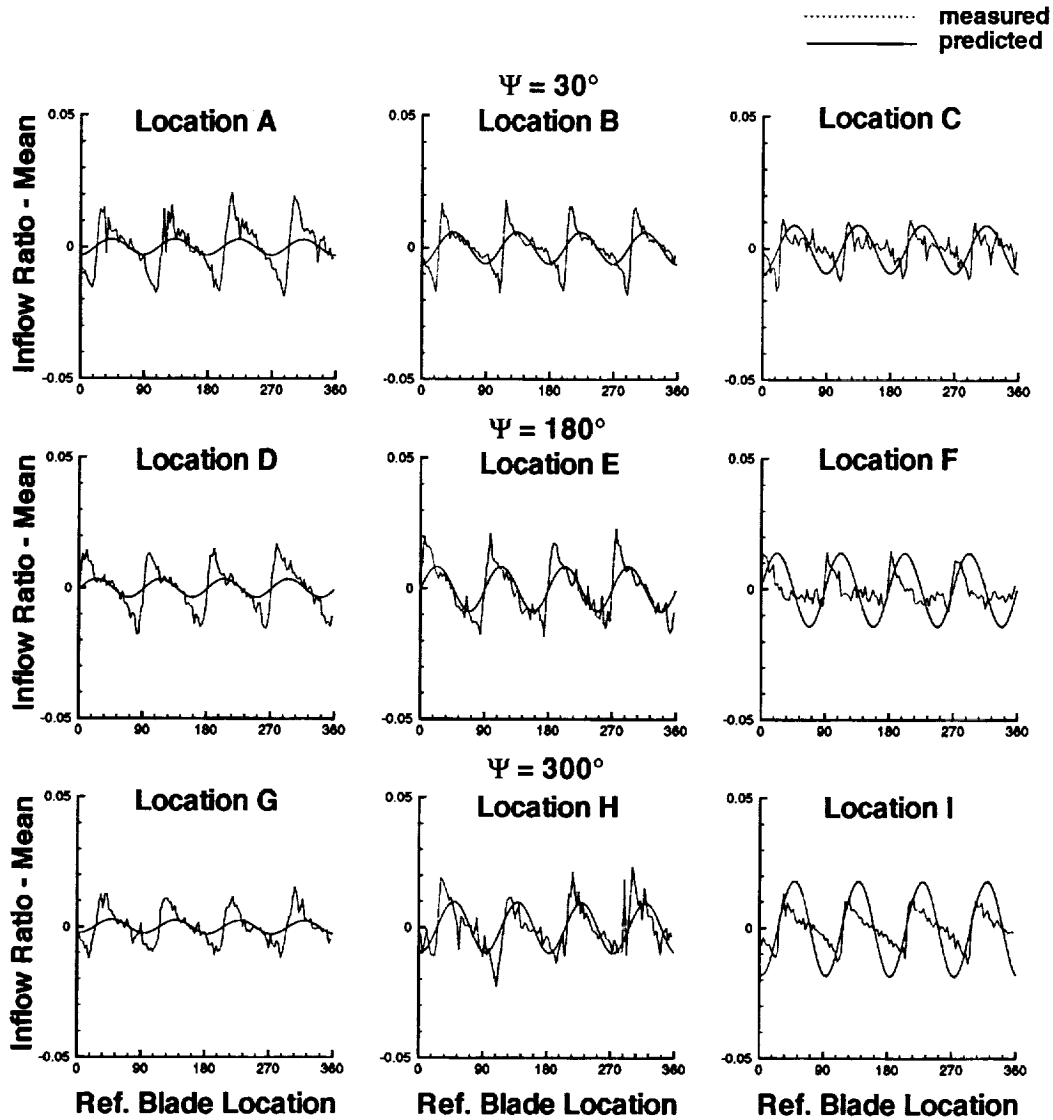
Figure 3.33: Measured and GDWT Predicted Unsteady Induced Inflow Ratio With Mean Values Removed; Tapered Planform, $\mu = 0.23$, 128 Azimuths, 4 Harmonics.
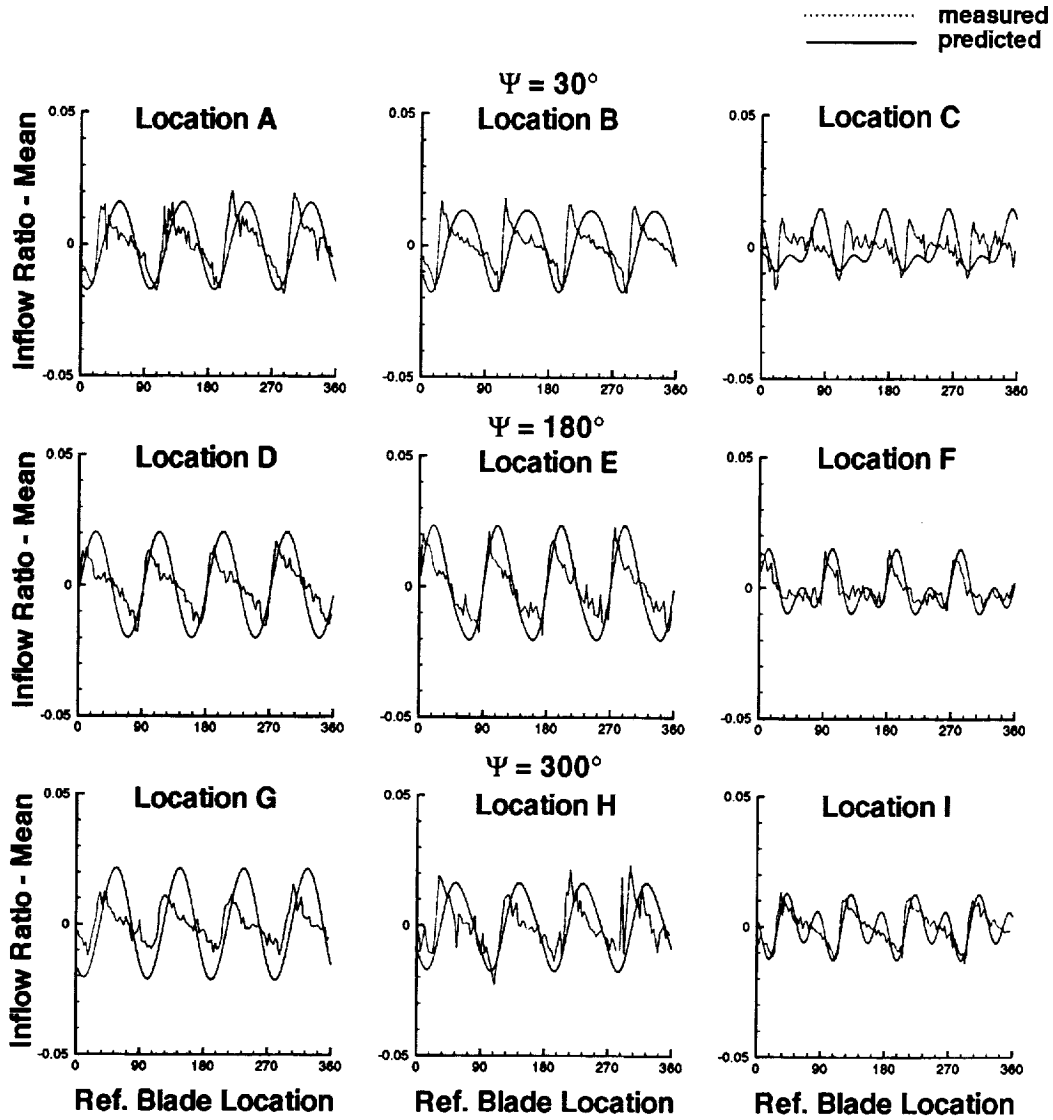
Figure 3.34: Measured and GDWT Predicted Unsteady Induced Inflow Ratio With Mean Values Removed; Tapered Planform, $\mu = 0.23$, 128 Azimuths, 8 Harmonics.

Chapter 4

Rotor/Fuselage Flowfield Model: OVERFLOW

4.1 Introduction

A rotor loading model which computes a distributed ΔP pressure jump value on the isolated rotor disk has been established and discussed extensively in chapters 2 and 3. From figure 1.2, it can be seen that these ΔP values are used in the rotor/fuselage flowfield model to compute the entire flow-field of the combined rotor/fuselage system. The rotor/fuselage flowfield is computed by solving the Navier-Stokes equations in conjunction with conservation of mass and energy. The Reynolds averaged Navier-Stokes equations in Cartesian coordinates are as follows:

$$\frac{\partial \vec{Q}}{\partial t} + \frac{\partial (\vec{F} - \vec{F}_v)}{\partial x} + \frac{\partial (\vec{G} - \vec{G}_v)}{\partial y} + \frac{\partial (\vec{H} - \vec{H}_v)}{\partial z} = 0 \tag{4.1}$$

where,

$$\vec{Q} = \left\{ \begin{array}{c} \rho \\ \rho u \\ \rho v \\ \rho w \\ \rho e_0 \end{array} \right\} \tag{4.2}$$

61

$$\vec{F} = \left\{ \begin{array}{c} \rho u \\ \rho u^2 + p \\ \rho u v \\ \rho u w \\ \rho u (e_0 + p) \end{array} \right\} \qquad \vec{F}_v = \left\{ \begin{array}{c} 0 \\ \tau_{xx} \\ \tau_{xy} \\ \tau_{xz} \\ (u\tau_{xx} + v\tau_{xy} + w\tau_{xz}) - q_x \end{array} \right\} \qquad (4.3)$$

$$\vec{G} = \left\{ \begin{array}{c} \rho v \\ \rho v u \\ \rho v^2 + p \\ \rho v w \\ \rho v (e_0 + p) \end{array} \right\} \qquad \vec{G}_v = \left\{ \begin{array}{c} 0 \\ \tau_{yx} \\ \tau_{yy} \\ \tau_{yz} \\ (u\tau_{yx} + v\tau_{yy} + w\tau_{yz}) - q_y \end{array} \right\} \qquad (4.4)$$

$$\vec{H} = \left\{ \begin{array}{c} \rho w \\ \rho w u \\ \rho w v \\ \rho w^2 + p \\ \rho w (e_0 + p) \end{array} \right\} \qquad \vec{H}_v = \left\{ \begin{array}{c} 0 \\ \tau_{zx} \\ \tau_{zy} \\ \tau_{zz} \\ (u\tau_{zx} + v\tau_{zy} + w\tau_{zz}) - q_z \end{array} \right\} \qquad (4.5)$$

In the above set of equations, ρ is the density, u, v, w are the velocity components, p is the pressure, e_0 is the total energy per unit volume, τ_{ij} are components of the stress tensor, and q_x, q_y, q_z are components of the heat flux.

The quantities above are all considered to be averaged, or mean-flow, quantities. Also, Newtonian flow is assumed. Thus, the stress tensor is proportional to the velocity gradients in the flow. The constant of proportionality is composed of the sum of two components. The first component is the molecular viscosity, μ_l, which accounts for laminar or molecular viscosity, and is a property of the fluid. The second component is the turbulent eddy viscosity, μ_t, which accounts for the turbulence in the flow and is computed using a turbulence model.

The above system of equations is then closed by introducing the perfect gas law as follows:

$$p = \rho \mathcal{R} T \qquad (4.6)$$

where $\mathcal{R}$ is the gas constant and T is the temperature.

For the current rotor/flowfield model, a time accurate, Reynolds averaged Navier-Stokes (RANS) tool known as OVERFLOW [29] is used to solve the above set of equations. OVERFLOW is a computer code that uses a finite difference technique to solve the compressible, RANS equations in generalized coordinates. Even though OVERFLOW is technically a RANS solver, it is typically used in a thin-layer mode by ignoring the viscous terms that are not associated with the direction normal to surfaces in the flowfield; that approach is used here as well. The code employs a chimera (overset) grid scheme [38], which is helpful for complex geometries. Several solution procedure options are available in this code. A second or fourth order central difference scheme with a second and fourth order artificial dissipation scheme is used for the convective and viscous terms. A Pulliam-Chaussee scalar diagonal inversion [39] is typically used for the left-hand of the equations, though other options are possible, namely a Beam-Warming [40] scheme and a Lower Upper Symmetric Gauss Seidel (LU-SGS) scheme [41]. For steady state computations, a local time stepping scheme and a multigrid scheme [42] are implemented to accelerate convergence. Also, for steady state computations at low Mach numbers, a low Mach number preconditioning scheme [42] is used. For unsteady computations, a "Newton sub-iteration" scheme [43] is implemented for each time step to reduce linearization and factorization errors and to increase the time accuracy of the scheme to approximately second order. Also available are several turbulence models and an extensive set of boundary condition options. Available turbulence models include a Baldwin-Lomax model, a Baldwin-Barth model, a Spalart-Allmaras model, and a $k - \omega$ model; the Spalart-Allmaras turbulence model is used for all computations presented here. Boundary condition options include conditions for inviscid walls, viscous walls, periodic grids, symmetry planes, singular axes, inflow, outflow, characteristic conditions, *etc.* For both steady and unsteady computations, all boundary conditions are applied explicitly; some of these boundary conditions may also be applied to any region inside the volume of the computational grid, not just at the outer grid boundary faces.

This chapter describes the manner in which OVERFLOW is used for the rotor/fuselage flowfield model depicted in figure 1.2.

4.2 New Boundary Conditions

For the purposes of the current research, OVERFLOW has been extended to include two new, novel, explicit boundary conditions which use the pressure jump previously computed by the

GDWT to model a helicopter rotor. One of the boundary conditions is used for time averaged computations and the other is used for unsteady, time accurate computations. Both are applied to two planes of a non-rotating, cylindrical grid with an "iblanked plane" in between. Figure 4.1a shows a top view schematic of the rotor disk used in the new boundary conditions. This schematic represents the non-rotating, cylindrical portion of the grid that is used to represent the rotor disk. This "rotor portion" of the grid is a subset of the much larger overset volume grid set that is used to represent the entire rotor/fuselage flowfield. This grid subset is where the new boundary conditions are applied.

The shaded area in this figure represents a small region of the cylindrical grid; the rectangle outlined by the dark lines represents a rotor blade. Both of these regions are enlarged in the figure for clarity of presentation. Figure 4.1b shows an edge view of this same schematic. In this view, five planes can be seen. These planes consist of an upper rotor plane, an iblanked plane, a lower rotor plane, and two planes, labeled A and B, which are used in the formulation of the boundary conditions.

Although the focus of the current research is on unsteady interactions, it is necessary to have both the time averaged and time accurate boundary conditions discussed above. These boundary conditions are used in a complementary manner as follows. First, the steady state flowfield around the isolated fuselage is determined. Then, using this isolated fuselage computation as a starting point, the steady state flowfield of the fuselage, including the time averaged rotor model, can be determined using the time averaged rotor boundary condition. The previous two stages are used to set up the steady state flow features so that the unsteady computations can be used as a final stage, which is executed until a periodic solution is obtained. This "building block" approach of using a steady state computation as an initial condition to a time averaged computation, and in turn, using the time averaged computation as an initial condition to the time accurate computation, is used to reduce the computational resources required relative to using a completely time accurate computation from inception.

Next, the details of each of the new boundary conditions will be described.

4.2.1　Time Averaged Boundary Condition

As stated above, the boundary conditions are applied on two planes, separated by an "iblank plane[1]". Use of the "iblank plane" between the upper and lower rotor planes prevents the artifical dissipation in OVERFLOW from being activated by the new pressure jump imposed across the two planes.

The steps in the application of this boundary condition are as follows:

1. Identify the two planes (labeled A and B in figure 4.1b) surrounding the upper and lower rotor planes,

2. Average the conservative flow quantities in planes A and B as follows:

$$Q_{i,avg} = \frac{(Q_{i,A} + Q_{i,B})}{2} \tag{4.7}$$

where Q_i are given in equation (4.2),

3. Replace the existing conservative flow quantities in the upper and in the lower rotor planes with these average values,

4. Add an "additional energy term" to the fifth conservative flow quantity (Q_5).

Steps 1, 2, and 3 above are relatively straightforward and are accomplished with application of existing boundary conditions. Step 4 is the new step in this process introduced here and is described below.

As stated above, both boundary conditions use the pressures from the GDWT with a few slight modifications. The first new boundary condition time averages the unsteady pressures at each radial and azimuthal location, multiplies by the ratio of the local blade area to the local computational cell area, $A(\bar{r})$, to maintain the same level of thrust between the two methods, and divides by $(\gamma - 1)$ to convert the pressures into an energy-like term that is compatible with the Q_5 variable above. This conversion to a Q_5 compatible quantity can be combined into one expression as follows:

$$[(\rho e_0)_{add}](\bar{r}, \psi) = \frac{A(\bar{r})}{(N_T)(\gamma - 1)} \sum_{t=1}^{N_T} \Delta P(\bar{r}, \psi, t) \tag{4.8}$$

---

[1]The term "iblank" refers to a technique employed in many methods that use the chimera scheme. This technique involves intentionally excluding certain points (here, a certain plane) from the computation of the flowfield.

where N_T is the number of time steps used in one revolution. The value of the left side of equation (4.8) is then split in half. One half of the term is added to the ρe_0 equation for the lower plane of the rotor grid at the current azimuth and radial location, the other half is subtracted from the ρe_0 equation for the upper plane in the rotor grid at the current azimuth and radial location; this effectively adds energy to the flowfield, to mimic an actuator disk. The splitting of the additional ρe_0 term and placement on either side of an "iblank plane" prevents the artificial dissipation in OVERFLOW from acting on the effective additional pressure jump; the artifical dissipation in OVERFLOW is designed so that it will not operate across an iblank region. Without this iblank plane, the artificial dissipation would operate on the pressure jump, smoothing the pressure jump unnecessarily.

4.2.2   Time Accurate Boundary Condition

The new time accurate boundary condition is applied in a manner similar to that used for the time averaged boundary condition above. The differences are that (1) the pressures are not time averaged before they are converted to energy-like terms, and (2) the pressures are evenly distributed over all azimuthal grid lines that cross the blade chord at the local blade radial station. Similar to the time averaged boundary condition (with exception (1) above), the following additional energy-like term is determined:

$$[(\rho e_0)_{add}](\bar{r},\psi,t) = \frac{A(\bar{r})}{(\gamma-1)}\Delta P(\bar{r},\psi,t) \qquad (4.9)$$

As in the time averaged boundary condition above, the value of the left side of equation (4.9) is then split in half. One half of the term is added to the ρe_0 equation for the lower plane of the rotor grid, the other half is subtracted from the ρe_0 equation for the upper plane in the rotor grid. As discussed above, splitting the additional term and applying it on either side of an iblank plane prevents the artifical dissipation term from acting on the pressure jump. Also, at each radial station on the blade, the number of grid lines that lie on the chord are computed based on the chord length and the arclength between successive azimuthal grid lines. The additional energy term above then is distributed evenly over these grid lines. This distribution allows the shape of the blade to be better modeled in the cylindrical grid.

4.3 Summary

Referring to figure 1.2, a rotor/fuselage flowfield model has been introduced in this chapter. This new model consists of a Navier-Stokes method in which several new boundary conditions have been developed. These boundary conditions use information from the GDWT to model an addition of energy to the flowfield as in an actuator disk method, but in an time accurate setting. In the next chapter, the third box in figure 1.2, "coupling model", will be discussed.
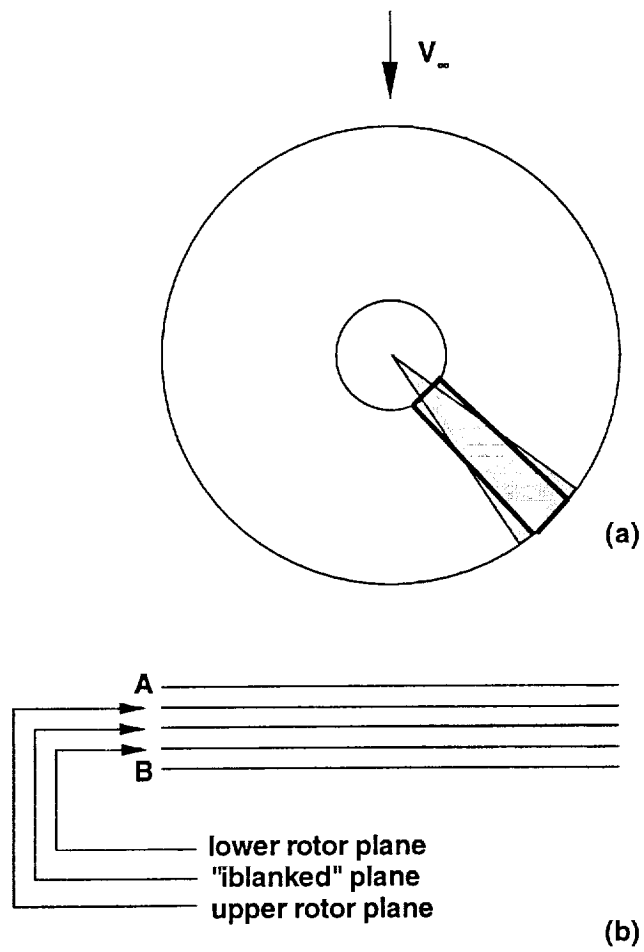
Figure 4.1: Rotor Schematic for New Boundary Conditions.

Chapter 5

Coupling Model

5.1   Introduction

Since the pressure jump determined by the isolated rotor loading model depends on the inflow ratio distribution over the rotor disk, and since the presence of a fuselage alters this inflow ratio distribution, some type of coupling model is needed to adjust the inflow ratio and pressure jump distributions to reflect the effects of the fuselage. The current coupling method adopts an "inflow correction" model. In this type of model, the loading on the rotor is determined based on the inflow at the rotor disk, including additional inflow, or inflow corrections, generated by the presence of the fuselage. Presently, the forces and moments on the fuselage are not accounted for directly in the computation of the rotor forces; the rotor forces are, however, computed using inflow corrections to account for the presence of the fuselage. Since typically, for a model in a wind tunnel, the rotor is trimmed to a specified thrust, independent of the forces acting on the fuselage, this modeling assumption is valid here.

In previous chapters, discussions of the rotor loading model and the rotor/fuselage flowfield model were presented. In this chapter, the lower box of figure 1.2, the "coupling model" will be discussed.

5.2   Isolated Rotor Configurations

Previous literature [24] used a hybrid method similar to that presented here. The current research builds on the idea presented in reference [24], which is a subset of the current work. This subset is contained inside the dashed box region in figure 5.1. For an isolated rotor computation, no coupling model, or feedback loop, is needed to provide fuselage correction information to the rotor loading model. Therefore, an isolated rotor computation is determined by a single pass through the method, stopping at the end of the rotor/fuselage flowfield computation. This was the method employed in reference [24].

5.3   Rotor/Fuselage Configurations

When there is a fuselage present in the rotor/fuselage flowfield model, a correction scheme is needed to feed information back into the isolated rotor loading model to account for the fuselage presence. The direction of the arrows in figure 5.1 indicates that the correction scheme should reflect the effects of the fuselage on the rotor system, as opposed to the rotor effects on the fuselage.

In observing effects of a fuselage on the rotor system, it can be noted that time scales associated with the flow around the fuselage are much larger than those associated with the rotation of the rotor system. The effect of the fuselage on the surrounding fluid is one of slow displacement. However, due to its rotation, the rotor blade will pass this fluid particle at a much higher speed. Thus, for a given time increment, the rotor blade will traverse far more distance than a fluid particle traveling along the fuselage.

Based on these scale differences, it is expected that the presence of the fuselage produces effects on the rotor disk that are not spatially or temporally concentrated when viewed in the fuselage fixed, spatial frame of reference. However, when this effect is viewed in the rotor blade rotating frame of reference, the rotor blade "sees" the spatial distribution of inflow generated by the presence of the fuselage as a slowly varying (temporal) inflow quantity. This leads to the conclusion that the influence of the fuselage on the rotor system can be viewed as a time averaged perturbation[1] to the isolated rotor configuration in the fuselage fixed reference frame.

With the view that the fuselage effect on the rotor system can be considered to be a time averaged

---

[1]Note that here, a perturbation is not necessarily small.

inflow ratio correction distributed over the rotor disk, an efficient coupling method which accounts for the primary fuselage effects on the rotor inflow ratio, can be developed. The coupling method developed here is of that type.

To determine the inflow corrections to be fed back into the rotor loading model, a difference is taken between the time averaged, filtered inflow ratio from the rotor/fuselage flowfield model and the time averaged inflow ratio from the GDWT:

$$\Delta \bar{\lambda}_i = \mathcal{F}(\bar{\lambda}_i^{RFFM}) - \bar{\lambda}_i^{RLM} \tag{5.1}$$

where $\mathcal{F}(\cdot)$ is a filtering operation performed on $\bar{\lambda}_i^{RFFM}$. To show the reason for the filtering operation on the $\bar{\lambda}_i^{RFFM}$ term, it is necessary to examine the frequency limitations of each component in the method. For the rotor loading model component, the spatial frequency content of the induced inflow ratio determined by the GDWT, $\bar{\lambda}_i^{RLM}$, is limited to the number of harmonics chosen in the method. For example, it was shown in chapter 3 that eight harmonics of rotor inflow are sufficient for that model in this context. Therefore inflow ratio information, time averaged or time accurate, is limited to eight harmonics (in this example). Note that this limitation does <u>not</u> imply that the loading distribution computed by the GDWT is limited to the given number of harmonics. This is because the GDWT computes the inflow ratio (up to a specified number of harmonics) given <u>any</u> loading distribution. This computed inflow ratio influences the loading distribution through the w term in equation (2.15). Thus, the otherwise two dimensional loading distribution reflects inflow corrections up to the number of harmonics in the model.

While the GDWT limits the number of inflow harmonics computed to a specified value, the inflow computed by the rotor/fuselage flowfield model, $\bar{\lambda}_i^{RFFM}$, is only limited by the spatial resolution found in the rotor grid. For example, a typical rotor grid used in this method [24] uses 128 azimuthal grid lines per rotor revolution. Using the Nyquist cutoff concept, this means that the limit of the frequency content in the azimuthal direction is 64 harmonics. If $\Delta \bar{\lambda}_i$ were computed and used in the rotor loading model without the filtering operation, inflow corrections (and therefore loading distribution corrections) would be made inside the GDWT that are inconsistent with the inflow corrections made internal to the model using the w term in equation (2.15). To eliminate this inconsistency, the $\bar{\lambda}_i^{RFFM}$ term is filtered to match the frequency content of the $\bar{\lambda}_i^{RLM}$ term.

A consistent filtering operation, $\mathcal{F}(\cdot)$, is derived from the GDWT method and is given in Appendix A. Applying this filtering, $\mathcal{F}(\bar{\lambda}_i^{RFFM})$, then computing $\Delta \bar{\lambda}_i$ from equation (5.1) above, this term may be included in equation (2.15) to complete the coupling loop. With this coupling method,

all of the boxes of figure 1.2 have been described. The next few chapters will discuss applications of entire method.
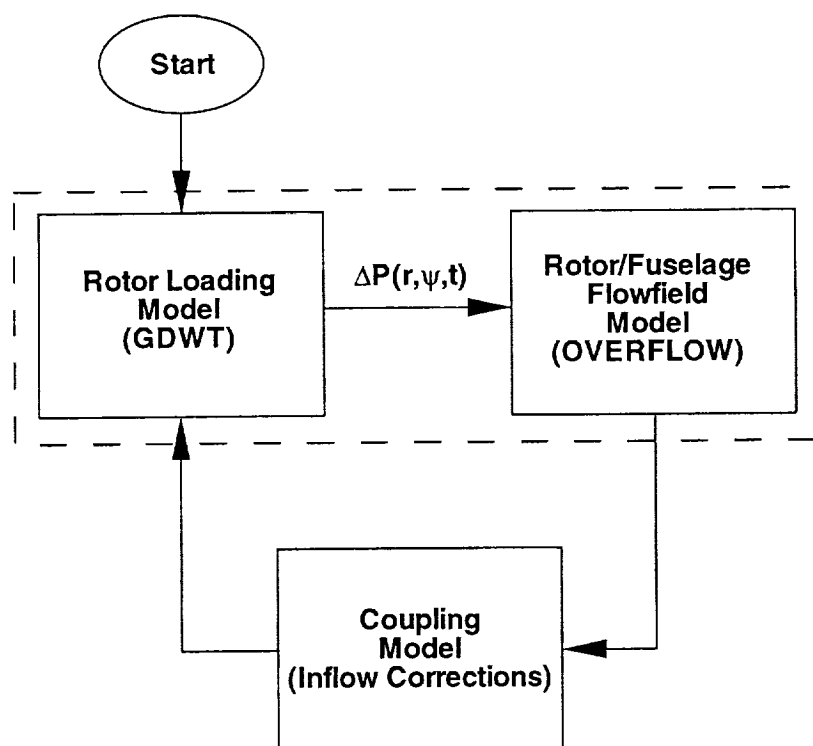
Figure 5.1: Current Hybrid Method.

Chapter 6

Results: Isolated Fuselage

6.1 Introduction

Chapters 1, 2, 4, and 5, have described the components of the new computational model for rotor/fuselage unsteady interactional aerodynamics and how they are used. In the next three chapters, a full configuration will be constructed from basic components: (1) an isolated fuselage, (2) an isolated rotor, and (3) a rotor/fuselage combination. The subject of this chapter is the isolated fuselage component. Even though, strictly speaking, an isolated fuselage model is not a new computational model, it is necessary to establish that the computations can be compared favorably to measured data.

6.2 Experimental Setup

The experimental setup for the comparisons in this isolated fuselage chapter are described in detail in Freeman and Mineck [37]. However, for completeness, the setup will be discussed here in brief.

A test was conducted in the NASA Langley Research Center 14- by 22-Foot Subsonic Tunnel, in which steady state surface pressures were obtained at one hundred and sixty-two locations on a generic helicopter fuselage shape for a number of flight conditions with and without a rotor installed. This fuselage shape, which is derived mathematically using "super-ellipse" equations [37], is known as the ROtor Body INteraction (ROBIN) fuselage (see figure 6.1). In the photograph

shown in figure 6.1, the ROBIN is sting mounted, with the rotor installed. For the isolated fuselage portion of the test, the blades were removed, but the hub was left in place. Though test conditions included configurations with and without the rotor installed, only steady state pressures were measured on the fuselage. As such, only the isolated fuselage pressures will be used here.

6.3 Computational Grid System

A system of thirteen grids, combined using the chimera grid capabilities in OVERFLOW, is used to represent the ROBIN fuselage geometry and flowfield. The sting mount, rotor hub, and wind tunnel walls are not modeled. A listing of all of grid names and sizes are displayed in table 6.1. From table 6.1 it can be seen that five of these grids involve surface grids associated with the fuselage. These surface grids are shown and labeled in figure 6.2. Note that, for clarity of presentation, only every third grid line is plotted in figure 6.2. All remaining grids are field volume grids. Figure 6.3 shows a view of the grids immediately surrounding the fuselage. For clarity of presentation, every second grid line in this figure has been removed. Also seen is the positioning of the rotor grid with respect to the fuselage. For the isolated fuselage computations presented in this chapter, the rotor grid is simply another volume grid (*i.e.,* there is no rotor boundary condition applied on the rotor grid). The far field grid extents approximately 2.5 fuselage lengths upstream of the fuselage nose, downstream of the fuselage tail, to the left and right of the fuselage, and above and below the fuselage.

These grids were developed such that, with minimal effort and minimal grid modification, all configurations used in the current research (including an isolated fuselage, an isolated rotor, and a rotor/fuselage combination) could be modeled simply by "grid replacement". As an example, when converting from a rotor/fuselage configuration to an isolated rotor configuration, only the grids containing the fuselage need to be replaced; these are replaced by regular volume grids that maintain the outer boundary shape of the fuselage grids. All other grids remain the same.

These grids were also designed to maintain a "double fringe" overlap between all overlapping grids (except for the outer field grid) to maintain the second and fourth order artificial dissipation scheme used in OVERFLOW. In addition, grid spacings were refined to maintain viscous spacings at the fuselage surface such that there is at least one grid point in the laminar sub-layer region of the boundary layer and to maintain approximately 1.5 million total grid points in order to keep the computational expense reasonable.

One novel feature of this grid system is the manner in which the rotor grid is included. In previous isolated fuselage studies of the ROBIN fuselage [44, 45] the grid system did not include a rotor grid, thus a hyperbolic grid generator was used to "grow" the volume grids out from the surface grids without regard to the location of the outer boundaries of these grids. However, due to the geometry of the outer boundaries of grids produced by a hyperbolic grid generator, inclusion of a cylindrical rotor grid by the technique of "hole cutting" [46], while maintaining a double fringe chimera scheme, is difficult. This problem arises due to the lack of control of the outer boundary shape of grids generated by hyperbolic grid generation methods. To alleviate this problem, an elliptic grid generation method is used to control the outer boundary shape of some grids. With this technique, the overlap of the grids can be better controlled to produce a double fringe overlap and the amount of "hole cutting" can be substantially reduced.

For the current research, a hybrid set of grids generated by hyperbolic and elliptic grid generators [47, 48, 49, 50] is used. For volume grids in which no control was needed over the outer boundary shape, a hyperbolic grid generator was used. If control over the outer boundary geometry was desired, an elliptic grid generator was used.

6.4   Steady State Pressure Prediction

As discussed previously, the first step in the OVERFLOW computations is to execute the isolated fuselage configuration in a steady state mode. For the current computations, the default settings recommended for OVERFLOW [29] are used, except where noted. These defaults include central differencing of the right hand side of the equations, scalar diagonal inversion of the left hand side of the equations, a matrix dissipation scheme, low Mach number preconditioning, multigrid, full multigrid (mesh sequencing), local time stepping with a minimum CFL number constraint, and the Spalart-Allmaras turbulence model. The case presented here is for an angle of attack of $0°$ and a freestream Mach number of 0.1265.

Figure 6.4 shows the force coefficients in the lift, drag, and sideward directions as a function of iteration number in OVERFLOW. These force and moment coefficients are defined as follows [51]:

$$C_f = \frac{\hat{f}}{\hat{Q}_\infty \hat{A}_{ref}}$$

(6.1)

$$C_m = \frac{\hat{\mathcal{M}}}{\hat{Q}_\infty \hat{A}_{ref} \hat{L}_{ref}} \tag{6.2}$$

$$\hat{Q}_\infty = \frac{1}{2}\hat{\rho}_\infty \hat{V}_\infty^2 \tag{6.3}$$

where a list and derivation of reference quantities for these is given in reference [51]. Though these do not directly correspond to the standard lift, drag, and side force coefficients, they do provide a useful insight into the convergence behavior of the OVERFLOW iteration from an engineering standpoint.

Figure 6.5 shows the pressure tap locations on the ROBIN fuselage. The locations are shown with respect to the downstream coordinate (*x*-direction). Along the top of the figure, the lowercase letters indicate the locations where predictions are compared to measurements in the subsequent figure.

Figure 6.6 compares measured and predicted pressure coefficients *vs* the vertical location on the fuselage at various places stations along the length of the fuselage. The vertical axis in figure 6.6 is plotted in the standard negative C_p format and the horizontal axis is the vertical location (*z* coordinate) of the current section; the solid lines are the predictions and the symbols are the measured values.

The pressure coefficient used here is defined in equation (6.4). From a practical standpoint, computation of C_p inside OVERFLOW is accomplished using equation (6.5) and equation (4.2), taking into account the nondimensionalizations used in OVERFLOW.

$$C_p = \frac{P - P_\infty}{\frac{1}{2}\rho V_\infty^2} \tag{6.4}$$

$$C_p = \frac{2(\gamma-1)}{M_\infty^2} \left[Q_5 - \frac{Q_2^2 + Q_3^2 + Q_3^2}{2Q_1} - \frac{1}{\gamma(\gamma-1)} \right] \tag{6.5}$$

In figure 6.6 it can be seen that predicted pressure coefficients match the experimental data well in most areas. At locations (f) and (g), discrepancies can be seen on the upper and lower portions of the fuselage. These differences could be due to the presence of the hub and sting mount in the experimental setup. In this figure, predicted C_p values are plotted from both sides of the fuselage for this symmetric flight condition. In this figure, predicted pressure coefficients from both sides of the fuselage are plotted since the computation included the full fuselage instead of a half body

fuselage plus a symmetry condition. As, expected, no difference is seen between the two sides. In addition to matching well the experimental data, these predictions are consistent with similar predictions in the literature [45], which used other Navier-Stokes methods (codes), for the same configuration and flight condition.

6.5 Observations

OVERFLOW has the capability to predict the steady state pressure coefficients on an isolated fuselage configuration in an incompressible flight condition, and these predictions are consistent with similar computations in the literature.

Table 6.1: Computational Grid System

Grid Name/Description	Dimensions
Fuselage Grid	93 x 117 x 25
Nose Grid	30 x 117 x 33
Tail Grid	28 x 117 x 33
Collar Grid	29 x 111 x 25
Top Grid	41 x 41 x 25
Lower Field Grid	55 x 50 x 12
Upper Field Grid	55 x 50 x 22
Nose Field Grid	42 x 70 x 43
Tail Field Grid	30 x 39 x 29
Left Field Grid	55 x 32 x 30
Right Field Grid	55 x 32 x 30
Outer Field Grid	93 x 82 x 26
Rotor Grid	37 x 129 x 43
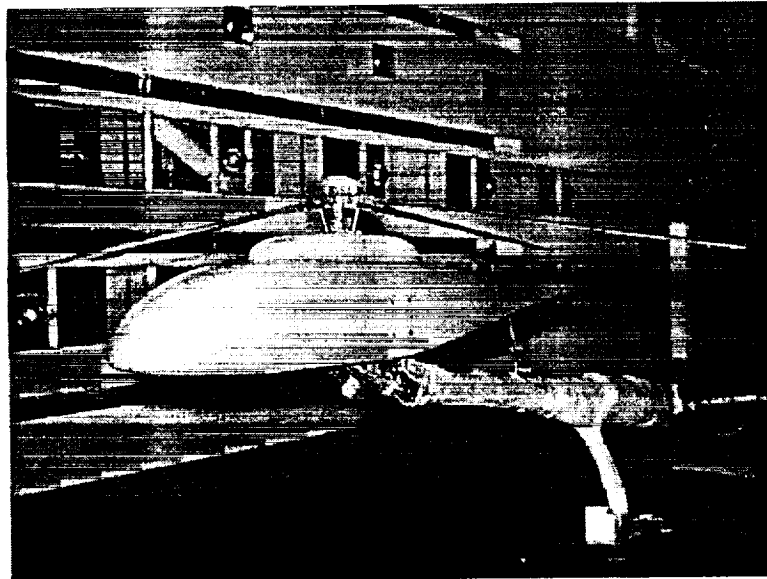
Figure 6.1: ROBIN Fuselage in the NASA Langley Research Center 14- by 22-Foot Subsonic Tunnel.
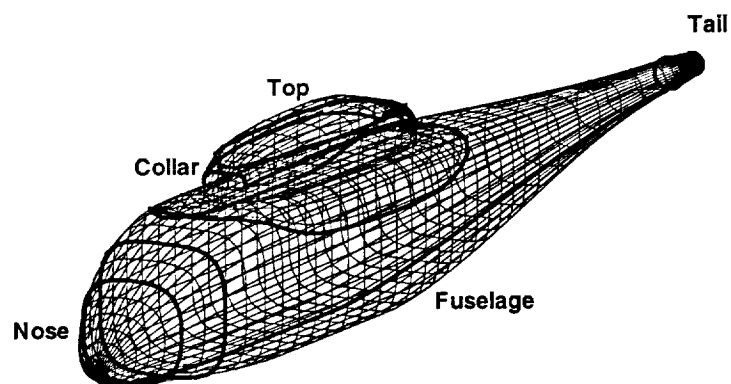
Figure 6.2: ROBIN Fuselage Surface Grids.
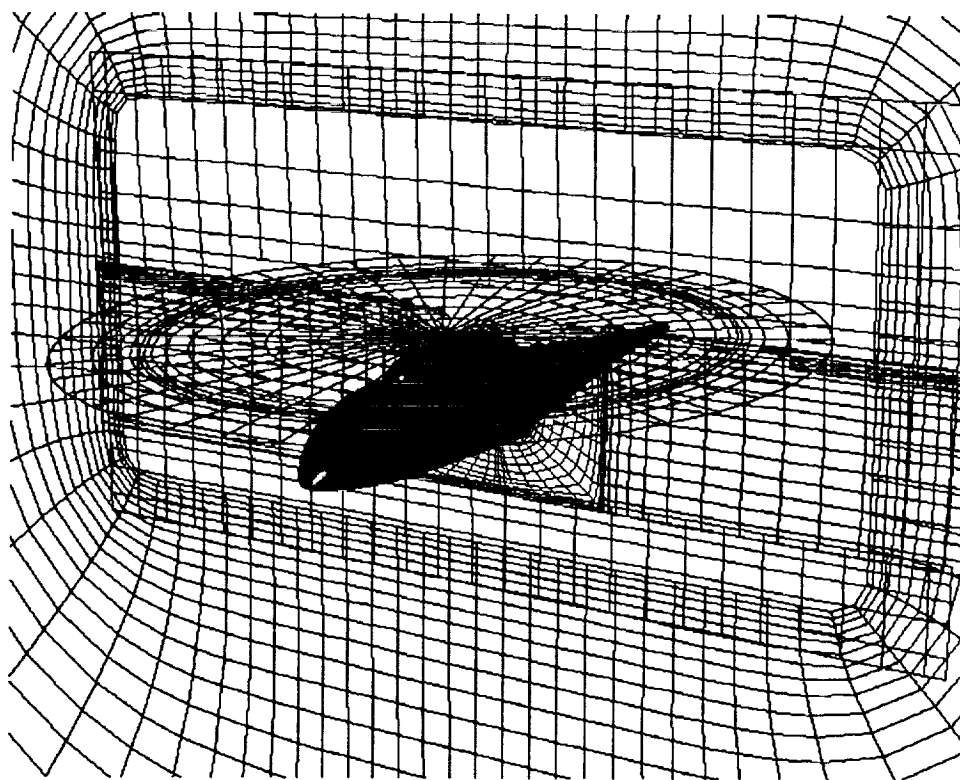
Figure 6.3: Grid System Used in Computations.
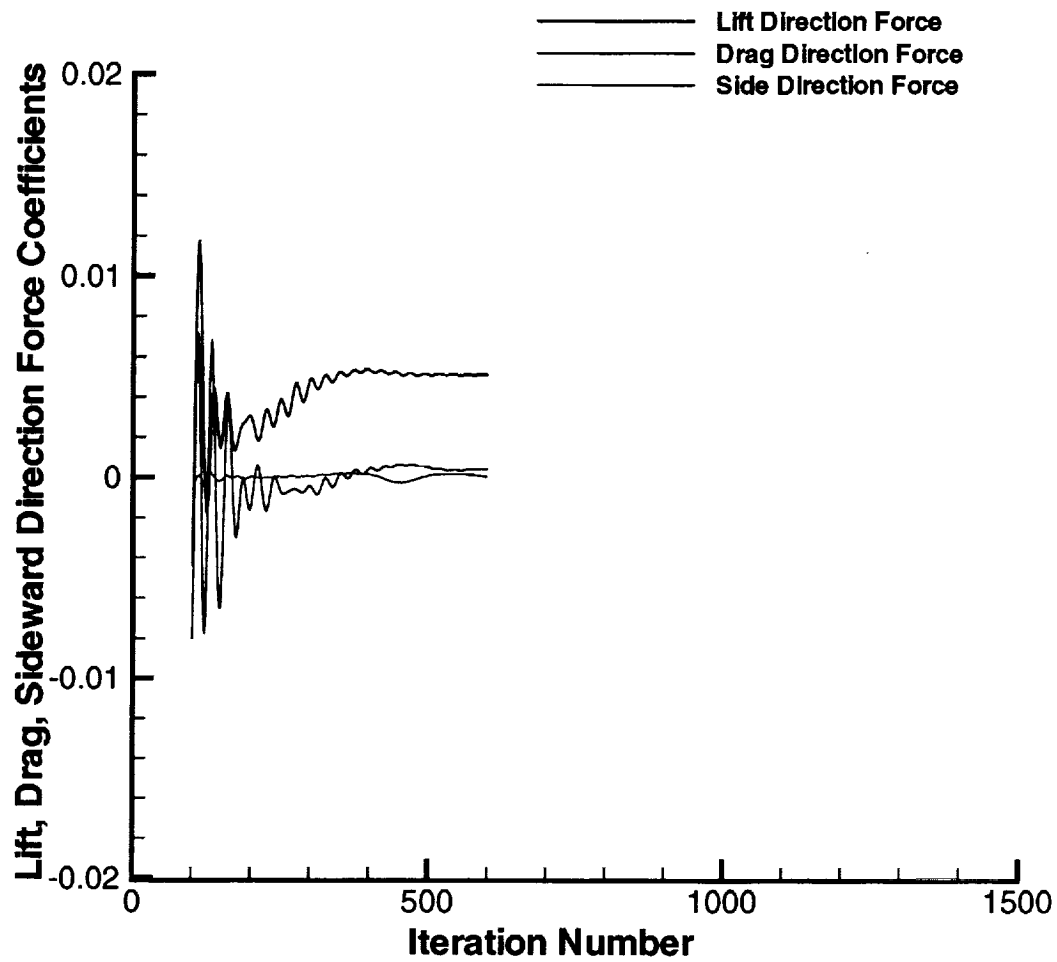
Figure 6.4: Lift, Drag, and Sideward Direction Force Coefficients. Steady State Computation.
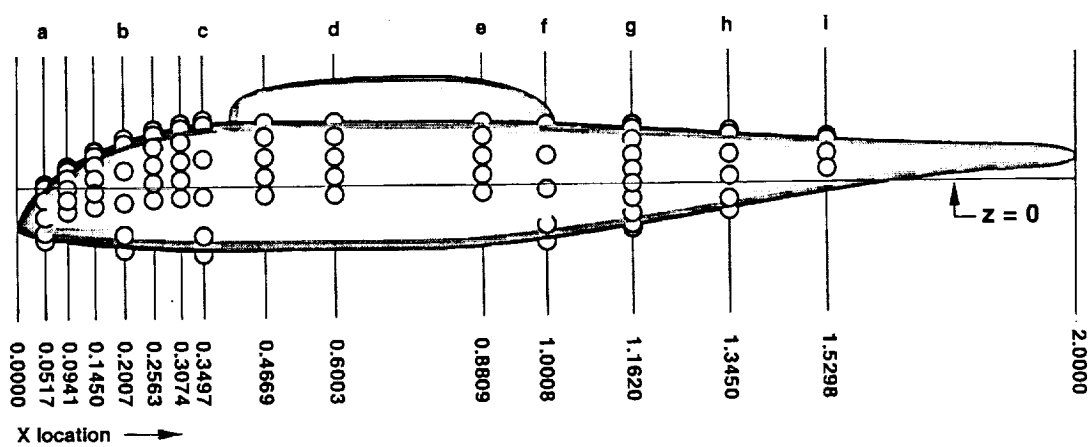
Figure 6.5: Pressure Tap Locations.
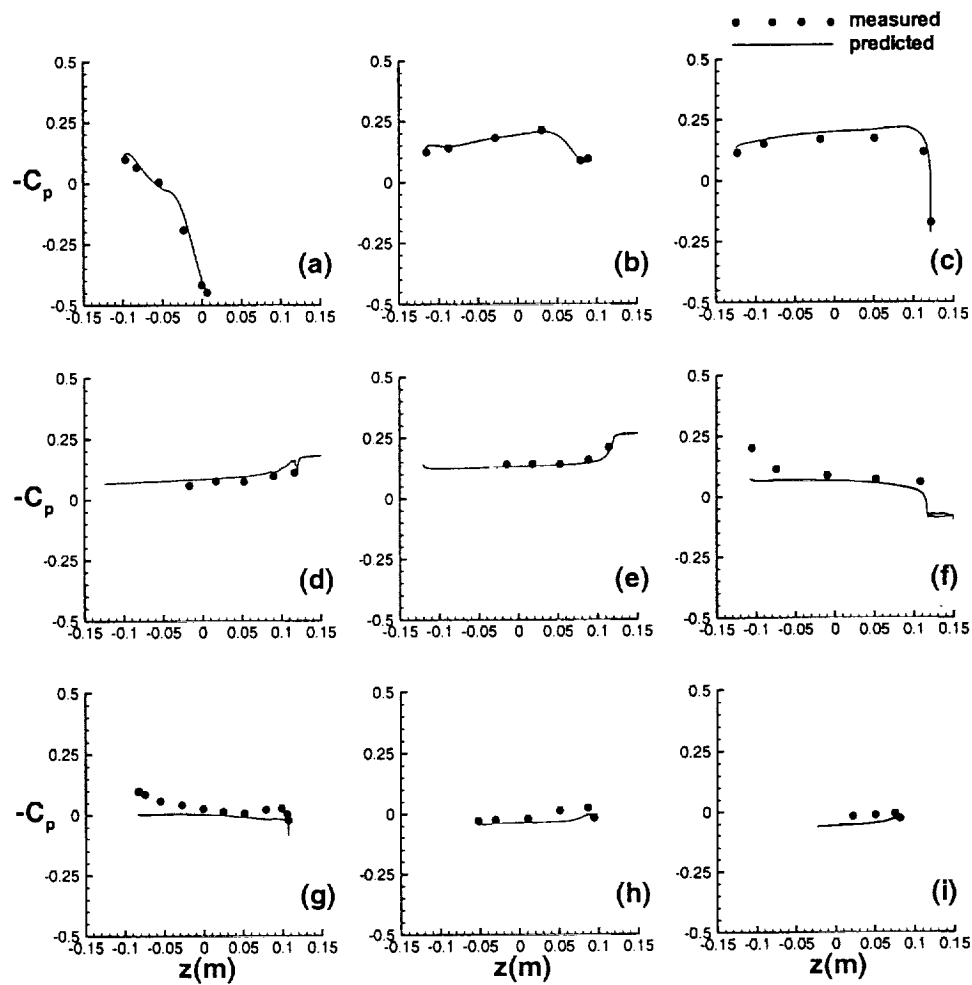
Figure 6.6: Measured and Predicted Pressure Coefficients *vs* Vertical Location for $\alpha = 0°$ and $M_\infty = 0.1265$.

Chapter 7

Results: Isolated Rotor

7.1 Introduction

Chapter 6 showed that the pressure distribution could be predicted on the isolated ROBIN fuselage configuration for a representative forward flight condition of a rotorcraft. This chapter will employ the isolated rotor method as described in chapter 5. Previous predictions using the current model [24] compared well with time averaged and time accurate laser velocimeter (LV) data. In that work, the predictions were for an isolated rotor, whereas the experimental data contained the effects of a fuselage. Subsequent to those predictions, new experimental data has been acquired on an isolated rotor configuration (described below). Comparisons between these data and the current method are the subject of this chapter.

7.2 Experimental Setup

For comparisons in this section, results from an isolated rotor configuration in the NASA Langley Research Center 14- by 22-Foot Subsonic Tunnel are shown. The isolated rotor test system (IRTS) [52, 53] is shown in figure 7.1. Here, it can be seen that the rotor is suspended from the ceiling of the tunnel from a tapered, cylindrical shaped sting. A three component laser velocimeter (LV) system was used to measure the three components of velocity at a point at an azimuth of 84°, a radial station of $r/R = 0.81$, and one blade chord above the tip path plane of the rotor. The rotor was trimmed to a nominal 0° flapping angle (*e.g.*, the first flapping harmonics are $\beta_{1c} = \beta_{1s} = 0°$),

85

a nominal thrust coefficient of 0.0064, a nominal shaft tilt, α_s, of 3° nose down, and a freestream Mach number of 0.1265. The LV data was processed at 128 samples per rotor revolution.

7.3 Computational Grid System

As discussed in chapter 6 for the isolated fuselage configuration, a grid system was developed that, among other things, had the ability to be used for an isolated rotor configuration with minimal changes to the grid system. For this isolated rotor configuration, several minor changes were made to the grids. These changes are as follows:

1. The nose grid has been eliminated,

2. The tail grid has been eliminated,

3. The collar grid has been eliminated,

4. The top grid has been eliminated,

5. The fuselage grid has been replaced by a volume field grid that maintains the outer boundary shape of the original fuselage grid.

Since the nose, tail, collar, and top grids from items 1, 2, 3, and 4 above were "overset" into other background grids, it was only required to delete these grids and leave the remaining background grids unchanged. The only new grid in the system is the volume grid that replaces the fuselage grid. All other grids in the system are unchanged. In essence, what remains, is a set of volume grids, identical to the full configuration, minus the fuselage surface. However, now, the new rotor boundary condition in OVERFLOW will be applied in the rotor grid as discussed in chapter 4. As with the isolated fuselage configuration, the sting mount and the wind tunnel walls are not modeled. This new grid system is shown in figure 7.2; every second grid line has been removed from this figure for clarity. The farfield extent of the grid is the same as that in figure 6.3.

7.4 Time Averaged Computation

The isolated rotor computations will be started with a prediction of the time averaged flowfield due to the rotor. For this, the time averaged rotor boundary condition discussed in chapter 4 is used.

This is done to minimize the number of time accurate computations that must be executed. Since this time averaged flow field is only an intermediate stage of the computation, and since there is no time averaged induced inflow data for the isolated rotor test stand available, no comparisons are made to experimental data.

7.5   Time Accurate Computation

Once the time averaged computation discussed above has been obtained, OVERFLOW is restarted in a unsteady mode and the method is continued until a periodic solution is achieved. The state of "periodicity" in this context refers to the lack of differences in the induced inflow ratio predictions for successive blade passages. Boyd and Barnwell [24] explored the sensitivities of several parameters in OVERFLOW for the time accurate computations of this type. Following the conclusions of that paper, the computations are executed with six Newton sub-iterations and no viscous terms. Since fourth order central flux differencing in space is now available in OVERFLOW, that is used as well.

Figure 7.3 compares the measured and predicted unsteady induced inflow in directions parallel and perpendicular to the rotor tip path plane at location "J" as shown in figure 3.18. This position is located radially at $r/R = 0.80$ and azimuthally at $\psi = 84°$. Figure 7.3a is the induced inflow comparison in the direction parallel to the tip path plane (the u-velocity, or "inplane" velocity) and figure 7.3b is the induced inflow comparison in the direction perpendicular to the tip path plane (w-velocity, or "out-of-plane" velocity). For clarity, both of the comparisons show only the unsteady components of induced inflow. It can be seen that the unsteady u-velocity comparison is excellent in magnitude, phase, and waveform shape. The w-velocity predictions match the phase and waveform shape well, but slightly under-predicts the magnitude of the pulse. The slight discrepancies in the phase for both plots may be explained by realizing that the location of the entire experimental signal has an error band that is equal to $\pm \frac{1}{2}$ of the azimuthal resolution at which the data was acquired. This error band is equivalent to $\pm 1.4°$ in azimuth. Here, the data has been plotted at the center of the error band. Also, the position of the measurement location in space and the position of the point in space used for the prediction comparisons do not exactly coincide since there is not a computational grid point that falls exactly on the measurement location; the closest point in the grid to the measurement location is shown. Comparing the coordinates for location J in the measurements and in the predictions, the error in radial location is less than 1%

of the rotor radius; the error in azimuthal location is less than $0.4°$, and the vertical location error is negligible ($\ll 1\%$ of the rotor radius).

Even though the distributed time averaged data was not measured in this experiment, it is worthwhile to examine this quantity from the predictions in the same manner as done by Boyd and Barnwell [24]. Figure 7.4 shows a contour plot comparison of the time averaged induced inflow (w-velocity). Figure 7.4a shows the out-of-plane component of the measured, time averaged induced inflow ratio for the rectangular planform rotor shown in chapter 3. This is the same experimental data from figure 3.8. As discussed in chapter 3, this experimental data contains a fuselage, whereas, the current prediction does not. Figure 7.4b shows the current, predicted, time averaged induced inflow ratio which as been filtered to roughly match the experimental data frequency content as discussed in Appendix A.

Comparing these two figures, it can be seen that the prediction contains the same general features of the measured data. It can be seen that there is an upwash on the front of the disk, that there is a downwash at the rear of the disk with more concentrated downwash in the first and fourth quadrants, and that the magnitudes of the downwash are similar. These features and the level of prediction shown are similar to those shown in reference [24] for a different rotor system. In addition, figure 7.4b shows a curious feature that has been seen before in the literature for both the current method and for the purely GDWT [25]. This feature, seen on the retreating side of the rotor in the fourth quadrant near the blade root, appears to be a region where the induced inflow is quite small compared to the induced inflow surrounding that region; this feature is not seen in the measured data. That feature can be explained by examining the rotor loading in that region. Since, physically, the rotor induced inflow is generated as a fluid reaction to the rotor loading distribution, and since the rotor loading is very small in that region due to the very low dynamic pressure there, the induced inflow is small in that region. Chapter 8 will show that this feature is affected by the isolated rotor assumption made in previous investigations.

7.6 Observations

The inplane and out-of-plane components of unsteady induced inflow at points above, but still close to, the rotor plane are well predicted and are consistent with previous literature. In addition, though time averaged results are not available for the isolated rotor configuration, the time averaged predicted results are consistent with previously published time averaged results at similar

conditions for similar rotor systems.
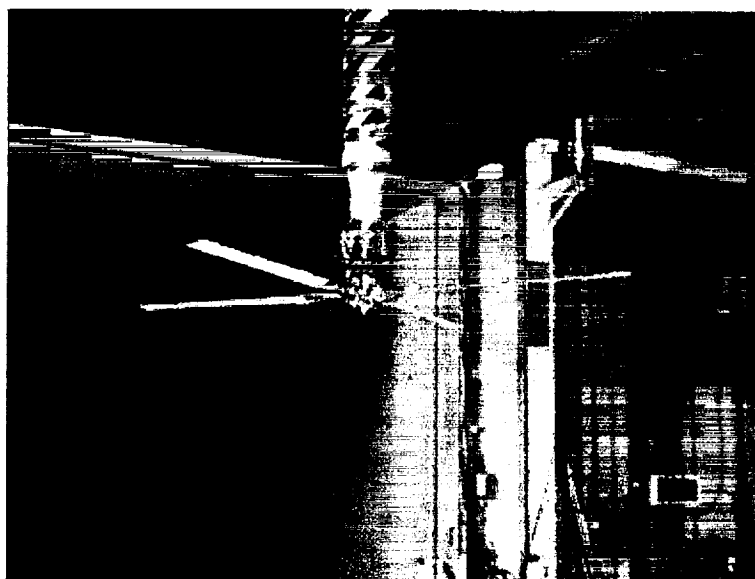
Figure 7.1: IRTS in the NASA Langley Research Center 14- by 22-Foot Subsonic Tunnel.
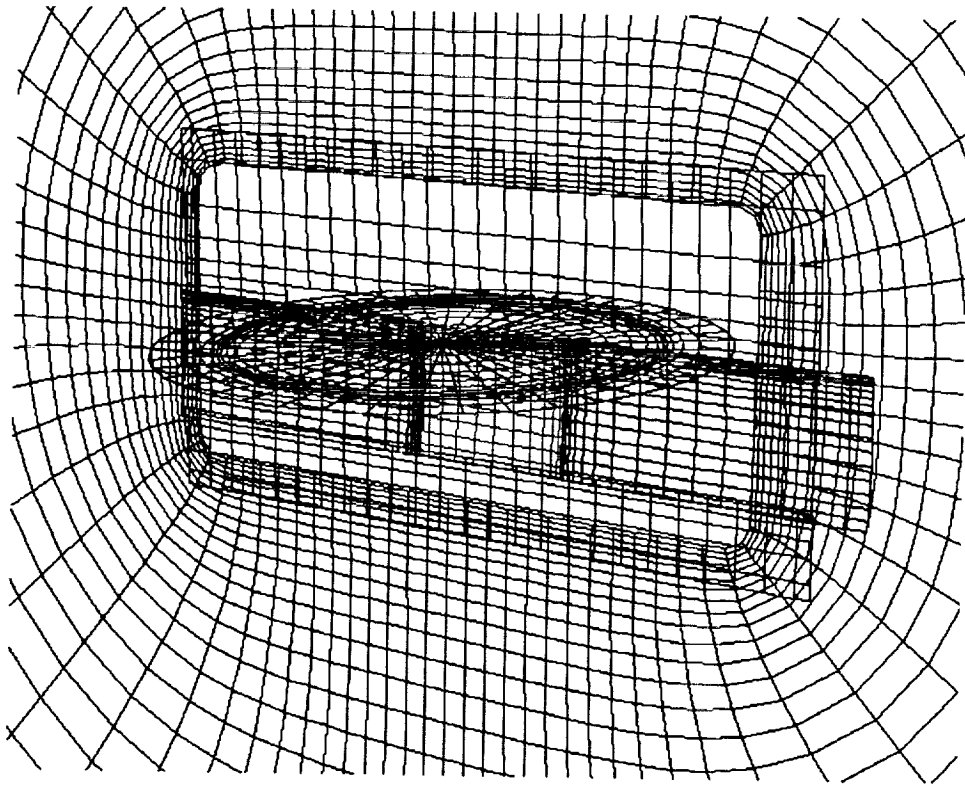
Figure 7.2: Grid System Used in Computations.
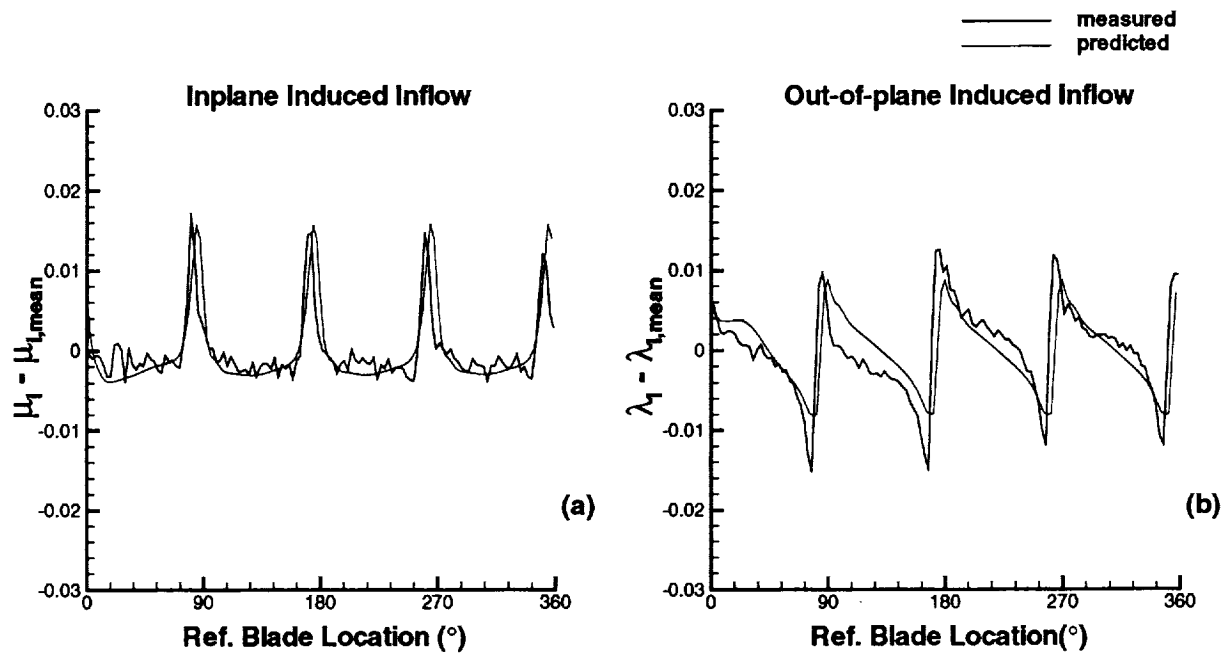
Figure 7.3: Measured and Predicted Induced Inflow in Two Directions at Location J for the IRTS.
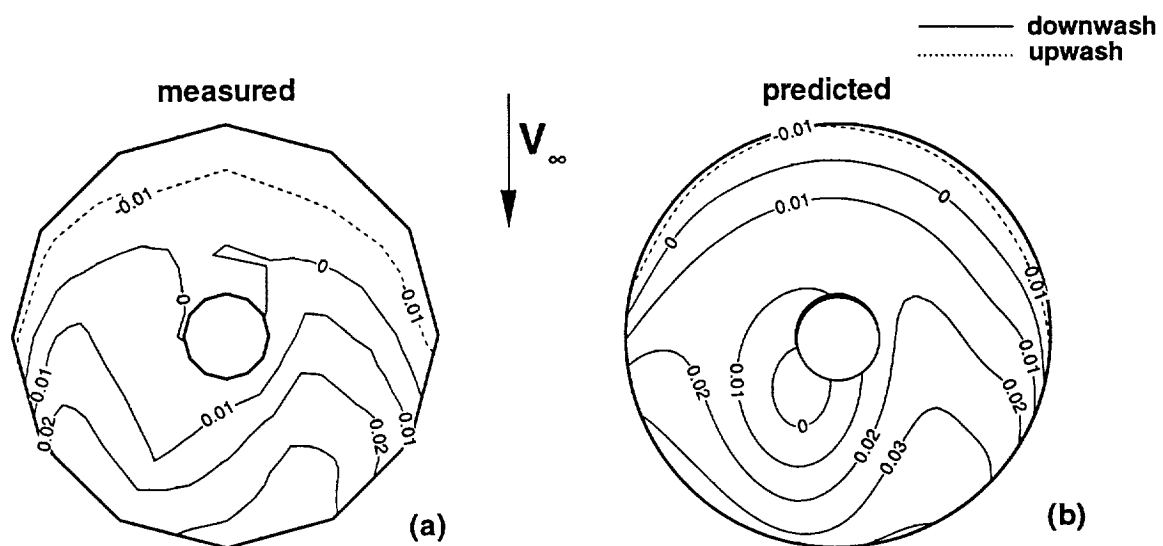
Figure 7.4: Measured and Predicted Time Averaged Induced Inflow Ratio for the IRTS (Measured Data Includes Fuselage).

Chapter 8

Results: Rotor/Fuselage

8.1 Introduction

Chapters 6 and 7 showed various predictions made with the current computational model on the two separate components of a full configuration: an isolated fuselage and an isolated rotor. In this chapter, these two components are combined into a single unit using the entire computational model. For comparisons between measured and predicted quantities, several experimental data sets are used since there are no available data sets that contain measurements of all quantities of interest.

8.2 Experimental Setup

The experimental setup used is a combination of the IRTS discussed in chapter 7 and the 2-meter ROBIN fuselage [33, 34, 35, 36]. This configuration is shown in figure 8.1. In this particular test, no LV data were taken as was done in the IRTS test discussed previously. Instead, unsteady fuselage pressures were measured at several locations on the fuselage. The locations included a row of pressure taps near the top centerline of the fuselage. This row of taps nominally followed the top centerline, but were offset 0.25 inches to the advancing side of the fuselage. This offset was needed since the construction of the fuselage shell consisted of two halves which overlapped on the centerline of the fuselage. In addition, there were six unsteady pressure taps at fuselage station "e" (see figure 6.5) at several vertical locations on the left and right sides of the fuselage. Three of

these taps were on the left side and three on the right side of the fuselage. The unsteady pressure data was processed at 256 points per rotor revolution.

8.3 Computational Grid System

The grid system for the combined rotor/fuselage configuration is similar to that used in chapter 6, figure **??**. Since the rotor grid was already included in the isolated fuselage configuration, no grid changes are needed to proceed directly from the isolated fuselage steady state results in chapter 6 to the time averaged rotor/fuselage configuration. However, for the time accurate computations, slight modifications were made to the grid which do not affect the grid shape or distribution of points. These modifications were made to accommodate a solution scheme in OVERFLOW that is very efficient in the unsteady mode.

For the unsteady rotor/fuselage configuration computations in OVERFLOW, the LU-SGS scheme is used. However, current implementation of this scheme does not allow for the use of spatially periodic boundary conditions. In OVERFLOW, spatially periodic grids and spatially periodic boundary conditions, have identical first and last planes. Figure 8.2(a) represents a schematic of a spatially periodic grid with k being the index in the periodic direction. It can be seen that $k = 1$ and $k = kmax$ are actually the same point; for a three dimensional grid, these would be planes. To account for the fact that the LU-SGS scheme cannot be used with spatially periodic boundary conditions, the periodic grids in the rotor/fuselage grid system (excluding the rotor grid), are converted to grids that can still pass information to themselves through an extended overlap region. These grids then use a new boundary condition combination, created by using several existing OVERFLOW boundary conditions in succession, to pass information spatially in a manner similar to the traditional spatially periodic boundary condition. In this new boundary condition combination, the grids are slightly modified so that an overlap, or one-to-one match, of four grid planes is made in each of the computational grids' spatially periodic direction. This overlap of four grid planes is used to replace the single overlap plane used in the spatially periodic boundary condition. A schematic of this is shown in figure 8.2(b). With these new overlapped planes, the "copy-to" and "copy-from" boundary conditions in OVERFLOW are used to pass information from one end of the computational grid to the other to simulate a spatially periodic condition. In table 8.1, the "copy-to" and "copy-from" columns show which information is passed between computational grid planes in the computational k-direction (the spatially periodic direction used in these grids).

Table 8.1: LU-SGS "Periodic" Boundary Condition

Copy-from (k value)	Copy-to (k value)
$kmax - 3$	1
$kmax - 2$	2
3	$kmax - 1$
4	$kmax$

There were some configuration anomalies in the experimental setup for the rotor/fuselage configuration that were also incorporated into the grid system. First, due to offsets in the wind tunnel floor and ceiling, the rotor center of rotation was offset approximately two inches to the advancing side of the centerline of the fuselage. This placed the rotor rotation center at approximately the advancing side edge of the pylon atop the fuselage. Second, the fuselage shell was yawed at approximately 0.76° nose-left. Both of these anomalies have been accounted for in the grid system.

8.4 Time Averaged Computation

The isolated fuselage configuration results shown in chapter 6 are used as a starting point for the time averaged rotor computations with the combined configuration. These calculations involve using the time averaged rotor boundary condition discussed in chapter 4. As before, this portion of the calculation is an intermediate step between the steady state isolated fuselage computation and the unsteady rotor/fuselage configuration. It uses the same grid system defined above for the steady state computation. Since this is an intermediate stage of the computation, only the force convergence history will be examined to show that this portion of the computation is well behaved. Figure 8.3 is a continuation of figure 6.4 with the new portion beginning at iteration number 601 and ending at iteration number 1100.

8.5   Time Accurate Computation

For the time accurate computations, OVERFLOW is executed in an unsteady mode using the LU-SGS scheme to invert the left hand side of the equations using the new overlapping grid scheme to eliminate the spatially periodic boundary conditions. The unsteady rotor model boundary condition is applied as discussed in chapters 4 and 7. These computations are executed until a periodic result is obtained in the unsteady pressures on the fuselage.

8.6   Coupled Model Predictions

In subsequent sections, the new, coupled, computational model predictions will be presented for several iterations. The first subsection will show the unsteady fuselage pressure predictions for the first iteration[1] *vs* the corresponding measured quantities from the current rotor/fuselage configuration experiment. The second subsection will compare measured and predicted, unsteady induced inflow ratios from the first iteration. The third subsection will compare predicted, time averaged induced inflow ratio contours from the first iteration, which have been derived from the unsteady model, to the corresponding measured induced inflow ratio contours, taken from the experimental data presented in chapter 3. The fourth subsection will compare measured and predicted lateral and longitudinal induced inflow ratios. Subsequent sections and subsections will show the comparisons for the second and third iterations, including the coupling. Finally, an examination of the pressure contours on the fuselage surface will be made, as well as an examination of the convergence of the method in terms of the trim pitch settings as a function of iteration.

8.6.1   Iteration 1

Unsteady Fuselage Pressures

Figure 8.4 shows a comparison between the measured and predicted unsteady modified pressure coefficient on the top centerline of the ROBIN fuselage for various downstream locations (x-direction). Plotted on the vertical axis is the negative of the modified pressure coefficient, C_p'.

---

[1]Here, an iteration refers to one pass through the rotor loading model followed by one pass through the rotor/fuselage flowfield model. Typically, only two rotor revolutions are required in each rotor/fuselage flowfield model iteration.

Along the horizontal axis is the reference blade location in the rotor azimuthal coordinates. Since the measurement location is fixed in the non-rotating frame, this horizontal axis can also be viewed as a temporal axis spanning one rotor revolution. The modified pressure coefficient used in these comparisons is defined by the following:

$$C_p' = \frac{100(P - P_\infty)}{\frac{1}{2}\rho(\Omega R)^2} \tag{8.1}$$

where the typical velocity in the denominator of the C_p definition had been changed to ΩR. This modified C_p is designated C_p'. Using a superscript u simply denotes that this is the unsteady component. This change in definition is needed since, for a rotorcraft, a freestream velocity approaching zero is possible as the hover condition is approached. If the normal definition of C_p were used, the values of C_p would approach infinity as the hover condition is approached. The factor of 100 on the C_p' simply serves as a convenient factor to scale the modified pressure coefficient function. Comparing the standard C_p definition and the C_p' definition above, the following relation holds between C_p and C_p':

$$C_p' = 100\mu_\infty^2 C_p \tag{8.2}$$

where μ_∞ is the freestream advance ratio. To show the relation between these quantities more clearly, consider a perfect fluid. For a perfect fluid, stagnation occurs at $-C_p = -1.0$. Using the current flight condition for the rotor/fuselage configuration, and using equation (8.2), this equates to $-C_p' = -5.29$. Referring this to figure 8.4, a value of $-C_p' = -1.0$ corresponds to $-C_p \approx -0.19$.

Examining features in figure 8.4, it can be seen in that there is a dominant blade passage event at a frequency of four pulses per rotor revolution in the measured pressure signature. Here, the phase of the pressure signal is well matched, and the magnitude is slightly over-predicted.

Figure 8.5 shows the measured and predicted $-C_p'^u$ as a function of the reference blade location. Whereas figure 8.4 showed the predictions on the top centerline of the fuselage, figure 8.5 shows the predictions on the retreating and advancing sides of the fuselage (*i.e.*, the left and right sides) for various vertical locations at the same downstream location. It can be seen that the magnitude and phase are predicted well for the advancing side locations; however, the retreating side amplitudes are slightly over-predicted.

Time Accurate Induced Inflow Ratios

Figure 8.6 shows the in-plane and out-of-plane components of unsteady induced inflow for the same location as that in figure 7.3. Figure 8.6, however, is a comparison between the unsteady induced inflow velocities for an isolated rotor (obtained from figure 7.3) and that for the first iteration of the method, including the fuselage. It can be seen that the presence of the fuselage has little effect on the unsteady induced inflow components at these particular locations.

Time Averaged Induced Inflow Ratios

At this point, it is worthwhile to check the validity of the time averaged results, obtained by time averaging the time accurate calculations, by comparing them to measured data.

Figure 8.7 shows a comparison between the measured and predicted induced inflow ratio perpendicular to the rotor tip path plane. For each of the predictions, the same pressure distribution is used in the rotor boundary condition. Figures 8.7b and 8.7c show the predicted induced inflow ratio for the isolated rotor and the predicted induced inflow ratio for the rotor/fuselage combination, using the same unsteady rotor boundary condition and pressure information. Several improvements can be seen in the induced inflow ratio prediction between the isolated rotor prediction and the rotor/fuselage combination. First, the inflow anomaly, seen in the isolated rotor prediction in the fourth quadrant near the blade root, is not present in the rotor/fuselage combination prediction. The induced inflow in this region now matches the measured data in that region. Second, the induced inflow near the forward portion of the rotor disk matches the experimental data well. For example, examining the contour line of "zero" induced inflow in the measured data and in the rotor/fuselage combination prediction, it can be seen that the upwash on the forward section of the disk now extends toward the center of the rotor. This upwash region is generated by the presence of the fuselage and is therefore not predicted in the isolated rotor prediction.

Figure 8.7d shows the difference between the induced inflow ratio for the rotor/fuselage combination and that of the isolated rotor. This difference shows the effects of the fuselage on the time averaged flowfield. As expected, there is an increased upwash near the nose of the fuselage and forward section of the pylon and an increased downwash behind the pylon. The regions of additional induced inflow in this figure show the source of the improved induced inflow predictions shown in figure 8.7c.

Figure 8.8 shows a comparison between the measured and predicted induced inflow ratio parallel

to the rotor tip path plane for the same conditions shown above. Figures 8.8b and 8.8c show the predicted induced inflow ratio parallel to the tip path plane for the isolated rotor and the predicted induced inflow ratio parallel to the tip path plane for the rotor/fuselage combination. Comparing the figures, it can be seen that the rotor/fuselage combination better predicts the induced inflow ratio. For example, examining the induced inflow contour line with a value of 0.015, it can be seen that the isolated rotor prediction is almost symmetric left-to-right, whereas the measured and predicted induced inflow ratios are both skewed at about 45° counterclockwise to the oncoming flow. Here, again, it can be seen that inclusion of the fuselage is necessary to correctly predict the time averaged induced inflow ratio.

Figure 8.8d shows the difference between the induced inflow ratio parallel to the tip path plane for the rotor/fuselage combination and that of the isolated rotor. This difference, again, shows the effect of the fuselage on the time averaged flowfield and the sources of the improved predictions with the fuselage included. As expected, there is a decrease in u-velocity near the nose of the fuselage and an acceleration near the rear of the fuselage pylon. It can be seen that, to capture the u-velocity distribution accurately, the fuselage must be included in the computation.

Lateral/Longitudinal Induced Inflow Ratios

Figure 8.9 compares the lateral and longitudinal subsets of the measured and predicted induced inflow ratio. The measured data comes from figure 8.7a, while the predicted data is taken from the combined rotor/fuselage case in 8.7c. Comparing the prediction here to the prediction using 8 harmonics in figure 3.9, it can be seen that the longitudinal induced inflow ratio is well predicted using the combined rotor/fuselage model. Whereas the peak-to-peak amplitude of the lateral induced inflow ratio was over-predicted by the GDWT isolated rotor model, it is well predicted for the combined rotor/fuselage model. However, there is a slight over-prediction of the inflow ratio near the advancing and retreating blade tip regions.

8.6.2   Iteration 2

Unsteady Fuselage Pressures

With the first iteration complete, induced inflow corrections are computed as described in chapter 5. With these induced inflow corrections, the GDWT is used to recompute the rotor loading.

With this new rotor loading, OVERFLOW is used to recompute the rotor/fuselage flowfield. This computation, or "iteration 2", is presented in the current and subsequent sections.

Figure 8.10 shows the top centerline modified pressure coefficient in a manner similar to figure 8.4. Comparison of these two figures shows only very small differences.

Figure 8.11 shows the the modified pressure coefficient on the retreating and advancing sides of the fuselage in a manner similar to figure 8.5. Comparison of these two figures, again, shows only very small differences.

Time Accurate Induced Inflow Ratios

Figure 8.12 shows the in-plane and out-of-plane components of unsteady induced inflow for the same location as that in figure 7.3. As was seen in the first iteration, the fuselage has little influence on the unsteady components of induced inflow at this point in the flowfield.

Time Averaged Induced Inflow Ratios

Figure 8.13 shows the same information as figure 8.7, but this is the second iteration. Figures 8.13a and 8.13b show the identical information as that in figures 8.7a and 8.7b. Plots 8.13c and 8.13d are the new parts of this figure. Comparing figures 8.13c and 8.7c, it can be observed that there are only small changes between these figures except on the advancing side of the rotor disk in the first quadrant. In the first iteration, the time averaged induced inflow in that region was over-predicted. In the second iteration, it is seen that the time averaged induced inflow quantities are now closer to the measured values. However, overall, the shape of the contours did not change significantly. Comparing figures 8.13d and 8.7d, it can be observed that there are only small changes between these difference plots. Thus the effect of the fuselage on the time averaged induced inflow is quite similar between the first and second iterations.

Figure 8.14 shows the same information as figure 8.8, except it is for the second iteration. As before, figures 8.14a and 8.14b show the same information as figures 8.8a and 8.8b. Comparing figures 8.14c and 8.8c, it can be seen, again that there are only small differences between the first and second iterations. This time, however, the small differences that do occur are on the advancing side in the first part of the second quadrant of the rotor disk. A similar conclusion holds for figures figures 8.14d and 8.8d.

Lateral/Longitudinal Induced Inflow Ratios

Figure 8.15 compares the lateral and longitudinal subsets of the measured and predicted induced inflow ratio in a manner similar to figure 8.9. The measured data comes from figure 8.13a (and is the same as in figure 8.7a), while the predicted data is taken from the combined rotor/fuselage case in 8.13c. The predictions shown in this figure are similar to those shown in figure 8.9, and similar trends are present.

Even though differences are small between the first and second iterations, a third iteration is also presented to show that the iteration process has converged.

8.6.3   Iteration 3

Unsteady Fuselage Pressures

After iterating once again through the coupling technique, the rotor loading model, and the rotor/fuselage flowfield model, the third iteration is complete. Figures 8.16 and 8.17 once again show the unsteady modified pressure coefficient on both the top centerline and the sides of the fuselage. As with the comparison between the first and second iterations, there is no significant difference between this iteration and the previous iteration.

Time Accurate Induced Inflow Ratios

Again comparing two components of unsteady induced inflow ratio for the current iteration to the isolated rotor results in figure 8.18 shows no significant difference between the two results. In addition, there are no significant differences between this iteration and the previous iteration.

Time Averaged Induced Inflow Ratios

Examining the in-plane and out-of-plane time averaged induced inflow ratios in figures 8.19 and 8.20, as was done for the second iteration, it can be seen that there are no significant differences between the current iteration and the previous iteration.

Since there are no significant differences between the second and third iteration in the unsteady

modified pressure coefficient, in the time accurate inflow ratio, or in time averaged induced inflow ratio, it can be concluded that the iteration process is complete.

Lateral/Longitudinal Induced Inflow Ratios

Figure 8.21 compares the lateral and longitudinal subsets of the measured and predicted induced inflow ratio in a manner similar to figures 8.9 and 8.15. The measured data comes from figure 8.19a (and is the same as in figures 8.7a and 8.13a), while the predicted data is taken from the combined rotor/fuselage case in 8.19c. Again, the predictions shown in this figure are similar to those shown in figures 8.9 and 8.15, and similar trends are present.

8.7 Examination of Pressure Contours

In the preceding sections, a detailed examination of the unsteady component of the modified pressure coefficient, of the time averaged inflow ratio, and of the unsteady inflow ratio was presented for several iterations of the current method. For the final result (at the end of the third iteration), it is constructive to examine pressure distribution on the fuselage with and without the effects of the rotor. Figure 8.22(a) is a contour plot of surface pressure coefficient on the isolated fuselage configuration presented in chapter 6. It can be seen there is a typical stagnation region on the nose of the fuselage.

Figure 8.22(b) is a contour plot of the time averaged surface pressure coefficient for the rotor/fuselage configuration. This plots contains data from the "iteration 3" above. As with figure 8.22(a), there is a stagnation region on the fuselage nose region and behind the pylon. However, comparing figures (a) and (b), it can be seen that the gross time averaged effect of the rotor is to increase the pressure coefficient on the sides of the fuselage and downstream of the pylon. Figures 8.23 and 8.24 are top views of figures 8.22(a) and (b), respectively.

Figure 8.25 shows a set of surface pressure coefficient contour plots similar to those presented in figure 8.22. For comparison purposes, figure 8.25(a) shows the same data as presented in figure 8.22(b). Figure 8.25(b) shows the surface pressure coefficient for the instant at which the reference blade is at the $\psi = 0°$ location. All four blades are plotted as rectangles extending from the blade root at $r/R = 0.24$ to the blade tip at $r/R = 1.0$ and are drawn "to-scale" in their actual position and orientation with respect to the fuselage; The blade chord is drawn "to-scale" as well. In this contour

plot from the unsteady computation, a large pressure pulse can be seen on the upper surface of the tail boom. This pressure pulse is a direct result of the rotor blade at the $\psi = 0°$ location passing over the tail boom. Figure 8.26 shows this pressure pulse in a top view of figure 8.25(b).

Figures 8.27 to 8.35 present surface pressure coefficient contour plots at azimuth locations of $\psi = 15°, 30°, 45°, 60°, 75°$, and $90°$. These plots again show a pressure pulse traveling on and around the fuselage. It can be seen that this pulse motion is correlated with the motion of the blade. This point is made especially clear in the "Top View" plots presented here. Examination of this set of plots reveals that, locally, the unsteady surface pressure coefficient can be substantially higher than the time averaged surface pressure coefficient and that the pulses are typically of short temporal duration. In addition, the asymmetry of the unsteady loading can be seen clearly in the "Top View" figures.

8.8   Iteration Effects on Rotor Trim

The effect of the coupled computation on the rotor trim can be assessed by examining the pitch control settings required at each stage of the iteration at the end of the trim procedure in the rotor loading computation. These blade pitch settings are a function of rotor azimuth, are referenced to the 0.75R radial location on the blade, and are defined as follows:

$$\theta(\psi) = \theta_0 + \theta_c \cos \psi + \theta_s \sin \psi \qquad (8.3)$$

where θ_0 is the collective pitch, θ_c is the longitudinal pitch, and θ_s is the lateral pitch. The first row in table 8.2 shows the measured collective, longitudinal, and lateral pitch settings, along with the magnitude and phase of the longitudinal/lateral combination. All quantities in table 8.2 are in degrees. The magnitude of the first harmonic of pitch, θ_1, and phase of the first harmonic of pitch, ψ_1 can be defined as follows:

$$\theta(\psi) \;=\; \theta_0 + \theta_1 \cos(\psi - \psi_1) \qquad (8.4)$$

$$\theta_1 \;=\; \sqrt{\theta_c^2 + \theta_s^2} \qquad (8.5)$$

$$\psi_1 \;=\; \arctan\left(\frac{\theta_s}{\theta_c}\right) \qquad (8.6)$$

where ψ_1 is placed in the range $0° < \psi_1 \leq 360°$.

Table 8.2: Pitch Control Settings [deg] as a Function of Iteration Number

Type	Iteration	θ_0	θ_c	θ_s	θ_1	ψ_1
Measured	N/A	8.16	1.52	-4.13	4.40	290.2
Isolated Rotor	1	6.84	1.45	-3.42	3.71	293.0
Rotor+Fuselage	2	8.06	2.73	-3.69	4.59	306.5
Rotor+Fuselage	3	8.02	2.67	-3.71	4.57	305.7

From this table, it can be seen that the collective pitch setting matches the measured collective pitch for the rotor/fuselage combination cases, but is under-predicted for the isolated rotor case as expected. It can also be seen that the magnitude of the first harmonic of pitch is well matched for all of the iterations, especially for the iterations that include the fuselage in the computation. A plot of these quantities *vs* iteration number are shown in figure 8.36. From this figure, it can be seen that these settings have converged in just two iterations. For the computations that include the complete configuration, a phase difference of approximately 16° can be seen. The explanation of this phase difference can be attributed to the assumption that the blade flap hinge offset is at the center of rotation. To show this, it is only necessary to examine the effect of the blade hinge offset on the rotor flap response. Gessow and Myers [54] showed that the rigid flapping natural frequency of a rotor is a function of blade hinge offset and is given by the following formula:

$$\omega_n = \sqrt{1 + \left(\frac{3}{2}\right)\bar{h}} \tag{8.7}$$

where ω_n is the flapping natural frequency in cycles per revolution and $\bar{h}$ is the hinge offset location as a fraction of rotor radius. Examination of equation (8.7) for $\bar{h} = 0$ shows that the flap natural frequency $\omega_n = 1.0$ per revolution and for $\bar{h} = 0.06$, the flap natural frequency is $\omega_n = 1.044$ per revolution. The difference in these two natural frequencies is $\Delta\omega_n = 0.044$ per revolution. Since there are 360° in one revolution, the natural frequency difference equates to approximately 16° of rotor azimuth. This means that in the experiment, which included the blade hinge offset, the phasing of the first harmonic of pitch should preceed the predicted phasing by approximately 16° of rotor azimuth. This is precisely the amount seen in table 8.2.

8.9 Resource Usage Summary

Table 8.3 lists the resource usage for each component of the current rotor/fuselage combination computations using the GDWT with 8 harmonics and 128 azimuth steps per revolution. The items listed are the CPU times in hours and minutes [hr:min] required for each iteration stage, main memory required in mega-words [mw], and which machine was used for each phase.

Table 8.3: Resource Usage as a Function of Iteration Number

Type	CPU [hr:min]	Memory [mw]	Machine
GDWT (with 8 harmonics, 128 azimuths)	<0:07	5	Cray C-90
Isolated Fuselage	3:43	18	Cray C-90
Time Averaged, Isolated Rotor	2:16	15	Cray C-90
Time Accurate, Isolated Rotor (per rev.)	1:52	17	Cray C-90
Time Averaged, Rotor/Fuselage	3:38	18	Cray C-90
Time Accurate, Rotor/Fuselage (per rev.)	2:42	22	Cray C-90

Each of the rows in table 8.3 is for a particular component of the method for this particular case. Since execution times will differ for each particular case, these should only be used as reference quantities. It should be noted that OVERFLOW does not have a convergence criterion that halts execution at a particular convergence level. It is executed for a specified number of iterations or time steps. Each of the components involving time accurate computations are given as the CPU time required to execute each rotor revolution. For the case presented here, each time accurate stage of the computation was executed for two complete rotor revolutions to assure periodicity, even though periodicity may be achieved in fewer actual blade passage events. Thus, the CPU times above are conservative values for this case. Also, note that the GDWT is executed in a conservative manner at the same resolution required by OVERFLOW. Thus, CPU time for the GDWT computations is conservative as well. To compute the total execution time for the isolated rotor results and the first iteration of the rotor/fuselage configuration, the following formulae can be used:

Isolated Rotor:

CPU Time	=	GDWT
	+	(Time Averaged, Isolated Rotor)
	+	2(Time Accurate, Isolated Rotor)
	=	6:07 (Cray C-90)

Rotor/Fuselage, Iteration 1:

CPU Time	=	(Isolated Fuselage)
	+	GDWT
	+	(Time Averaged, Rotor/Fuselage)
	+	2(Time Accurate, Rotor/Fuselage)
	=	12:52 (Cray C-90)

where the factor of two on the time accurate components indicates that two complete revolutions were executed for this particular case.

8.10 Observations

This chapter has presented results from the full hybrid method for a rotor/fuselage configuration. From the evidence presented above, several conclusions can be drawn as follow:

- The unsteady modified pressure coefficient on the top centerline of the fuselage and on the sides of the fuselage shown above, are insensitive to the small trim changes made by the time averaged induced inflow corrections which account for the presence of the fuselage.

- The in-plane and out-of-plane unsteady induced inflow velocity components are also insensitive to the small trim changes made by the time averaged induced inflow corrections which account for the presence of the fuselage.

- The time averaged induced inflow velocities are improved through the iteration/coupling process presented above. For the case presented here, it appears that one iteration is a good approximation to the correct solution and that two iterations is sufficient to capture the time averaged and time accurate induced inflow effects.

- The primary effect of the fuselage on the trimmed blade pitch settings is on the collective

pitch (for this particular case). The presence of the fuselage improves the pitch setting predictions over those from the isolated rotor case.

- For this flight condition, the primary effects of the rotor on the fuselage are a higher time averaged surface pressure coefficient below and downstream of the rotor and short duration surface pressure pulses imposed by the individual blade passages over the fuselage surfaces.
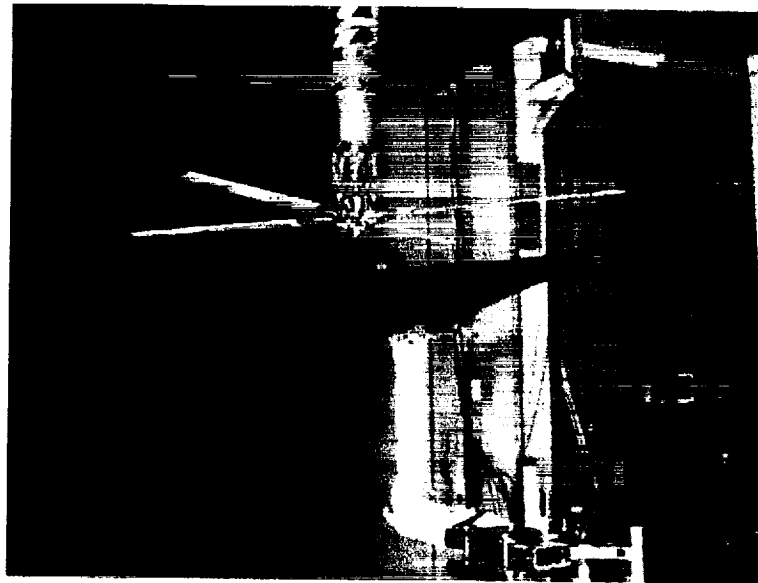
Figure 8.1: IRTS/Fuselage Configuration in the NASA Langley Research Center 14- by 22-Foot Subsonic Tunnel.
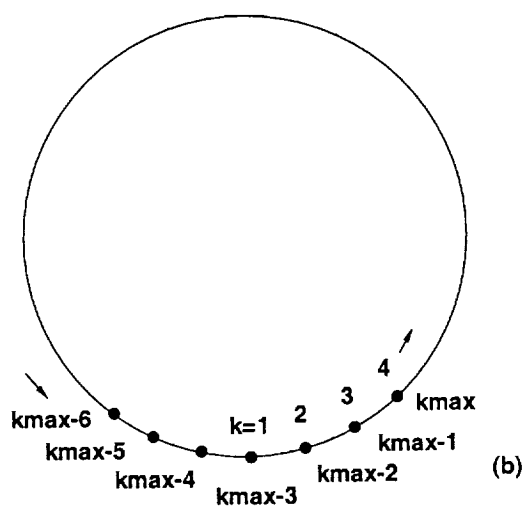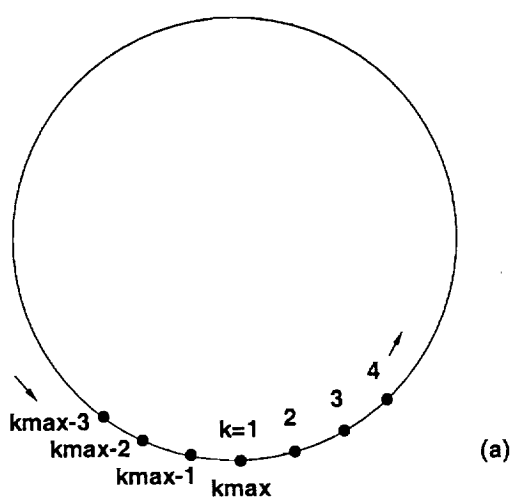
Figure 8.2: Schematic of a Periodic Grid and Replacement for Periodic Grid in LU-SGS Scheme.
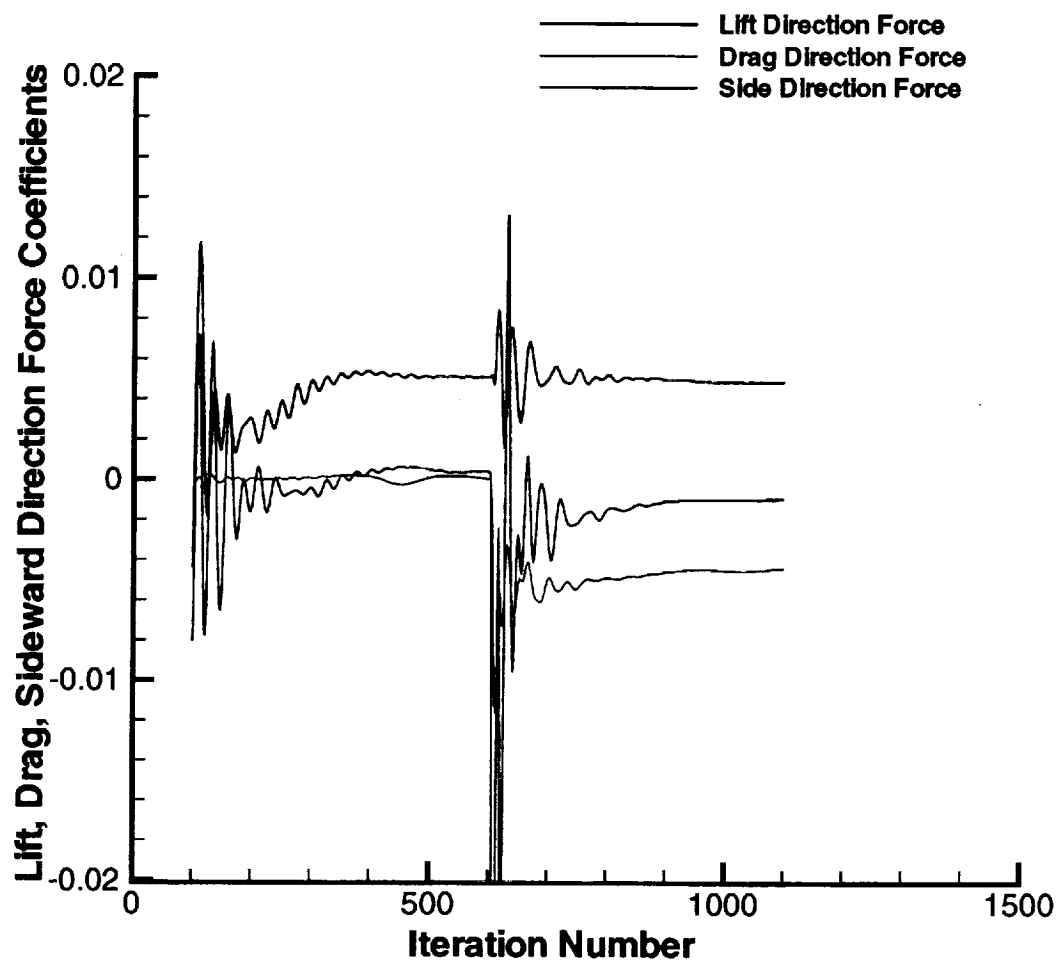
Figure 8.3: Lift, Drag, and Sideward Direction Force Coefficients, Time Averaged Computation.
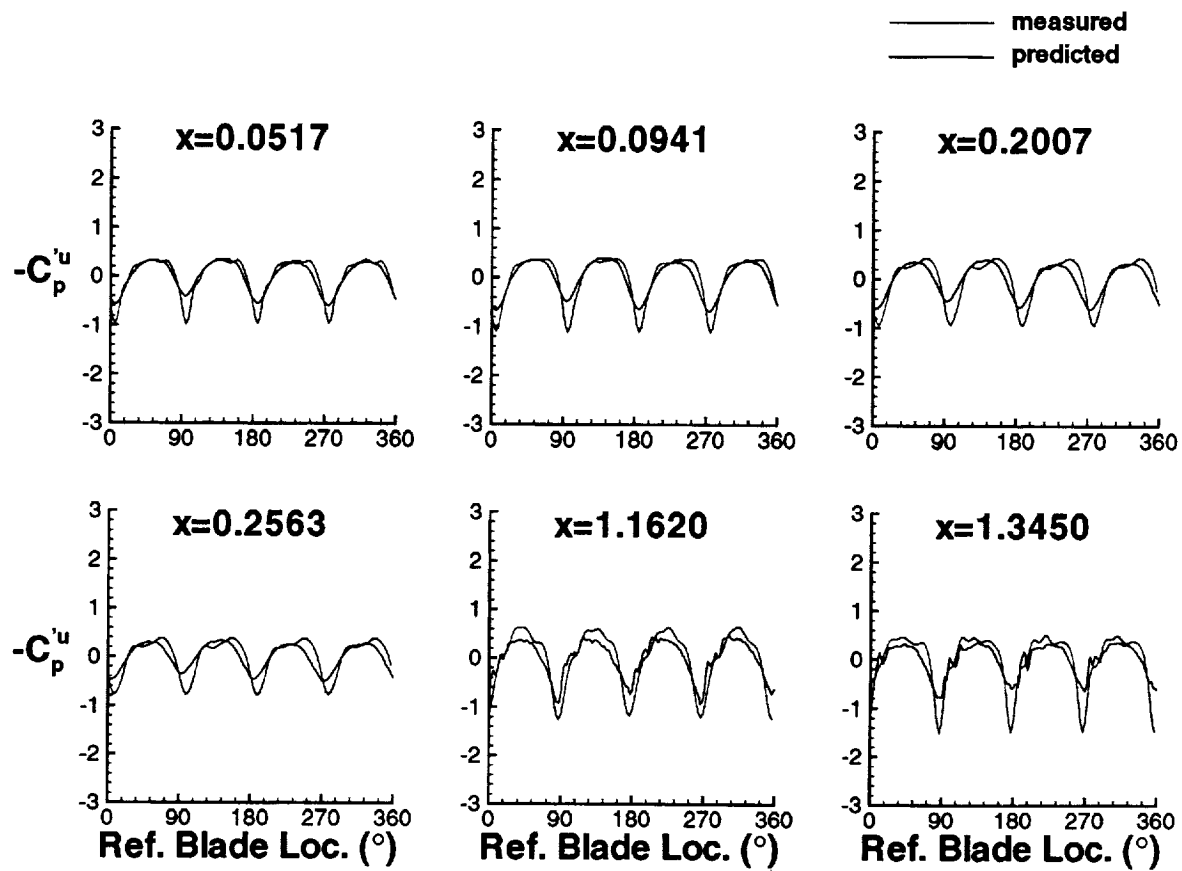
Figure 8.4: Measured and Predicted Unsteady Modified Pressure Coefficient on the Top Centerline of the ROBIN Fuselage, Iteration 1.
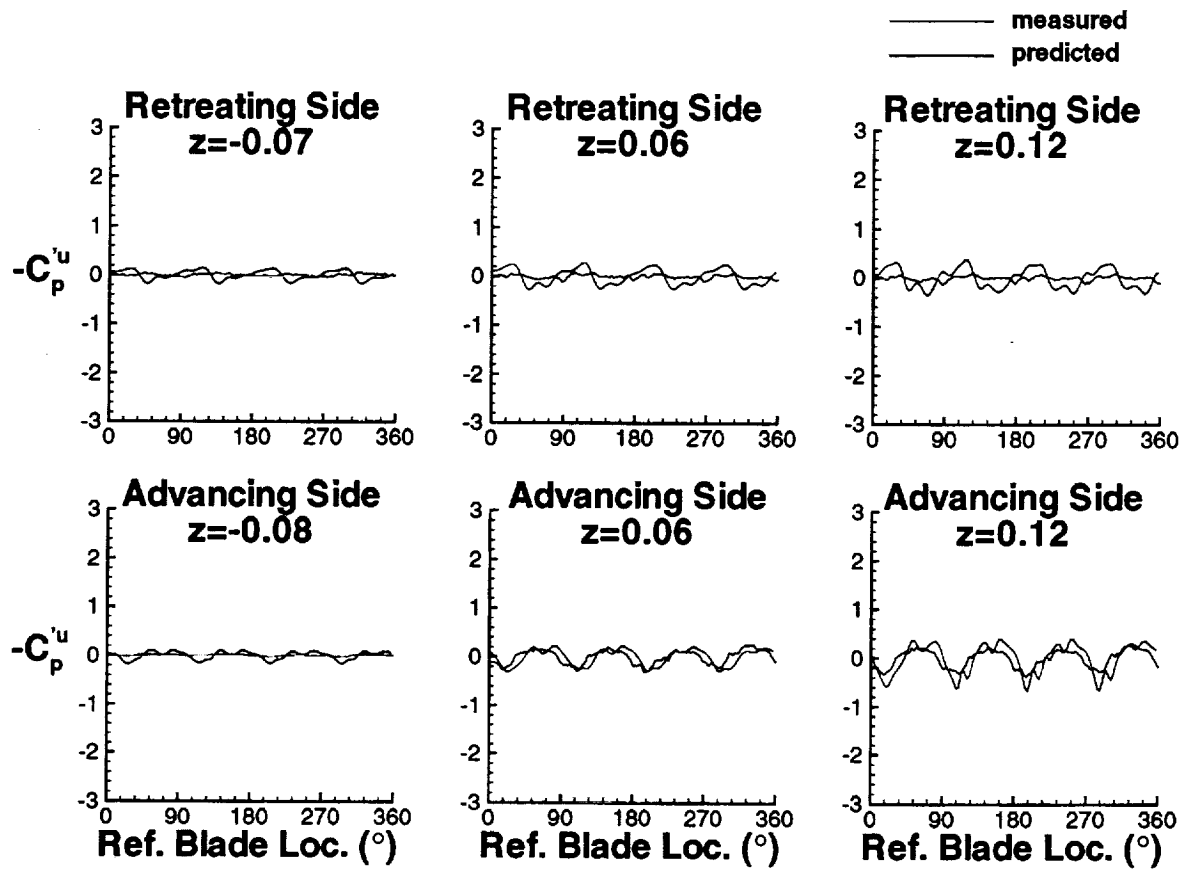
Figure 8.5: Measured and Predicted Unsteady Modified Pressure Coefficient on the Retreating and Advancing Sides of the ROBIN Fuselage, Iteration 1.
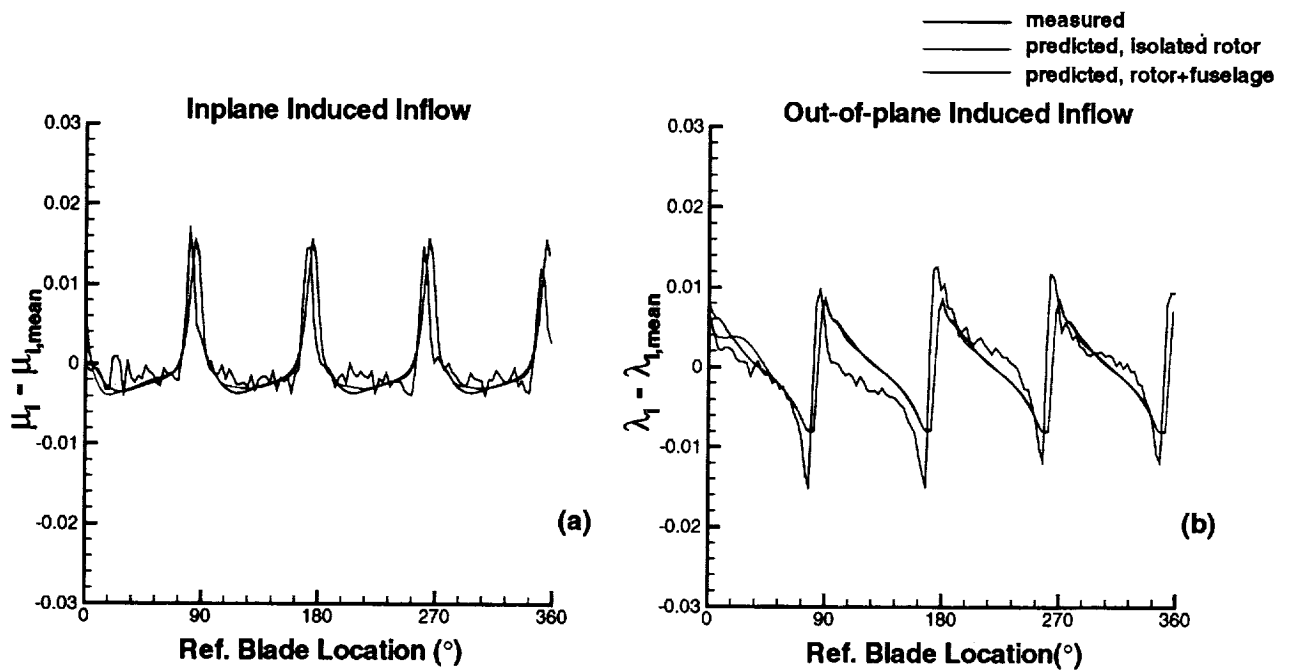
Figure 8.6: Measured and Predicted Induced Inflow in Two Directions for an Isolate Rotor and a Rotor/Fuselage Combination, Iteration 1.

Figure 8.7: Measured and Predicted Time Averaged Induced Inflow Ratio from Time Accurate Computations, Iteration 1.

Figure 8.8: Measured and Predicted Time Averaged Parallel Induced Inflow Ratio from Time Accurate Computations, Iteration 1.

Figure 8.9: Measured and Predicted Lateral and Longitudinal Time Averaged Induced Inflow Ratio from Time Accurate Computations, Iteration 1

Figure 8.10: Measured and Predicted Unsteady Modified Pressure Coefficient on the Top Centerline of the ROBIN Fuselage, Iteration 2.

Figure 8.11: Measured and Predicted Unsteady Modified Pressure Coefficient on the Retreating and Advancing Sides of the ROBIN Fuselage, Iteration 2.

Figure 8.12: Measured and Predicted Induced Inflow in Two Directions for an Isolate Rotor and a Rotor/Fuselage Combination, Iteration 2.
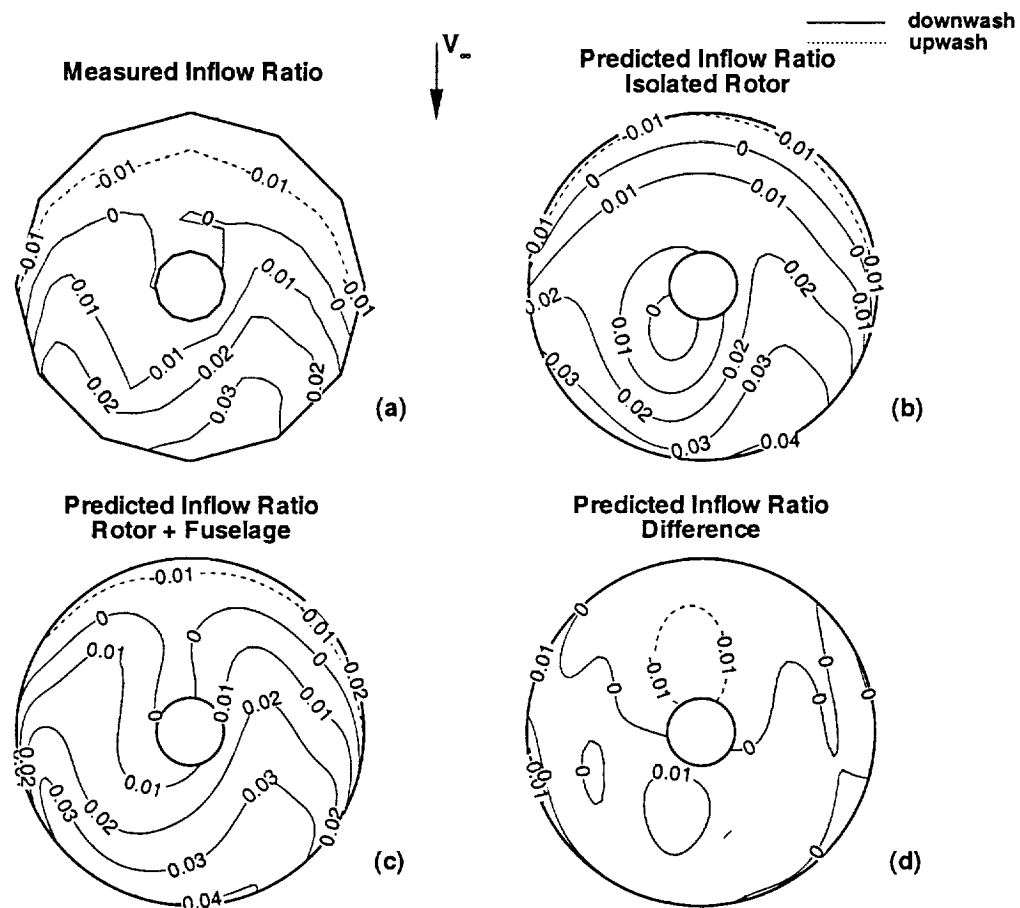
Figure 8.13: Measured and Predicted Time Averaged Induced Inflow Ratio from Time Accurate Computations, Iteration 2.
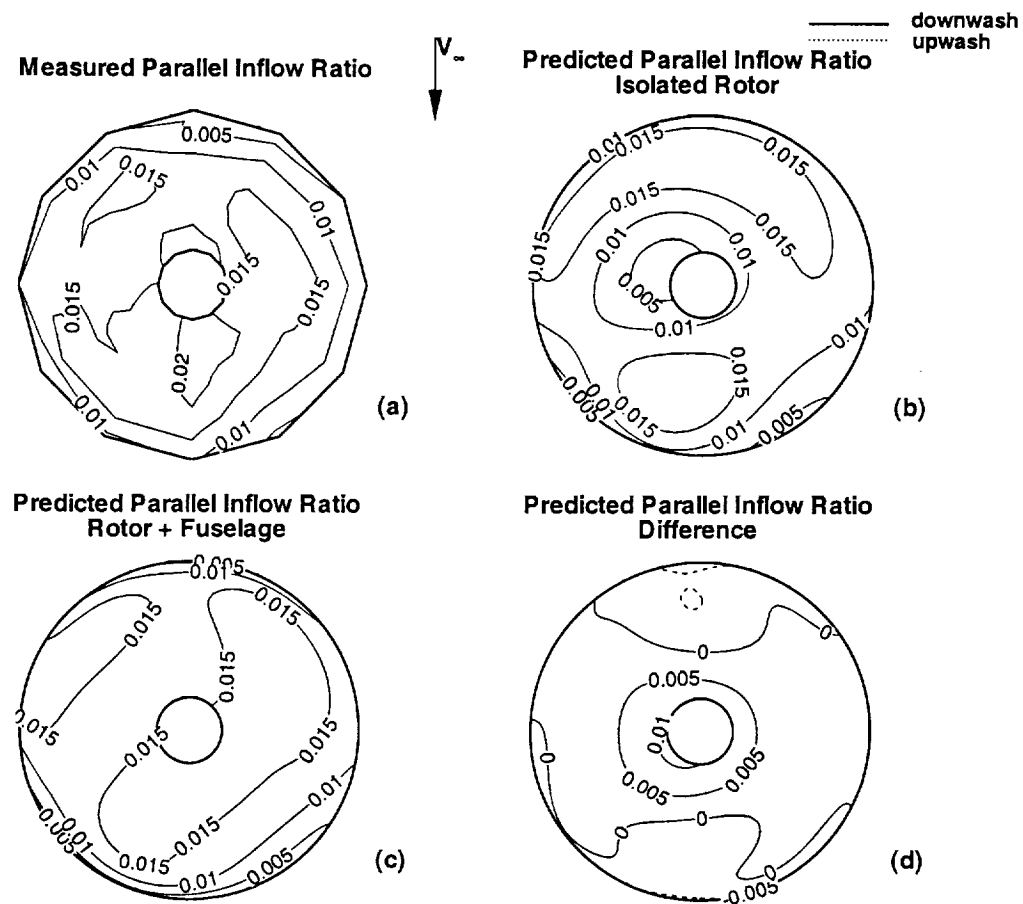
Figure 8.14: Measured and Predicted Time Averaged Parallel Induced Inflow Ratio from Time Accurate Computations, Iteration 2.
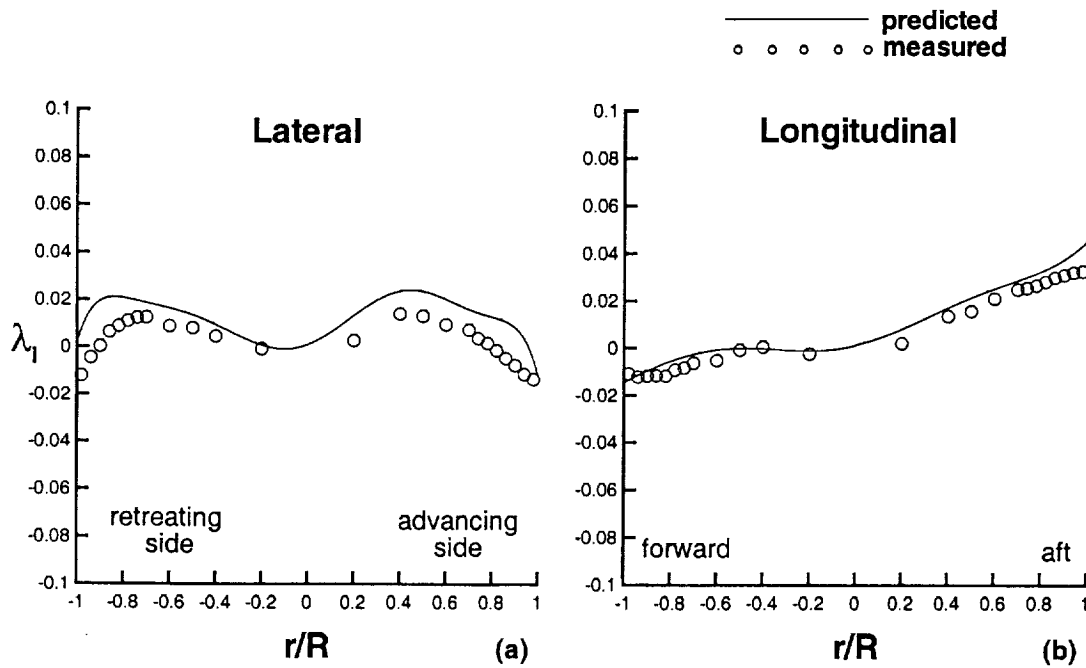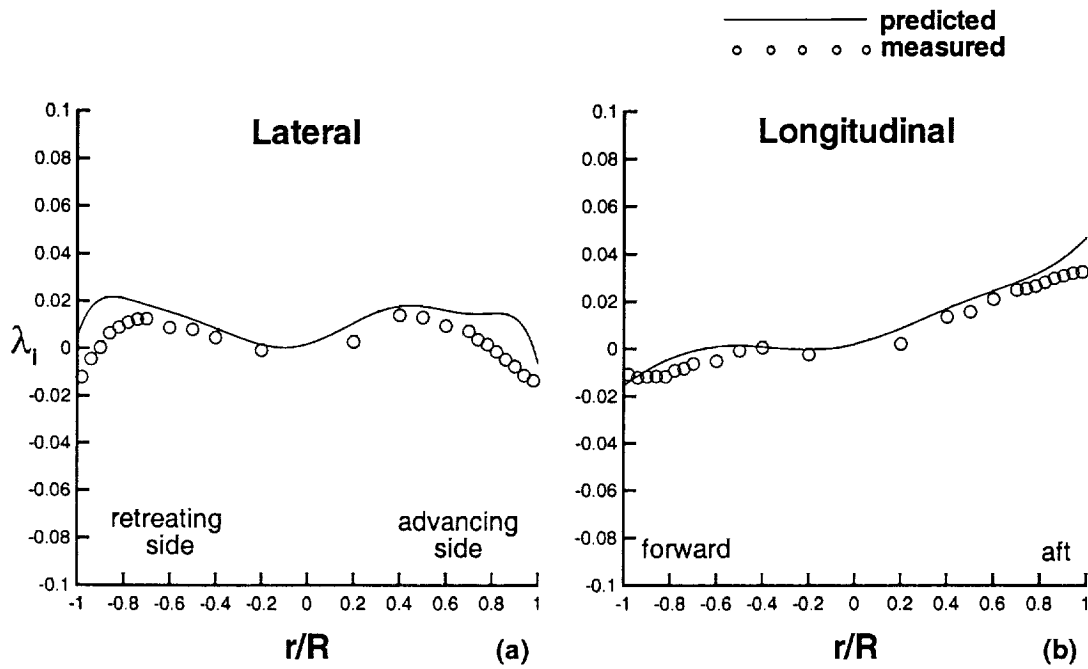
Figure 8.15: Measured and Predicted Lateral and Longitudinal Time Averaged Induced Inflow Ratio from Time Accurate Computations, Iteration 2
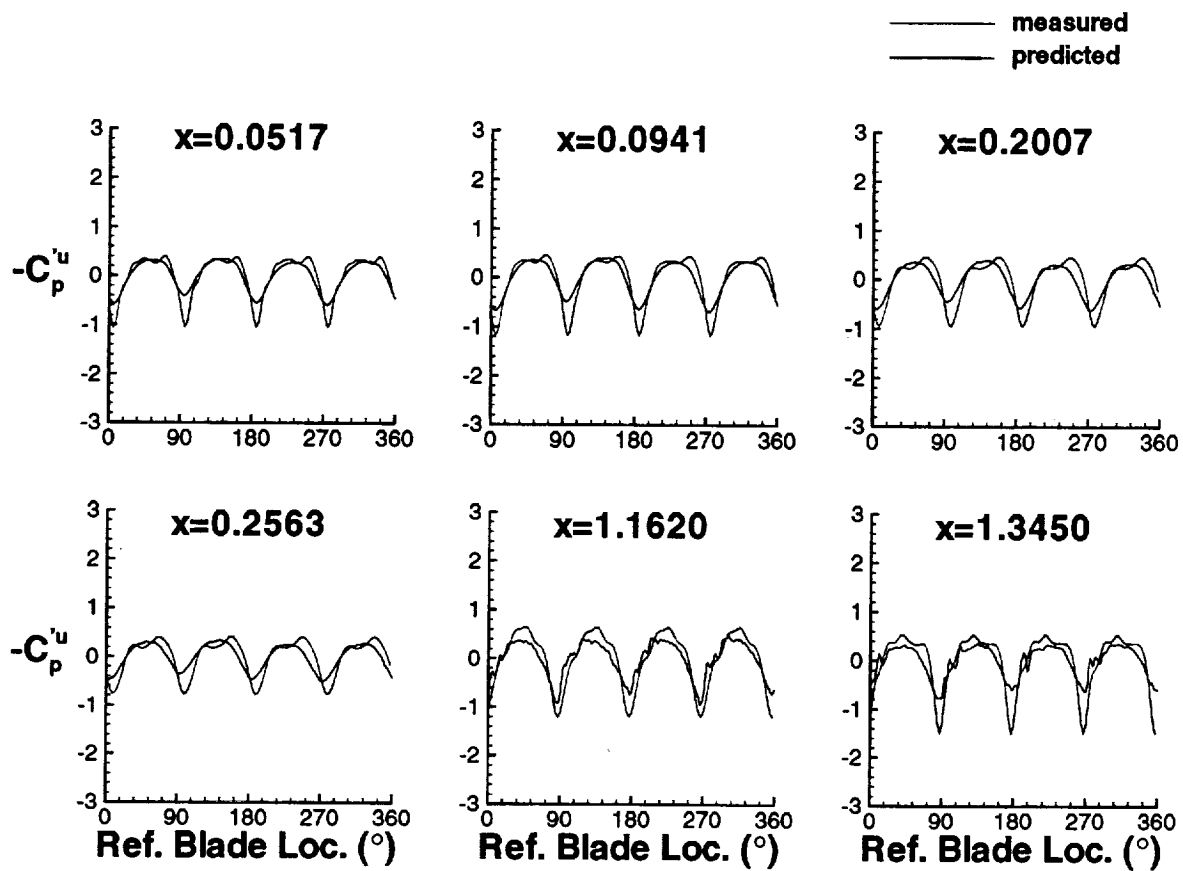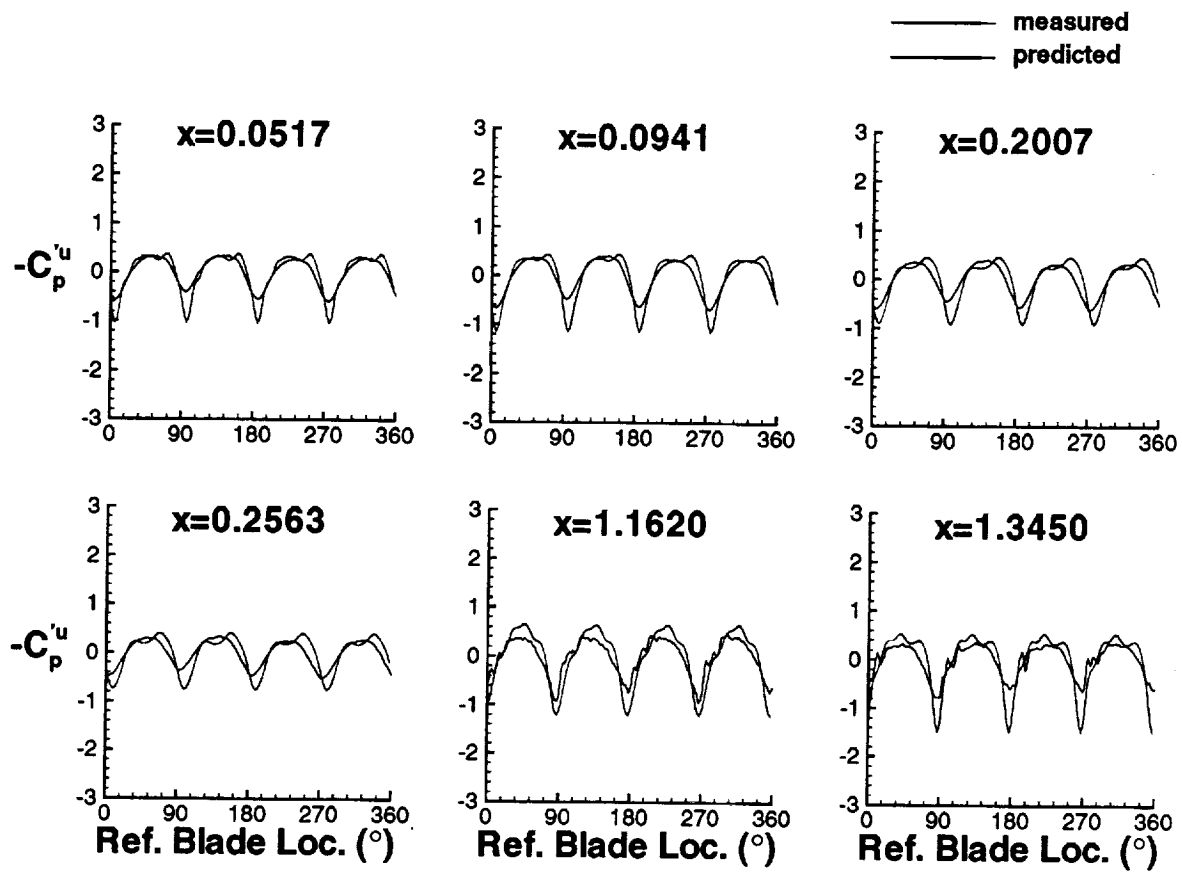
Figure 8.16: Measured and Predicted Unsteady Modified Pressure Coefficient on the Top Centerline of the ROBIN Fuselage, Iteration 3.
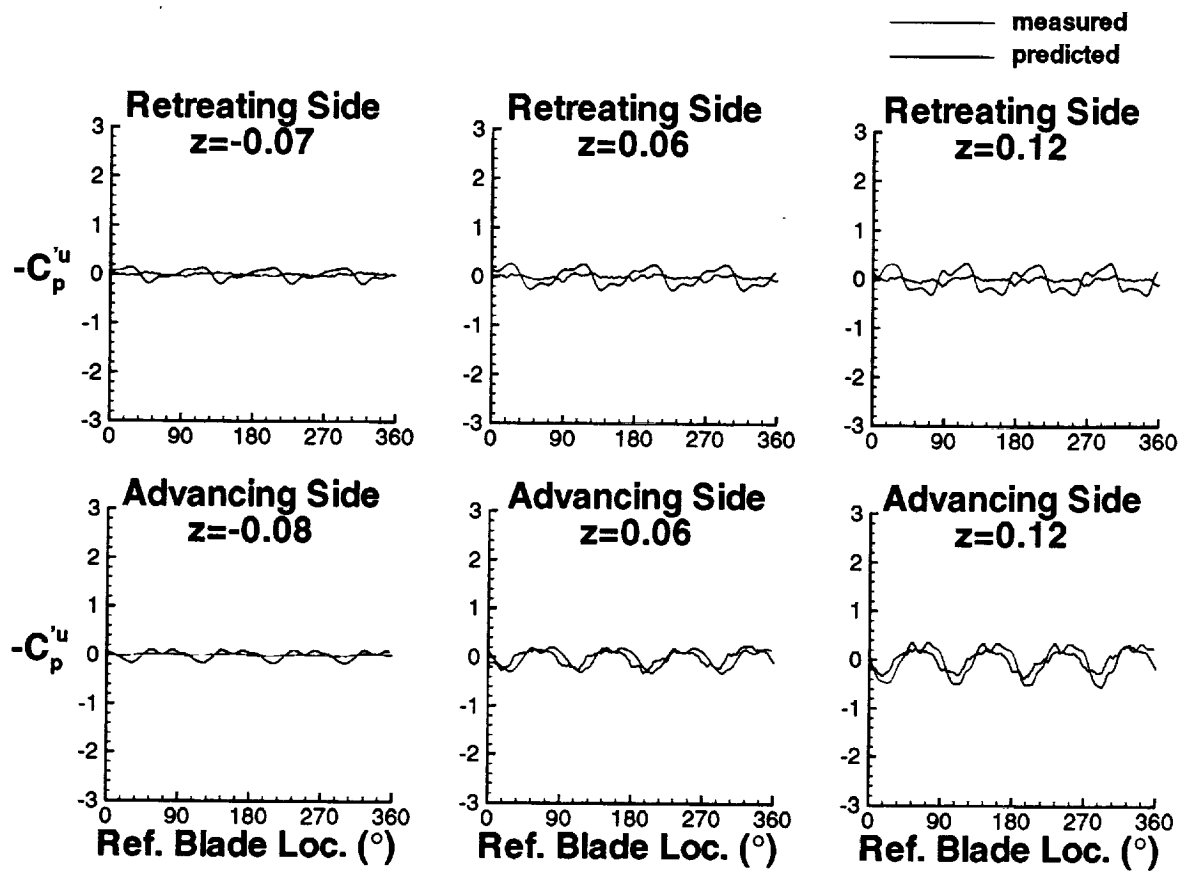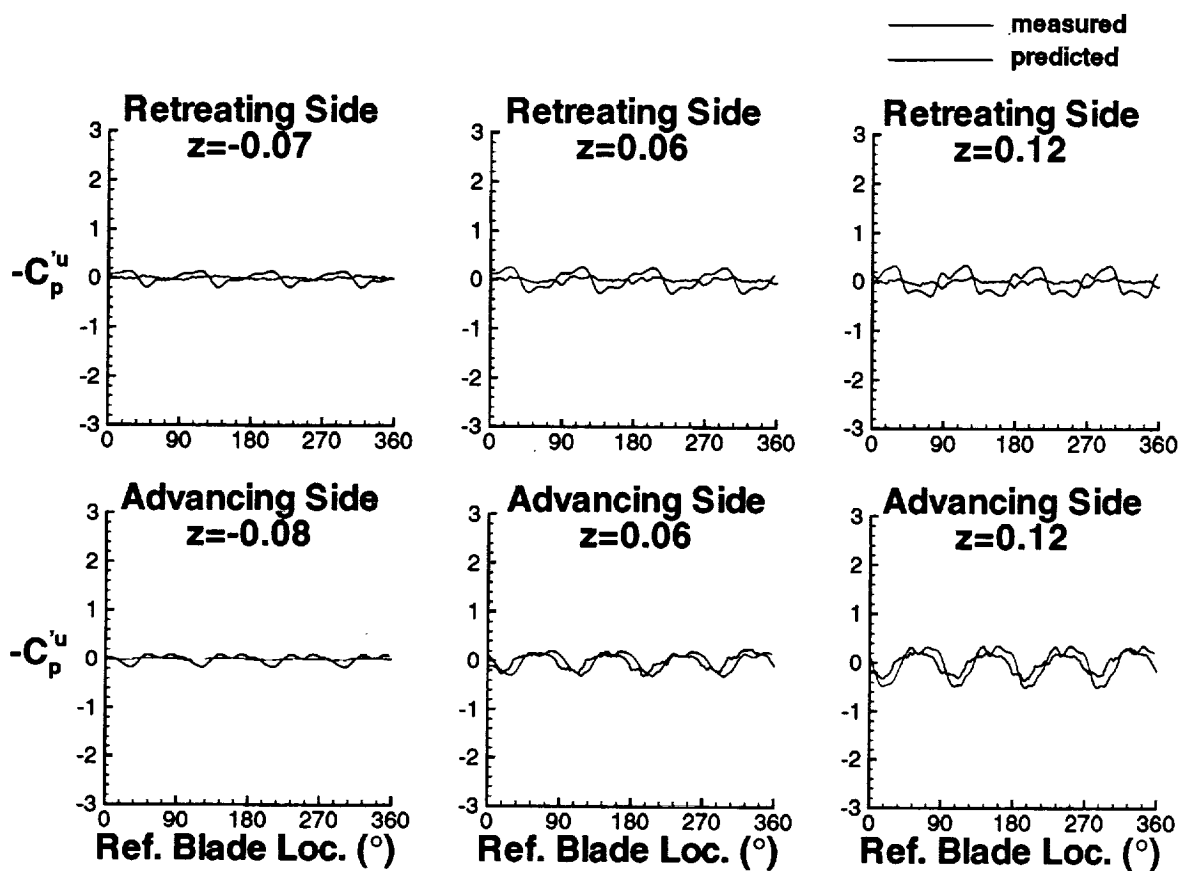
Figure 8.17: Measured and Predicted Unsteady Modified Pressure Coefficient on the Retreating and Advancing Sides of the ROBIN Fuselage, Iteration 3.
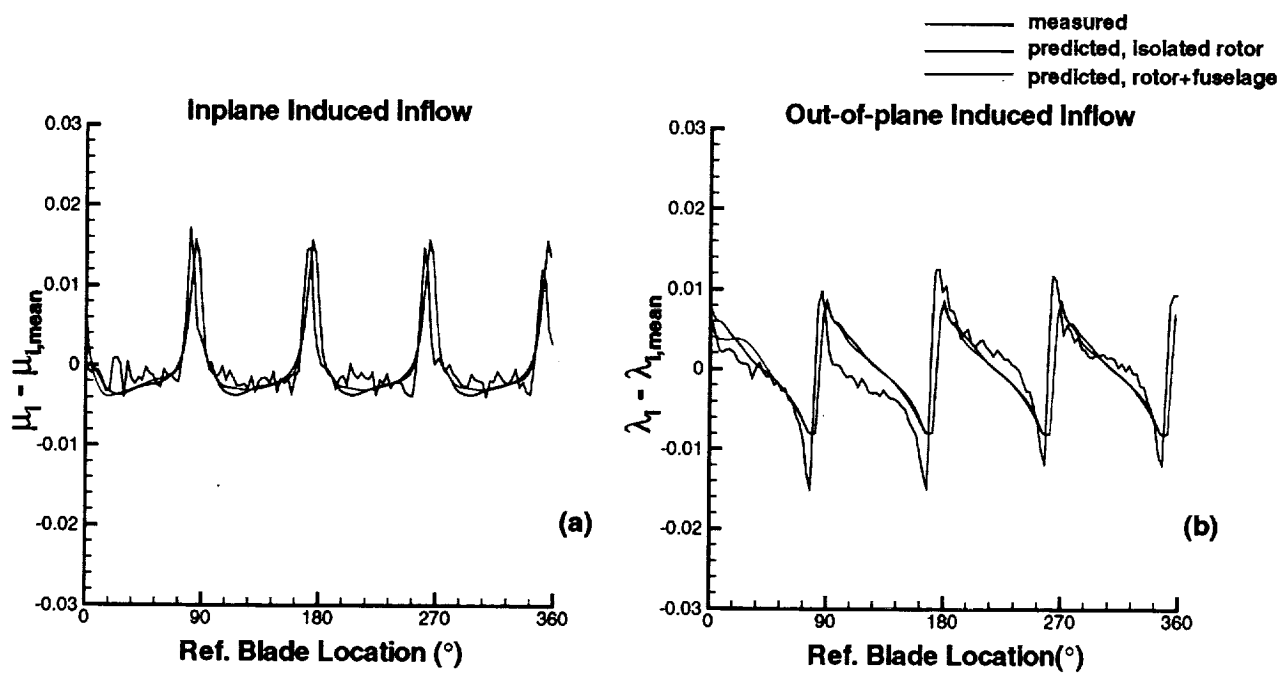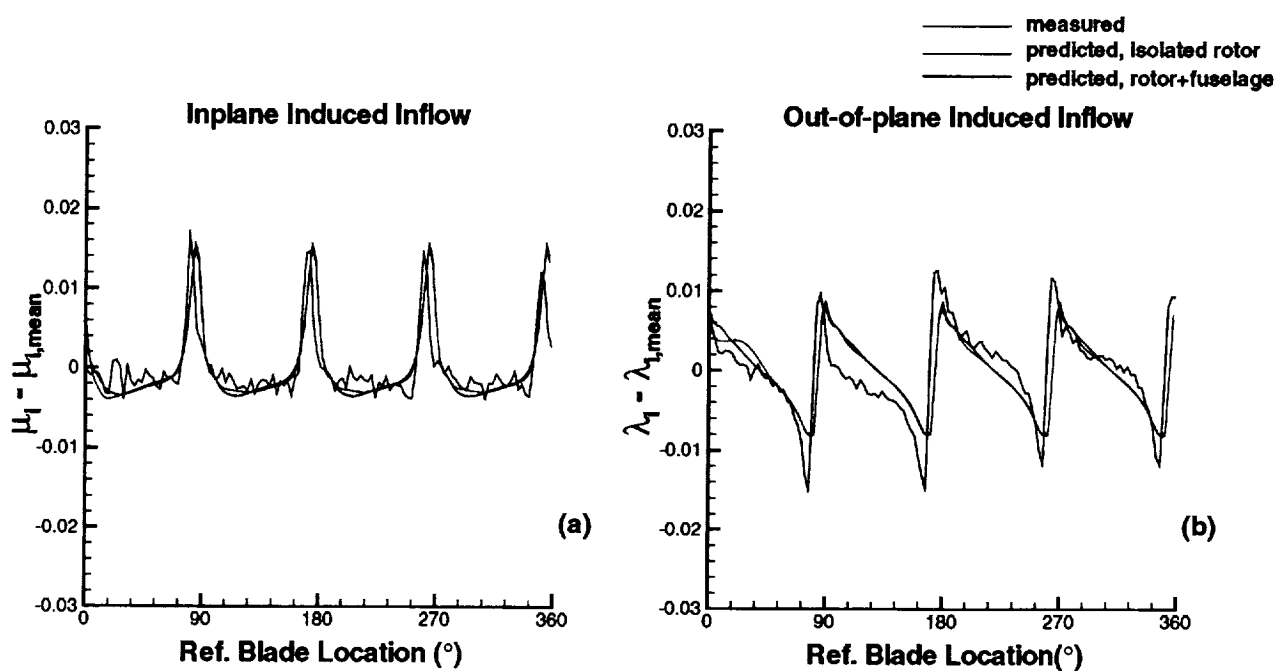
Figure 8.18: Measured and Predicted Induced Inflow in Two Directions for an Isolate Rotor and a Rotor/Fuselage Combination, Iteration 3.
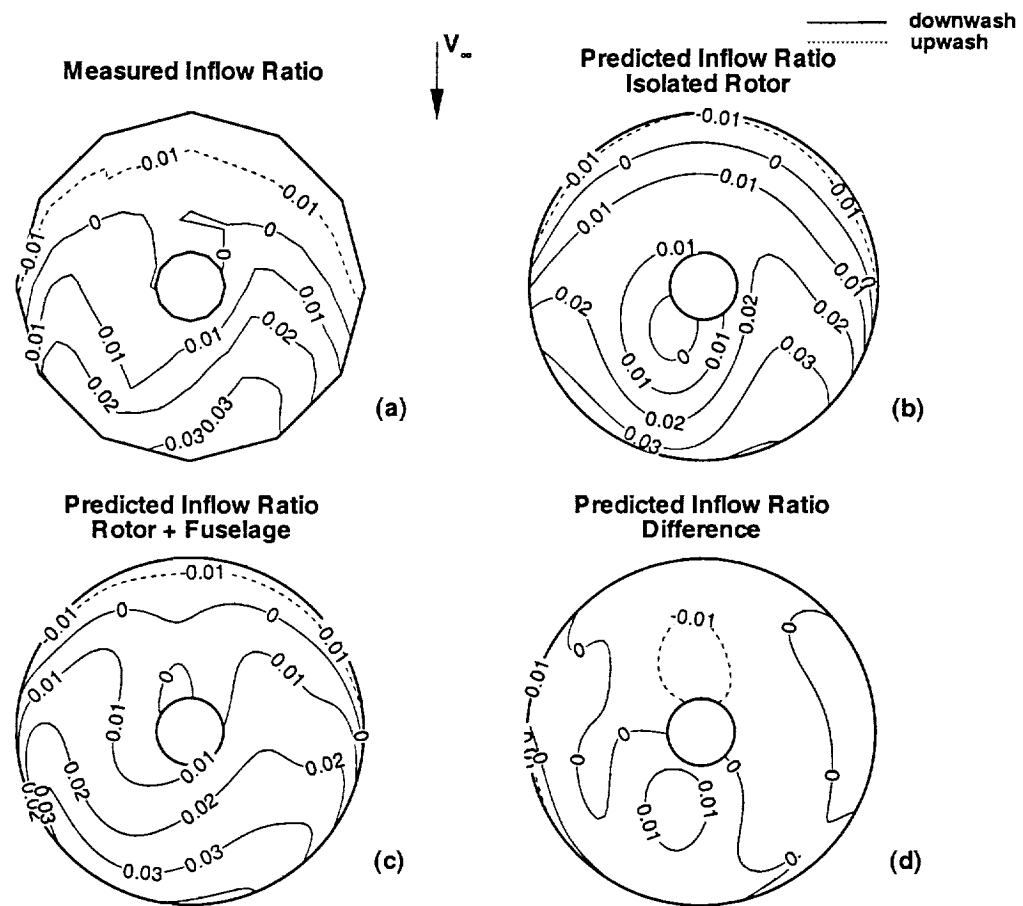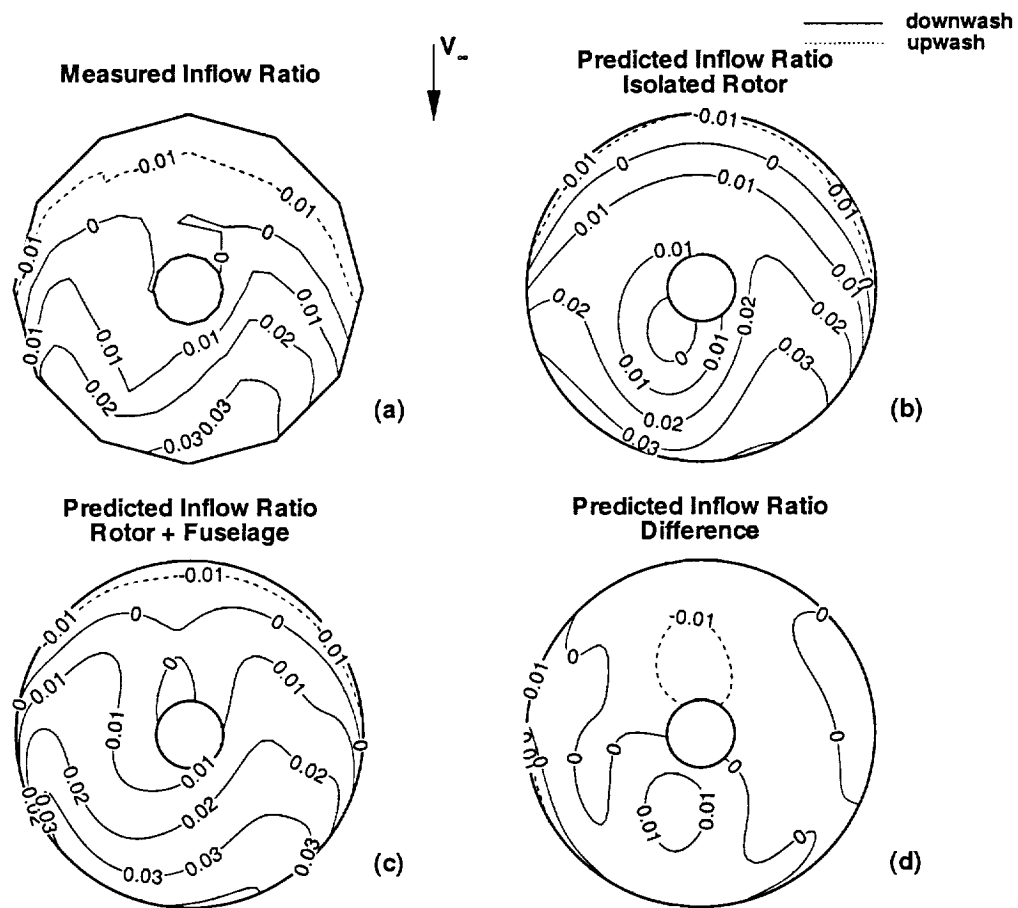
Figure 8.19: Measured and Predicted Time Averaged Induced Inflow Ratio from Time Accurate Computations, Iteration 3.
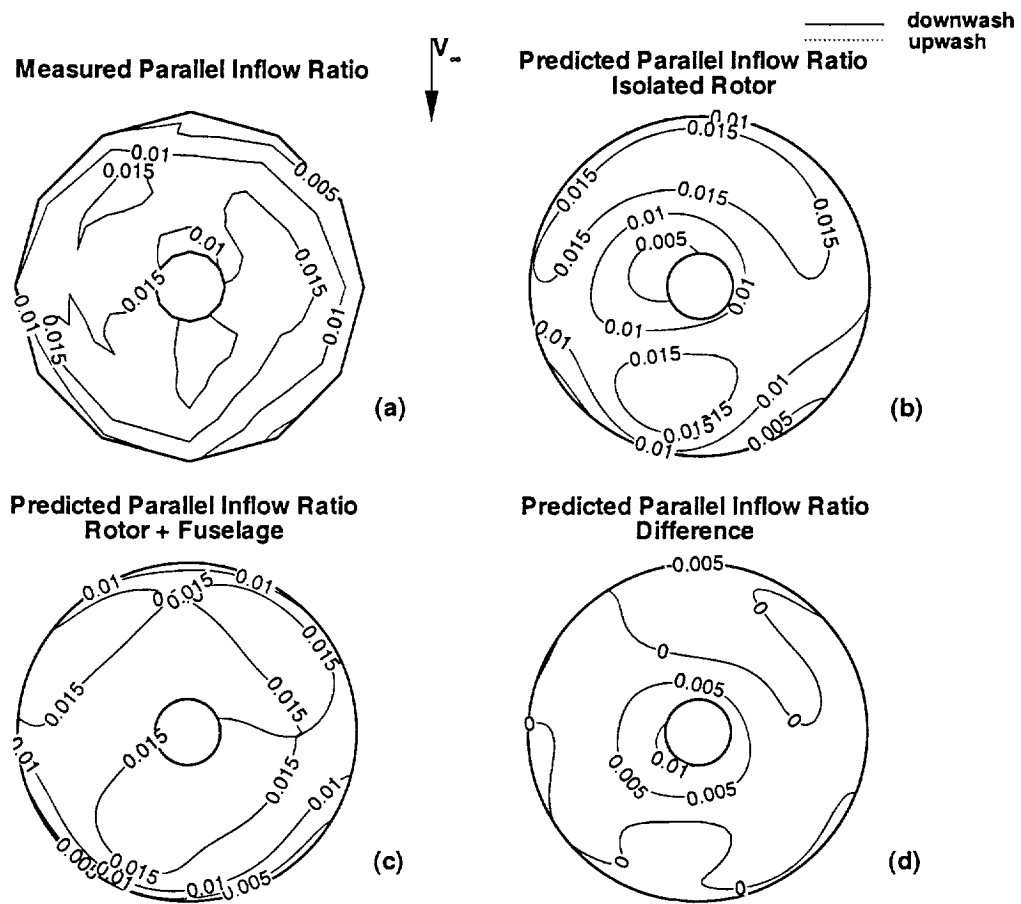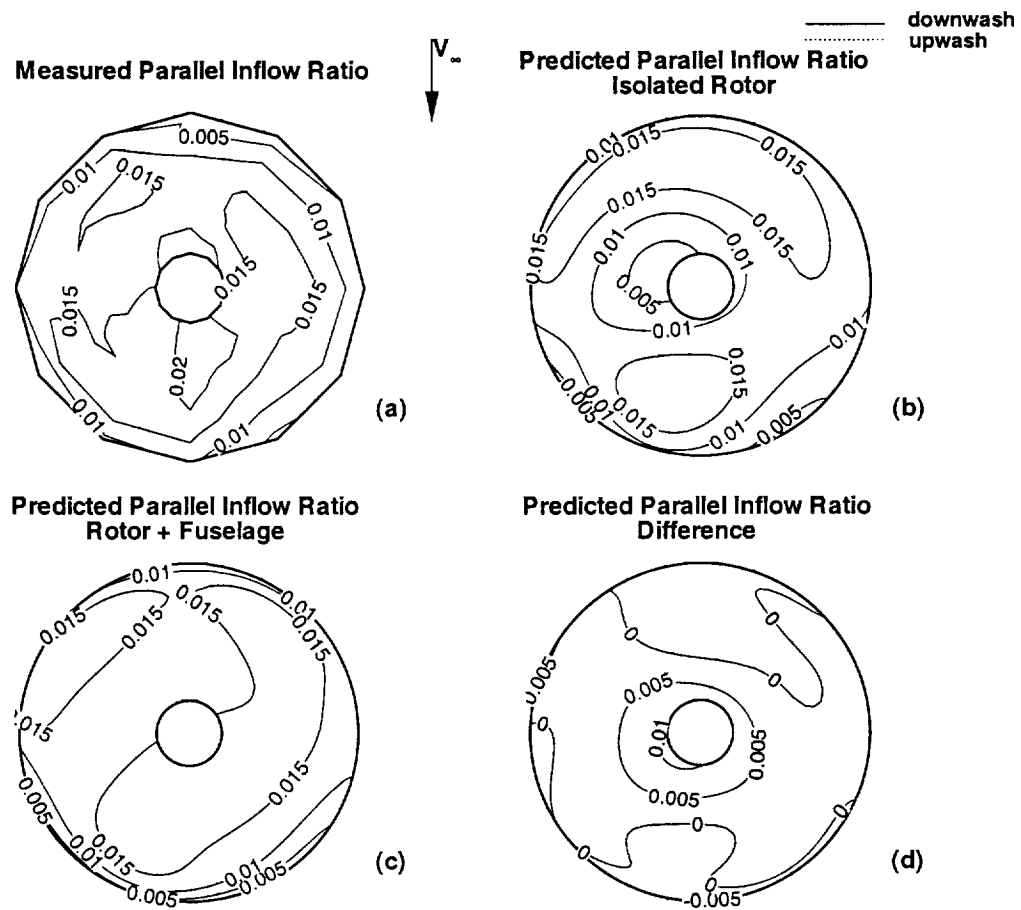
Figure 8.20: Measured and Predicted Time Averaged Parallel Induced Inflow Ratio from Time Accurate Computations, Iteration 3.
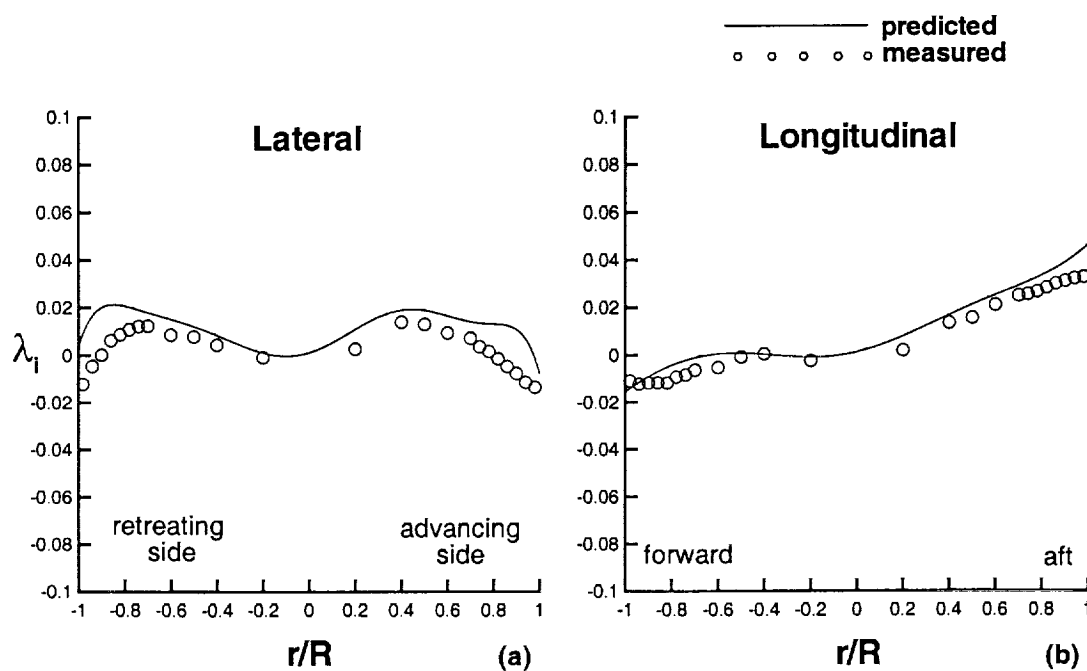
Figure 8.21: Measured and Predicted Lateral and Longitudinal Time Averaged Induced Inflow Ratio from Time Accurate Computations, Iteration 3
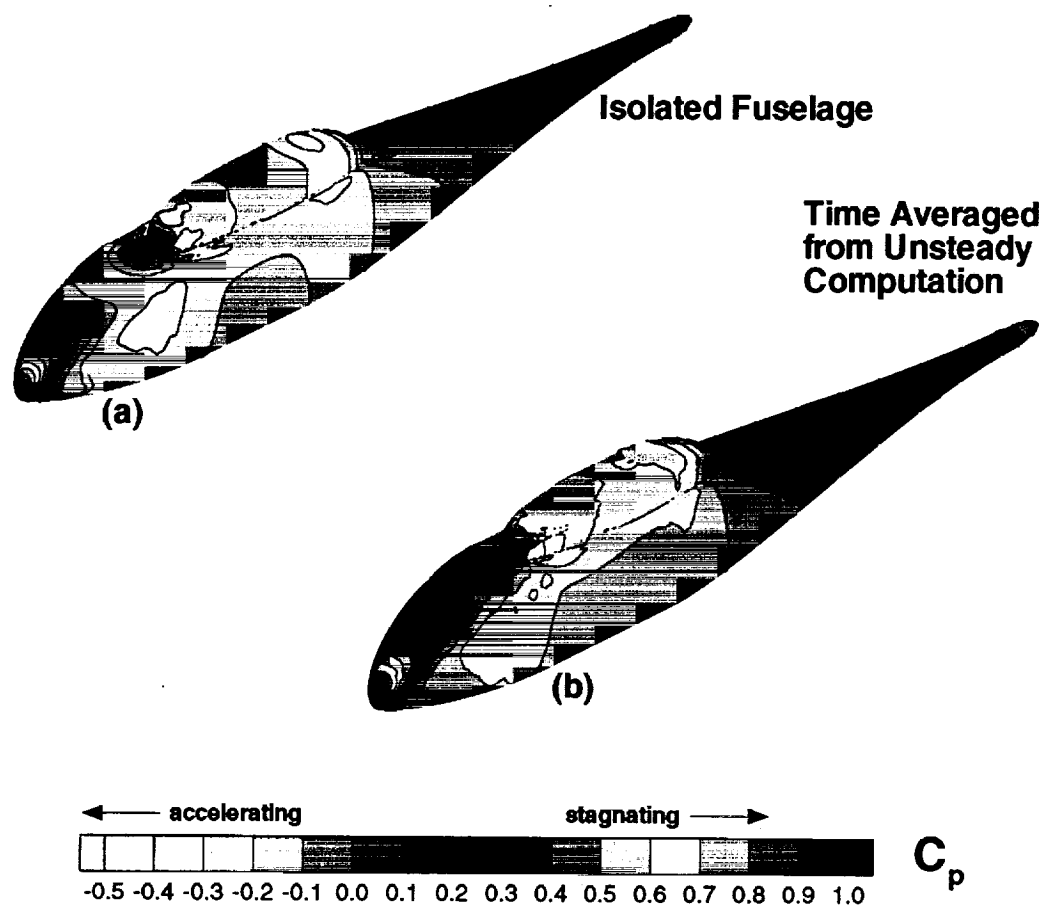
Figure 8.22: Isolated Fuselage and Rotor/Fuselage, Time Averaged Surface Pressure Coefficients

**Top View
Isolated Fuselage**

accelerating ◄───   stagnating ───►

-0.5 -0.4 -0.3 -0.2 -0.1 0.0 0.1 0.2 0.3 0.4 0.5 0.6 0.7 0.8 0.9 1.0 C_p
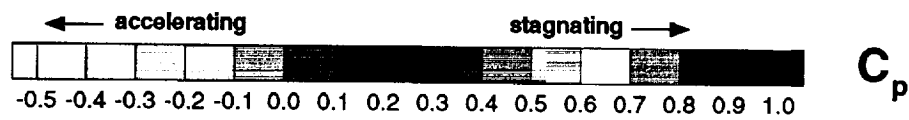
Figure 8.23: Surface Pressure Coefficient on Isolated Fuselage Configuration, Top View

Top View
Time Averaged
from Unsteady
Computation

◄— accelerating   stagnating —►

-0.5 -0.4 -0.3 -0.2 -0.1 0.0 0.1 0.2 0.3 0.4 0.5 0.6 0.7 0.8 0.9 1.0 C_p

Figure 8.24: Time Averaged Surface Pressure Coefficient on Complete Rotor/Fuselage Configuration, Top View
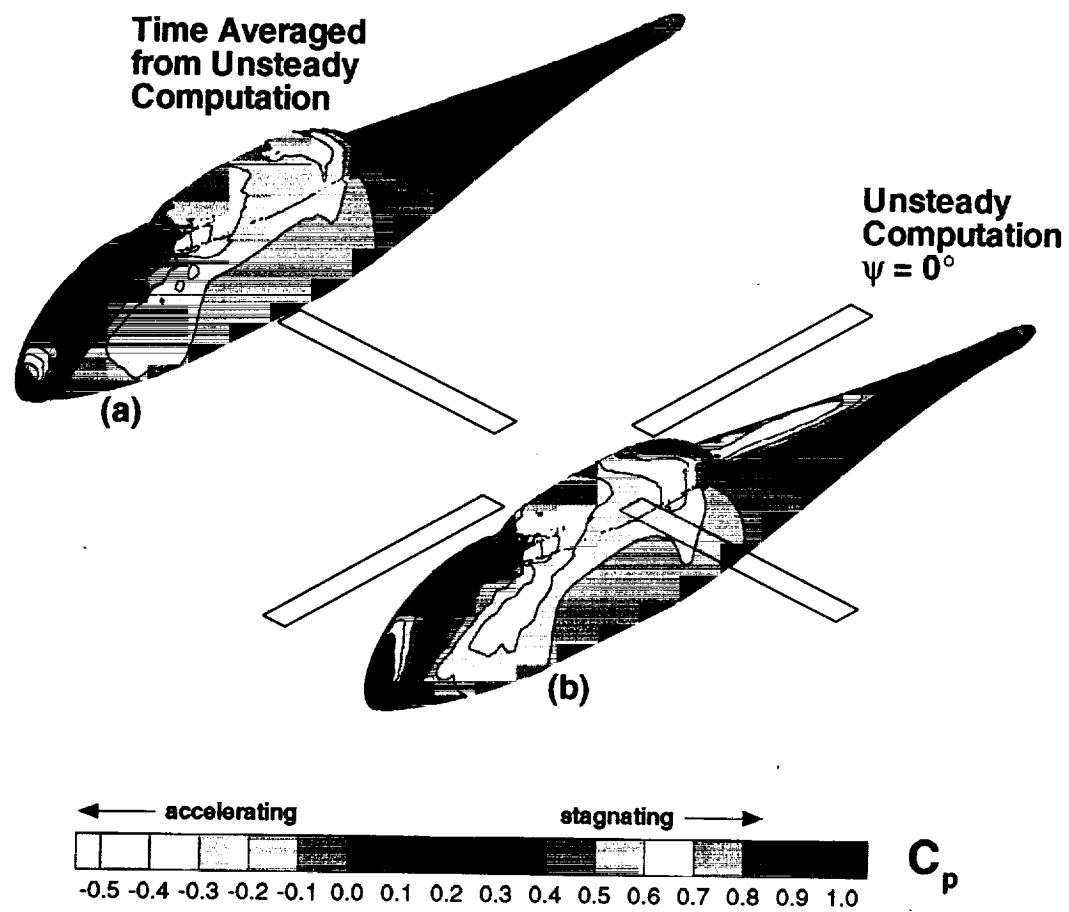
Figure 8.25: Time Averaged and Time Accurate Surface Pressure Coefficients, $\psi = 0°$
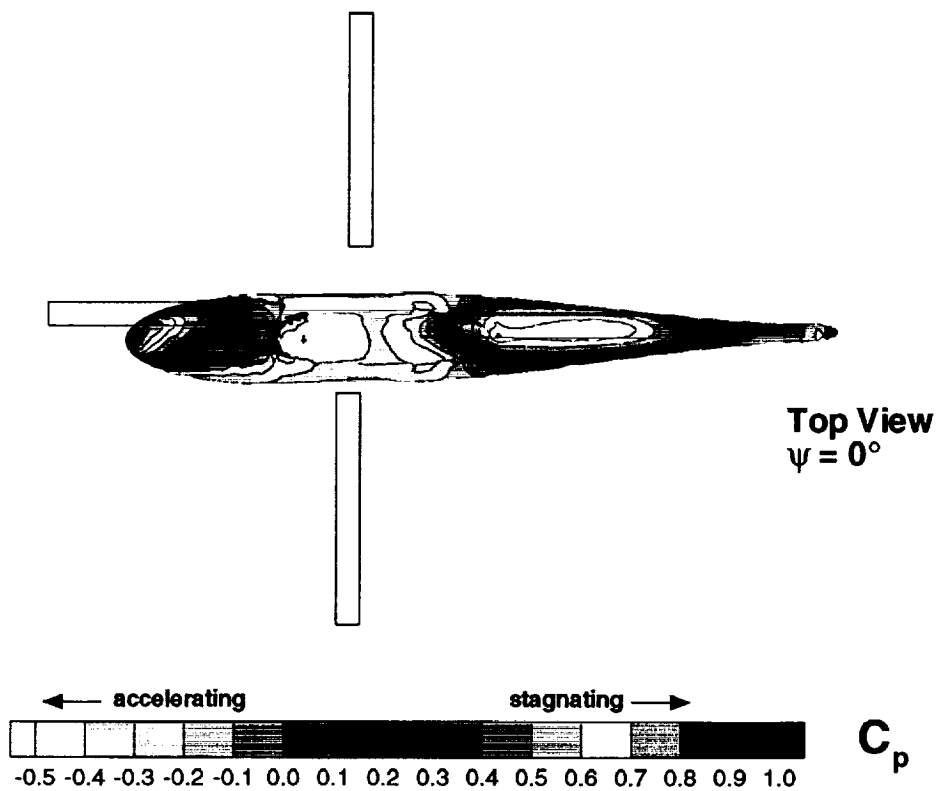
Figure 8.26: Time Accurate Surface Pressure Coefficient on Complete Rotor/Fuselage Configuration, $\psi = 0°$, Top View
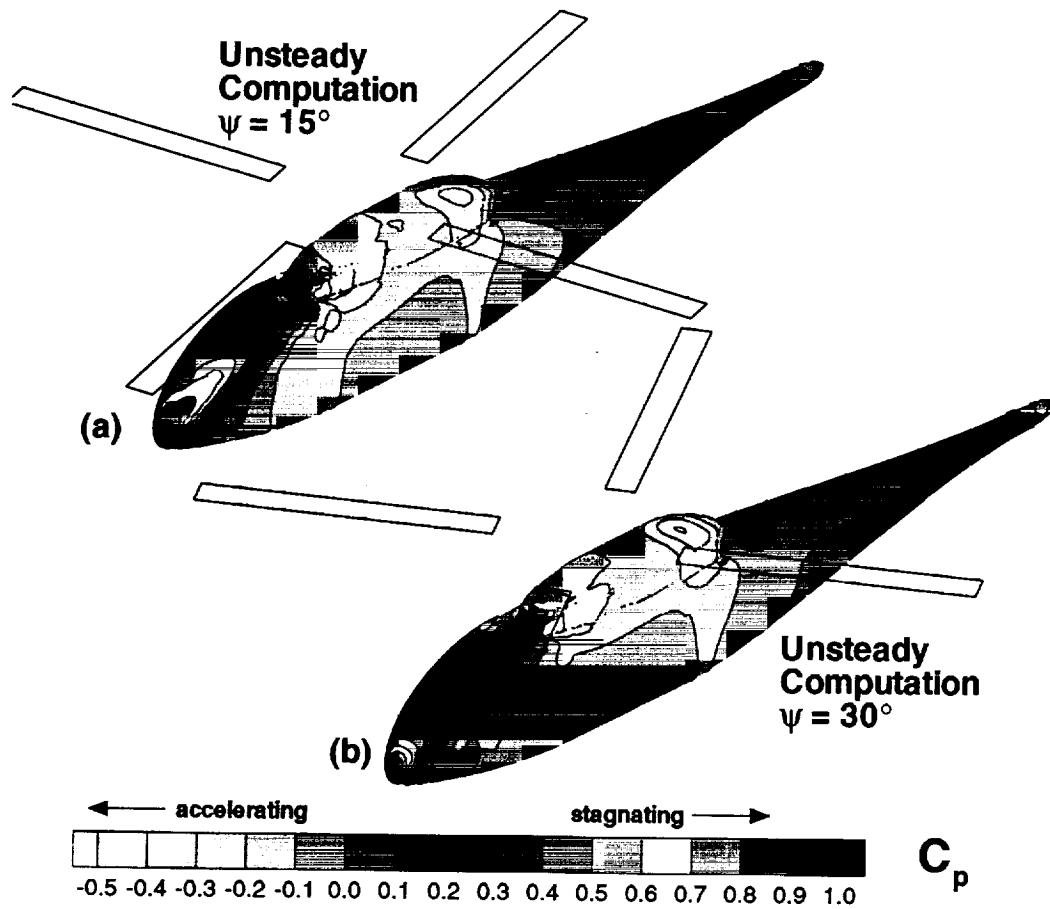
Figure 8.27: Time Accurate Surface Pressure Coefficients at $\psi = 15°$ and $\psi = 30°$
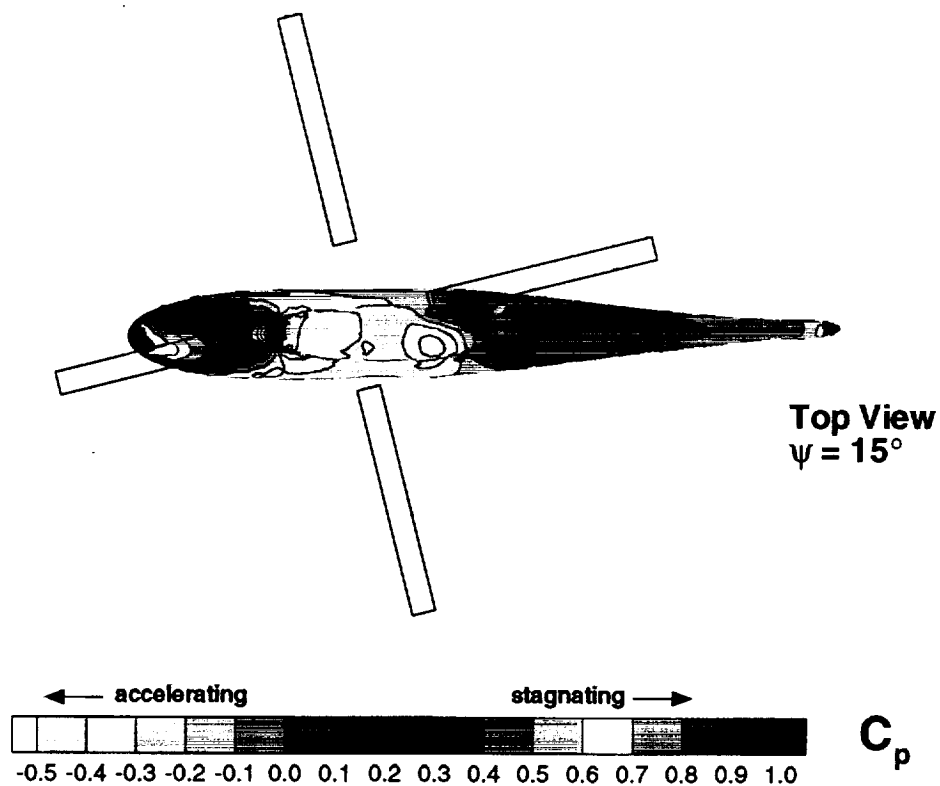
Figure 8.28: Time Accurate Surface Pressure Coefficient on Complete Rotor/Fuselage Configuration, $\psi = 15°$, Top View
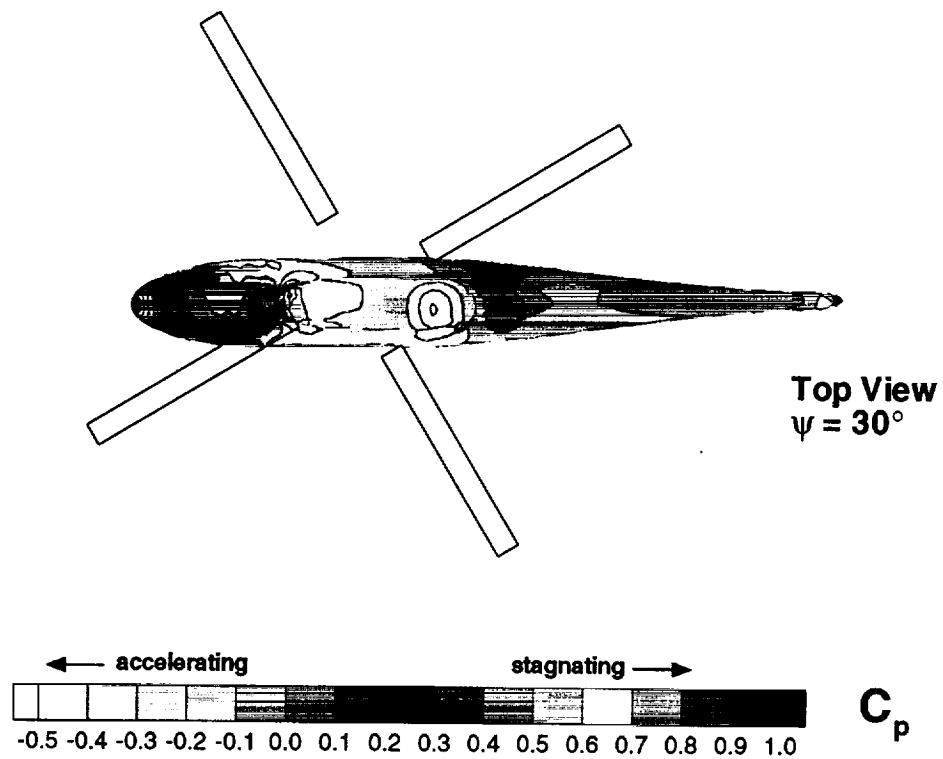
Figure 8.29: Time Accurate Surface Pressure Coefficient on Complete Rotor/Fuselage Configuration, $\psi = 30°$, Top View
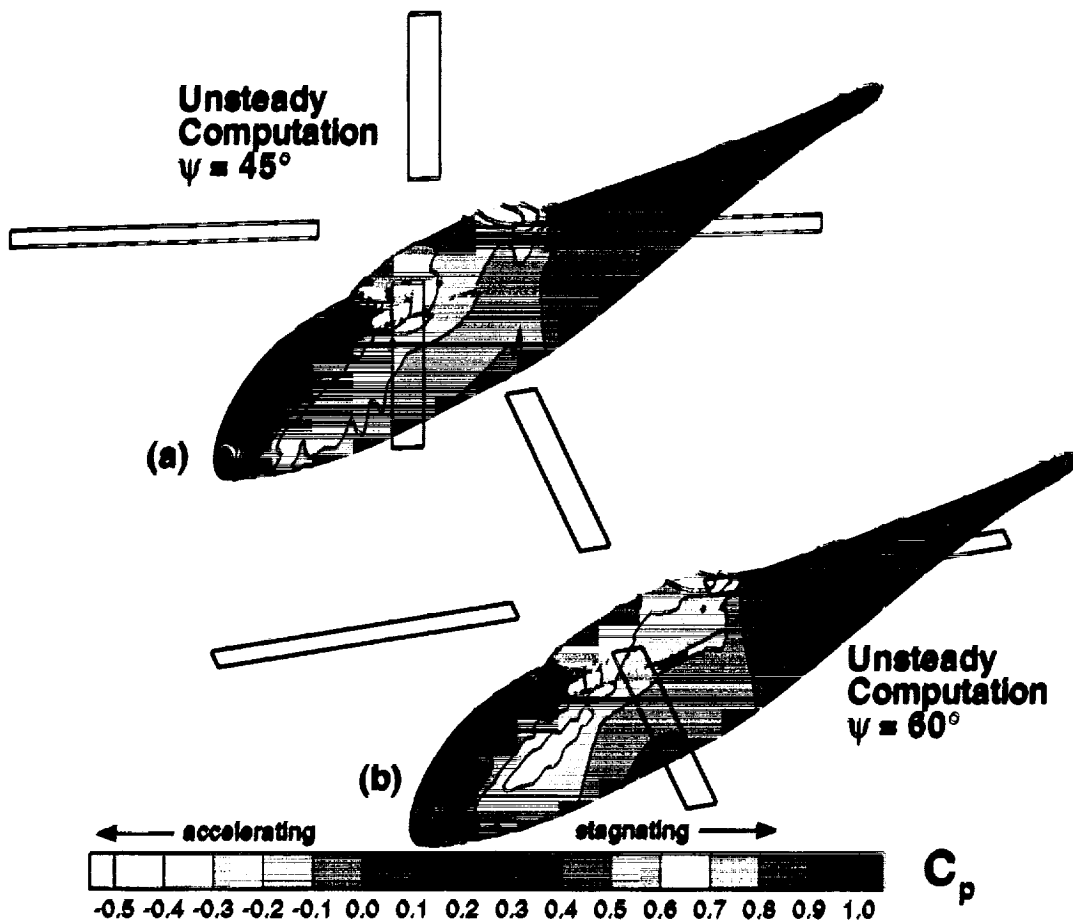
Figure 8.30: Time Accurate Surface Pressure Coefficients at $\psi = 45°$ and $\psi = 60°$
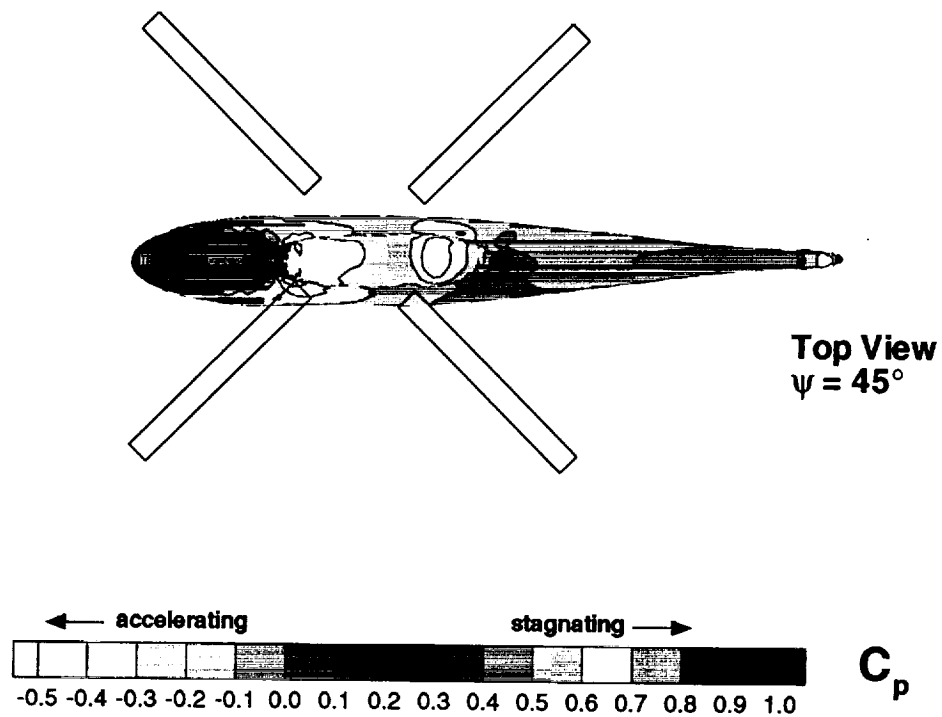
Figure 8.31: Time Accurate Surface Pressure Coefficient on Complete Rotor/Fuselage Configuration, $\psi = 45°$, Top View
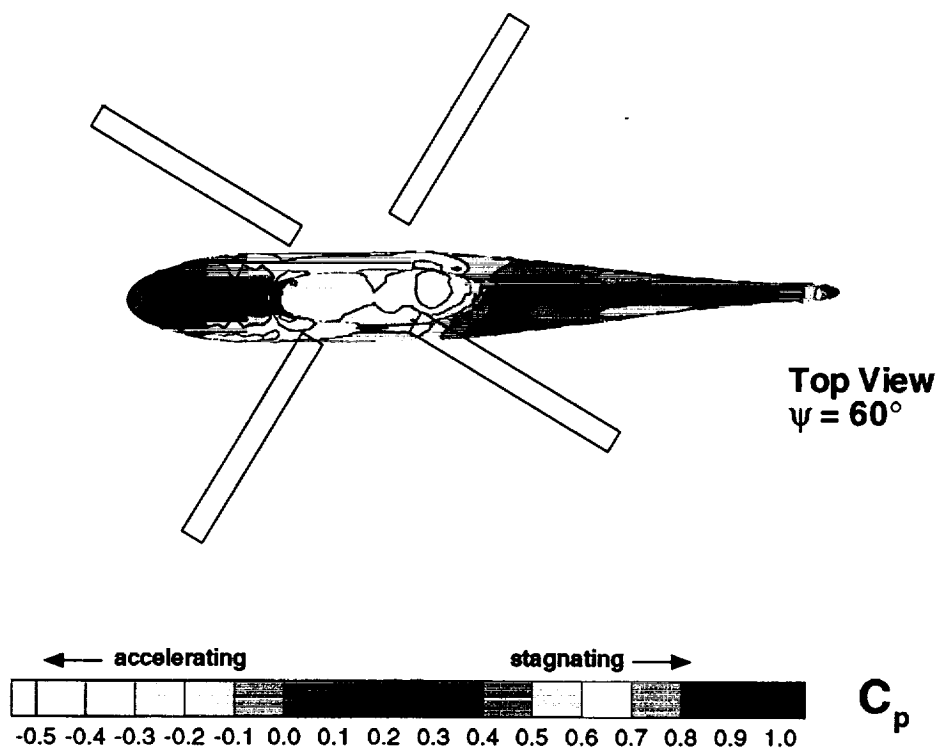
Figure 8.32: Time Accurate Surface Pressure Coefficient on Complete Rotor/Fuselage Configuration, $\psi = 60°$, Top View
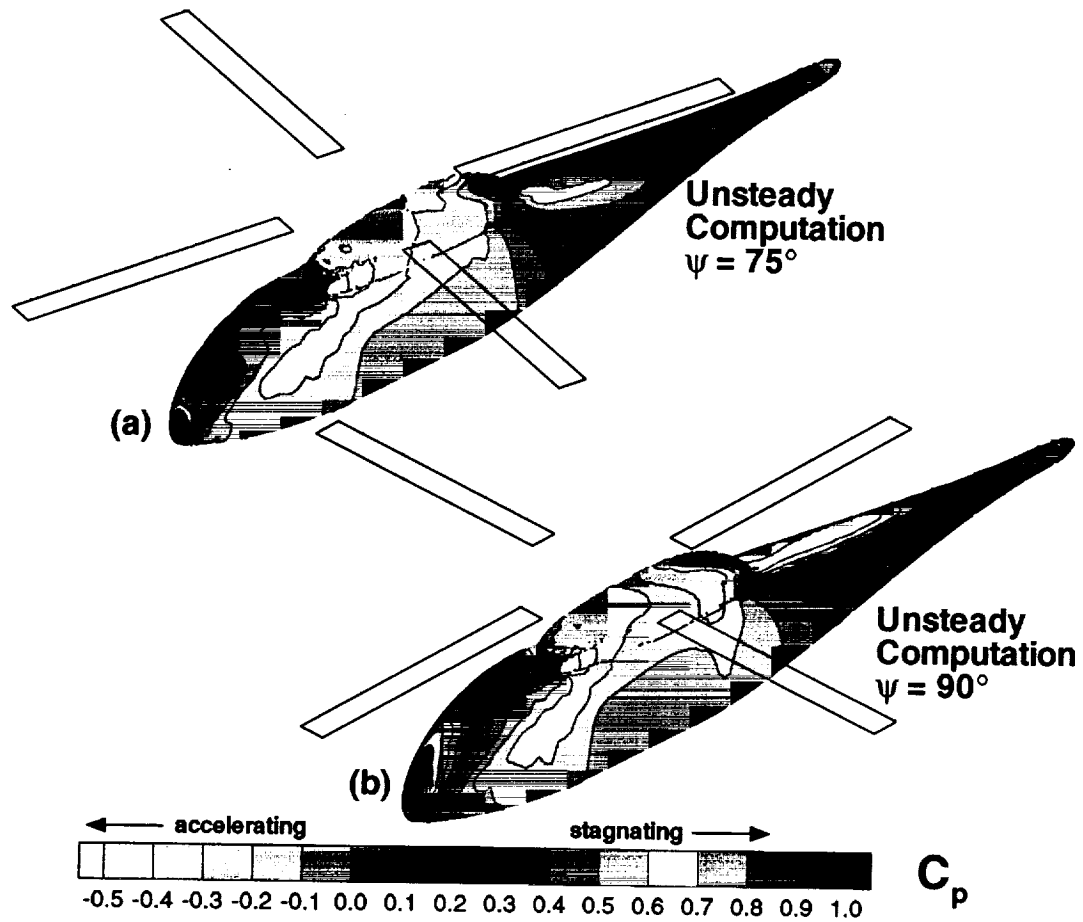
Figure 8.33: Time Accurate Surface Pressure Coefficients at $\psi = 75°$ and $\psi = 90°$

Top View
$\psi = 75°$

accelerating   stagnating

-0.5 -0.4 -0.3 -0.2 -0.1 0.0 0.1 0.2 0.3 0.4 0.5 0.6 0.7 0.8 0.9 1.0 C_p
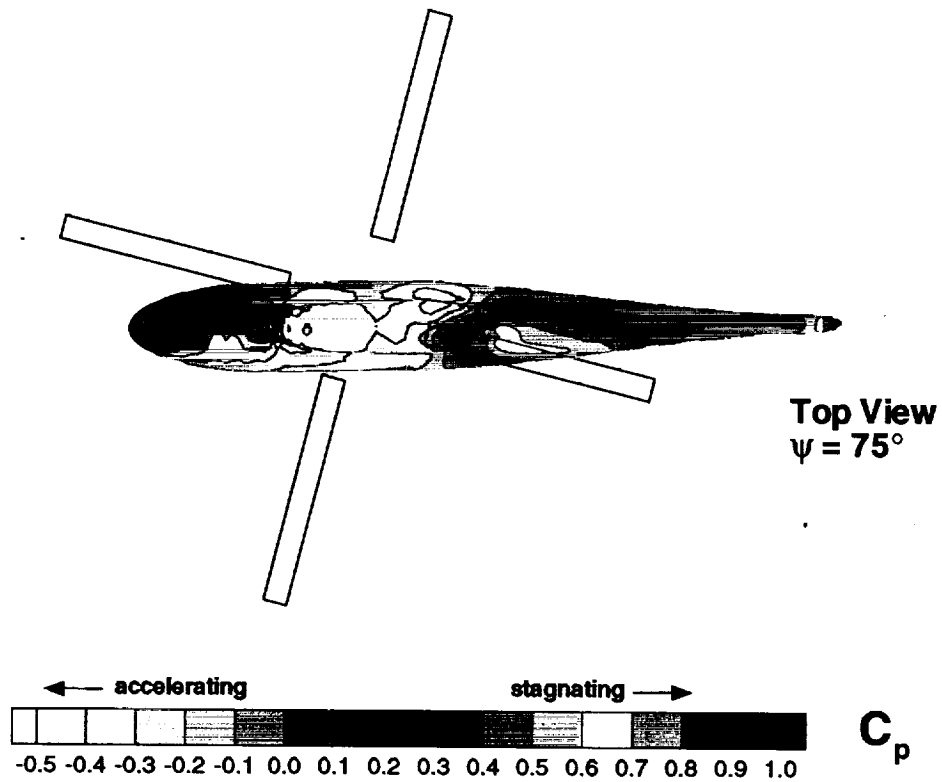
Figure 8.34: Time Accurate Surface Pressure Coefficient on Complete Rotor/Fuselage Configuration, $\psi = 75°$, Top View
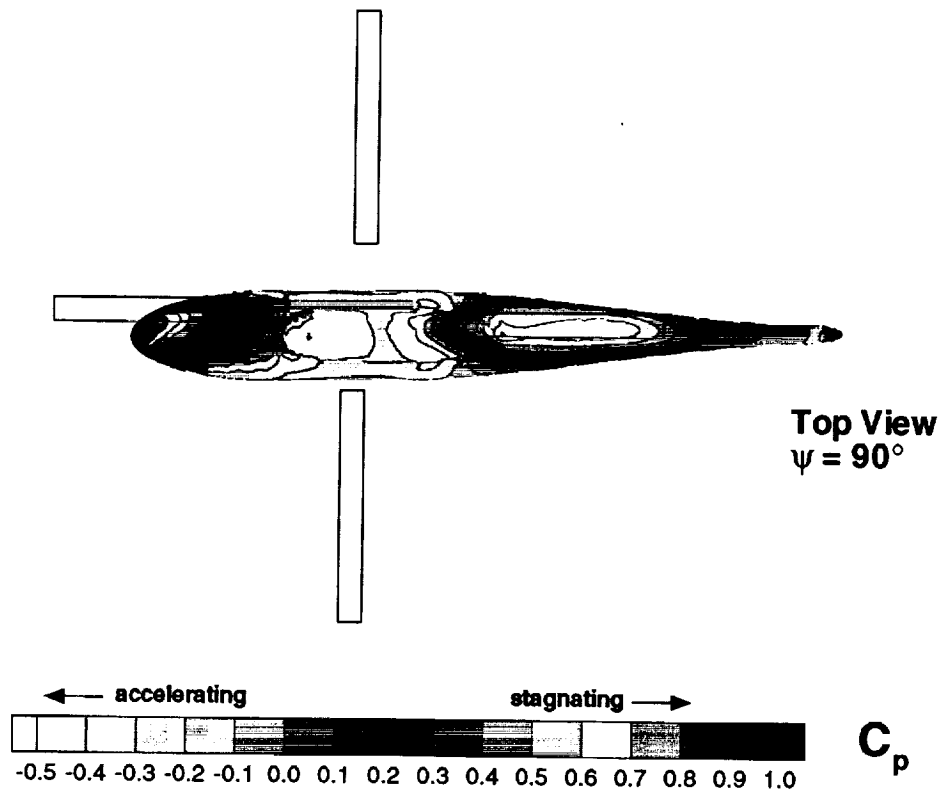
Figure 8.35: Time Accurate Surface Pressure Coefficient on Complete Rotor/Fuselage Configuration, $\psi = 90°$, Top View
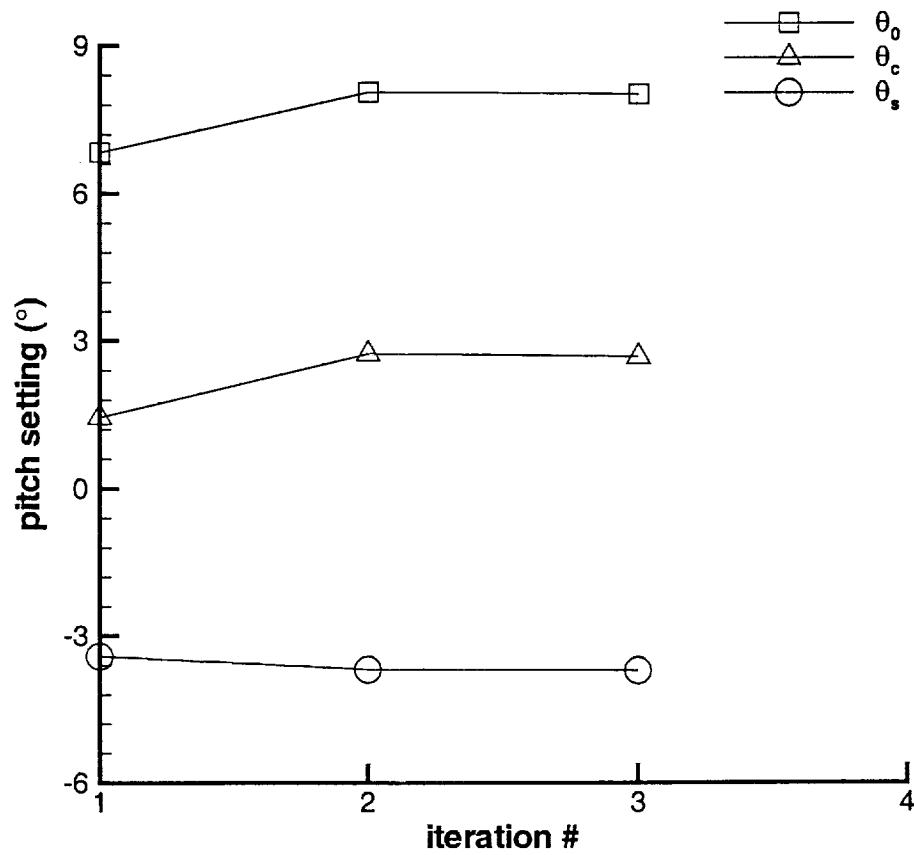
Figure 8.36: Pitch Settings as a Function of Iteration Number

Chapter 9

Summary

In this research, an efficient and accurate, hybrid method, combining a rotor loading model, a rotor/fuselage flowfield model, and a coupling technique, has been developed. This method uses the GDWT for the rotor loading model, OVERFLOW for the rotor/fuselage flowfield model, and a new coupling technique developed in this resear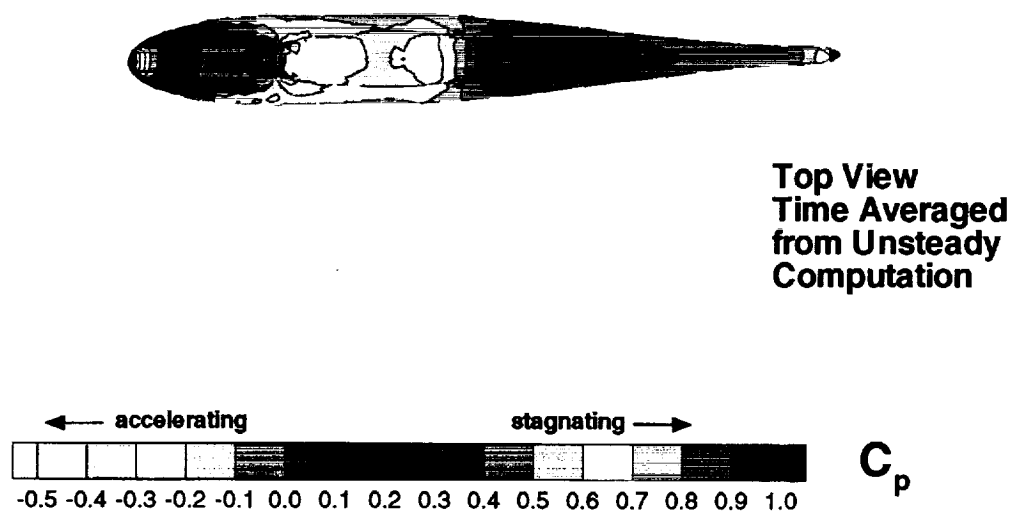ch. The motivations for development of such a model have been discussed and the relationships between the current model and other models in use today have been discussed.

A description of the Rotor Loading Model used for the first component of the model has been presented. In addition, the solution procedures employed in this model have been discussed, along with a validation study of the Rotor Loading Model. In this study, it was shown that predicted time averaged inflow distributions over a rotor disk matched measured time averaged inflow distributions well for a several flight conditions and for several rotor configurations. The sensitivity of the results to parameters (such as the number of azimuth steps and the number of harmonics used) was shown. In addition, predicted time accurate inflow quantities were compared to measured quantities. These comparisons showed that the predictions of the unsteady quantities do not match the experimental values well in waveform, but are comparable in magnitude and phase. It is also noted here that these predictions match well with previously published predictions in the literature for these rotor configurations.

A discussion of the method used for the second component of the current model, the Rotor/Fuselage Flowfield Model was also provided. The method used to solve the Navier-Stokes equations was discussed; theory and implementation of the new time averaged and time accurate boundary conditions is discussed as well. These new rotor boundary conditions are a unique feature of the

current model, and this is the first time this type of condition has been used for such a computation.

A coupling model was developed, which links the Rotor Loading Model and the Rotor/Fuselage Flowfield Models through the time averaged induced inflow of the rotor. This coupling model is a unique feature of the current model. The derivation of a novel inflow filtering technique has been presented also.

Computations which use the model presented in the first several chapters are compared with experimental data. These comparisons include results for an isolated fuselage, an isolated rotor, and a rotor/fuselage configuration. Predictions of the pressure coefficient on the surface of the isolated fuselage were shown to match experimental data well. Predictions of the time average and time accurate inflow above the rotor tip path plane for the isolated rotor configuration were shown also to match experimental data well.

Predictions of time averaged and time accurate inflow velocities above the rotor disk and predictions of unsteady pressure coefficients on the top centerline of the fuselage were shown to match experimental data well. A unique feature of this model is that predictions of the pressure coefficient on the sides of the fuselage match well with measured data. This is a significant accomplishment; previous methods have been unable to match unsteady pressures on the sides of the fuselage.

Bibliography

[1] Sheridan P.F. and R.P. Smith. Interactional Aerodynamics - A New Challenge to Helicopter Technology. Washington, D.C., May 1979. *Proceedings of the 35th Annual American Helicopter Society Forum*, Paper Number A79-49109; Preprint Number 79-59.

[2] W. Johnson. Recent Developments in Rotary-Wing Aerodynamic Theory. *AIAA Journal*, 24(8):1219–1244, August 1986.

[3] T.A. Egolf and P.F. Lorber. An Unsteady Rotor/Fuselage Interactional Method. Arlington, TX, February 25-27, 1987. *Presented at the American Helicopter Society Specialists' Meeting on Aerodynamics and Aeroacoustics.*

[4] D.N. Mavris, S.G. Liou, N.M. Komerath, and H.M. McMahon. Measurement and Computation of the Velocity Field of a Cylinder in the Wake of a Rotor in Forward Flight. Buffalo, NY, June 12-14, 1989. *Presented at the 20th AIAA Fluid Dynamics, Plasma Dynamics, and Lasers Conference*, Paper AIAA-89-1844.

[5] J.D. Berry. *A Method of Computing the Aerodynamic Interactions of a Rotor-Fuselage Configuration in Forward Flight*. PhD thesis, Georgia Institute of Technology, Atlanta, GA, May 1990.

[6] T.R. Quackenbush, C-M.G. Lam, D.B. Bliss, and A. Katz. Computational Methods for the Analysis of Rotor Wake/Airframe Interactions. C.D.I. Report No. 91-02, 1991.

[7] G.L. Crouse, Jr. *An Analytical Study of Unsteady Rotor/Fuselage Interaction in Hover and Forward Flight*. PhD thesis, University of Maryland, College Park, MD, November 1992.

[8] D.D. Boyd, Jr., T.F. Brooks, C.L. Burley, and J.R. Jolly, Jr. Aeroacoustic Codes for Rotor Harmonic and BVI Noise - Camrad.Mod1/HIRES: Methodology and Users' Manual. NASA TM 207640, 1998.

[9] C.S. Chen and J.O. Bridgeman. Three-Dimensional Viscous Rotor Flow Calculations Using Boundary Layer Equations. Amsterdam, Netherlands, September 12-15, 1989. *Presented at the 15th European Rotorcraft Forum*, Paper Nr.:13.

[10] J.O. Bridgeman, D.S. Prichard, and F.X. Caradonna. The Development of a CFD Potential Method for the Analysis of Tilt-Rotors. In *Presented at the AHS Technical Specialists Meeting on Rotorcraft Acoustics and Fluid Dynamics*, Philadelphia, PA, October 15-17, 1991.

[11] R.C. Strawn. Wing-Tip Vortex Calculations with an Unstructured Adaptive-Grid Euler Solver. In *Proceedings of the 47th Annual American Helicopter Society Forum*, pages 65–76, Pheonix, AZ, May 1991.

[12] T.J. Barth. A 3-D Upwind Euler Solver for Unstructured Meshes. Honolulu, HI, June 1991. Paper AIAA-91-1548.

[13] R.C. Strawn and T.J. Barth. A Finite-Volume Euler Solver for Computing Rotary-Wing Aerodynamics on Unstructured Meshes. In *Proceedings of the 48th Annual American Helicopter Society Forum*, pages 419–428, Washington, D.C., June 1992.

[14] L.A.J. Zori and R.G. Rajagopolan. Navier-Stokes Calculations of Rotor-Airframe Interaction in Forward Flight. pages 489–512, Washington, D.C., June 1992. *Proceedings of the 48th Annual American Helicopter Society Forum*.

[15] R.G. Rajagopolan and Z. Zhaoxing. Performance and Flow Field of a Ducted Propellor. Monterey, CA, July 10-12, 1989. *Presented at the AIAA/ASME/SAE/ASEE 25th Joint Propulsion Conference*, Paper AIAA-89-2673.

[16] R.G. Rajagopolan and S.J. Mathur. Three Dimensional Analysis of a Rotor in Forward Flight. *Journal of the American Helicopter Society*, pages 14–25, July 1993.

[17] M.S. Chaffin and J.D. Berry. Navier-Stokes Simulation of a Rotor Using a Distributed Pressure Disk Method. In *Proceedings of the 51st Annual American Helicopter Society Forum*, volume I, pages 112–136, Ft. Worth, TX, May 1995.

[18] J.D. Berry, V.B. Letnikov, I. Bavykina, and M.S. Chaffin. A Comparison of Interactional Aerodynamics Methods for a Helicopter in Low Speed Forward Flight. In *Proceedings of the 23rd European Rotorcraft Forum*, volume I, pages 33.1–33.9, Dresden, Germany, September 16-18, 1997.

[19] R. Meakin. Moving Body Overset Grid Methods for Complete Aircraft Tiltrotor Simulations. Orlando, FL, June 6-9, 1993. *Presented at the 11th AIAA Computational Fluid Dynamics Conference*, Paper AIAA-93-3350.

[20] G.R. Srinivisan and J.U. Ahmad. Navier-Stokes Simulation of Rotor-Body Flowfield in Hover Using Overset Grids. Cernobbio, France, September 14-16, 1993. *Presented at the 19th European Rotorcraft Forum*, Paper No. C15.

[21] J. Ahmad and Earl P.N. Duque. Helicopter Rotor Blade Computation in Unsteady Flows Using Moving Embedded Grids. In *12th AIAA Applied Aerodynamics Conference*, Colorado Springs, CO, June 20-22, 1994. Paper AIAA-94-1922.

[22] L. Tang and J.D. Baeder. Time-Accurate Euler Simulations of Vortex Convection. In *Proceedings of the 52th Annual American Helicopter Society Forum*, pages 1489–1499, Washington, D.C., June 4-6 1996.

[23] J. Steinhoff, W. Yonghu, T. Mersch, and H. Senge. Computational Vorticity Capturing: Application to Helicopter Rotor Flow. In *30th Aerospace Sciences Meeting and Exibit*, Reno, NV, January 6-9, 1992. Paper AIAA-92-0056.

[24] D.D. Boyd, Jr. and R.W. Barnwell. Rotor-Fuselage Interactional Aerodynamics: An Unsteady Rotor Model. In *Proceedings of the 54th Annual American Helicopter Society Forum*, volume I, pages 23–44, Washington, D.C., May 20-22, 1998.

[25] D.A. Peters and C.J. He. Correlation of Measured Induced Velocities with a Finite-State Wake Model. pages 533–550, Boston, MA, May 1989. *Proceedings of the 45th Annual American Helicopter Society Forum*.

[26] D.A. Peters, D.D. Boyd, Jr., and C.J. He. Finite State Induced Inflow Model for Rotors in Hover and Forward Flight. pages 839–866, St. Louis, MO, May 18-20, 1987. *Proceedings of the 43rd Annual American Helicopter Society Forum*.

[27] C.J. He. *Development and Application of a Generalized Dynamic Wake Theory For Lifting Rotors*. PhD thesis, Georgia Institute of Technology, Atlanta, GA, July 1989.

[28] D.A. Peters and C.J. He. Finite State Induced Inflow Models Part II: Three Dimensional Rotor Disk. *Journal of Aircraft*, Volume 32((2)):323–333, March-April 1995.

[29] P.G. Buning, D.C. Jespersen, T.H. Pulliam, W.M. Chan, J.P. Slotnick, S.E. Krist, and K.J. Renze. OVERFLOW User's Manual: Version 1.8, February 23 1998.

[30] W. Kinner. The Potential Theory of Airfoils of Circular Planform. *Ingenieur-Archiv*, 8(1):47–80, February 1937.

[31] C. Hirsch. *Numerical Computation of Internal and External Flows. Volume 2: Computational Methods for Inviscid and Viscous Flows*. John Wiley and Sons, 1990.

[32] W. Johnson. A Comprehensive Analytical Model of Rotorcraft Aerodynamics and Dynamics. Part I: Analytical Development. NASA TM 81182, June 1980.

[33] J.W. Elliot, S.L. Althoff, and R.H. Sailey. Inflow Measurement Made With a Laser Velocimeter on a Helicopter Model in Forward Flight - Volume I: Rectangular Planform Blades at an Advance Ratio of 0.15. NASA TM 100541, April 1988.

[34] J.W. Elliot, S.L. Althoff, and R.H. Sailey. Inflow Measurement Made With a Laser Velocimeter on a Helicopter Model in Forward Flight - Volume II: Rectangular Planform Blades at an Advance Ratio of 0.23. NASA TM 100542, April 1988.

[35] S.L. Althoff, J.W. Elliot, and R.H. Sailey. Inflow Measurement Made With a Laser Velocimeter on a Helicopter Model in Forward Flight - Volume IV: Tapered Planform Blades at an Advance Ratio of 0.15. NASA TM 100544, April 1988.

[36] S.L. Althoff, J.W. Elliot, and R.H. Sailey. Inflow Measurement Made With a Laser Velocimeter on a Helicopter Model in Forward Flight - Volume V: Tapered Planform Blades at an Advance Ratio of 0.23. NASA TM 100545, April 1988.

[37] C.E. Freeman and R.E. Mineck. Fuselage Surface Pressure Measurements of a Helicopter Wind-Tunnel Model With a 3.15-Meter Diameter Single Rotor. NASA TM 80051, March 1979.

[38] J.A. Benek, P.G. Buning, and J.L. Steger. A 3-D Chimera Grid Embedding Technique. Cincinnati, OH, July 15-17, 1985. Paper AIAA-85-1523-CP.

[39] T.H. Pulliam and D.S. Chaussee. A Diagonal Form of an Implicit Approximate Factorization Algorithm. *Journal of Computational Physics*, 39, 1981.

[40] R.M. Beam and R.F. Warming. An Implicit Finite-Difference Algorithm for Hyperbolic System in Conservation Law Form. *Journal of Computational Physics*, 22:87–109, 1976.

[41] M. Kandula and P.G. Buning. Implementation of LU-SGS Algorithm and Roe Upwinding Scheme in OVERFLOW Thin-Layer Navier-Stokes Code. In *25th AIAA Fluid Dynamics Conference*, Colorado Springs, CO, June 20-23, 1994. Paper AIAA-94-2357.

[42] D. Jespersen, T.H. Pulliam, and P.G. Buning. Recent Enhancements to OVERFLOW. 1997. Paper AIAA-97-0644.

[43] T.H. Pulliam. Time Accuracy and the use of Implicit Methods. 1993. Paper AIAA-93-3360-CP.

[44] M.S. Chaffin and J.D. Berry. Navier-Stokes and Potential Theory Solutions for a Helicopter Fuselage and Comparison With Experiment. NASA TM 4566, June 1994.

[45] J.D. Berry, M.S. Chaffin, and E.P.N. Duque. Helicopter Fuselage Aerodynamic Predictions: Navier-Stokes and Panel Method Solutions and Comparison With Experiment. San Francisco, CA, January 19-21, 1994. *Presented at the 1994 Annual American Helicopter Society Aeromechanics Specialist Conference.*

[46] N.E. Suhs and R.W. Tramel. PEGSUS 4.0 User's Manual, 1991.

[47] W.M. Chan. Innovative Software Streamlines Overset Grid Generation. volume 3, NAS Systems Division, Ames Research Center, Mail Stop 258-6, Moffett Field, California, 94035-1000, May-June 1998. NAS News.

[48] J.P. Steinbrenner, J.R. Chawner, and C.L. Fouts. The GRIDGEN 3D Multiple Block Grid Generation System. WRDC-TR-90-3022, October 1989. Wright Research and Development Center Report.

[49] S.J. Alter and K.J. Weilmuenster. The Three-Dimensional Multi-Block Advanced Grid Generation System (3DMAGGS). NASA TM 108985, May 1993.

[50] S.J. Alter. The Volume Grid Manipulator (VGM): A Grid Reusability Tool. NASA CR 4772, April 1997.

[51] W.M. Chan and P.G. Buning. User's Manual for FOMOCO Utilities - Force and Moment Computation Tools for Overset Grids. NASA TM 110408, July 1996.

[52] J.F. Meyers, S.A. Gorton, and J.D. Berry. Instantaneous Doppler Global Velocimetry Measurements of a Rotor Wake: Lessons Learned. Lisbon, Portugal, July 13-16, 1998. *Presented at the 9th International Symposium on Applications of Laser Techniques to Fluid Mechanics.*

[53] G.A. Fleming and S.A. Gorton. Measurement of Rotorcraft Blade Deformation using Projection Moiré Interferometry. Ancona, Italy, June 6-19, 1998. *Presented at the 3rd International Conference on Vibration Measurements by Laser Techniques.*

[54] A. Gessow and G.C. Myers, Jr. *Aerodynamics of the Helicopter.* Fredrick Ungar Publishing, Co., New York, NY, 1952.

Appendix A

Filtering Operation

A consistent filtering operation can be derived from the GDWT. This appendix gives a derivation of the filtering operation, derived using various functions introduced in the GDWT development of reference [28]. This operation takes a quantity, $\Lambda(\bar{r}, \psi)$, which is a function of the radial and azimuthal coordinate, and derives the expressions for coefficients of an infinite series given below. The $\Lambda(\bar{r}, \psi)$ quantity is then filtered by truncating the infinite series to a finite number of harmonics and shape functions.

Starting with a given quantity that is a function of the radial and azimuthal coordinates, one can express that quantity as a double summation over the harmonics and shape functions in the GDWT as follows:

$$\Lambda(\bar{r}, \psi) = \sum_m^\infty \sum_n^\infty \bar{\phi}_n^m(\bar{r}) \left[a_n^m \cos(m\psi) + b_n^m \sin(m\psi) \right] \tag{A.1}$$

where Λ is the given function, m is the harmonic number ($m = 0, 1, 2\ldots$), n is the shape function number ($n = m+1, m+3, \ldots$), $\bar{r}$ and ψ are the radial and azimuthal coordinates, $\bar{\phi}_n^m$ is a function of $\bar{r}$ from the GDWT, and a_n^m and b_n^m are the unknown coefficients. These coefficients could be, in general, a function of time. In that case, the process outlined below would be followed at each discrete time step of interest.

Multiply equation (A.1) by $\cos(p\psi)$ and integrate over ψ from 0 to 2π to get the following:

$$\int_0^{2\pi} \Lambda(\bar{r}, \psi) \cos(p\psi)\, d\psi$$

$$= \sum_m^\infty \sum_n^\infty \bar{\phi}_n^m(\bar{r}) [a_n^m \int_0^{2\pi} \cos(m\psi) \cos(p\psi)\, d\psi$$

$$+ b_n^m \int_0^{2\pi} \sin(m\psi) \cos(p\psi)\, d\psi] \tag{A.2}$$

Using the orthogonality relations for sine and cosine functions, the right hand side of equation (A.2) can be rewritten. The resulting form of equation (A.2) can be written as follows:

$$\int_0^{2\pi} \Lambda(\bar{r}, \psi) \cos(p\psi)\, d\psi = \sum_m^\infty \sum_n^\infty \bar{\phi}_n^m(\bar{r}) a_n^m [\bar{c}(m) \delta_{mp}]$$

$$= \sum_n^\infty \bar{\phi}_n^p(\bar{r}) a_n^p \bar{c}(p) \tag{A.3}$$

where $m = 0, 1, 2, \ldots, \infty$, for both equations above, and $n = m+1, m+3, \ldots, \infty$, for the first equation of (A.3) and $n = p+1, p+3, \ldots, \infty$, for the second equation of (A.3). Also, δ_{mp} is the Dirac delta function. The function $\bar{c}(p)$ is given as follows:

$$\bar{c}(p) = \begin{cases} \pi & for \quad p \neq 0 \\ 2\pi & for \quad p = 0 \end{cases} \tag{A.4}$$

Multiplying equation (A.3) by $[\bar{\phi}_q^p(\bar{r}) \cdot \bar{r} \cdot \sqrt{1 - \bar{r}^2}]$ and integrating from $\bar{r} = 0$ to $\bar{r} = 1$ gives the following:

$$\int_0^1 \bar{\phi}_q^p(\bar{r}) \bar{r} \sqrt{1 - \bar{r}^2} \left[\int_0^{2\pi} \Lambda(\bar{r}, \psi) \cos(p\psi)\, d\psi \right] d\bar{r} = \sum_n^\infty \overbrace{\left[\int_0^1 \bar{\phi}_n^p(\bar{r}) \bar{\phi}_q^p(\bar{r}) \bar{r} \sqrt{1 - \bar{r}^2}\, d\bar{r} \right]}^{\textit{Integral A}} a_n^p \bar{c}(p)$$

$$\tag{A.5}$$

Into "Integral A", substitute the definition of $\bar{\phi}$ in terms of Legendre functions, and perform a change of variables from $\bar{r}$ to v using the fact that $v = \sqrt{1 - \bar{r}^2}$. The resulting "Integral A" component of the above equations becomes:

$$\int_0^1 \bar{\phi}_n^p(\bar{r}) \bar{\phi}_q^p(\bar{r}) \bar{r} \sqrt{1 - \bar{r}^2} \, d\bar{r}$$

$$= \int_0^1 \frac{\bar{P}_n^p(\nu)}{\nu} \frac{\bar{P}_q^p(\nu)}{\nu} \frac{\nu^2}{4} \sqrt{\frac{\pi}{H_n^p}} \sqrt{\frac{\pi}{H_q^p}} \, d\nu$$

$$= \frac{\pi}{4\sqrt{H_n^p H_q^p}} \int_0^1 \bar{P}_n^p(\nu) \bar{P}_q^p(\nu) \, d\nu$$

$$= \frac{\pi}{4\sqrt{H_n^p H_q^p}} \delta_{mp} \tag{A.6}$$

where H_n^m is defined in the GDWT as follows:

$$H_n^m = \frac{(n+m-1)!!(n-m-1)!!}{(n+m)!!(n-m)!!} \tag{A.7}$$

where the double factorial is defined in Peters, *et al.* [26], as follows:

$$(n)!! = \begin{cases} (n)(n-2)(n-4)\ldots(2) & \textit{for} \quad n = even \\ (n)(n-2)(n-4)\ldots(1) & \textit{for} \quad n = odd \\ 1 & \textit{for} \quad n = 0 \\ 1 & \textit{for} \quad n = -1 \\ -1 & \textit{for} \quad n = -3 \end{cases}$$

Substituting equation (A.6) back into equation (A.5) gives the following:

$$\int_0^1 \bar{\phi}_q^p(\bar{r}) r \sqrt{1 - \bar{r}^2} \left[\int_0^{2\pi} \Lambda(\bar{r}, \psi) \cos(p\psi) \, d\psi \right] d\bar{r}$$

$$= \sum_n^\infty \left[\frac{\pi}{4\sqrt{H_n^p H_q^p}} \delta_{mp} \right] a_n^p \bar{c}(p)$$

$$= \frac{\pi \bar{c}(p)}{4 H_q^p} a_q^p \tag{A.8}$$

Solving equation (A.8) for the unknown coefficient a_q^p one gets:

$$a_q^p = \frac{4 H_q^p}{\pi \bar{c}(p)} \int_0^1 \bar{\phi}_q^p(\bar{r}) \bar{r} \sqrt{1 - \bar{r}^2} \left[\int_0^{2\pi} \Lambda(\bar{r}, \psi) \cos(p\psi) \, d\psi \right] d\bar{r} \tag{A.9}$$

noting that $p = 0, 1, 2, \ldots, \infty$ and $q = p + 1, p + 3, \ldots, \infty$. Equation (A.9) gives the unknown a_q^p coefficients of equation (A.1) given a function $\Lambda(\bar{r}, \psi)$. A similar derivation can be performed for the b_q^p coefficients, which results in the following:

$$b_q^p = \frac{4H_q^p}{\pi \bar{c}(p)} \int_0^1 \bar{\phi}_q^p(\bar{r}) \bar{r} \sqrt{1 - \bar{r}^2} \left[\int_0^{2\pi} \Lambda(\bar{r}, \psi) \sin(p\psi) \, d\psi \right] d\bar{r} \qquad (A.10)$$

noting that $p = 1, 2, \ldots, \infty$ and $q = p + 1, p + 3, \ldots, \infty$. For this application, the integrals in equations (A.9) and (A.10) are computed using the trapezoidal rule.

In order to filter the function to a contain a particular frequency content, it is necessary to truncate the summation to limit the number of a_q^p and b_q^p coefficients to a specified number of harmonics such that $p = 0, 1, 2, \ldots, p_{max}$ for the a_q^p coefficient and $p = 1, 2, \ldots, p_{max}$ for the b_q^p coefficient. In this implementation, the above limits set the number of shape functions to $q = p + 1, p + 3, \ldots, p_{max}$. Renaming the indices, and applying truncation to the summations, the filtered value of $\Lambda(\bar{r}, \psi)$, shown below as $\bar{\Lambda}(\bar{r}, \psi)$, is as follows:

$$\bar{\Lambda}(\bar{r}, \psi) = \sum_m^{m_{max}} \sum_n^{m_{max}+1} \bar{\phi}_n^m(\bar{r}) \left[a_n^m \cos(m\psi) + b_n^m \sin(m\psi) \right] \qquad (A.11)$$

where, m is the harmonic number index, n is the shape function index, and m_{max} is the number of harmonics used. It should be noted that the number of shape functions used is equal the number of harmonics used, plus one ($n_{max} = m_{max} + 1$). Thus, compacting the above notation and referring to the terminology of chapter 5, the following filtering operation is defined:

$$\mathcal{F}(\Lambda) = \bar{\Lambda} \qquad (A.12)$$

Vita

David Douglas Boyd, Jr. (Doug) was born in Atlanta, Georgia on July 1, 1965. He graduated from Tucker High School, Tucker, Georgia, in 1983. He then entered the Georgia Institute of Technology where he received his Bachelor of Science and Master of Science degrees in Aerospace Engineering in 1987 and 1988, respectively. Thereafter, from 1990 to 1996, he was employed by Lockheed Engineering and Sciences Company where he provided support to the Fluid Mechanics and Acoustics Division at the NASA Langley Research Center in the area of rotorcraft comprehensive analysis and rotorcraft acoustic predictions. Currently, he is employed by Virginia Polytechnic Institute and State University, working on a cooperative research agreement with the Subsonic Aerodynamics Branch of NASA Langley Research Center exploring the unsteady, aerodynamic interactional effects between a helicopter rotor and fuselage. Doug is a member of the American Helicopter Society and the American Institute of Aeronautics and Astronautics. To date, he has been author and/or coauthor of eleven technical publications.

APPENDIX III

AIAA 2000-0256

A Computational Model for Rotor-Fuselage Interactional Aerodynamics

D. Douglas Boyd, Jr. and Richard W. Barnwell
Virginia Polytechnic Institute and State University
Virginia Consortium of Engineering and Sciences Universities
Hampton, Virginia

Susan Althoff Gorton
Aeroflightdynamics Directorate (AvRDEC)
U.S. Army Aviation and Missile Command
NASA Langley Research Center
Hampton, Virginia

38th Aerospace Sciences
Meeting & Exhibit
January 10-13, 2000/Reno, NV

A COMPUTATIONAL MODEL FOR ROTOR-FUSELAGE INTERACTIONAL AERODYNAMICS

D. Douglas Boyd, Jr.[*] and Richard W. Barnwell[†]
Virginia Polytechnic Institute and State University
Virginia Consortium of Engineering and Sciences Universities
Hampton, Virginia

Susan Althoff Gorton[‡]
Aeroflightdynamics Directorate (AvRDEC)
U.S. Army Aviation and Missile Command
NASA Langley Research Center
Hampton, Virginia

Abstract

A novel unsteady rotor-fuselage interactional aerodynamics model has been developed. This model loosely couples a Generalized Dynamic Wake Theory (GDWT) to a thin-layer Navier-Stokes solution procedure. This coupling is achieved using an unsteady pressure jump boundary condition in the Navier-Stokes model. The new unsteady pressure jump boundary condition models each rotor blade as a moving pressure jump which travels around the rotor azimuth and is applied between two adjacent planes in a cylindrical, non-rotating grid. Comparisons are made between measured and predicted time-averaged and time-accurate rotor inflow ratios. Additional comparisons are made between measured and predicted unsteady surface pressures on the top centerline and sides of the fuselage.

Introduction

It is well known that rotorcraft aerodynamics is a complicated topic. Due to the combination of various systems associated with rotorcraft, these aerodynamic phenomena are unsteady, even in level, unaccelerated flight. Complicating these issues are the facts that typical rotorcraft in service today have bluff aft regions, which can lead to large regions of flow separation, and that there can be significant aerodynamic interaction or interference between the rotating and non-rotating components of the system.

When designing a new rotorcraft, as with any flight vehicle, an understanding of the aerodynamic environment, including aerodynamic interaction of the different vehicle components, is essential. These interactional effects have been known and categorized for many years. This paper focuses on the "rotor-fuselage" and "fuselage-rotor" subsets of the categories offered by Sheridan and Smith.[1] In practice, information on specific interactional effects may be obtained using any combination of wind tunnel testing and/or computational modeling.

Wind tunnel testing has been relied upon heavily in designing new rotorcraft and diagnosing and correcting aerodynamic anomalies discovered on actual flight vehicles because computational modeling of rotorcraft aerodynamics is still in its infancy and lags well behind the computational capabilities used for fixed wing vehicle modeling. Several factors have led to this situation. One of these is the fact that, as mentioned above, even in level, unaccelerated flight, a rotorcraft is operating in an unsteady aerodynamic environment due to the rotation of the rotor system. A fixed wing aircraft in the same situation would be in a steady state environment. The computational implication of this is that a complete rotorcraft simulation would necessarily be a time-accurate computation, whereas the fixed wing simulation could be a steady-state computation. Another factor is associated with the vastly different time and length scales associated with rotorcraft. Some unsteady aerodynamic events, such as blade-vortex interaction, occur at length scales that are a small fraction of a blade chord and at time scales that are equivalent to a tiny fraction of a rotor revolution. To capture these effects, very small time steps would be required. However, determining the trim state of a rotorcraft requires balancing the gross forces on the rotorcraft that have a length scale on the order of the ro-
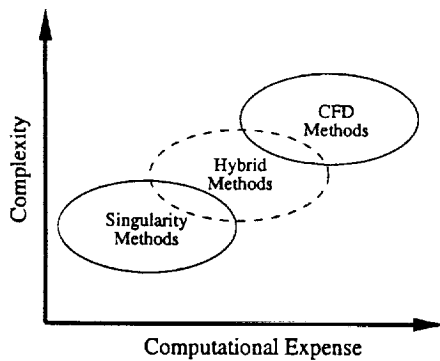
Figure 1. Analysis types for coupled solutions.

tor radius (*i.e.*, many chord lengths) over a relatively long time scale, equivalent to a number of rotor revolutions. The computational implication of these vastly different time scales is that a time-accurate simulation would need to be executed for many time steps.

There are a number of methods available for computation of the interactional aerodynamic effects associated with rotorcraft. Figure 1 categorizes these methods into three areas: Singularity Methods, Hybrid Methods, and Computational Fluid Dynamic (CFD) Methods. Each of these methods has been used in the past for computation of rotorcraft interactional aerodynamics, and each method has advantages and disadvantages.

Singularity Methods

Singularity methods typically use linear superpositions of solutions of Laplace's equation (*i.e.*, source, sink, doublet, vortex elements) to model systems that may include the fuselage, the fuselage wake, the rotor blades, and the rotor wake. Johnson[2] provides an extensive discussion of singularity methods used for rotorcraft analyses up through the year 1986. Boyd[3] discusses other examples of analyses along these lines that have been published since that time. These analyses have shown varying degrees of success. It is apparent from these references that (1) one of the primary advantages of these methods is that they are typically computationally efficient and (2) one of the primary disadvantages is the inability to adequately account for viscous effects.

CFD Methods

In recent years, CFD methods, including methods to solve the full potential equation, the Euler equations, and the Navier-Stokes equations, have become available.[4-14] In general, the full potential and Euler methods, like the singularity methods, have the advantage that they are relatively efficient computationally and are quite useful in some applications where viscous effects are not domi-

nant. However, a disadvantage is that, for computing rotor-fuselage interactional effects that include viscous effects, a boundary layer coupling model must be employed with these methods. To fully integrate the viscous computation, Navier-Stokes methods should be employed. Only a few examples of Navier-Stokes computations are present in the literature. In one of these, Meakin[14] used the Navier-Stokes equations to compute the time-accurate flowfield around a V-22 tiltrotor vehicle, including the rotor. This computation was primarily geared toward demonstrating moving, chimera grid technology and is not currently a practical capability due to the large CPU times required. In general, solutions to the Navier-Stokes equations for interactional aerodynamics problems, where everything is modeled in one large computation, are not currently practical for routine use.

Hybrid Methods

With the expense of Navier-Stokes methods for compete rotorcraft out of reach for routine computations, a practical, engineering solution is to use a hybrid approach. In hybrid approaches, several different methods complement each other. For example, Steinhoff, *et al.*[15] combined a vorticity capturing method with a Navier-Stokes method to reduce artificial dissipation effects on rotor wake vortices, which in turn relaxes the grid resolution requirement to resolve and maintain a rotor wake vortex in the solution procedure. Boyd and Barnwell[16] first introduced a hybrid method that loosely couples a Generalized Dynamic Wake Theory[17-20] (GDWT) with a Navier-Stokes method. Boyd[3] extended that method to include both a fuselage and a rotor and computed unsteady fuselage surface pressures and unsteady inflow for a complete configuration.

The current work uses the method of Boyd[3] and presents results using that method. Below, a brief description of the method is provided for completeness.

Computational Method

The current computation method is a hybrid method that loosely couples the GDWT to a Navier-Stokes method, OVERFLOW . The details of this coupling can be found in Boyd,[3] but a brief outline is presented here.

As discussed earlier, determination of the gross loading and rotor trim requires many revolutions of the rotor. As such, this computationally expensive portion of the method is separated from the CFD portion of the computation. This separation greatly reduces the time spent on time-accurate computations in the CFD portion of method. Based on the above assumption, the current method splits the interactional aerodynamics problem into three distinct pieces: (1) the Rotor Loading
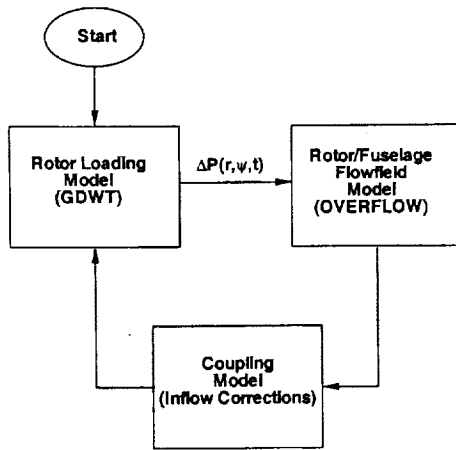
Figure 2. Current hybrid method.

Model, (2) the Rotor/Fuselage Flowfield Model, and (3) the Coupling Model. The arrangement of these pieces is shown in figure 2.

Rotor Loading Model

To reduce the computational expense of the entire process, a model is used to determine the loading distribution on and the trim state of the helicopter rotor. The model used here is based on the GDWT as discussed above. This model uses a solution of the Laplace equation for a isolated, circular wing developed by Kinner.[21] Essentially, Kinner's solution provides admissible acceleration potential functions on the circular wing. To determine the unknown coefficients in Kinner's solution, Peters, Boyd, He,[18] He,[17] and Peters and He,[19] used the linearized Euler equations, the continuity equation, and special rotor boundary conditions, to relate the Kinner acceleration potential to the induced inflow at the rotor disk. For the current research, the resulting closed form matrix equations are iteratively solved in conjunction with a modified Newton-Raphson trim technique to determine the unsteady induced inflow, the trim state, and the unsteady loading distribution of the isolated rotor.

With the solution of the GDWT for the isolated rotor, the "Rotor Loading Model" portion of figure 2 is complete. In figure 2 it can be seen that the pressure (loading) distribution from the Rotor Loading Model is used in the "Rotor/Fuselage Flowfield Model".

Rotor/Fuselage Flowfield Model

Now, with a known pressure distribution on the rotor disk, a Rotor/Fuselage Flowfield Model is used to solve the Navier-Stokes equations. For this model, a thin-layer, Navier-Stokes code (OVERFLOW[22]) has been modified to include an unsteady boundary condition. For this new boundary condition, a cylindrical, non-rotating grid is

used to represent the rotor. The predetermined pressure distribution is applied as an additional term in the energy equation as follows:

$$\Delta(\rho e_0) = \frac{A(\bar{r})\Delta P}{\gamma - 1} \qquad (1)$$

where equation (1) is in terms of the non-dimensional quantities used in OVERFLOW and $A(\bar{r})$ is the ratio between the local actual blade area and the local computational cell area at a given radial station on the blade. This ratio is used to maintain the correct overall thrust. The additional conservative energy term in equation (1) is then split into two parts. One half of the term is applied to the "upper rotor plane" (see figure 3b) and the negative of the other half of the term is applied to the "lower rotor plane". This procedure effectively creates a pressure jump between two planes in the rotor grid, separated by an "iblanked plane" which ensures that the artificial dissipation terms, which operate on a pressure discontinuity, do not modify the input pressure distribution at the rotor plane. All remaining flow quantities on the upper and lower rotor planes are determined by averaging the quantities at planes "A" and "B" in figure 3b. Figure 3a shows a top view of the rotor grid used in figure 3b. In this top view, a rectangular section is used to represent the actual blade area, and a shaded wedge represents the computational area (these areas are not to scale). Only one blade is represented in this figure.

For a multibladed rotor, one of these computational wedges exists for each blade. A radially varying, additional conservative energy term is applied along each of these computational wedges for each blade. At each time step in the time-accurate solution procedure, the pressure jump "travels" around the rotor azimuth direction, one grid line per time step. This unsteady boundary condition effectively represents the rotor blades as a pressure jump traveling around the rotor azimuth on a non-rotating, cylindrical grid.

Using the chimera grid techniques available in OVER-FLOW, the above rotor grid is combined with other grids which represent the fuselage and the remaining flowfield. OVERFLOW then solves the time-accurate, thin-layer Navier-Stokes equations on this set of grids, along with the unsteady, pressure jump boundary condition. The solution procedure is executed until the initial transients are removed and a periodic flowfield is obtained.

Since the specified pressure jump was originally determined by an isolated rotor model, the pressure jump boundary condition does not represent the combined rotor-fuselage system. Therefore, once a periodic solution has been obtained with the original pressure jump boundary condition, an "Inflow Correction" method is used to account for the presence of the fuselage in the Rotor Loading Model. Discussion of this method is be-
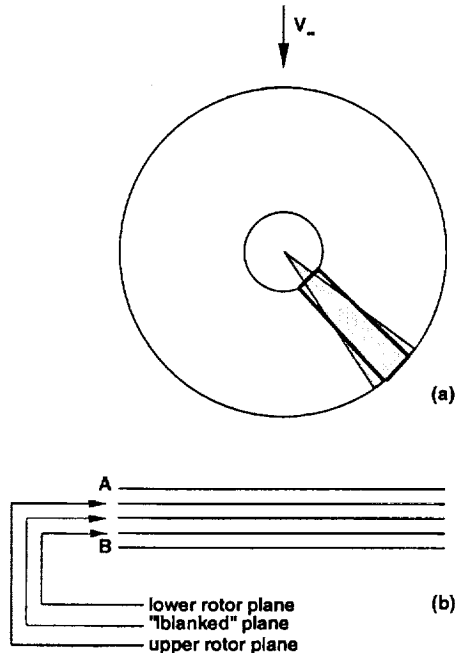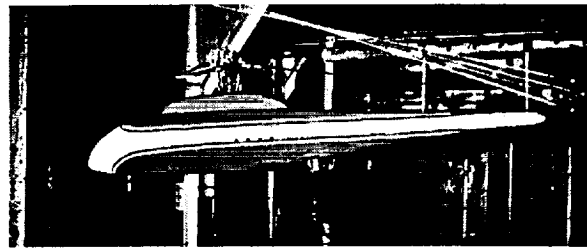
Figure 4. Laser velocimeter experiment, NASA Langley Research Center 14- by 22-Foot Subsonic Tunnel.

The LV measurements were processed at an azimuthal resolution of approximately 2.8°. Comparisons to both the time-averaged and the time dependent measured data will be made subsequently.

Figure 3. Schematic of new boundary condition.
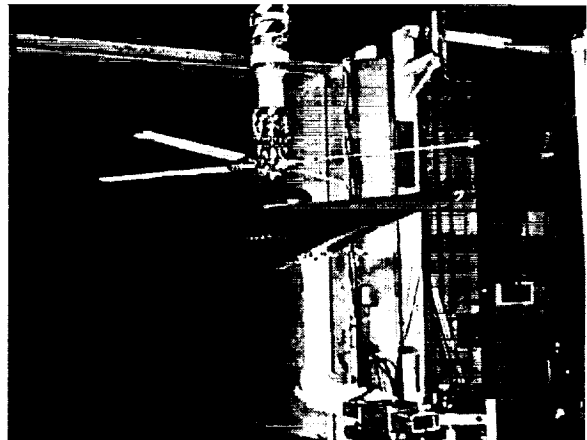
Figure 5. Unsteady surface pressure experiment, NASA Langley Research Center 14- by 22-Foot Subsonic Tunnel.

yond the scope of this paper, but is discussed in detail in Boyd.[3] Figure 2 shows the location of the "Coupling Model (Inflow Corrections)" portion of the model.

With these inflow corrections, the GDWT model is re-executed to obtain a new unsteady pressure jump boundary condition that has been corrected to account for the presence of the fuselage. This cycle is repeated until there is no significant solution change between iterations.

Results

Experimental Setup

Results from the computational method discussed above will be compared to experimental data. The experiments used here are discussed in other references,[3,23] but are discussed briefly here for completeness. There are two experiments that are used here. The first experiment ("Experiment 1"), reported by Elliott, Althoff, and Sailey,[23] used a Laser Velocimetry (LV) system to measure the induced inflow in a plane that was one rotor blade chord above the rotor tip path plane. These measurements were carried out for the combination of a generic helicopter fuselage (known as the ROtor Body INteraction (ROBIN) fuselage) and a four-bladed, rect-angular rotor system in the NASA Langley Research Center 14- by 22-Foot Subsonic Tunnel (see figure 4).

The second experiment ("Experiment 2") used here was carried out by the third author and her colleagues, again using the ROBIN fuselage with the same rectangular rotor system. The primary difference in the configuration between the first and second experiments is that, in the first experiment, the rotor drive system was contained inside the fuselage shell, whereas, in the second experiment, the rotor and fuselage were mounted on separate systems. That is, in the second experiment, the rotor drive system was mounted to the tunnel ceiling and the fuselage was sting mounted on a post attached to the tunnel floor (see figure 5). This experiment was conducted in two phases: (1) an isolated rotor configuration (with the fuselage lowered to the tunnel floor) and (2) a rotor/fuselage configuration (with the fuselage in place). In the first phase of this test, unsteady inflow measurements were made at a limited number of locations on the advancing side of the rotor, one chord above the tip path

plane. In the second phase of the experiment, unsteady surface pressures were measured along the top centerline of the fuselage and at several locations on the sides of the fuselage. The data presented here are a small subset of the total data taken in the second experiment. Subsequent comparisons will be made to these unsteady inflow and unsteady surface pressure data. Table 1 lists several of the operating conditions and rotor parameters associated with both Experiments 1 and 2.

Table 1. Operating conditions and rotor parameters.

Property	Value
Blade planform	Rectangular
radius	0.8606 meters
root chord	0.0660 meters
tip chord	0.0660 meters
number of blades	4
root cutout location	0.24R
flap/lag hinge location	0.06R
airfoil section	NACA 0012
twist	-8°
nominal thrust coefficient	0.0065
solidity	0.0977
nominal hover M_{tip}	0.55
approx. mean coning angle	1°
shaft tilt	3° nose down

Induced Inflow Comparisons

Time-Averaged Induced Inflow

Once the iteration procedure has concluded, as discussed in Boyd,[3] comparisons between a number of quantities are possible. For these comparisons, the current model was executed with and without a fuselage in the solution procedure. As shown in Boyd and Barnwell[16] and Boyd,[3] the current model is also applicable to an isolated rotor configuration (i.e., no fuselage).

First, a comparison is presented between the measured and predicted, time-averaged induced inflow. Inflow ratio is defined as the local velocity divided by the rotor tip speed. The measurement data are from Experiment 1 at a plane that is one blade chord above the tip path plane of the rotor at a rotor advance ratio of $\mu = 0.23$. The predicted results are from the same location above the rotor tip path plane and are at the same operating condition used in Experiment 1. The rotor tip speed is used to make the data and predicted results nondimensional.

Figure 6a shows the measured, time-averaged induced inflow ratio parallel to the rotor tip path plane from Experiment 1. These experimental data show an induced inflow pattern that is not symmetric between the advancing and retreating sides of the rotor. For example, the contour

line with a value of 0.015 shows that the induced inflow is asymmetric about the fore-aft plane of the rotor. Figure 6b shows the predicted, time-averaged induced inflow ratio parallel to the rotor tip path plane for the isolated rotor configuration. Although the magnitudes are similar to the measured values, the inflow distribution does not match the measured distribution well. Here, unlike the measured data, the predicted induced inflow is somewhat symmetric between the advancing and retreating sides of the rotor. Figure 6c shows the predicted, time-averaged induced inflow ratio parallel to the rotor tip path plane for the full rotor-fuselage configuration. It is seen that the fuselage has a large impact on the inflow distribution. As with the isolated rotor configuration, the magnitude of the inflow matches the measured data well. In addition, the distribution of inflow now matches the experimental data well, including the asymmetric pattern seen in the measured data. Figure 6d shows the difference between the full rotor-fuselage configuration and the isolated rotor configuration. This difference plot shows the effect of the fuselage on the in-plane induced inflow. As would be expected for a fuselage, there is a deceleration of the flow over the forward portion of the rotor disk due to the upward slope of the nose of the fuselage and a subsequent re-direction of the flow. Over the rear portion of the rotor disk, there is an acceleration of the flow due to the downward slope of the rear portion of the pylon.

Figure 7a shows the measured, time-averaged induced inflow ratio perpendicular to the rotor tip path plane from Experiment 1. These measured data show several typical features of time-averaged induced inflow. First, there is an upwash on the forward portion of the rotor disk. Second, there is an increased downward inflow toward the rear portion of the disk with concentrations in the first and fourth rotor quadrants. Figure 7b shows the predicted, time-averaged induced inflow ratio perpendicular to the rotor tip path plane for the isolated rotor configuration. This configuration exhibits many of the same features as the measured data. For example, there is an upwash on the forward portion of the rotor disk, but that upwash is not as prominent as in the measured data. Figure 7c shows the predicted, time-averaged induced inflow ratio perpendicular to the rotor tip path plane for the full rotor-fuselage configuration. The magnitude as well as the inflow distribution is well matched when the fuselage is included in the computation. Figure 7d shows the difference between the full rotor-fuselage configuration and the isolated rotor configuration. Again, this figure displays features that are expected due to the presence of a fuselage. For example, there is an increased upwash over the forward portion of the disk as the flow is deflected upward over the nose of the fuselage, and there is an increased downwash at the rear of the rotor disk, just aft of the pylon, as the flow accelerates downward just

behind the fuselage pylon.

<u>Time-Accurate Induced Inflow</u>

The previous section showed that the time-averaged induced inflow in the parallel and perpendicular directions (relative to the rotor tip path plane) are well predicted by the current unsteady method. This section will present comparisons of the measured and predicted unsteady inflow data corresponding to the same flight conditions used in Experiment 1. The measured data presented here is from the first phase of Experiment 2 (isolated rotor configuration).

Figure 8 shows the measured and predicted unsteady induced inflow ratios. These inflow ratios are at an azimuthal location of $\psi = 84°$ and a blade radial location of $r/R = 0.80$. Both the isolated rotor and combined rotor-fuselage configuration are shown. Both components are well predicted, especially the inplane component. For this particular location, the presence of the fuselage has only a minor impact on the predicted unsteady induced inflow. Previous literature has shown[3,16] that these induced inflow ratios are typically well predicted over the entire rotor disk.

<u>Unsteady Surface Pressure</u>

In Experiment 2, unsteady surface pressure measurements were made for the same flight configuration and the same flight conditions as in Experiment 1. These measurements were made along the top centerline of the fuselage and at several locations on the sides of the fuselage. Comparisons are made here between the measured and predicted unsteady surface pressures along the top centerline and at several locations on the advancing and retreating sides of the fuselage. These pressure taps on the sides of the fuselage were located at several vertical locations and at a constant 44% of the fuselage length.

For these comparisons, a modified pressure coefficient is used. This modified pressure coefficient is defined in equation (2) and is used to avoid numerical problems associated with the definition of the standard pressure coefficient when the freestream velocity approaches zero (as would be the case in hover).

$$C_p' = \frac{100(P - P_\infty)}{\frac{1}{2}\rho(\Omega R)^2} \quad (2)$$

In equation (2), P is the local pressure, P_∞ is the freestream pressure, ρ is the freestream density, ΩR is the rotor tip speed, and the factor of 100 is included for numerical convenience. For reference, equation (3) shows the relation between the standard pressure coefficient and the modified pressure coefficient used here.

$$C_p' = 100\mu_\infty^2 C_p \quad (3)$$

In equation (3), μ_∞ is the standard rotor advance ratio and C_p is defined in the usual way.

Figure 9 shows a comparison of the unsteady component of the measured and predicted modified pressure coefficient on the top centerline of the fuselage at various stations along the length of the 2 meter long fuselage. The location of the reference blade is plotted along the horizontal axis, and the negative of the modified pressure coefficient is plotted along the vertical axis. Since this is a four-bladed rotor, a dominant pressure pulse can be seen at a frequency of four pulses per rotor revolution. This is indicative of the four blades individually passing over each measurement location. It can be seen that the phase of each of the predictions matches the measured phase well; however, the amplitudes are slightly overpredicted.

Figure 10 shows a comparison of the unsteady component of the measured and predicted modified pressure coefficient on the left and right sides (retreating and advancing sides, respectively) of the fuselage at a constant downstream location of $x = 0.8809$ meters ($x/L \approx 0.44$) for several vertical locations. Again, the reference blade location is on the horizontal axis, and the negative of the modified pressure coefficient is on the vertical axis. The retreating side comparisons show that the unsteady pressures are slightly overpredicted, while the advancing side unsteady pressures are well matched in magnitude and phase.

<u>Conclusions</u>

A novel computational model for unsteady rotorcraft interactional aerodynamics has been presented. This new hybrid model couples a rotor loading model and a rotor/fuselage flowfield model in a manner that is efficient and capable of predicting time-averaged and time-accurate rotor inflow ratios and unsteady surface pressures on the fuselage due to blade passages.

<u>References</u>

1. Sheridan P.F. and R.P. Smith. Interational Aerodynamics - A New Challenge to Helicopter Technology. Washington, D.C., May 1979. *Presented at the 35th Annual American Helicopter Society Forum.*

2. W. Johnson. Recent Developments in Rotary-Wing Aerodynamic Theory. *AIAA Journal*, 24(8):1219–1244, August 1986.

3. D.D. Boyd, Jr. *Rotor-Fuselage Interaction Aerodynamics: A New Computation Model.* PhD thesis, Virginia Polytechnic Institute and State University, July, 1999.

4. C.S. Chen and J.O. Bridgeman. Three-Dimensional Viscous Rotor Flow Calculations Using Boundary Layer Equations. Amsterdam, Netherlands, Septem-

ber 12-15, 1989. *Presented at the 15th European Rotorcraft Forum.*

5. J.O. Bridgeman, D.S. Prichard, and F.X. Caradonna. The Development of a CFD Potential Method for the Analysis of Tilt-Rotors. In *Preceedings of the AHS Technical Specialists Meeting on Rotorcraft Acoustics and Fluid Dynamics*, Philadelphia, PA, October 15-17, 1991.

6. R.C. Strawn. Wing-Tip Vortex Calculations with an Unstructured Adaptive-Grid Euler Solver. In *Preceedings of the 47th Annual American Helicopter Society Forum*, Pheonix, AZ, May 1991.

7. T.J. Barth. A 3-D Upwind Euler Solver for Unstructured Meshes. Honolulu, HI, June 1991. Paper AIAA-91-1548.

8. R.C. Strawn and T.J. Barth. A Finite-Volume Euler Solver for Computing Rotary-Wing Aerodynamics on Unstructured Meshes. In *Preceedings of the 48th Annual American Helicopter Society Forum*, Washington, D.C., June 1992.

9. L.A.J. Zori and R.G. Rajagopolan. Navier-Stokes Calculations of Rotor-Airframe Interaction in Forward Flight. Washington, D.C., June 1992. *Presented at the 48th Annual American Helicopter Society Forum.*

10. R.G. Rajagopolan and Z. Zhaoxing. Performance and Flow Field of a Ducted Propellor. Monterey, CA, July 10-12, 1989. *Presented at the AIAA/ASME/SAE/ASEE 25th Joint Propulsion Conference.*

11. R.G. Rajagopolan and S.J. Mathur. Three Dimensional Analysis of a Rotor in Forward Flight. *Journal of the American Helicopter Society*, July 1993.

12. M.S. Chaffin and J.D. Berry. Navier-Stokes Simulation of a Rotor Using a Distributed Pressure Disk Method. In *Preceedings of the 51st Annual American Helicopter Society Forum*, volume I, pages 112–136, Ft. Worth, TX, May 1995.

13. J.D. Berry, V.B. Letnikov, I. Bavykina, and M.S. Chaffin. A Comparison of Interactional Aerodynamics Methods for a Helicopter in Low Speed Forward Flight. In *Proceedings of the 23rd European Rotorcraft Forum*, volume I, pages 33.1–33.9, Dresden, Germany, September 16-18, 1997.

14. R. Meakin. Moving Body Overset Grid Methods for Complete Aircraft Tiltrotor Simulations. Orlando, FL, June 6-9, 1993. *Presented at the 11th AIAA Computational Fluid Dynamics Conference.*

15. J. Steinhoff, W. Yonghu, T. Mersch, and H. Senge. Computational Vorticity Capturing: Application to Helicopter Rotor Flow. In *30th Aerospace Sciences Meeting and Exibit*, Reno, NV, January 6-9, 1992. Paper AIAA-92-0056.

16. D.D. Boyd, Jr. and R.W. Barnwell. Rotor-Fuselage Interactional Aerodynamics: An Unsteady Rotor Model. In *Preceedings of the 54th Annual American Helicopter Society Forum*, volume I, pages 23–44, Washington, D.C., May 20-22, 1998.

17. C.J. He. *Development and Application of a Generalized Dynamic Wake Theory For Lifting Rotors*. PhD thesis, Georgia Institute of Technology, Atlanta, GA, July 1989.

18. D.A. Peters, D.D. Boyd, Jr., and C.J. He. Finite State Induced Inflow Model for Rotors in Hover and Forward Flight. St. Louis, MO, May 18-20, 1987. *Presented at the 43rd Annual American Helicopter Society Forum.*

19. D.A. Peters and C.J. He. Correlation of Measured Induced Velocities with a Finite-State Wake Model. Boston, MA, May 1989. *Presented at the 45th Annual American Helicopter Society Forum.*

20. D.A. Peters and C.J. He. Finite State Induced Inflow Models Part II: Three Dimensional Rotor Disk. *Journal of Aircraft*, Volume 32(Number 2), March-April 1995.

21. W. Kinner. The Potential Theory of Airfoils of Circular Planform. *Ingenieur-Archiv*, 8(1):47–80, February 1937.

22. P.G. Buning, D.C. Jespersen, T.H. Pulliam, W.M. Chan, J.P. Slotnick, S.E. Krist, and K.J. Renze. OVERFLOW User's Manual: Version 1.8, February 23 1998.

23. J.W. Elliott, Susan L. Althoff, and R.H. Sailey. Inflow Measurement Made With a Laser Velocimeter on a Helicopter Model in Forward Flight - Volume II: Rectangular Planform Blades at an Advance Ratio of 0.23. NASA TM 100542, April 1988.
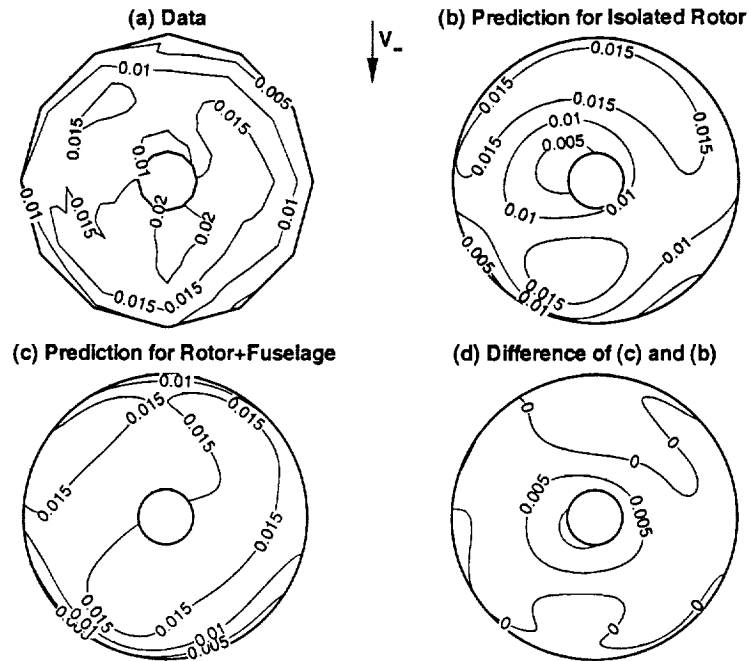
(a) Data　　　　　　　**(b) Prediction for Isolated Rotor**

(c) Prediction for Rotor+Fuselage　　**(d) Difference of (c) and (b)**

Figure 6. Measured and predicted time averaged parallel induced inflow ratio from time accurate computations.

(a) Data　　　　　　　**(b) Prediction for Isolated Rotor**

—— downwash
– – upwash

(c) Prediction for Rotor+Fuselage　　**(d) Difference of (c) and (b)**
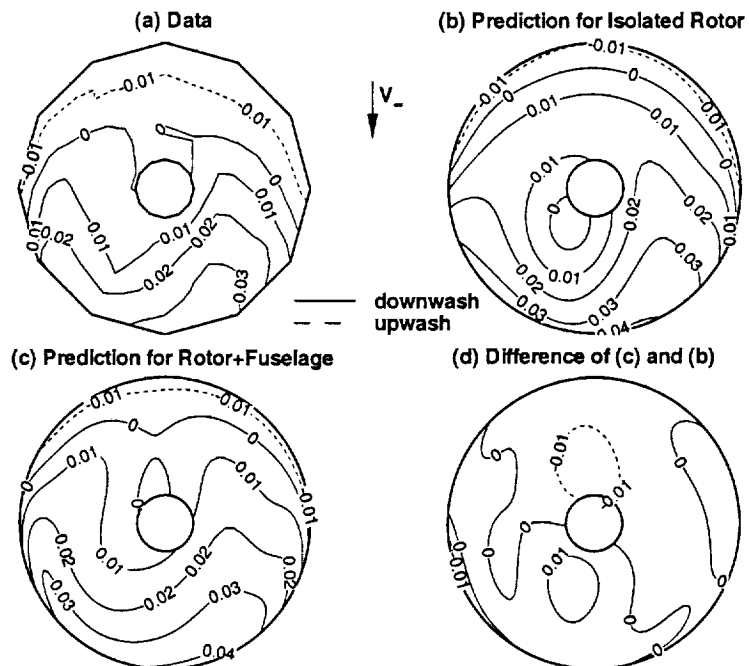
Figure 7. Measured and predicted time averaged perpendicular induced inflow ratio from time accurate computations.
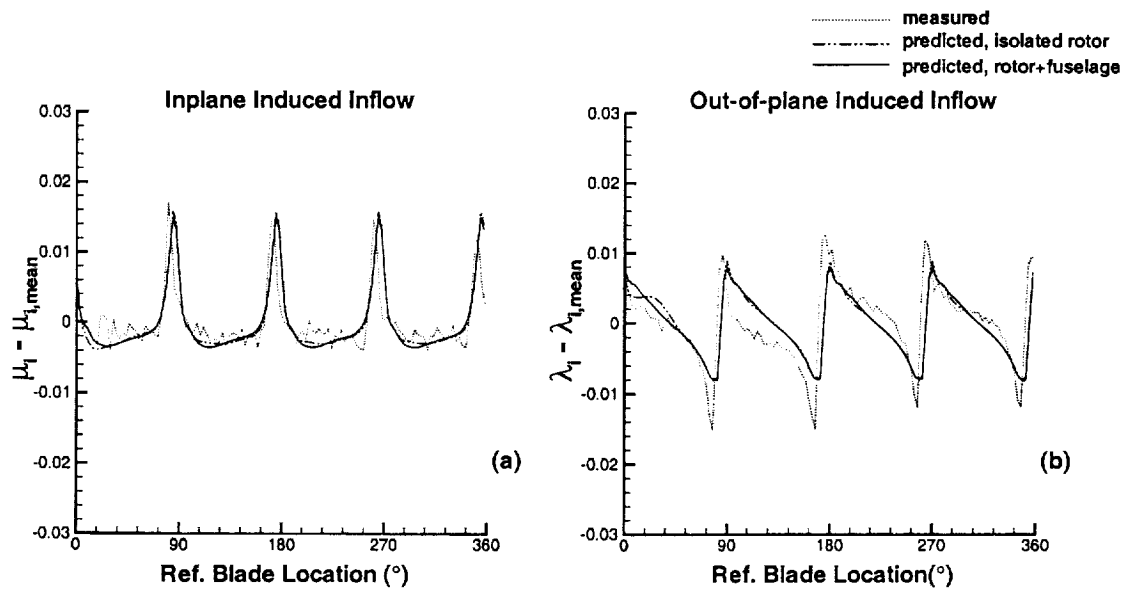
Figure 8. Measured and predicted induced inflow in two directions for an isolated rotor and a rotor/fuselage combination.
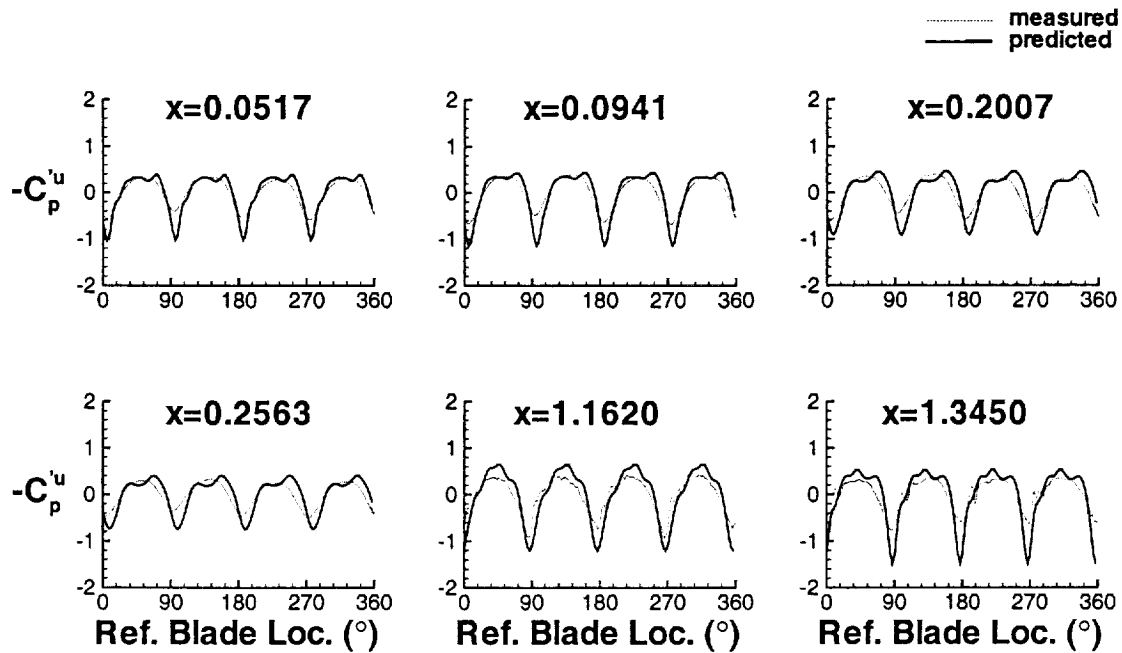
Figure 9. Measured and predicted unsteady modified pressure coefficient on the top centerline of the ROBIN fuselage. "x" denotes the distance in meters from the nose of the 2 meter long fuselage.
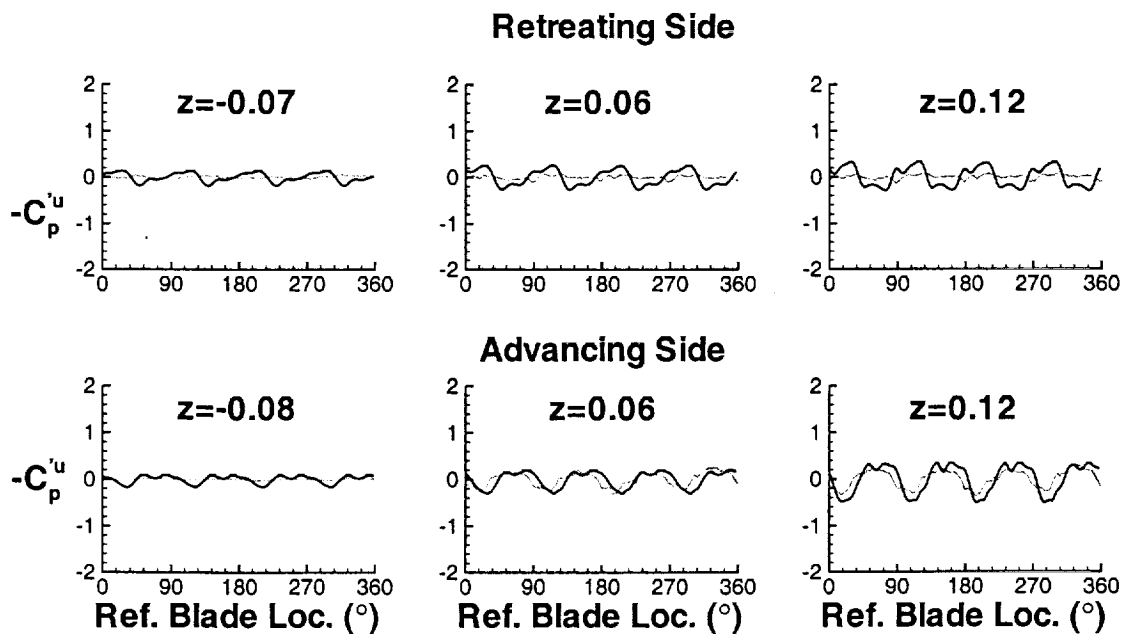

Figure 10. Measured and predicted unsteady modified pressure coefficient on the retreating and advancing sides of the ROBIN fuselage. "z" denotes the distance measured in meters from the horizontal reference line of the fuselage.